Technische Universität München
TUM School of Natural Sciences

Komplexe Telluride mit schaltbaren Eigenschaften

Anna Vogel

Vollständiger Abdruck der von der TUM School of Natural Sciences der Technischen Universität München zur Erlangung einer

Doktorin der Naturwissenschaften (Dr. rer. nat.)

genehmigten Dissertation.

Vorsitz: Prof. Dr. Thomas F. Fässler

Prüfer*innen der Dissertation:

1. Prof. Dr. Tom Nilges
2. Prof. Dr. Klaus Köhler
3. apl. Prof. Dr. Thomas Doert

Die Dissertation wurde am 05.08.2022 bei der Technischen Universität München eingereicht und durch die TUM School of Natural Sciences am 12.10.2022 angenommen.

„Ein Element des Erfolgs, egal in welchem Beruf, ist die Lust am Handwerk."

Irène Joliot-Curie

Danksagung

In der Zeit meiner Promotion habe ich große Unterstützung von vielen Seiten erhalten, sowohl fachlicher als auch persönlicher Natur. Dafür möchte ich mich herzlich bedanken. Insbesondere gilt mein Dank:

Meinem Doktorvater Prof. Tom Nilges für die Möglichkeit der Promotion in seiner Arbeitsgruppe, die interessante und offene Themenstellung, die immer offene Tür, Rat und Hilfe bei Problemen und die langen gemeinsamen Aufenthalte im reziproken Raum.

Lucia Weissenborn, nicht nur für das ausgezeichnete Management der Arbeitsgruppe und qualifizierte Hilfe in allen organisatorischen Belangen, sondern auch ihr persönliches Engagement, das offene Ohr und die Sorge dafür, dass jeder gut aufgehoben war.
Luci, du fehlst! ♡

Den aktuellen und ehemaligen Mitgliedern meiner Arbeitsgruppe für die konstruktive Arbeitsatmosphäre und gute Zeit innerhalb und außerhalb der Universität. Dabei besonders:
Dr. Claudia Ott für die Betreuung meiner Masterarbeit und die Einweisung in die festkörperchemischen Arbeitsweisen.
Dr. Maximilian Baumgartner für die Einführung in mein Thema, die Weitergabe seines kristallographischen Könnens und und die Einstiegshilfe in die wissenschaftliche Welt.
Patrick Walke für die Impedanzmessungen, Unterstützung bei der Elektro~~magie~~chemie und unzählige Mittags- und Kaffeepausen seit dem ersten Semester.
Philipp Deng und Alfred Rabenbauer für die Mühe und Beharrlichkeit bei der Ausführung der Strom/Spannungs-Messungen sowie Ruben Steib für das PCB-Design.
Dr. Janio Venturini für wissenschaftlichen Input, konstruktive Diskussionen sowie die Koordination einer Vielzahl von Kooperationspartnern.

Thomas Miller und Dr. Constantin Hoch von der Ludwig-Maximilians-Universität München für Hoch- und Tieftemperatur-Pulver-XRD-Messungen.

Matthias Jakob und Prof. Oliver Oeckler von der Universität Leipzig, sowie Thorben Böger und Prof. Wolfgang Zeier von der Universität Münster für die Laser-Flash-Messungen.

Dr. Renée Siegel und Prof. Jürgen Senker von der Universität Bayreuth für die Festkörper-NMR-Messungen.

Kurzfassung

Neue leistungsfähige Materialien für thermoelektrische oder elektronische Anwendungen spielen eine wichtige Rolle bei der Reduzierung des Ausstoßes klimaschädlicher Treibhausgase. In diesem Zusammenhang weist die Substanzklasse der Münzmetall(poly)chalkogenidhalogenide mit hoher Ionenmobilität und Dynamik in der Chalkogenteilstruktur bemerkenswerte Eigenschaften auf. Im Rahmen der Untersuchung dieser Klasse wurde 2009 mit $Ag_{10}Te_4Br_3$ die erste Verbindung charakterisiert, die einen reversiblen Wechsel zwischen p- und n-Halbleitung ohne Änderung der Elementzusammensetzung zeigt. In dieser Arbeit wurden der Substanzklasse drei neue Verbindungen hinzugefügt, darunter die ersten beiden Münzmetallpolychalkogenidhalogenide mit ausschließlich Cu als Münzmetall. $Cu_{9,1}Te_4Cl_3$ ist eine thermoelektrische Verbindung mit hoher elektrischer Leitfähigkeit und geringer Wärmeleitfähigkeit. Wie bei der Substanzklasse üblich, führt die hohe Ionenmobilität zu mehreren Ordnungs-Unordnungs-Phasenübergängen. Auch $Cu_{20}Te_{11}Cl_3$ ist eine polymorphe Verbindung mit hochkomplexer Kristallchemie und vergleichbarer thermoelektrischer Leistungsfähigkeit. Beide Verbindungen zeigen starke strukturelle Ähnlichkeit zur pnp-schaltenden Verbindung $Ag_{10}Te_4Br_3$ ohne selbst pnp-Schaltung aufzuweisen. Durch den Vergleich der Systeme war es möglich, Erkenntnisse über den auslösenden Mechanismus zu gewinnen. Durch Anwendung dieser Erkenntnisse konnte durch Substitution von Cu durch Ag in $Cu_{20}Te_{11}Cl_3$ die pnp-schaltende Verbindung $Ag_{18}Cu_3Te_{11}Cl_3$ synthetisiert werden. Dabei handelt es sich nicht nur um das Material mit dem höchsten bisher gemessenen Seebeck-Sprung, sondern auch um die erste Verbindung dieser Art, die pnp-Schaltung nicht bei erhöhter Temperatur, sondern bei Raumtemperatur zeigt, was mögliche Anwendungen begünstigt. An dieser Verbindung gelang es, die erste schaltbare ortsunabhängige Einkomponenten-Diode zu messen.

Abstract

New high-performance materials for thermoelectric or electronic applications play an important role in reducing emissions of greenhouse gases. In this context, the substance class of coinage metal (poly)chalcogenide halides with high ion mobility and dynamics in the chalcogen substructure has remarkable properties. As part of the investigation of this class in 2009, $Ag_{10}Te_4Br_3$ was characterized as the first compound that shows reversible switching between p- and n-type of semiconduction without changing the elemental composition. In this work, three new compounds were added to the substance class, including the first two coinage metal polychalcogenide halides with only Cu as coinage metal. $Cu_{9.1}Te_4Cl_3$ is a thermoelectric compound with high electrical and low thermal conductivity. As is usual within the substance class, the high ion mobility leads to several order-disorder phase transitions. $Cu_{20}Te_{11}Cl_3$ is also a polymorphic compound with highly complex crystal chemistry and comparable thermoelectric performance. Both compounds show strong structural similarities to the pnp compound $Ag_{10}Te_4Br_3$ without showing pnp switching themselves. By comparing the systems, it was possible to gain knowledge about the mechanism behind. By applying these findings, the pnp compound $Ag_{18}Cu_3Te_{11}Cl_3$ could be synthesized by substituting Ag for Cu in $Cu_{20}Te_{11}Cl_3$. This is the material with the highest Seebeck jump observed so far and the first compound of this type that shows pnp switching at room temperature, which favors possible applications. On this compound, the first switchable position-independent one-component diode was successfully measured.

Erklärung

Diese Arbeit ist als publikationsbasierte Dissertation verfasst. Die Motivation sowie der wissenschaftliche Hintergrund werden als einleitender Teil in **Kapitel 1** behandelt. **Kapitel 2** gibt Auskunft über Synthese- und Charakterisierungsmethoden. **Kapitel 3** enthält die in international anerkannten Fachzeitschriften veröffentlichten und im Peer-Review-Verfahren geprüften Artikel, inklusive einer Zusammenfassung, des genehmigten Abdrucks, der vollständigen bibliographischen Daten sowie der Kennzeichnung der Beiträge der Autoren. Eine Gesamtzusammenfassung und ein Ausblick werden in **Kapitel 4** gegeben. Eine Liste der Veröffentlichungen findet sich in **Kapitel 5**.

Inhaltsverzeichnis

Abkürzungen

DSC	Dynamische Differenzkalorimetrie (Differential Scanning Calorimetrie)
EDX	Energiedispersive Röntgenspektroskopie (Energy Dispersive X-ray spectroscopy)
LFA	Laser Flash Analyse
M	Münzmetall
MAS	Magic Angle Spinning
NMR	Kernspinresonanzspektroskopie (Nuclear Magnetic Resonance spectroscopy)
PCB	Leiterplatte (Printed Circuit Board)
PL	Photolumineszenz
Q	Chalkogen
RLZ	Raumladungszone
SEM	Rasterelektronenmikroskopie (Scanning Electron Microscopy)
SMU	Source Meter Unit
X	Halogen
XRD	Röntgenbeugung (X-Ray Diffraction)

1 Einleitung

Die Herausforderung unserer Zeit ist die Abmilderung des menschgemachten Klimawandels durch die Reduktion des Ausstoßes von klimaschädlichen Treibhausgasen. Um dieses Ziel zu erreichen, müssen sowohl neue, klimafreundliche „grüne" Energiequellen erschlossen, als auch bestehende Technologien hinsichtlich ihrer Energieeffizienz optimiert werden. Eine Möglichkeit die Energieeffizienz von Prozessen zu maximieren, ist der Einsatz von thermoelektrischen Materialien, welche in der Lage sind Abwärme in elektrische Energie umzuwandeln. Ein Maß für die thermoelektrische Leistung eines Materials ist die dimensionslose thermoelektrische Gütezahl ZT. Diese ist definiert als $\sigma \cdot S^2 \cdot \kappa^{-1} \cdot T$, wobei σ die elektrische Leitfähigkeit, S der Seebeck-Koeffizient und κ die Wärmeleitfähigkeit ist. [1] ZT-Werte > 2 werden im Labormaßstab durch Optimierung der Wärmeleitfähigkeit durch Nanostrukturierung, wie Quantenpunkte und Überstrukturen, erreicht. [2–4] Allerdings ist es oft schwierig diese Materialien in größerem Maßstab herzustellen, Sinterung bei höheren Temperaturen im Herstellungsprozess zu vermeiden, sowie die Produktionskosten zu decken. [5] Um anwendbare thermoelektrische Materialien zu erhalten, ist es daher vorteilhaft den ZT-Wert in Bulk-Materialien zu optimieren. [6]

Eine interessante Verbindungsklasse hinsichtlich dessen sind die Münzmetall(poly)chalkogen(id)halogenide. Hohe Ionenmobilität und Dynamik in der Chalkogenteilstruktur begünstigt Phononenstreuung und führt zu extrem niedrigen Wärmeleitfähigkeiten im Bulk-Material. [7] Bei ternären Verbindungen eröffnet sich außerdem die Möglichkeit zahlreicher Substitutionsreaktionen, was die Optimierung der elektronischen Struktur und damit der elektronischen und thermoelektrischen Eigenschaften vereinfacht. [8]

Desweiteren wurde in dieser Verbindungsklasse mit $Ag_{10}Te_4Br_3$ das erste Material gefunden, das durch Änderung der Temperatur reversibel zwischen p- und n-Halbleitung wechseln kann. [9] Diese Eigenschaft eröffnet die Perspektive zahlreicher elektronischer Anwendungen in Datenspeicherung oder Computertechnik. [8]

Im Rahmen dieser Arbeit wurden der Substanzklasse der Münzmetall(poly)chalkogen(id)halogenide drei neue Vertreter hinzugefügt und hinsichtlich ihrer thermoelektrischen Eigenschaften untersucht. Daraus resultierte eine neue pnp-schaltende Verbindung, die diesen Effekt bei Raumtemperatur zeigt, was mögliche Anwendungen begünstigt. An diesem Material konnte die erste schaltbare ortsunabhängige Einkomponenten-Diode gemessen werden, was nicht nur Anwendungsoptionen im Bereich der Elektronik als temperaturgesteuerter Bipolar- oder Feldeffekttransistor in greifbare Nähe rückt, sondern auch Anwendungen in der Elektrokatalyse oder die Realisierung von Einkomponenten-Solarzellen vorstellbar macht.

1.1   Münzmetall(poly)chalkogen(id)halogenide
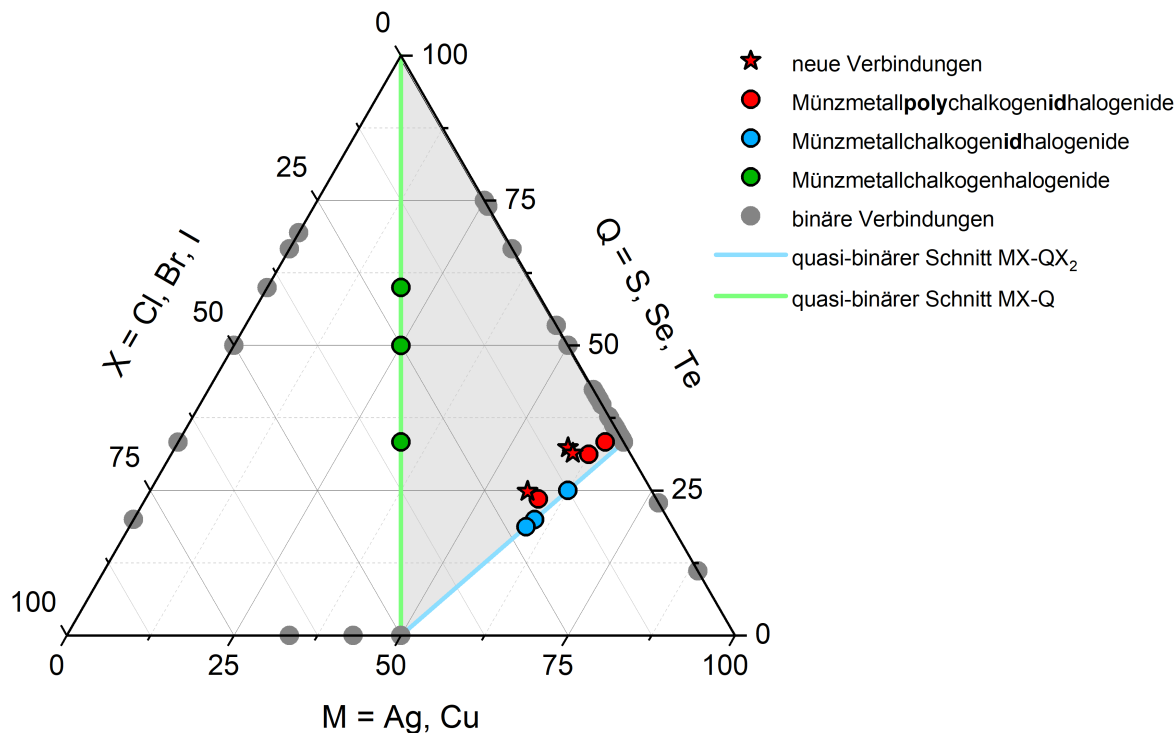
Abbildung 1.1: Ternäres Phasendiagramm der Münzmetall(poly)chalkogen(id)halogenide, ausgenommen der Oxide. Das von den quasi-binären Schnitten MX-Q (grün, kovalente Chalkogenteilstruktur) und MX-MQ$_2$ (blau, ionische Chalkogenteilstruktur) begrenzte, grau hinterlegte Dreieck enthält die Polychalkogenidhalogenide mit ionischer sowie kovalenter Chalkogenteilstruktur. [8]

Ternäre Verbindungen aus Münzmetallen (M = Cu, Ag, Au), Chalkogenen (Q = S, Se, Te) und Halogenen (X = Cl, Br, I) werden in drei Verbindungsklassen unterteilt: Münzmetallchalkogenhalogenide, -chalkogenidhalogenide und -polychalkogenidhalogenide. [8] Die Münzmetallchalkogenhalogenide mit der allgemeinen Formel MQyX mit y = 1, 2, 3 liegen auf dem quasi-binären Schnitt MX-Q und enthalten ausschließlich vollständig kovalent gebundene Chalkogenteilstrukturen. In MQX sowie MQ$_2$X liegen im Fall von Cu und Ag helikale Chalkogenketten vergleichbar den Elementstrukturen vor [10–26], während diese im Fall von Au in Q$_2$-Hanteln zerfallen [27–29]. Neutrale Q$_6$-Ringe treten in MQ$_3$X im Fall von Cu und Ag auf. [30–35]

Auf dem quasi-binären Schnitt MX-M$_2$Q liegen die Münzmetallchalkogenidhalogenide, die lediglich isolierte Q^{2-}-Anionen enthalten. Hier sind bis heute nur Verbindungen mit dem Münzmetall Ag bekannt. Beispiele sind Ag$_3$QX mit Q = S, Se, Te und X = Br, I [36–43], Ag$_5$Q$_2$X mit Q = Te und X = Cl, Br [44–50] und Ag$_{19}$Q$_6$X$_7$ mit Q = S, Se, Te und X = Br, I [51,52]. Im Fall von Ag$_3$SBr und Ag$_{19}$Te$_6$Br$_7$ existieren Substitutionsvarianten mit Cu. [52,53] Die Münzmetallchalkogenidhalogenide sind Mischleiter: sie vereinen die physikalischen Eigenschaften der ionenleitenden Münzmetallhalogenide

und der gemischtleitenden -chalkogenide. Eine typische Eigenschaft ist Polymorphie, die durch die anisotrope Kationenverteilung und hohe Silbermobilität hervorgerufen wird und maßgeblich die elektronischen Eigenschaften beeinflusst. [8]

Die dritte Substanzklasse sind die Münzmetallpolychalkogenidhalogenide, die sowohl kovalent gebundene Chalkogeneinheiten als auch isolierte Q^{2-}-Anionen enthalten. Der erste Vertreter dieser Klasse ist $Ag_{10}Te_4Br_3$, ein Mischleiter, der isolierte Te^{2-}-Anionen und $[Te_2]^{2-}$-Hanteln enthält und in einem kleinen Temperaturfenster von etwa 100 K drei Phasenübergänge zeigt. [54,55] Hierbei tritt ein reversibler, temperaturabhängiger Übergang zwischen p- und n-Halbleitung auf, welcher weiter unten näher erläutert wird. [9] Von $Ag_{10}Te_4Br_3$ existieren Substitutionsvarianten der anionischen sowie der kationischen Teilstruktur, wobei Te durch S und Se [56], Br durch Cl und I [57] und Ag durch Cu [58] teilweise ersetzt wurden. Weitere Vertreter der Münzmetallpolychal-kogenidhalogenide sind $Ag_{23}Te_{12}X$ mit X = Cl, Br [59] und $Ag_{20}Te_{10}BrI$ [7]. Neben den bekannten Silberpolytelluridhalogeniden wurden der Substanzklasse im Rahmen dieser Arbeit drei weitere Vertreter hinzugefügt: $Cu_{9,1}Te_4Cl_3$ und $Cu_{20}Te_{11}Cl_3$, sowie $Ag_{18}Cu_3Te_{11}Cl_3$, welches ähnliche elektronische Eigenschaften wie $Ag_{10}Te_4Br_3$ zeigt.

Die Kupferhalogenidthiometallate $(CuI)_3Cu_2TeS_3$, $(CuCl)_3Cu_2TeS_3$ und $(CuBr)_3Cu_{1,2}TeS_3$ enthalten komplexe Thiometallat-Anionen wie $[TeS_2]^-$ oder $[TeS_3]^{2-}$ und sind damit nur quasi-ternär. [60–65] Sie werden, genau wie die Au-Komplexe $[SCl_2][AuCl_3]$, $[QCl_3][AuCl_4]$ mit Q = S, Se, Te und $[TeBr_3][AuBr_4](Br_2)_{0,5}$, welche ebenfalls positiv geladenes Chalkogen in komplexen Anionen enthalten, [66–70] nicht obigen Substanzklassen zugerechnet. [8]

1.2 $Ag_{10}Te_4Br_3$

1.2.1   Struktureller Hintergrund

Das Silberpolytelluridhalogenid $Ag_{10}Te_4Br_3$ wurde 2006 als erster Vertreter der Münzmetallpolychalkogenidhalogenide von Stefan Lange synthetisiert und charakterisiert. [54] Die Verbindung kristallisiert in vier Polymorphen, welche sich durch reversible Ordnungs-Unordnungs-Phasenübergänge ineinander umwandeln. Bei Raumtemperatur ist die orthorhombische γ-Phase stabil, welche bei 317 K in die hexagonale β- und überhalb von 410 K in die hochsymmetrische hexagonale α-Phase übergeht. Unterhalb von 290 K existiert die δ-Phase, bei welcher alle Silberpositionen ausgeordnet und voll besetzt sind. [55]

Tabelle 1.1: Polymorphe von $Ag_{10}Te_4Br_3$. [54, 55]

Polymorph	Kristallsystem Raumgruppe	Gitterparameter
α-$Ag_{10}Te_4Br_3$ T = 410 K	hexagonal $P6/mmm$ (191)	$a = 7{,}984(2)$ Å $c = 7{,}688(2)$ Å $V = 424{,}4(2)$ Å^3
β-$Ag_{10}Te_4Br_3$ T = 340 K	hexagonal $P6_3/mmc$ (194)	$a = 13{,}748(2)$ Å $c = 13{,}382(2)$ Å $V = 2518{,}0(6)$ Å^3
γ-$Ag_{10}Te_4Br_3$ T = 293 K	orthorhombisch $Cmcm$ (36)	$a = 15{,}374(1)$ Å $b = 15{,}772(1)$ Å $c = 13{,}715(1)$ Å $V = 3325{,}6(4)$ Å^3
δ-$Ag_{10}Te_4Br_3$ T = 223 K	orthorhombisch $Cmc2_1$ (36)	$a = 15{,}400(1)$ Å $b = 15{,}654(1)$ Å $c = 13{,}699(1)$ Å $V = 3302{,}4(4)$ Å^3

Raumtemperaturmodifikation γ-$Ag_{10}Te_4Br_3$.   Die Anionenteilstruktur besteht aus alternierend gestapelten, leicht verzerrten Br^--6.3.6.3-Kagomé- und Te^{2-}-6^3-Wabennetzen, welche senkrecht von überwiegend kovalent gebundenen $[Te_4]^{6-}$-Einheiten durchdrungen werden (dargestellt in Abbildung 1.2). Die Abstände der Anionen innerhalb der Netze betragen im Br-Kagoménetz zwischen 3,963(1) und 3,978(1) Å und im Te-Wabennetz zwischen 4,188(4) und 5,481(3) Å und liegen damit über den jeweiligen doppelten Van-der-Waals-Radien nach Pauling ($d_{VdW}(Br^-) = 1.85$ Å, $d_{VdW}(Te^{2-}) = 2.06$ Å). [71] Die $[Te_4]^{6-}$-Einheiten zentrieren jeden zweiten Te-Sechsring und bestehen aus einer $[Te_2]^{2-}$-Hantel und zwei zusätzlichen linear koordinierenden Te^{2-}-Ionen. Der Te-Te-

Abstand in den Hanteln beträgt 2,803(1) Å, was zum im Durchschnitt in der Literatur genannten Wert von 2.79 Å für $[Te_2]^{2-}$-Einheiten passt. [72–75] Der Abstand von einem Hantel-Te-Atom zum koordinierenden Te^{2-}-Ion beträgt 3,60(1) Å und liegt damit deutlich unter dem doppelten Van-der-Waals-Radius von 4,12 Å. [71] Die Te_4-Einheiten sind voneinander durch Silberionen (Ag1) getrennt, welche in den Zentren der zweiten Hälfte der Sechsringe des Te-Wabennetze liegen, jeweils zwei Te_4-Einheiten im Abstand von 2,707(2) Å annähernd linear koordinieren und so die Te-Einheiten zu unendlichen $[Te_4Ag]_n$-Strängen verknüpfen. Wie in Abbildung 1.2 rechts oben dargestellt ist, liegt eine zweite Silberlage (Ag2) in den Te-Wabennetzen, wo sie im Abstand von 2,702(1) Å von zwei Te^{2-}-Ionen annähernd linear koordiniert wird. Das restliche Silber liegt, ringförmig um die $[Te_4Ag]_n$-Stränge verteilt, mobil zwischen den Kagomé- und Wabennetzen vor (siehe Abbindung 1.2 links).
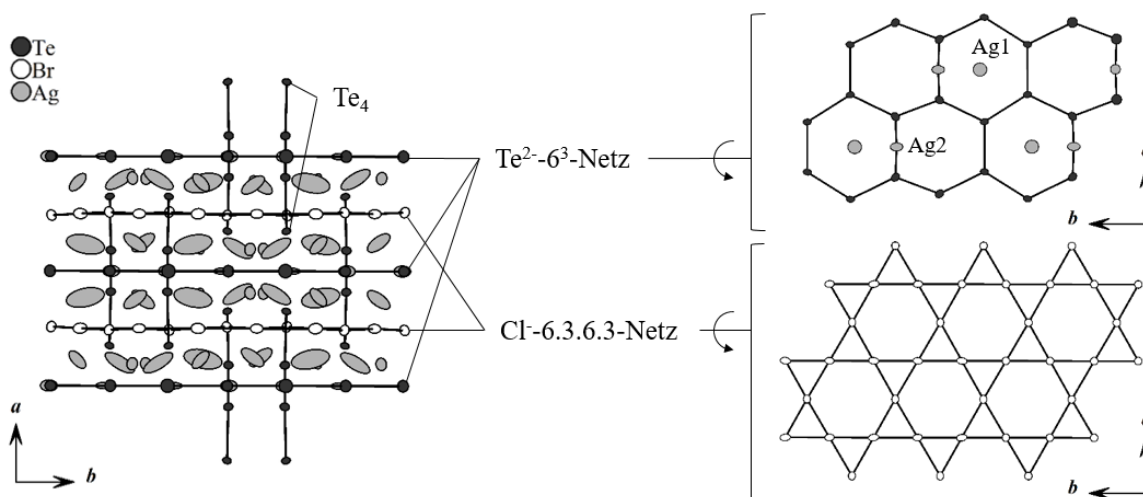
Abbildung 1.2: Strukturausschnitt von γ-$Ag_{10}Te_4Br_3$. Verzerrte Br^--6.3.6.3-Kagomé- und Te^{2-}-6^3-Wabennetze sind alternierend in a-Richtung gestapelt und werden von $[Te_4]^{6-}$-Einheiten durchdrungen. Diese sind durch ein linear koordiniertes Ag-Kation (Ag1) von einander getrennt. [54]

Hochtemperaturmodifikationen β- und α-$Ag_{10}Te_4Br_3$. Die erhöhte Silbermobilität bei steigender Temperatur verursacht zwei Ordnungs-Unordnungs-Phasenübergänge bei 317 und 390 K. Die Ag1-Position in den $[Te_4Ag]_n$-Strängen ist zunehmend unterbesetzt, was zur Frustration der Stränge und zur Bildung hochmobiler Te-Ketten führt. In Abbildung 1.3 sind Strukturausschnitte der Raum- und Hochtemperaturmodifikationen, sowie die frustrierten Te-Stränge gezeigt. Im β-Polymorph ist ein Drittel der Stränge auf diese Weise frustriert, in α-$Ag_{10}Te_4Br_3$ sind nur noch frustrierte Te-Ketten vorhanden. Im hochsymmetrischen α-Polymorph liegen die Br-Kagomé- und Te-Wabennetze ideal

vor und alle Ag-Positionen sind unterbesetzt. Große Auslenkungsparameter weisen auf eine hohe Silbermobilität hin.
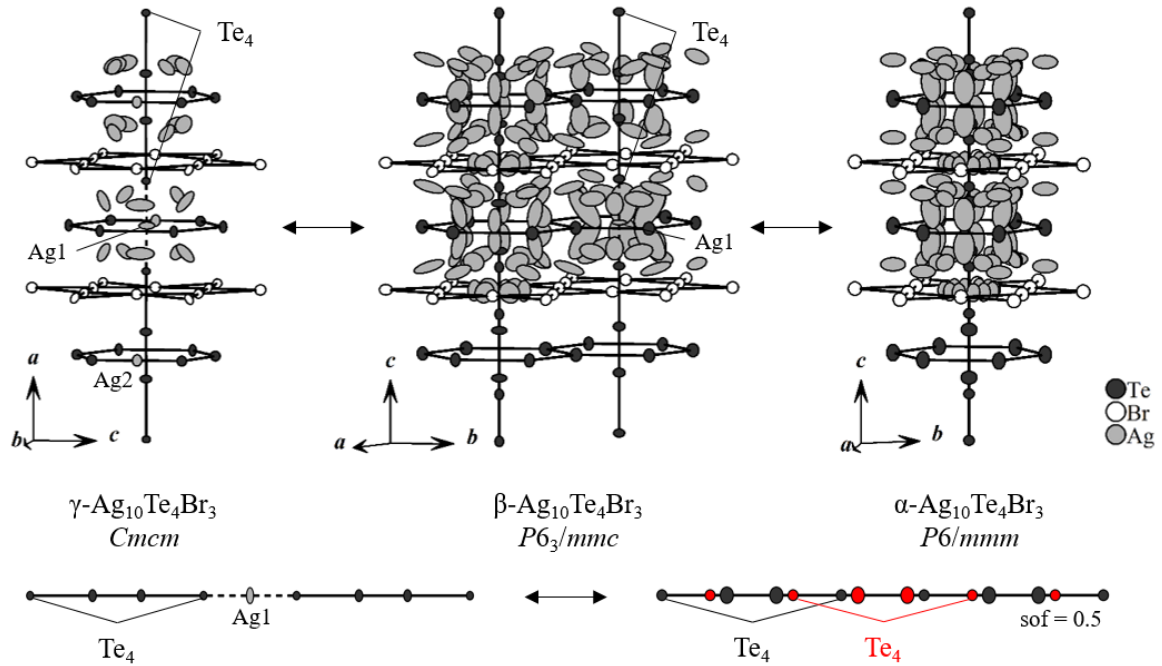
Abbildung 1.3: Strukturausschnitte der Raum- und Hochtemperaturmodifikationen γ-, β- und α-$Ag_{10}Te_4Br_3$. Die Unterbesetzung der Ag1-Position durch zunehmende Silbermobilität verursacht die Frustration der $[Te_4Ag]_n$-Stränge. [55]

1.2.2 Thermoelektrische Eigenschaften

$Ag_{10}Te_4Br_3$ zeigt im Bereich des $\alpha - \beta$-Phasenübergangs bei 390 K einen Sprung des Seebeck-Koeffizienten mit Wechsel von p- zu n-Halbleitung und zurück. Der Seebeck-Koeffizient fällt von $+310\ \mu V\ K^{-1}$ auf $-940\ \mu V\ K^{-1}$ und steigt zurück auf $+540$ $\mu V\ K^{-1}$ innerhalb eines kleinen Temperaturintervalls (siehe Abbildung 1.4). Ausgelöst wird dieses Verhalten durch die strukturelle Umordnung in der Chalkogenteilstruktur, wobei sich voneinander isolierte polyanionische $[Te_4]^{6-}$-Einheiten über einen Peierls-verzerrten Übergangszustand zu einer äquidistanten Te-Kette mit hoher Mobilität umwandeln (siehe Abbildung 1.2). Die vorrübergehende n-Halbleitung wird durch eine Aufwärtsverschiebung des Fermi-Niveaus und damit in Verbindung stehende Besetzung höherer Energieniveaus mit zusätzlichen Leitungselektronen ausgelöst. Diese Elektronen werden während dem Phasenübergang durch interne Redoxprozesse freigesetzt, wenn Te-Ketten, die formal von isolierten Te^{2-} gebildet werden, und polyanionische Einheiten wie $[Te_4]^{6-}$ miteinander im Gleichgewicht stehen:

$$4\,Te^{2-} \longrightarrow Te_4^{6-} + 2\,e^-$$
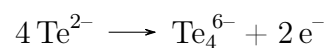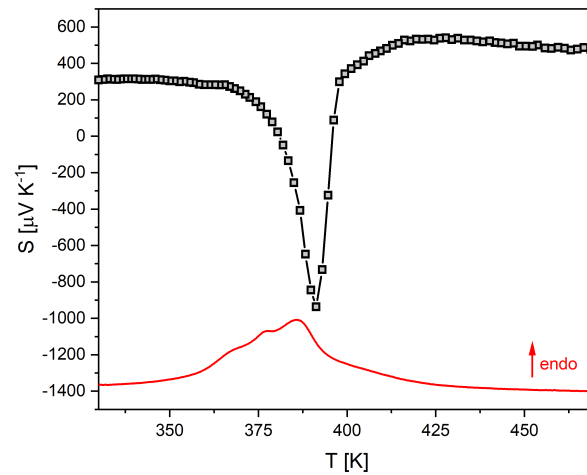
Abbildung 1.4: Seebeck-Koeffizient (schwarz) und DSC (rot) von $Ag_{10}Te_4Br_3$. [9]

$Ag_{10}Te_4Br_3$ zeigt niedrige Wärmeleitfähigkeit zwischen 0,27 und 0,43 W m^{-1} K^{-1} im Tempertaurbereich zwischen 250 und 390 K. Es ergibt sich ein maximaler ZT-Wert von $1,7 \times 10^{-2}$ bei 390 K. [9]

1.3 Weitere pnp-wechselnde Materialien

Neben $Ag_{10}Te_4Br_3$ existieren weitere Materialien, die reversibel zwischen p- und n-Halbleitung schalten können: $Tl_2Ag_{12}Se_7$, $AgBiSe_2$ und $AgCuS$. [76–78] Alle diese Materialien haben gemeinsam, dass die pnp-Schaltung wärend einem Ordnungs-Unordnungs-Phasenübergang bei erhöhter Temperatur stattfindet.

1.3.1 Tl$_2$Ag$_{12}$Se$_7$
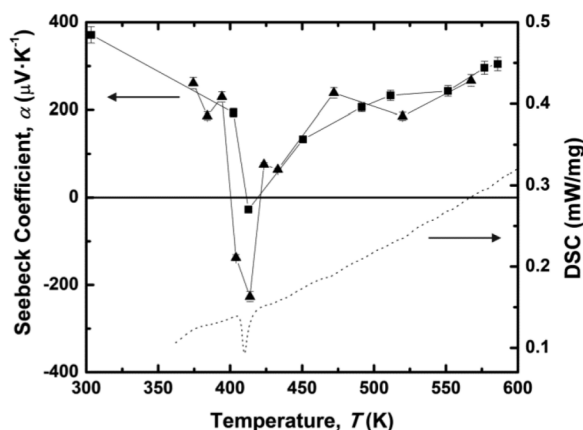
Abbildung 1.5: Seebeck-Koeffizient und DSC von $Tl_2Ag_{12}Se_7$. Genehmigter Abdruck von [76]. Copyright © 2017, American Chemical Society.

$Tl_2Ag_{12}Se_7$ zeigt pnp-Schaltung während eines Ordnungs-Unordnungs-Phasen- übergangs bei 410 K. Wie in Abbildung 1.5 dargestellt, sinkt der Seebeck-Koeffizient rapide von +230 $\mu V\ K^{-1}$ bei 394 K auf −227 $\mu V\ K^{-1}$ bei 414 K, um direkt wieder auf +76 $\mu V\ K^{-1}$ bei 423 K und langsam zurück auf +305 $\mu V\ K^{-1}$ bei 586 K zu steigen. Dieses Verhalten wird, genauso wie bei $Ag_{10}Te_4Br_3$, auf strukturelle Umwandlungen in der Chalkogenteilstruktur (in diesem Fall Se) während der Phasenumwandlung zurückge-führt. [76]

1.3.2 AgBiSe$_2$

Der pnp-Übergang bei $AgBiSe_2$ findet beim Wechsel vom rhomboedrischen zum kubischen Kristallsystem bei 580 K statt. Wie in Abbildung 1.6 gezeigt, fällt der Seebeck-Koeffizient dabei von +480 $\mu V\ K^{-1}$ auf −250 $\mu V\ K^{-1}$ und steigt bei leichter Erhöhung der Temperatur wieder auf +470 $\mu V\ K^{-1}$. Ausgelöst wird dieses Verhalten durch einen quasimetallischen Übergangszustand, der durch Brechen und Neubildung von Ag-Bi-Bindungen entsteht. [77]
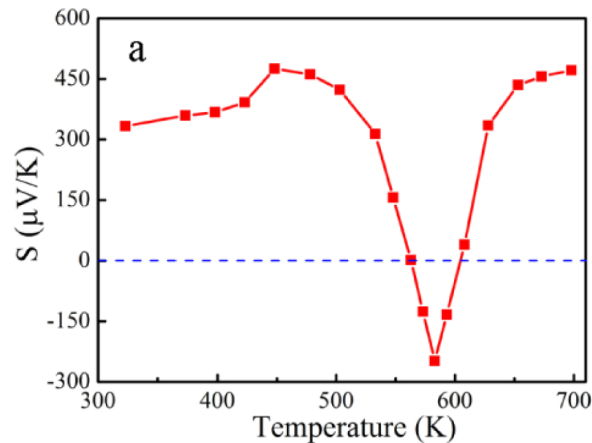
Abbildung 1.6: Seebeck-Koeffizient von AgBiSe$_2$. Genehmigter Abdruck von [77]. Copyright © 2017, American Chemical Society.

1.3.3 AgCuS
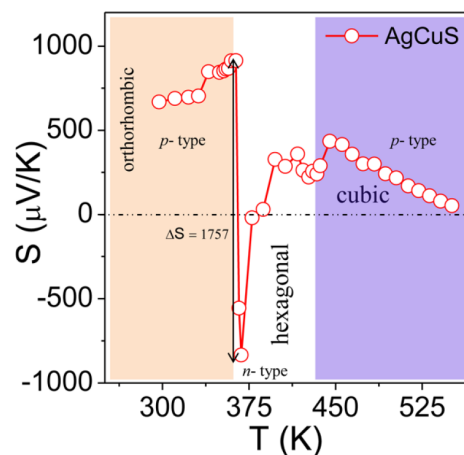
Abbildung 1.7: Seebeck-Koeffizient von AgCuS. Genehmigter Abdruck von [78]. Copyright © 2017, American Chemical Society.

AgCuS zeigt pnp-Schaltung mit einem relativ großen Sprung des Seebeck-Koeffizienten um 1757 μV K^{-1} (siehe Abbildung 1.7). Beim Übergang von der orthorombischen, bei Raumtemperatur stabilen, Modifikation zur hexagonalen Hochtemperaturmodifikation bei 364 K stürzt der Seebeck-Koeffizient von +917 auf -840 μV K^{-1} um dann ab 385 K wieder auf positive Werte zu steigen. Bandstrukturrechnungen belegen, dass der quasimetallische Übergangszustand, der zu n-Leitung während des Phasenübergangs führt, maßgeblich durch Cu-S-Wechselwirkungen verursacht wird. [78].

Von den hier aufgeführten Materialien zeigt AgCuS nicht nur den größten Seebecksprung, sondern auch die tiefste, das heißt am nächsten an Raumtemperatur liegende, Sprungtemperatur, was das Material als das am besten für mögliche Anwendungen geeignete auszeichnet. [78] Allerdings übertrifft die neue Verbindung Ag$_{18}$Cu$_3$Te$_{11}$Cl$_3$ AgCuS

sowohl hinsichtlich des Betrags des Seebecksprungs als auch durch ihre Sprungtempertur
bei Raumtemperatur.

1.3.4 Ag$_5$Te$_2$Cl
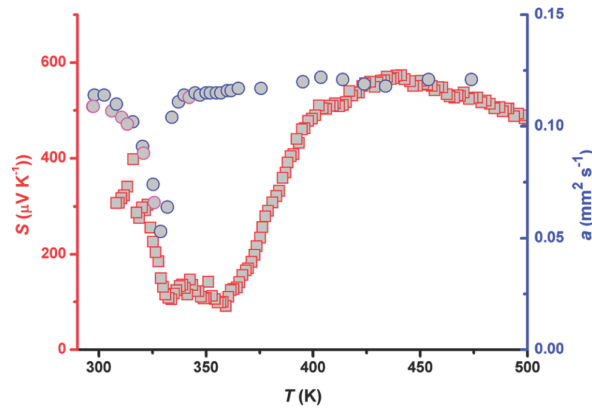
Abbildung 1.8: Seebeck-Koeffizient (rot) und DSC (blau) von Ag$_5$Te$_2$Cl. Genehmigter
Abdruck von [79]. Copyright © 2017, American Chemical Society.

Zwar zeigt Ag$_5$Te$_2$Cl keine pnp-Schaltung aber einen verwandten Sprung des Seebeck-
Koeffizienten. Wie Abbildung 1.8 zeigt, fällt der Seebeck-Koeffizient im Bereich des
Ordnungs-Unordnungs-Phasenübergangs bei 335 K stark von +397 μV K^{-1} bei 316
K auf +105 μV K^{-1} bei 334 K ab und bleibt bis 359 K auf diesem niedrigen Niveau,
um dann wieder auf das vorherige Niveau zu steigen und mit +573 μV K^{-1} bei 441
K ein Maximum zu erreichen. Da die Anionenteilstruktur von Ag$_5$Te$_2$Cl nur isolier-
te Te^{2-}- und Cl$^-$-Anionen enthält, deren Abstand zueinander mehr als zweimal den
van-der-Waals-Radius beträgt, sind anionische Wechselwirkungen in diesem Fall als
Auslöser des Seebecksprungs ausgeschlossen. Es lassen sich allerdings Anomalien in der
Entwicklung der Ag-Ag-Abstände mit der Temperatur beobachten: einige Ag-Positionen
nähern sich im Bereich des Seebecksprungs aneinander an, anstatt sich mit der ter-
mischen Expansion gleichmäßig auseinander zu bewegen. [79] Da sich die minimalen
Ag-Ag-Abstände hier im Bereich von d^{10}-d^{10}-Wechselwirkungen befinden, werden solche
Wechselwirkungen zur Erklärung des Seebeckeffekts herangezogen. [79, 80] Anders als
bei den oben beschriebenen pnp-Materialien, bei denen der pnp-Wechsel relativ scharf in
einem kleinen Temperaturintervall im Bereich des Phasenübergangs stattfindet, ist der
Seebecksprung bei Ag$_5$Te$_2$Cl vergleichsweise breit. Das lässt sich mit der Beobachtung
erklären, dass die minimalen Ag-Ag-Abstände nicht mit dem Phasenübergang überein-
stimmen, sondern erst in der Hochtemperaturphase im Bereich des Wiederanstiegs des
Seebeck-Koeffizienten auftreten. [79] Ein ähnlich breiter Seebecksprung, der mit dem
Auftreten von d^{10}-d^{10}-Wechselwirkungen in Verbindung zu stehen scheint, ist bei der
neuen Verbindung Ag$_{18}$Cu$_3$Te$_{11}$Cl$_3$ zu beobachten.

1.4   Der pn-Übergang

Der pn-Übergang ist ein Kontakt zwischen einem p- und einem n-Halbleiter und ist das Grundelement der meisten Bauelemente der Halbleitertechnik. Es wird zwischen homo- und hetero-Übergang unterschieden. Der homo-Übergang ist ein Kontakt zwischen einem p- und einem n-dotierten Halbleiter der selben Art, zum Beispiel p-Si und n-Si, wohingegen der hetero-Übergang zwischen unterschiedlichen p- und n-leitenden Halbleitermaterialien stattfindet, beispielsweise p-Si und n-GaAs. [81] Die oben behandelten pnp-Materialien zeigen die außergewöhnliche Eigenschaft in Abhängigkeit der Temperatur reversibel zwischen p- und n-Halbleitung zu wechseln. Dadurch ergibt sich die Möglichkeit, im selben Material nur durch Variation der Temperatur einen schaltbaren pn-Übergang zu erzeugen. Dieser stellt einen Sonderfall dar, da er sich nicht scharf in die Kategorien homo- und hetero-Übergang einordnen lässt. Zwar handelt es sich beim p- sowie n-leitenden Teil um die selbe Verbindung, allerdings um verschiedene Polymorphe, die sich strukturell unterscheiden und durch einen Ordnungs-Unordnungs-Phasenübergang ineinander umwandeln lassen.

1.4.1   Der pn-Übergang im thermodynamischen Gleichgewicht.

Unabhängig von der Dotierung sind durch die Eigenleitung in einem Halbleiter immer sowohl p- als auch n-Ladungsträger vorhanden. Je nachdem, welche Art im jeweiligen Bereich überwiegt, werden diese Majoritäts- bzw. Minoritätsladungsträger genannt. Beim pn-Kontakt fließen durch die starken Unterschiede in den Ladungsträgerkonzentrationen zwischen p- und n-Bereich Diffusionsströme, die zu Rekombination von Elektronen und Löchern im pn-Grenzgebiet führen. Die Diffusion bewirkt, dass jeweils ein schmaler Streifen auf der p-Seite negativ und auf der n-Seite positiv aufgeladen wird und die sogenannte Raumladungszone (auch Verarmungszone oder Sperrschicht) bildet. Das sich durch die Diffusionsvorgänge bildende elektrische Feld verhindert, dass ein vollständiger Konzentrationsausgleich der freien Ladungsträger erfolgt. Es stellt sich ein Gleichgewicht zwischen der Diffusionsspannung U_D und der in der Gegenrichtung wirkenden Kraft des elektrischen Feldes E_{RLZ} ein. [81]

1.4.2   Der pn-Übergang mit angelegter Spannung.

Durch das Anlegen einer äußeren Spannung liegt der pn-Übergang nicht mehr im thermodynamischen Gleichgewicht. In Abbildung 1.9 ist die Strom-Spannungs-Kennlinie des pn-Übergangs dargestellt.

Äußere Spannung in Durchlasspolung.   Legt man eine Spannung U_F (*forward voltage*) mit dem Pluspol am p-Gebiet und dem Minuspol am n-Gebiet an, so wirkt U_F
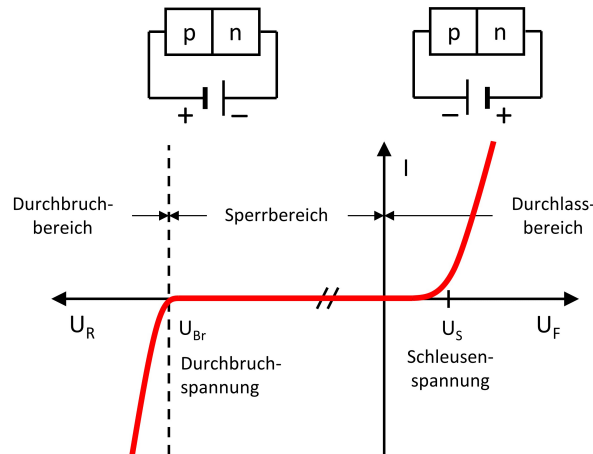
Abbildung 1.9: Beispielhafte Darstellung der Strom-Spannungs-Kennlinie eines pn-Übergangs. [81]

der Diffusionsspannung U_D entgegen und die Raumladungszone wird verkleinert. Bei $U_F = U_D$ ist die Grenzschicht vollständig abgebaut und der Strom steigt stark an. Man spricht in diesem Zusammenhang von der Schleusenspannung U_S. [81]

Äußere Spannung in Sperrpolung. Liegt der Minuspol am p- und der Pluspol am n-Gebiet, so wirken die äußere Spannung U_R (*reverse voltage*) und die Diffusionsspannung U_D in die gleiche Richtung, was zur Vergrößerung der Raumladungszone führt. Es ist kein Stromfluss durch die Majoritätsladungsträger über den pn-Übergang möglich und es fließt nur der durch die Minoritätsladungsträger hervorgerufene, sehr kleine Feldstrom (auch Sperrstrom). [81]

Durchbruchmechanismen. Wird U_R weiter vergrößert, so kommt es bei sehr hohen Spannungen zum Durchbruch: oberhalb einer gewissen Sperrspannung (Durchbruchspannung U_{Br}) steigt der Stromfluss durch Majoritätsladungsträger sehr steil an. Dieser Effekt kann nach verschiedenen Mechanismen ablaufen: Lawinendurchbruch (auch Avalanche-Effekt) oder Zener-Durchbruch (auch Tunnel-Durchbruch) sind reversibel (Durchbrüche 1. Art). Irreversibel ist der thermische Durchbruch, der duch unkontrollierten Anstieg der Sperrschichttemperatur und daraus folgender Zersetzung des Halbleitermaterials ausgelöst wird. Dieser Durchbruch 2. Art kann durch ausreichende Kühlung oder Begrenzung des Stromanstiegs verhindert werden. [81]

Beim Lawinendurchbruch kommt es zu Ladungsträgererzeugung durch Stoßionisation. Ladungsträger, die durch Diffusion in die Raumladungszone eindringen oder durch thermische Paarbildung erzeugt werden, erfahren durch das elektrische Feld Beschleunigung. Bei ausreichend hohen Sperrspannungen können diese über mehrere Stöße ihre kinetische Energie akkumulieren und dabei ΔE des Bandabstands erreichen.

Bei ausreichend hoher Beschleunigung können außerdem durch Zusammenstoß neue Ladungsträger erzeugt werden. Bei genügend langem Weg, dass heißt ausreichend großer Raumladungszone, findet erneut Beschleunigung statt und kann zu erneuter Stoßionisation führen. So steigt die Anzahl freier Ladungsträger lawinenartig an und führt zu einem sehr steilen Anstieg des Stroms. Der Lawinendurchbruch findet bei hoher elektrischer Feldstärke und weiter Raumladungszone, also bei niedrigen Dotierungen, statt. [81]

Bei beidseitig sehr hohen Dotierungen, und damit schmaler Raumladungszone, findet der Durchbruch bei niedrigeren Durchbruchspannungen durch den quantenmechanischen Tunneleffekt satt. Dabei handelt es sich um Ladungsträgererzeugung im starken elektrischen Feld und es wird von Zener- oder Tunnel-Durchbruch gesprochen. In diesem Fall ist die Sperrschicht zu schmal um einen Lawinendurchbruch zu ermöglichen, es können aber noch höhere Feldstärken auftreten als im ersten Fall. Bei sehr hohen Feldspannungen werden Valenzelektronen aus ihren Paarbindungen gerissen und ins Leitungsband befördert, wodurch neue Ladungsträger erzeugt werden. Betrachtet man den Effekt anhand des Bändermodells, so liegen sowohl Valenz- als auch Leitungsband auf der n-Seite energetisch tiefer als auf der p-Seite. Valenzelektronen aus dem p-Gebiet, die sich auf einem bestimmten Energieniveau unterhalb der Valenzbandkante befinden, wechseln auf einen freien Platz mit gleichem Energieniveau oberhalb der Leitungsbandkante im n-Gebiet. Dabei überqueren („durchtunneln") sie die verbotene Zone. Dieses Tunneln direkt vom Valenz- ins Leitungsband wird Zener-Tunneln genannt. [81]

Ein weiterer Mechanismus, der einem Durchbruch zugrunde liegen kann, ist der sogenannte Durchgriff. Bei sehr schwacher Dotierung kann sich die Raumladungszone so weit ausdehnen, dass sie die Kontakte des äußeren Stromkreises erreicht. Die in die Raumladungszone injizierten Ladungsträger werden durch das elektrische Feld nahezu ungehindert zum gegenüberliegenden Kontakt transportiert. Dabei handelt es sich um einen Kurzschluss. [81]

1.4.3 Der Schottky-Kontakt

Neben dem pn-Übergang ist der Halbleiter-Metall-Übergang von großer Bedeutung in der Halbleitertechnik. Je nach Materialeigenschaften zeigt der Kontakt ohmsches oder stark polungsabhängiges Verhalten wie beim pn-Übergang. Im zweiten Fall handelt es sich um einen Schottky-Kontakt. Das Fermi-Niveau von Metall und Halbleiter ist im Allgemeinen unterschiedlich, sodass bei der Kontaktierung Diffusionsvorgänge ähnlich wie beim pn-Übergang hervorgerufen werden können. Ob bei einem Halbleiter-Metall-Übergang ein Schottky-Kontakt vorliegt, hängt im wesentlichen von der Höhe der Austrittsarbeit ab, also der Energie, die aufgewendet werden muss, um Elektronen aus einem ungeladenen Festkörper zu entfernen. Für einen n-Halbleiter-Metall-Kontakt

gilt: ist die Austrittsarbeit im Metall höher als im n-Halbleiter, so fließen Elektronen vom n-Halbleiter ins Metall und es bildet sich eine Verarmungszone auf der Seite des n-Halbleiters, ähnlich der Raumladungszone beim pn-Übergang. In diesem Fall liegt ein Schottky-Kontakt vor. Im umgekehrten Fall wird die Randzone des Halbleiters mit Elektronen angereichert, es bildet sich keine Verarmungsschicht und ohmsches Verhalten liegt vor. Beim p-Halbleiter-Metall-Kontakt gilt der gegenteilige Fall: Bei höherer Austrittsarbeit im Metall reichern sich die positiven Ladungsträger in der Randzone des Halbleiters an und es tritt ohmsches Verhalten auf. Bei höherer Austrittsarbeit im p-Halbleiter fließen Elektronen vom Metall in den Randbereich des p-Halbleiters, es kommt zu Rekombination, die Verarmungsschicht bildet sich aus und es liegt ein Schottky-Kontakt vor. [81]

1.4.4   Die Diode

Das einfachste Halbleiter-Bauelement ist die Diode, welche die technische Ausführung des pn-Übergangs darstellt. Der elektrische Strom kann in der einen Richtung passieren und wird in der anderen gesperrt, weshalb man von Durchlass- und Sperrichtung spricht. Standart-Dioden werden zum Schalten und Begrenzen von Signalen, beispielsweise in der Informationstechnik, oder zum Gleichrichten von Wechselstrom eingesetzt. Sie können wegen der Temperaturabhängigkeit der Durchlasskennlinie auch zur Temperaturmessung genutzt werden. Zener- und Suppressordioden, die in Sperrrichtung betrieben werden, dienen zur Stabilisierung einer Spannung und zum Schutz vor hohen Spannungsspitzen. Mehrschichtdioden sind Spezialdioden, die mehr als einen pn-Übergang, aber nur zwei äußere Anschlüsse aufweisen. Ihre Strom-Spannungs-Kennlinien können symmetrisch sein und es kann somit auch Wechselstrom geschaltet werden. Weitere Spezialdioden sind Leucht- und Laserdioden. Sie nutzen die Eigenschaft direkter Halbleiter bei Rekombination Licht mit der Energie der Bandlücke zu emittieren. [81]

Die Fotodiode kann Licht durch den inneren Fotoeffekt in elektrischen Strom umwandeln. Sie wird in Sperrrichtung betrieben. Solange kein Licht auf die Raumladungszone fällt, fließt nur der kleine Sperrstrom, der hier als Dunkelstrom bezeichnet wird. Wird Licht mit mindestens der Energie der Bandlücke eingestrahlt, so können die Atome des Kristallgitters ionisiert werden. Ein Elektron wird vom Valenz- ins Leitungsband gehoben und so ein neues Elektron-Loch-Paar erzeugt. Durch das elektrische Feld in der Raumladungszone werden die Paare getrennt. Durch die Erhöhung der Ladungsträgerkonzentration wird der Sperrstrom erhöht. Zum Dunkelstrom kommt ein zur Beuleuchtungsstärke proportionaler Fotostrom hinzu. Fotodioden werden verwendet, um Licht in messbare Signale umzuwandeln. Auch die Solarzelle ist eine Fotodiode. Zur wirksamen Erzeugung eines elektrischen Stromes ist allerdings eine wesentlich größere Sperrschichtfläche nötig, als bei der klassischen Fotodiode. Handelsübliche Solarzellen

werden am häufigsten großflächig aus Silizium gefertigt. [81]

Ein Spezialfall ist die Schottky-Diode. Hier liegt kein pn-Übergang, sondern ein n-Halbleiter-Metall-Übergang vor. Zum Strom tragen nur Elektronen bei, die bei der Vorwärtspolung relativ viel Energie besitzen und deshalb als heiße Elektronen bezeichnet werden. Die Schottky-Diode wird deshalb auch *Hot-Carrier-Diode* genannt und schaltet sehr schnell. Anwendungen sind Höchstfrequenz-Dioden, Schaltdioden mit extrem kurzer Schaltzeit, Leistungsgleichrichter für hohe Schaltfrequenzen und optoelektronische Bauteile. [81]

2 Experimenteller Teil

2.1 Synthesen

Die eingesetzten Edukte sind in Tabelle 2.1 aufgeführt. Sie werden kommerziell erworben und in der Regel ohne weitere Aufreinigung eingesetzt. Ausnahmen sind Kupfer, die Kupfer(I)halogenide und angereichertes ^{125}Te. Die entsprechenden Reinigungsschritte sind im Folgenden aufgeführt:

Kupfer: Zur Entfernung der äußeren Oxidschicht werden die Granalien in der Wasserstoffflamme erhitzt und anschließend in Ethanol abgeschreckt.

Kupfer(I)halogenide: Kupfer(I)chlorid, Kupfer(I)bromid und Kupfer(I)iodid werden in der entsprechenden konzentrierten Halogenwasserstoffsäure gelöst und anschließend mit destilliertem Wasser wieder ausgefällt. Der Niederschlag wird mit destilliertem Wasser gewaschen und im Vakuum getrocknet.

^{125}Te: Zur Entfernung von Oxidspuren wurde das Pulver bei 673 K im Wasserstoffstrom gereinigt.

2.1.1 Verwendete Chemikalien

Tabelle 2.1: Auflistung der in dieser Arbeit verwendeten Chemikalien.

Chemikalie	Form	Reinheit [%]	Hersteller
Kupfer	Granalien	99,9999	CHEMPUR
Kupfer(I)chlorid	Pulver	97	ALFA AESER
Silber	Stücke	99,99	HERAEUS
Silber(I)chlorid	Pulver	99,9	ALFA AESER
Salzsäure rauchend (37 %)	Lösung	zur Analyse	EMSURE
Tellur	Stücke	99,999	CHEMPUR
^{125}Tellur	Pulver	94	STB ISOTOPE GERMANY

2.1.2 Festkörperreaktionen

Die Edukte werden, wenn nicht anders vermerkt, in stöchiometrischen Mengen mit Hilfe einer Analysenwaage (KERN, *AEJ*, Anzeigengenauigkeit 0.1 mg) in ausgeheizten Kieselglasampullen eingewogen. Diese werden dreimal evakuiert und mit getrocknetem Argon (WESTFALEN AG, Reinheitsgrad 4.8, 99,998 Vol.-%) gespült und unter Vakuum (Restdruck $< 10^{-3}$ mbar) mit einem Knallgasbrenner abgeschmolzen. Die Handhabung luft- oder feuchtigkeitsempfindlicher Edukte oder Produkte erfolgt in einer Glovebox (MBRAUN, H_2O-Gehalt $< 0,1$ ppm, O_2-Gehalt $< 0,1$ ppm) unter Inertgasatmosphäre (Argon,WESTFALEN AG, Reinheitsgrad 4.8, 99,998 Vol.-%).

Münzmetallpolytelluridhalogenide: Die Synthese erfolgt aus den Elementen und den entsprechenden Münzmetall(I)halogeniden. Die typische Ansatzgröße beträgt zwischen 500 und 1000 mg. Alle Münzmetallpolytelluridhalogenidansätze werden aufgeschmolzen und in Eiswasser abgeschreckt. Dafür werden kupferhaltige Ansätze für 3 h auf 1320 K erhitzt, bei Ansätzen, die Silber als einziges Münzmetall enthalten, wird die Temperatur auf 1170 K verringert. Die durch Abschrecken entstandenen Schmelzreguli werden fein gemörsert und zum Tempern erneut in Kieselglasampullen eingeschmolzen.

Im Fall von $Cu_{9,1}Te_4Cl_3$ und $Cu_{20}Te_{11}Cl_3$ wird die Selektivität durch die Synthesetemperatur beim Tempern gesteuert. Während $Cu_{9,1}Te_4Cl_3$ bei 660 K getempert wird, muss bei der Synthese von $Cu_{20}Te_{11}Cl_3$ die Tempertemperatur auf 750 K erhöht werden um die Bildung des Te-ärmeren Konkurrenzprodukts zu unterdrücken.

Bei Einführung von Ag in das System ändert sich die Ladung der Tellurteilstruktur durch Vergrößerung der Te-Te-Abstände in der Reihe von $Cu_{20}Te_{11}Cl_3$ zu $Ag_{18}Cu_3Te_{11}Cl_3$, weshalb der Münzmetallgehalt der Reihe zwischen $M_{20}Te_{11}Cl_3$ und $M_{21}Te_{11}Cl_3$ variiert. Die echte Produktzusammensetzung ist also $M_{20+\delta}Te_{11}Cl_3$ mit M = Cu, Ag und $0 \leq \delta \leq 1$. Die Einwaage ist jedoch einheitlich $Ag_xCu_{21-x}Te_{11}Cl_3$, da sich überschüssiges Münzmetallchlorid in der kälteren Ampullenmitte abscheidet und trotzdem phasenreines Produkt erhalten wird. Durch die Einführung von Silber wird die Bildung von $Cu_{9,1}Te_4Cl_3$ unterdrückt und es entsteht ausschließlich $M_{20+\delta}Te_{11}Cl_3$, weshalb die Tempertemperatur auf 660 K reduziert werden kann.

Die Dauer des Tempervorgangs richtet sich nach gewünschter Kristallgröße des Produkts und beträgt zwischen 7 und 42 d. Alle Synthesetemperaturen sind in Tabelle 2.2 zusammengefasst.

2.1.3 Herstellung von Tabletten

Wegen der begrenzten Größe von Einkristallen muss die Bestimmung einiger physikalischer Eigenschaften an aus Pulver gepressten Tabletten erfolgen. Zu deren Herstellung

Tabelle 2.2: Synthesetemperaturen für die Herstellung der Münzmetallpolytelluridchloride durch Aufschmelzen (T1) und anschließendes Tempern (T2).

Einwaage	T1 [K]	T2 [K]
$Cu_{9,1}Te_4Cl_3$	1320	660
$Cu_{20}Te_{11}Cl_3$	1320	750
$Ag_xCu_{21-x}Te_{11}Cl_3$, x = 1, 2, ..., 17	1320	660
$Ag_xCu_{21-x}Te_{11}Cl_3$, x = 18, 19, 20, 21	1170	660

werden die kristallinen Produkte zunächst zu feinen Pulvern gemörsert. Diese werden in das jeweilige Presswerkzeug eingefüllt und in einer MAASSEN *MP150* Laborpresse gepresst. Der Druck wird an die Vorgaben des jeweiligen Presswerkzeugs angepasst. Zum einfachen Pressen von leicht zu verpressenden Pulvern stehen selbstgebaute Presswerkzeuge, sowie Präzisions-Presswerkzeuge der Firma MAASSEN zur Verfügung.

Pressen unter Vakuum: Das Pulver wird in ein MAASSEN Präzisions-Presswerkzeug mit Vakuumeinsatz eingefüllt, welches an eine Vakuumpumpe angeschlossen ist. Während des Pressens wird der Druck im Presswerkzeug auf 10^{-2} mbar reduziert. Bei schwer zu verpressenden Pulvern kann als Hilfsmittel ein Lösungsmittel, welches nicht mit dem Produkt reagiert (hier z.B. Aceton) hinzugefügt werden. Dafür wird das Pulver im Presswerkzeug mit einigen Tropfen des Lösungsmittels aufgeschwemmt. Während des Pressvorgangs wird das Lösungsmittel mit Hilfe der Vakuumpumpe wieder abgezogen.

Heißpressen: Das Pulver wird in ein P/O/WEBER *10 H* Präzisions-Heißpresswerkzeug gefüllt und während dem Pressen mit Hilfe eines P/O/WEBER *TRG 1* Heizreglers aufgeheizt. Zur Vermeidung von Zersetzungsreaktionen an der Oberfläche wird bei den Münzmetallpolytelluridhalogeniden auf lediglich 100 °C aufgeheizt und nach einer Stunde durch Abschalten des Heizreglers wieder langsam auf Raumtemperatur abgekühlt. Um Spannungen in der Tablette und damit anschließendes Brechen zu vermeiden, wird darauf geachtet, dass der Druck beim Pressen nicht über 3 t steigt.

2.2 Röntgenographische Methoden

Alle Proben werden einer Phasenanalyse mittels Röntgenbeugung am Pulver unterzogen. Die genaue strukturelle Charakterisierung erfolgt durch Vermessung aus der Probe isolierter Einkristalle auf einem Einkristalldiffraktometer.

2.2.1 Pulverdiffraktometrie

Standartmäßig erfolgt die Charakterisierung pulverförmiger Proben mittels Röntgenbeugung in Flachbettgeometrie mit Hilfe eines STOE *Stadi-P* Pulverdiffraktometers (Cu-K$_{\alpha_1}$-Strahlung ($\lambda = 1{,}54051$ Å, Ge(111) Monochromator) und eines DECTRIS *mythen DCS 1K*-Festkörperdetektors in Transmissionsgeometrie. Zur Probenpräparation wird die Probe in einem Mörser zu feinem Pulver verrieben, zwischen zwei röntgenamorphen Klebestreifen (SCOTCH$^{®}$*Magic*™ Tape 810, 3M) fixiert und in einen Flachbettträger eingelegt. Die Messzeit zur standartmäßigen Phasenanalyse beträgt 15 min. Die Auswertung erfolgt mit der STOE WINXPOW Software. [82] Zum Vergleich mit Pulverdaten bekannter Phasen werden theoretische Streuwinkel aus cif-Daten aus Pearson's Crystallographic Database mit Hilfe des Programms LAZY-PULVERIX berechnet. [83, 84]

Temperaturabhängige Pulver-XRD-Messungen wurden von Thomas Miller an der Ludwig-Maximilians-Universität München an einem STOE *Stadi P* Pulver-Diffraktometer (Mo-K$_{\alpha_1}$-Strahlung ($\lambda = 0{,}71069$ Å)) mit EUROTHERM Heizsystem durchgeführt.

2.2.2 Einkristallstrukturanalyse

Zur Strukturauflärung werden unter dem Lichtmikroskop regelmäßige Kristalle aus dem Produkt separiert oder Stücke mit einem Skalpell von einem großen Kristall abgetrennt und mithilfe eines Polarisationsfilters auf Einkristallinität untersucht. Für Messungen unter 400 K werden die Einkristalle mit transparentem Nagellack auf Glasfäden geklebt. Da sich der Nagellack bei höheren Temperaturen zersetzt, werden die Einkristalle für Hochtemperaturmessungen in eine Glaskapillare gefüllt, der Kristall mit einer weiteren Kapillare darin fixiert und die Kapillare unter Vakuum verschlossen. Beispielhafte Einkristalle, sowie die beiden Montagearten werden in Abbildung 2.1 gezeigt.

Beugungsdaten werden auf verschiedenen Einkristalldiffraktometern erhoben. Messungen unterhalb von 400 K werden standartmäßig auf einem STOE *Stadivari* Einkristalldiffraktometer mit Microfocus-Röntgenquelle (XENOCS *Genix 3D^X*, Mo-K$_{\alpha_{1/2}}$-Strahlung ($\lambda = 0{,}71073$ Å)) und Pixeldetektor (DECTRIS *Pilatus3R 110K*) durchgeführt. Dabei werden Temperaturen zwischen 100 und 400 K mit einem OXFORD *Cryostream plus*) Kühl- und Heizsystem eingestellt. Hochtemperaturmessungen überhalb von 400 K
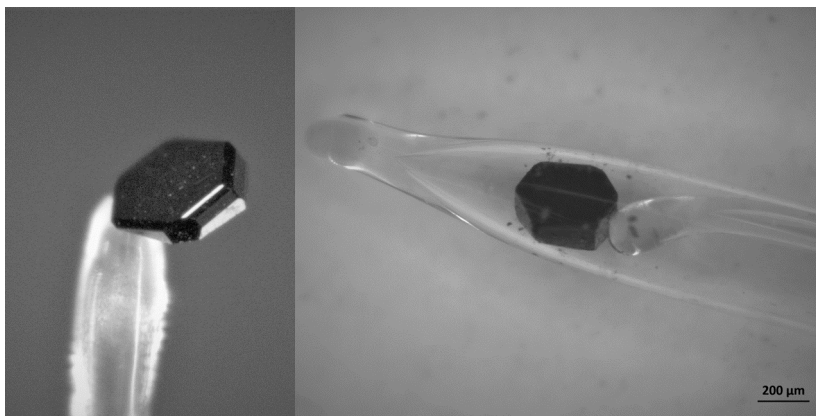
Abbildung 2.1: Lichtmikroskopaufnahmen von montierten Einkristallen der Verbindung $Cu_{9,1}Te_4Cl_3$. Links: Mit Nagellack auf Glasnadel geklebt. Rechts: In Glaskapillare montiert.

werden auf einem STOE *IPDS II* durchgeführt, welches mit einer Drehanode (Mo-K$_{\alpha_{1/2}}$-Strahlung ($\lambda = 0{,}71073$ Å), Graphitmonochromator), einem Flächenzähler ($d = 340$ mm) und einem STOE *Heatstream* Heizsystem ausgestattet ist.

Zusätzliche Hochtemperaturessungen wurden freundlicherweise von Tom Faske und Dr. Jens Meyer von der Firma STOE an einem hauseigenen *Stadivari* Einkristalldiffraktometer, ausgestattet mit Microfocus-Röntgenquelle (Ag-K$_{\alpha_{1/2}}$-Strahlung ($\lambda = 0{,}56378$ Å), DECTRIS *PILATUS3 X* CdTe-Detektor und STOE *Heatstream*, durchgeführt. Der Vorteil der Messung der hier behandelten Systeme mit Ag-Strahlung gegenüber Mo-Strahlung liegt in geringerer Absorption durch schwere Atomsorten (beispielsweise Te).

Zellbestimmung und Datenreduktion findet in allen drei Fällen mit dem STOE *X-Area* Programmpaket statt. [85] Eine nummerische Absorptionskorrektur erfolgt basierend auf symmetrieäquivalenten Reflexen mit Hilfe der Programme *XRed* und *XShape*. [86, 87]

Im Fall von systematischer Verzwilligung wird mit Hilfe von STOE *X-Area* Zwillingsintegration durchgeführt. Dafür werden alle Zwillingsindividuen einzeln indiziert und anschließend zusammen integriert. Die Reflexe werden dabei einzelnen oder mehreren Individuuen zugeordnet, sowie die Zwillingsmatrizen bestimmt. Anschließend wird Zwillingsabsorptionskorrektur durchgeführt.

Raumgruppen werden durch Analyse von Auslöschungsparametern, sowie Anwendung von Gruppe-Untergruppe Beziehungen mit Hilfe der *International Tables of Crystallography, Volume A: Space group symmetry* und *Volume A1: Symmetry relations between space groups* bestimmt. [88, 89]

Strukturlösung (Superflip) und Verfeinerung werden mit Hilfe des Programmpakets *Jana2006* durchgeführt. [90–92] Zur besseren Darstellung von Struktur und Bindungsverhältnissen innerhalb der hochmobilen Ionenleiter werden Auslenkungsparame-

ter nicht-harmonisch verfeinert. Hierbei wurden zur Reduktion der Parameteranzahl nicht-signifikante Parameter (3σ-Kriterium) gleich null gesetzt und nicht weiter verfeinert. [93–97] Systematisch verzwillingte Systeme werden mit Hilfe der zugeordneten Reflexe und nach maueller Eingabe der zuvor ermittelten Zwillingsmatrizen genauso in *Jana2006* gelöst und verfeinert. [98]

2.3   Bestimmung des Seebeck-Koeffizienten und der elektrischen Leitfähigkeit

Zur Untersuchung der thermoelektrischen Eigenschaften werden der Seebeck-Koeffizient und die elektrische Leitfähigkeit mit Hilfe eines Netzsch *SBA 458 Nemesis* Messgerätes bestimmt.
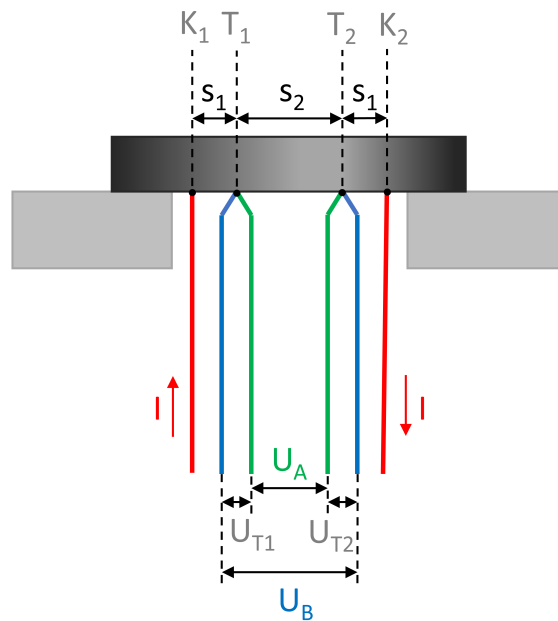
Abbildung 2.2: Schematische Darstellung des Messaufbaus zur Bestimmung des Seebeck-Koeffizienten und der elektrischen Leitfähigkeit.

Der Aufbau der Messzelle ist in Abbildung 2.2 dargestellt. Nachdem die Probe mittels des äußeren Ofens auf eine stabile definierte Temperatur geheizt wurde, erzeugen die beiden Mikroheizer (Typ K Thermoelemente) T_1 und T_2 einen Temperaturgradienten in der Probe. Während des Heizprozesses werden die gemessenen Seebeckspannungen U_A und U_B gegen die entsprechenden Temperaturdifferenzen aufgetragen. Nach linearer Regression über die Messpunkte wird aus den Steigungen der Geraden a_A und a_B und den Seebeckkoeffizienten der beiden Thermodrähte S_A und S_B mit folgender Gleichung der Seebeckkoeffizient S der Probe bestimmt:

$$S = \frac{1}{2}\left(\frac{a_A + a_B}{a_B - a_A} \cdot (S_A - S_B) + S_A + S_B\right)$$

Der Flächenwiderstand der Probe wird mittels einer linearen Viepunktanordnung gemessen. Über die Rhodiumkontakte K_1 und K_2, die rechts und links der Thermoelemente angeordnet sind, wird der Strom $+I$ und $-I$ in die Probe geprägt und die resultierende Potentialdifferenz ΔU an den beiden Thermoelementen T_1 und T_2 be-

stimmt. Da es sich um eine endlich große Probe handelt und das Potentialfeld an den Kanten gestört wird, müssen zur Berechnung der elektrischen Leitfähigkeit geometrieabhängige Korrekturfaktoren F_1 und F_2 miteinbezogen werden. [99, 100] Damit ergibt sich mit den Abständen s_1 und s_2 folgende Gleichung:

$$\sigma = \frac{\Delta I}{\Delta U} \cdot \left(\frac{1}{s_1} - \frac{1}{s_1 + s_2}\right) \cdot \pi \cdot F_1 \cdot F_2$$

Es wird eine Tablette mit mindestens 85 % der kristallographischen Dichte hergestellt und auf den Probenträger gelegt. Die Messung erfolgt senkrecht zur Pressrichtung unter Argondurchfluss von 60 mL min^{-1}. Wenn nicht anders vermerkt, wird mit einer Heizrate von 1 K min^{-1} und einer maximalen Heizspannung von 7 V zur Zieltemperatur geheizt. Die Messung findet nach Erreichen einer Temperaturstabilität mit einer maximalen Änderung um 0,05 K pro 30 s statt. Zur Messung der elektrischen Leitfähigkeit wird ein Gleichstrom von maximal 50 mA angelegt. Im direkten Anschluss an die Leitfähigkeitsmessung wird der Seebeck-Koeffizient bestimmt. Hierfür wird eine Temperaturdifferenz von mindestens 2 K induziert.

Weitere Messungen wurden freundlicherweise von Dr. Ekkerard Post von der Firma Netzsch an einem hauseigenen NETZSCH *SBA 458 Nemesis* unter Heliumatmosphäre durchgeführt. Dieses Gerät ist mit einer Stickstoffkühlung ausgestattet, was Tieftemperaturmessungen ermöglicht.

2.4 Strom/Spannungs-Messungen
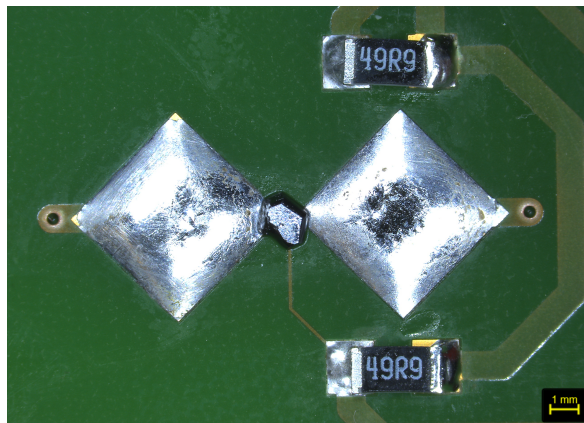
Abbildung 2.3: Lichtmikroskopaufnahme von einem zur Strom/Spannungs-Messung auf einer Leiterplatte montierten Einkristall.

Zur Aufnahme von Strom/Spannungs-Kennlinien wird ein Einkristall auf einer Leiterplatte (PCB, Printed Circuit Board) montiert und mit Hilfe von Indium (ALPHA AESER, 99,999%) oder Lötzinn (STANNOL, Zusammensetzung Sn:Pb:Cu = 60:39:1 Gew%) kontaktiert. Leitfähigkeitsmessungen werden mittels einer KEITHLEY 2450 SMU (Source Meter Unit) ausgeführt. Datenanalyse erfolgt mit Hilfe des KEITHLEY Kickstart IV Characterizer App Softwarepakets.

Tieftemperaturmessungen werden in einem Kühlschrank durchgeführt. Um einen Temperaturgradienten zu erzeugen, werden zwei Widerstände (49 Ω) neben einem der Kontakte platziert und durch einen externen Strom aufgeheizt, der mittels einem QJE PS6005 Netzteil bereitgestellt wird. Die Temperaturkontrolle erfolgt durch externe Thermoelemente an den Kontakten.

Die Messungen wurden von Philipp Deng und Alfred Rabenbauer durchgeführt. Das PCB-Design stammt von Ruben Steib.

2.5 Weitere analytische Methoden

2.5.1 Thermische Analyse (DSC)

Zur Detektion und Vermessung von Phasenübergängen wird an allen Verbindungen eine DSC (Differential Scanning Calorimetry)-Analyse an einem NETZSCH *DSC 200 F3 Maja* Kalorimeter durchgeführt. Dafür wird standartmäßig etwa 15 mg gemörserte Probe in einen Aluminiumtiegel gefüllt und mittels einer Presse (NETZSCH) luftdicht verschlossen. Wenn nicht anders vermerkt, erfolgt die Messung in Stickstoffatmosphäre mit einer Heizrate von 5 K min^{-1}. Es werden standartmäßig zwei vollständige Heizzyklen vermessen. Phasenübergänge erscheinen als endotherme Signale im Heizzyklus. Phasenübergangstemperaturen werden als Onset-Temperaturen bestimmt und Phasenübergangsenthalpien durch Integration.

2.5.2 Bestimmung der Wärmeleitfähigkeit (LFA)

Zur Bestimmung der thermischen Leitfähigkeit wird Laser Flash Analyse eingesetzt. Die Messungen wurden sowohl von Matthias Jakob an der Universität Leipzig, als auch von Thorben Böger an der Universität Münster durchgeführt und ausgewertet.

Im ersten Fall erfolgt die Messung der Temperaturleitfähigkeit an einem LINSEIS *LFA1000* Laserflashgerät mit einem InSb-Detektor mit 280 V Laserstärke. Korrekturen aufgrund von Wärmeverlust und endlicher Pulsdauer werden anhand von Duszas Modell durchgeführt. [101]

Im zweiten Fall wurde an einem SELB *LFA 467 HyperFlash* mit 250 V Laserstärke gemessen. Die Bestimmung der thermischen Diffusivität erfolgte mittels einer verbesserten Version des Modells von Cape und Lehman. [102, 103]

Die Wärmeleitfähigkeit wurde in beiden Fällen durch Multiplikation mit der Dulong-Petit-Wärmekapazität und der Dichte des Pellets erhalten. [104]

2.5.3 Rasterelektronenmikroskopie und EDX-Analyse

Zur Untersuchung von Zusammensetzung und Morphologie werden Aufnahmen an einem Rasterelektronenmikroskop (scanning electron mikroscope, SEM) vom Modell JEOL *JCM-6000 NeoScop TM* (5900LV, Si(Li)-Detektor) mit integrierter JEOL *JED-2200* EDX-Einheit (15 kV Beschleunigungsspannung) gemacht.

Weitere EDX-Messungen wurden von Katia Rodewald am Wacker-Lehrstuhl für Macromolekulare Chemie an einem JEOL *JCM-6000 NeoScop* mit integrierter JEOL *JED-2200* EDX-Einheit mit 15 V Beschleunigungsspannung durchgeführt.

2.5.4 Raman-Spektroskopie

Zur punktuellen Untersuchung mittels Raman-Spektroskopie werden Proben auf einem Glas-Objektträger plaziert. Die Messung erfolgt mit einem grünen Laser ($\lambda = 532$ nm, $P_{max} = 500$ mW) an einem RENISHAW *inVia* Raman-Spektrometer bei Raumbedingungen. Standartmäßig werden 500 Wiederholungen mit 0,5 % der maximalen Laserstärke und 1 s Belichtungszeit gemessen.

2.5.5 Photolumineszenz-Spektroskopie (PL)

PL-Spektren zur Untersuchung der optischen Eigenschaften werden an einem WITEC *alpha300R* Raman-Mikroskopsystem mit OLYMPUS *LMPlanFL N* 50x/0,5-Objektiv aufgenommen. Die Probe wird mit einem grünen Laser ($\lambda = 532$ nm, $P_{max} = 0,1$ mW, 300 g mm^{-1} Raster) angeregt. Die Integrationszeit beträgt 30 s mit 3 Akkumulationen.

Die PL-Messungen wurden von Katharina Nisi am Walter-Schottky-Institut der Technischen Universität München durchgeführt.

2.5.6 Bestimmung des Kompressionsmoduls

Zur Bestimmung des Kompressionsmoduls wurde druckabhängige Pulver-XRD mit Synchrotron-Strahlung ($\lambda = 0{,}4246$ Å) an der I15 Beamline der Diamond Light Source in Ditcot, Großbritannien durchgeführt. In einer Diamand-Druckzelle wurde bis zu 9,5 GPa Druck auf die Probe ausgeübt. Als interner Standart fungierte dabei Rubin. [105, 106] Die Reflexprofile wurden mit Hilfe der Software *Fityk* [107] mit Pseudo-Voigt-Kurven angepasst und mit *Jana2006* [90, 91] verfeinert. Das Kompressionsmodul K_0 wurde mit Hilfe der Zustandsgleichung nach Birch-Murnaghan ermittelt: [108]

$$p = \frac{3}{2} K_0 [(\frac{V}{V_0})^{-\frac{7}{3}} - (\frac{V}{V_0})^{-\frac{5}{3}}]\{1 + \frac{3}{4}(K' - 4)[(\frac{V}{V_0})^{-\frac{2}{3}} - 1]\}$$

Dabei ist p der Druck, K_0 das Kompressionsmodul, K' die Ableitung des Kompressionsmoduls nach dem Druck, V das Zellvolumen bei gegebenem Druck und V_0 das Zellvolumen bei Umgebungsdruck.

2.5.7 Festkörper-NMR

Zur Untersuchung von Bindungscharakter und Mobilität der anionischen und kationischen Teilstrukturen in $Ag_{18}Cu_3Te_{11}Cl_3$ wurde ^{125}Te-, ^{109}Ag- und ^{65}Cu-Festkörper-NMR durchgeführt. Zur Reduzierung der Messzeit bei der ^{125}Te-NMR wurde eine Probe mit angereichertem ^{125}Te synthtisiert. Die Festkörper-NMR-Experimente wurden von Dr. Renée Siegel an der Universität Bayreuth durchgeführt.

^{125}Te-Festkörper-MAS-NMR wurde an einem a BRUKER *400 Avance III HD* Spektrometer bei einer Feldstärke von $B_0 = 9,4$ T aufgenommen, was einer Frequenz von 126,1 MHz entspricht. Um die Ausbildung eines Temperaturgradienten zu verhindern, wurde die Probe ins mittlere Drittel des Rotors gesetzt und mit 62,5 kHz auf einem BRUKER 1,3 mm-Doppelresonanz-MAS-Messkopf rotiert. Als Standart dienen $(CH_3)_2$Te und Te(OH)$_2$.

^{109}Ag- und ^{65}Cu-Festkörper-NMR-Spektren wurden an einem BRUKER *600 Avance III HD* Spektrometer bei einer Feldstärke von $B_0 = 14,1$ T aufgenommen, was im Fall von ^{109}Ag einer Frequenz von 28,0 MHz, und im Fall von ^{65}Cu 170,5 MHz entspricht. Für die MAS-Experimente wurden die Proben mit 40, bzw 62,5 kHz auf einem BRUKER 1,3 mm-Doppelresonanz-MAS-Messkopf rotiert. Statische Experimente wurden auf einem Dreifachresonanz-Wideline-Messkopf aufgenommen. Als Standarts fungieren AgNO$_3$ und CuCl.

Zur Temperaturkalibierung dient in allem Fällen Ph(NO$_3$)$_2$.

3 Ergebnisse

3.1 Cu$_{9,1}$Te$_4$Cl$_3$: Ein thermoelektrisches Material mit niedriger Wärmeleitfähigkeit und hoher elektrischer Leitfähigkeit

Anna Vogel[1], Thomas Miller[2], Constantin Hoch[2], Matthias Jakob[3], Oliver Oeckler[3] und Tom Nilges[1]

[1] Technische Universität München, Fakultät für Chemie, Synthese und Charakterisierung innovativer Materialien, Lichtenbergstraße 4, 85748 Garching bei München, Deutschland
[2] Ludwig-Maximilian-Universität München, Fakultät für Chemie, Butenandtstraße 5-13, 81377 München, Deutschland
[3] Universität Leipzig, Institut für Mineralogie, Kristallographie und Materialwissenschaften, Fakultät für Chemie und Mineralogie, Scharnhornstraße 20, 04275 Leipzig, Deutschland

Der Artikel wurde im Februar 2019 bei der Zeitschrift *Inorganic Chemistry* eingereicht und im April 2019 veröffentlicht. Ein Teil der Ergebnisse wurde von Anna Vogel im Juli 2018 beim 19. *International Symposium on the Reactivity of Solids* in Bayreuth, Deutschland präsentiert.

Das Thema dieser Arbeit ist die neue polymorphe Verbindung Cu$_{9,1}$Te$_4$Cl$_3$ aus der Klasse der Münzmetallpolychalkogenidhalogenide. Kupfer ist hochmobil, was zu mehreren Ordnung-Unordnungs-Phasenübergängen im Temperaturbereich zwischen 240 und 370 K führt. Vor allem bedingt durch die Wärmetransporteigenschaften erreicht das Bulkmaterial einen thermoelektrischen Gütefaktor *ZT* von 0,15 bei 523 K. Hinsichtlich der Kristallstruktur ist Cu$_{9,1}$Te$_4$Cl$_3$ eng mit Ag$_{10}$Te$_4$Br$_3$ verwandt, einem anderen Münzmetallpolytelluridhalogenid, welches reversible, durch Temperaturänderung ausgelöste, pnp-Schaltung zeigt (näheres in Kapitel 1.2 auf Seite 4). Die neue Verbindung übertrifft Ag$_{10}$Te$_4$Br$_3$ hinsichtlich der thermoelektrischen Eigenschaften um eine Größenordnung, zeigt aber keinen pnp-Übergang. Sie kann daher als Bindeglied zwischen den thermoelektrischen Materialien und der Verbindngsklasse der pnp-Materialien (vorgestellt in Kapitel 1.3 auf Seite 8) gesehen werden.

Durch DSC-Messung wurde nachgewiesen, dass Cu$_{9,1}$Te$_4$Cl$_3$ temperaturabhängig in vier Polymorphen kristallisiert, wovon die beiden Hochtemperaturpolymorphe durch

Einkristall-XRD-Messungen charakterisiert wurden.

Die Kristallstruktur von $Cu_{9,1}Te_4Cl_3$ ist genau wie bei $Ag_{10}Te_4Br_3$ aus abwechselnd aufeinander gestapelten Tellurid-6^3-Bienenwabennetzen und Halogenid-6.3.6.3-Kagoménetzen aufgebaut, welche von Strängen teilweise kovalent gebundener polyanionischer Tellureinheiten durchdrungen werden. Die extrem mobilen Kationen sind in beiden Fällen um die Stränge herum lokalisiert. Im Fall von $Cu_{9,1}Te_4Cl_3$ sind diese Stränge nicht aus $[Te_2]^{2-}$-Hanteln und linear koordinierenden Te^{2-}-Anionen bestehenden Te_4-Einheiten aufgebaut, sondern aus leicht verlängerten $[Te_2]^{2-}$-Hanteln. Da $Cu_{9,1}Te_4Cl_3$ keinen pnp-Übergang zeigt, wird die Theorie untermauert, dass der Wechsel zwischen p- und n-Halbleitung bei $Ag_{10}Te_4Br_3$ durch strukturelle Umordnungen innerhalb der Stränge von Te_4-Einheiten ausgelöst wird, was zum Verständnis des Mechanismus der pnp-Schaltung beiträgt.

Neben DSC- und Einkristall-XRD-Messungen wurde temperaturanhängige Pulver-XRD und Raman-Spektroskopie durchgeführt und wird im Folgenden diskutiert.

Die thermoelektrischen Eigenschaften wurden durch Messung des Seebeck-Koeffizienten, der elektrischen Leitfähigkeit und der Wärmeleitfähigkeit durch LFA bestimmt.

Beiträge der Autoren: A.V. synthetisierte die Verbindung, führte die DSC, die Raman-Spektroskopie, die Messung des Seebeck-Koeffizienten und der elektrischen Leitfähigkeit, sowie die Einkristall-XRD durch und löste die Kristallstrukturen. T.M. und C.H. führten die temperaturabhängige Pulver-XRD durch. M.J. und O.O. führten die LFA durch. A.V. und T.N. schrieben das Manuskript. Alle Autoren diskutierten die Ergebnisse und überarbeiteten das Manuskript.

Cu$_{9.1}$Te$_4$Cl$_3$: A Thermoelectric Compound with Low Thermal and High Electrical Conductivity

Anna Vogel,[†] Thomas Miller,[‡] Constantin Hoch,[‡] Matthias Jakob,[§] Oliver Oeckler,[§] and Tom Nilges*,[†]

[†]Synthesis and Characterization of Innovative Materials, Department of Chemistry, Technical University Munich (TUM), Lichtenbergstraße 4, 85748 Garching bei München, Germany

[‡]Department of Chemistry, University of Munich (LMU), Butenandtstraße 5-13, 81377 Munich, Germany

[§]Faculty of Chemistry and Mineralogy; Institute for Mineralogy, Crystallography and Materials Science, Leipzig University, Scharnhorststraße 20, 04275 Leipzig, Germany

Ⓢ *Supporting Information*

ABSTRACT: Cu$_{9.1}$Te$_4$Cl$_3$ is a new polymorphic compound in the class of coinage metal polytelluride halides. Copper is highly mobile, which results in multiple order−disorder phase transitions in a limited temperature interval from 240 to 370 K. Mainly as a consequence of thermal transport properties, the compound's thermoelectric figure of merit reaches values up to ZT = 0.15 in the temperature range between room temperature and 523 K. Its structure is closely related to that of Ag$_{10}$Te$_4$Br$_3$, another coinage metal polytelluride halide, which represents the first p−n−p-switchable semiconductor approachable by a simple temperature change. The title compound outperforms Ag$_{10}$Te$_4$Br$_3$ in terms of thermoelectric properties by 1 order of magnitude and therefore acts as a link between the class of p−n−p compounds and thermoelectric materials.
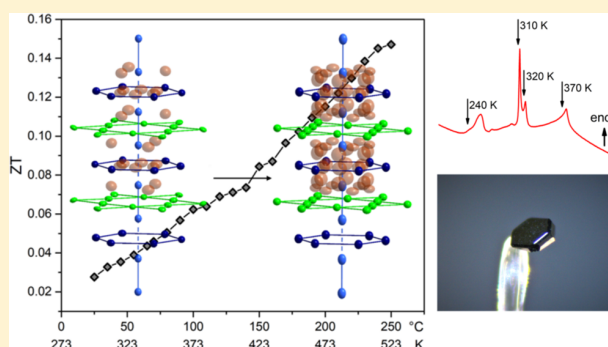
■ INTRODUCTION

Thermoelectric materials offer various opportunities for "green" energy applications by directly converting waste heat to electric energy. The dimensionless figure of merit ZT is often used as measure of thermoelectric performance. As ZT is defined as $S^2\sigma\kappa^{-1}T$, where S is the Seebeck coefficient, σ the electrical conductivity, and κ the thermal conductivity, a high Seebeck coefficient and electrical conductivity together with low thermal conductivity are requirements for high-performance thermoelectric compounds.[1] Hence, narrow-band-gap semiconductors are candidates for high ZT values because of their combination of relatively high Seebeck coefficients and low electronic thermal conductivity. Mixed solid ion and electron conductors, like the title compound, are another class of materials frequently investigated as candidates for thermoelectrics. Here, the presence of ion conduction is detrimental to their use in thermoelectric applications, but this fact is often ignored. Our interest to determine the thermoelectric properties of the title compound is aimed at another aspect that is not directly related to energy conversion:

The class of semiconductors designated as p−n−p compounds is a class of materials capable of reversible switching between p- and n-type semiconduction without a change of composition. Potential applications are semiconductor switches, sensors, or devices reacting reversibly to

temperature or voltage changes.[2] These compounds undergo ion-mobility-driven order−disorder phase transitions showing typical phonon softening effects. This has been confirmed to be usually accompanied by band gap variation and significant change of the density of states at the Fermi level. As a consequence, this feature leads to an intermediate quasi-metallic state in which valence electron conduction increases.[3,4] The first representative in the class of p−n−p compounds is the tetramorphic coinage metal polychalcogenide halide Ag$_{10}$Te$_4$Br$_3$.[5,6] It undergoes p−n−p-switching accompanied by a huge jump of the Seebeck coefficient activated simply by variation of the temperature.[2] Other materials exhibiting this behavior are the chalcogenides AgBiSe$_2$, AgCuS, and Tl$_2$Ag$_{12}$Se$_7$.[3,7−9] In$_4$Se$_{3−x}$ does not undergo a p−n−p switch but it shows similar modulations (changes in the Seebeck value in a small temperature range) of the Seebeck coefficient.[10,11]

The structure of the new compound Cu$_{9.1}$Te$_4$Cl$_3$ is closely related to Ag$_{10}$Te$_4$Br$_3$. Both compounds contain isolated Te$^{2−}$ ions and predominantly covalently bonded Te-units but show quite different electrical properties. With low thermal and high electrical conductivity, Cu$_{9.1}$Te$_4$Cl$_3$ outperforms Ag$_{10}$Te$_4$Br$_3$ in

terms of thermoelectric performance. Hence, the new compound is a model system to carve out the features leading to p−n−p switching by comparison with the structurally related p−n−p compound and thus serves as a proof of concept concerning the proposed mechanism. In addition, it serves as a link between p−n−p materials and common thermoelectric compounds.

■ EXPERIMENTAL SECTION

Synthesis. $Cu_{9.1}Te_4Cl_3$ was prepared from a 6.1:3:4 mixture of copper (Chempur, 99.999%), copper(I) chloride (Alfa Aesar, 97%), and tellurium (Chempur, 99.999%) on a gram scale. The starting materials were sealed into evacuated silica glass ampules, heated to 1320 K, held at this temperature for 3 h, and quenched in an ice bath. The crude product was finely ground and annealed at 660 K for 7 days followed by slow cooling to room temperature. This synthesis route leads to a black crystalline material containing large single crystals of the title compound (major phase), a second copper polychalcogenide halide (polycrystalline material, minor phase), and a few, very small crystals of copper(I) chloride which acted as a starting material and transport agent at the same time (see the Supporting Information for additional information and phase analysis). The main fraction, large single crystals of $Cu_{9.1}Te_4Cl_3$, were separated from the minor phases and used for further characterization. $Cu_{9.1}Te_4Cl_3$ is stable in air.

XRD Experiments. X-ray powder diffraction phase analysis was used to verify the phase purity of $Cu_{9.1}Te_4Cl_3$ separated from the bulk material. Temperature-dependent measurements were performed on a Stoe Stadi P powder diffractometer equipped with an imaging plate detector and an Eurotherm high temperature device using Mo $K\alpha_1$ radiation (λ = 0.71069 Å). Low-temperature measurements were performed at 173, 193, 223, 273, and 283 K and high-temperature measurements from 293 to 773 K in 10 K steps. Data are given in Figure 4.

Intensity data of two different crystals (crystal 1 was used for the 440 and 350 K and crystal 2 for the 290 and 200 K measurements) were collected on a Stoe IPDS 2T imaging plate diffractometer (440 and 350 K measurements) and a Stoe STADIVARI diffractometer with a Dectris hybrid pixel detector (290 and 200 K measurements) fitted with Mo $K\alpha_1$ radiation (λ = 0.71069 Å). Temperature-dependent measurements were performed using an Oxford Cryostream plus system (290 and 200 K measurements) and a Stoe heating system (440 and 350 K measurements).

The data sets were corrected for Lorentz and polarization effects, and a numerical absorption correction based on optimized crystal shapes, derived from symmetry-equivalent reflections, was applied using the Stoe X-Area[12] software. The structures were solved by the charge-flipping algorithm[13] implemented in the Jana 2006 program suite.[14] All space groups were derived from a careful analysis of Laue symmetry and extinction conditions as well as group−subgroup relations leading to a chemically correct structure model. Structure refinements were performed using the Jana 2006 program.[14] Coordinates, anisotropic and third-order anharmonic displacement parameters, and the site occupancy factors (sof) of copper atoms in α-$Cu_{9.1}Te_4Cl_3$ were refined without constraints. Details of the structure determination are given in the Supporting Information. For β-$Cu_{9.1}Te_4Cl_3$, the same composition as determined for the α-phase was used, and the overall copper content was restricted to this value.

Raman Spectroscopy. Raman spectra were recorded at 300 K by using a Renishaw inVia RE04 Raman microscope equipped with a Nd:YAG laser (λ = 532 nm) and a CCD detector. In order to avoid decomposition of the sample, a low laser power of 0.05 mW was applied, recording a total number of 300 scans.

Thermal Analyses. A finely ground sample of phase pure $Cu_{9.1}Te_4Cl_3$ (16.3 mg) was transferred to an aluminum crucible and was measured with a rate of 5 K h^{-1} using a Netzsch DSC 200 F3Maia apparatus. All measurements were performed under N_2 atmosphere. The thermal effects were derived as onset temperatures. Enthalpies were determined by integration.

Measurements of Electrical Conductivity and Seebeck Coefficient. Finely ground $Cu_{9.1}Te_4Cl_3$ crystals were hot-pressed to a pellet of 15 mm diameter and 1.08 mm thickness reaching 87% of the crystallographic density using a P/O/Weber 10 H hot press tool with a P/O/Weber TRG 1 temperature control unit. The sample was pressed with 12 t in a Maassen MP150 lab press while it was heated to 100 °C during 30 min, kept at this temperature for 1 h, and cooled to room temperature during 3 h. Electrical conductivity and Seebeck coefficient were measured simultaneously perpendicular to the pressing direction with a NETZSCH SBA 458 Nemesis under a continuous argon flow with a rate of 60 mL min^{-1}. For the determination of the Seebeck coefficient, a temperature difference of at least ΔT = 2 K was used, and for the determination of the electrical conductivity, a DC current of 50 mA was applied. Three full cycles were measured, as shown in the Supporting Information.

Measurement of Thermal Conductivity. Finely ground $Cu_{9.1}Te_4Cl_3$ crystals were pressed with a pressure of 10 t to a pellet of 6 mm diameter and 0.95 mm thickness reaching 90% of the crystallographic density. A self-made wolfram carbide pressure die was used. Thermal diffusivity measurements were performed across the pellet under static helium atmosphere using a Linseis LFA1000 laser-flash device equipped with an InSb detector. A laser power of 280 V was applied. Heat loss and finite pulse corrections were calculated applying Dusza's model.[15] Thermal conductivity was obtained by multiplying the values with the Dulong−Petit heat capacity and the measured density of the pellet, which was determined using Archimedes' principle.

■ RESULTS AND DISCUSSION

The following section deals with the structural characterization and the determination of the electrical and thermal transport properties of the new copper(I) polychalcogenide halide. Temperature-dependent single-crystal structure determinations at various temperatures are reported in order to get a detailed insight into the structural properties of the new material. Bonding properties are illuminated by Raman spectroscopy. Thermal analysis and measurements of the electrical conductivity and the Seebeck coefficient outline thermal and electrochemical properties of $Cu_{9.1}Te_4Cl_3$ at various temperatures.

Thermal Analysis. The thermal behavior of $Cu_{9.1}Te_4Cl_3$ was determined by differential scanning calorimetry (DSC) in the temperature range of 180−500 K. Four endothermic effects at 370, 320, 310, and 240 K can be observed that have been assigned to the $\alpha-\beta$, $\beta-\beta'$, $\beta'-\gamma$, and $\gamma-\delta$ phase transitions, respectively. The $\beta-\beta'$ and the $\beta'-\gamma$ phase transitions are rather close to each other; hence, it is very difficult to separate them. In the following, they are interpreted as one phase transition in two steps, called the $\beta-\gamma$ phase transition. Figure 4 A and Table 1 give an overview of the

Table 1. Results from Thermal Analysis of $Cu_{9.1}Te_4Cl_3$

phase transition	T (onset value) (K)	enthalpy (J g^{-1})
$\delta \rightarrow \gamma$	240	0.60
$\gamma \rightarrow \beta$	310	0.96
$\beta \rightarrow \alpha$	370	0.82

effects observed in the temperature range of 200 to 450 K. As can be seen in Figure S4 in the Supporting Information, all effects are reversible and have been measured from different independently prepared samples over two consecutive cycles for each run. The four endothermic effects are different regarding the shape of the curves. At 370 and 240 K, the signals are slightly broadened; in contrast, the effects at 310 and 320 K are very sharp peaks. Regarding the phase-transition

enthalpies, all effects range in the same magnitude, pointing toward order−disorder phase transitions (second-order-like).

Crystal Structure. Temperature-dependent structure investigations have been performed within the temperature range of 200−440 K. A total number of four measurements have been carried out at 200, 290, 350, and 440 K in order to analyze the structural changes undergoing the observed phase transitions. Four different structures could be identified starting with δ-Cu$_{9.1}$Te$_4$Cl$_3$ at 200 K to α-Cu$_{9.1}$Te$_4$Cl$_3$ at 440 K. The structures of the two low temperature polymorphs γ and δ could not be determined reliably at this time. A brief summary of crystallographic details of the two high-temperature polymorphs α and β is given in Table 2.

Table 2. Crystallographic Data of Polymorphic Cu$_{9.1}$Te$_4$Br$_3$

	α-Cu$_{9.1}$Te$_4$Cl$_3$	β-Cu$_{9.1}$Te$_4$Cl$_3$
refined composition	Cu$_{9.1(2)}$Te$_4$Cl$_3$	Cu$_{9.1}$Te$_4$Cl$_3$
molar mass (g mol^{-1})	1194.5	1195.0
crystal size (mm)	0.2 × 0.07 × 0.07	0.2 × 0.07 × 0.07
crystal shape/color	block/black	block/black
crystal system	hexagonal	hexagonal
space group	$P6/mmm$ (191)	$P6_3/mmc$ (194)
Z	1	8
a (Å)	7.2962(7)	14.5019(11)
c (Å)	7.0940(7)	14.190(11)
V (Å^3)	327.05(5)	2584(2)
T (K)	440	350
$\rho_{calc.}$ (g cm^{-3})	6.065	6.1428
diffractometer	STOE IPDS 2T	STOE IPDS 2T
radiation	Mo Kα (0.71069 Å)	Mo Kα (0.71069 Å)
μ (mm^{-1})	23.778	24.087
F(000)	523	4183
θ range (deg)	3.22−33.21	4.02−33.39
hkl range	−11/+11, −11/+10, −10/+10	−22/+20, −22/+22, −21/+21
no. of reflections	4214	64009
R$_{int}$	0.0919	0.1325
data/parameters	212/35	1748/125
R/wR [$I > 3\sigma(I)$]	0.0278/0.0589	0.0595/0.0991
R/wR (all)	0.0424/0.0663	0.2174/0.1270
goodness of fit	1.46	1.65
res. elec. dens. max/min (e Å^{-3})	−1.09/+1.48	−1.84 /+1.87

The complex crystal structure is discussed by a separate description of the anion and cation substructures. The structure of Cu$_{9.1}$Te$_4$Cl$_3$ is closely related to Ag$_{10}$Te$_4$Cl$_3$ but significant differences can be found in the cationic substructure including the transition-metal content and in the type and distribution of covalently bonded Te-units leading to severe deviations in the electronic properties.

Anion Substructure. The Cl$^-$ ions are arranged to Kagomé 3.6.3.6 nets, whereas discrete Te^{2-} ions form honeycomb 6^3 networks. The distances d(Te−Te) between 4.14 and 4.26 Å and d(Cl−Cl) between 3.61 and 3.64 Å correspond to slightly more than two times the van der Waals radii according to Pauling (d_{vdW}(Te^{2-}) = 2.06 Å, d_{vdW}(Cl$^-$) = 1.80 Å).[16] While there are ideal, high symmetric nets in the high-temperature polymorph, distortions appear at lower temperatures. Both anion nets are stacked alternately along one direction. Predominantly covalently bonded Te$_2$-dumbbells with distances d(Te−Te) from 3.20 to 3.27 Å interpenetrate the Cl$^-$

Kagomé networks in a perpendicular fashion. The dumbbells are arranged to one-dimensional Te-strands with alternating short and long Te−Te distances (3.20−3.27 and 3.83−3.88 Å) parallel to the stacking direction of the networks (see Figure 1). We found no hint for disorder or diffuse scattering in the
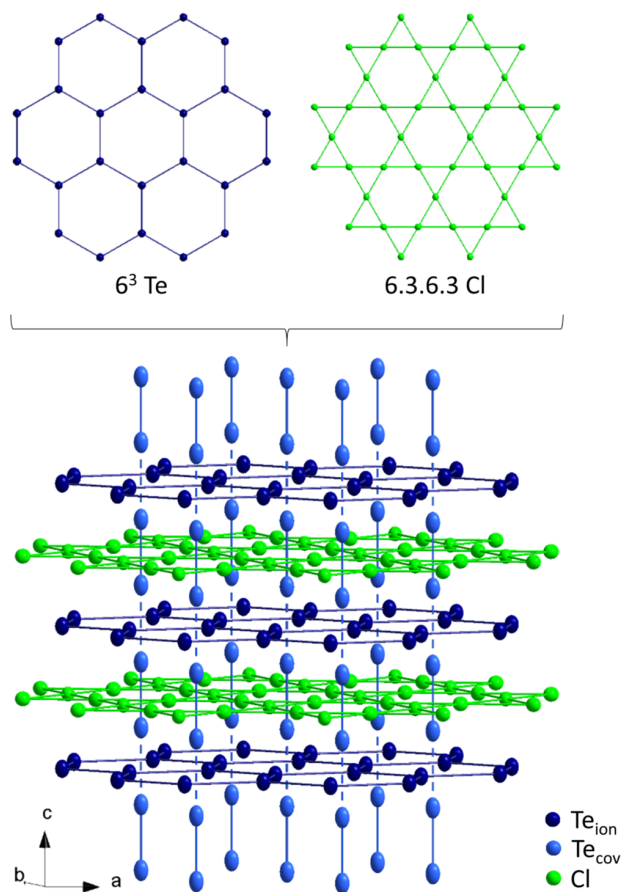
Figure 1. Anionic substructures in Cu$_{9.1}$Te$_4$Cl$_3$: 3.6.3.6 Cl nets (green spheres) and 6^3 Te nets (dark blue spheres) are stacked along [001]. Predominantly covalently bonded Te$_2$ dumbbells (light blue spheres) forming linear strands center the six-membered rings of the 3.6.3.6 Cl nets. Displacement parameters are shown with 90% probability.

XRD experiments pointing toward a disorder or tendency within the Te-chain to realize an equidistant arrangement. The displacement parameters of Te are only slightly elongated along the Te-chain axis (see Figure 1, displacements shown at 90% probability level).

The distances are longer than in common covalent Te−Te-bonds. For instance, in the case of [Te$_2$]$^{2-}$ dumbbells, they range between 2.70 Å in MgTe$_2$[17] and 2.86 Å in α-K$_2$Te$_2$,[18] while in the infinite Te-chains in elemental tellurium, d(Te−Te) is 2.83 Å.[19] Nonetheless, the distances are much shorter than twice the van der Waals radius, which is a first indicator for covalent Te−Te interactions within the strands.

Considering the oxidation states in the anionic substructure, while regarding the present Te$_2$-dumbbell as a proper covalently bonded unit, a formal ionic electron count leads to (Cu$^+$)$_9$[Te$_2$]$^{2-}$(Te^{2-})$_2$(Cl$^-$). Here d(Te−Te) is elongated, leading to a higher formal charge than only −1 per Te atom which results in a small excess of copper and subsequently to the sum formula Cu$_{9.1}$Te$_4$Cl$_3$ (see Table 2). In Ag$_{10}$Te$_4$Br$_3$, we

find a Te_4 unit consisting of a fully covalently bonded Te_2 dumbbell linearly coordinated by two additional Te^{2-}-ions. This unit interpenetrates the anionic tellurium network resulting in $(Ag^+)_{10}([Te_2]^{2-})_{0.5}(Te^{2-})_3(Cl^-)_3$. As a result, the silver compound contains a higher amount of transition metal while in $Cu_{9.1}Te_4Cl_3$, the ratio of $[Te_2]$ dumbbells vs isolated Te^{2-} ions is higher.

Cation Substructure. As shown in Figure 2, partially occupied copper positions are located in the voids of the 6^3
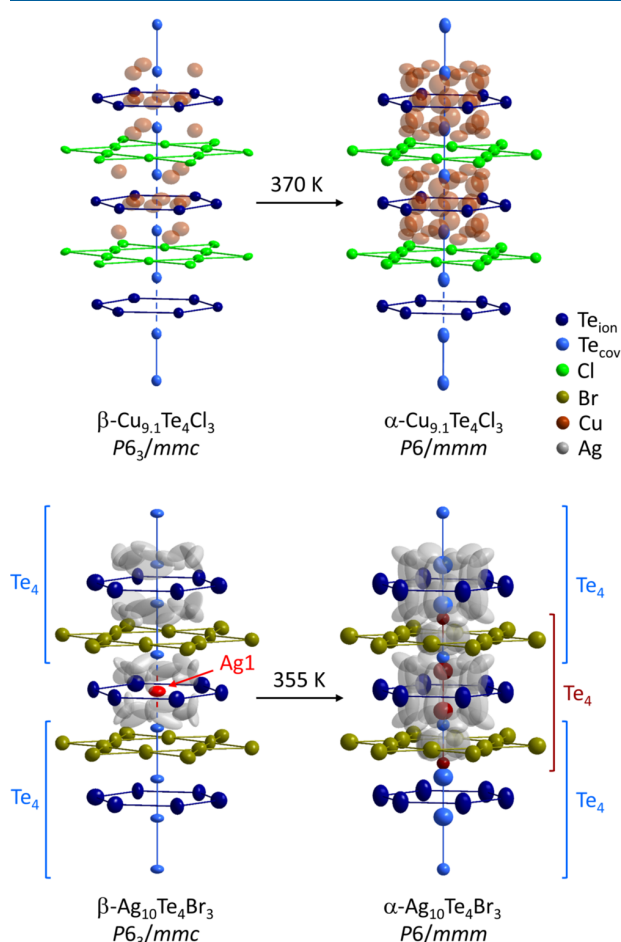
Figure 2. Structure sections featuring the predominantly covalent bonded Te strands in β- and α-$Cu_{9.1}Te_4Cl_3$ and β- and α-$Ag_{10}Te_4Br_3$. Displacement parameters are drawn at the 90% probability level.

Te nets and between the anionic layers surrounding the Te-strands in both high temperature polymorphs of $Cu_{9.1}Te_4Cl_3$. In the α-polymorph, copper atoms tend to occupy positions within and in direct neighborhood of the 6^3 Te nets while the occupation of interstitial sites within the 3.6.3.6 Kagomé nets is avoided. This is in contrast to the situation in α-$Ag_{10}Te_4Br_3$, where silver ions interpenetrate both anion nets (see Figure 2, bottom right). The copper distribution in α-$Cu_{9.1}Te_4Cl_3$ is much more comparable to the silver distribution in β-$Ag_{10}Te_4Br_3$, where silver ions are located around and within the 6^3 Te nets (Ag1 position marked in red in Figure 2) separating the Te_4 units. In β-$Cu_{9.1}Te_4Cl_3$, the amount of copper positions in the neighborhood of the 6^3 Te nets is reduced from 12 to 3 partially occupied copper positions forming 3-membered rings below and above the 6^3 network

(see Figure 2, top left part). Within the 6^3 nets, copper atoms remain disordered on different and not fully occupied sites. Due to the reduced distance between two neighbored 6^3 Te nets caused by (a) the reduced ion radius of the halide ions forming the 3.6.3.6 halide nets (precisely: smaller chloride vs larger bromide ions) in the silver and copper compounds and (b) the type and size of cation (copper vs silver ions), the available space for copper ions within the Te 6^3 net in β-$Cu_{9.1}Te_4Cl_3$ is reduced. This is why the space within the 6^3 Te net, in the center of a six-membered Te ring where the Te chain axis intersect, is not available as a possible site for copper ions. They can therefore not coordinate the covalent Te-units in a linear fashion during cooling and ion ordering, as observed during the $\beta-\alpha$ order–disorder phase transition in $Ag_{10}Te_4Br_3$. As a result, copper atoms are still disordered within the 6^3 nets in β-$Cu_{9.1}Te_4Cl_3$ and cannot fully order at this stage (Figure 1, upper left part). As a second consequence of this finding, we assume that a certain disorder (either statistical or dynamical disorder) remains in the two low temperature polymorphs. This will be the case if the interstitial sites within the 6^3 nets remain occupied.

Two out of the $Cu_{9.1}Te_4Cl_3$ polymorphs, the α and β phase, are structurally characterized and reported in this study. There are at least two additional polymorphs below and around room temperature with very complex crystal structures, where the structural and physical properties still need to be determined. During the $\alpha-\beta$ phase transition, a symmetry reduction by a klassengleiche transition of index 2 and an isomorphic transition of index 4 from space group $P6/mmm$ to $P6_3/mmc$ takes place connected with the decreasing Cu mobility. The cell volume is multiplied by 8 by doubling all three lattice parameters (see Figure 3). After careful analysis of the data we
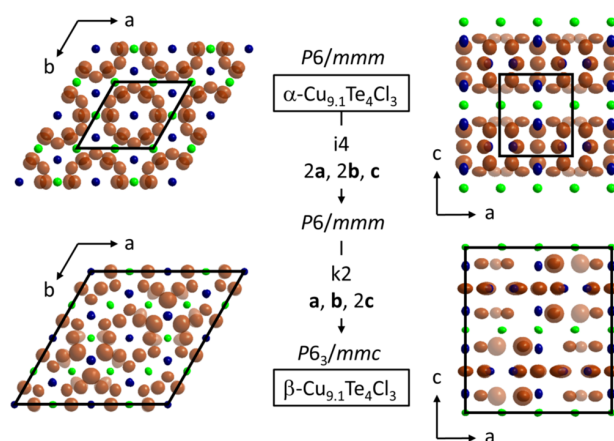
Figure 3. Unit cells of α- and β-$Cu_{9.1}Te_4Cl_3$. During the $\alpha-\beta$ phase transition, the cell volume is multiplied by 8 by doubling all cell parameters.

assume that twinning occurs after undergoing the 320 K phase transition ($\beta/\beta'-\gamma$) associated with an additional symmetry reduction from the hexagonal to the orthorhombic crystal system. Here, the translationengleiche transition of index 3 often leads to 3-fold twins and to a possible space group $Cmcm$. Reconstructed representations of the reciprocal space suggest that, besides twinning at about 320 K, the unit cell might also be enlarged to a 3×3 supercell during the 310 K transition of γ-$Cu_{9.1}Te_4Cl_3$. At this point the only information we can derive is that the C entering is maybe lost in δ-$Cu_{9.1}Te_4Cl_3$ below
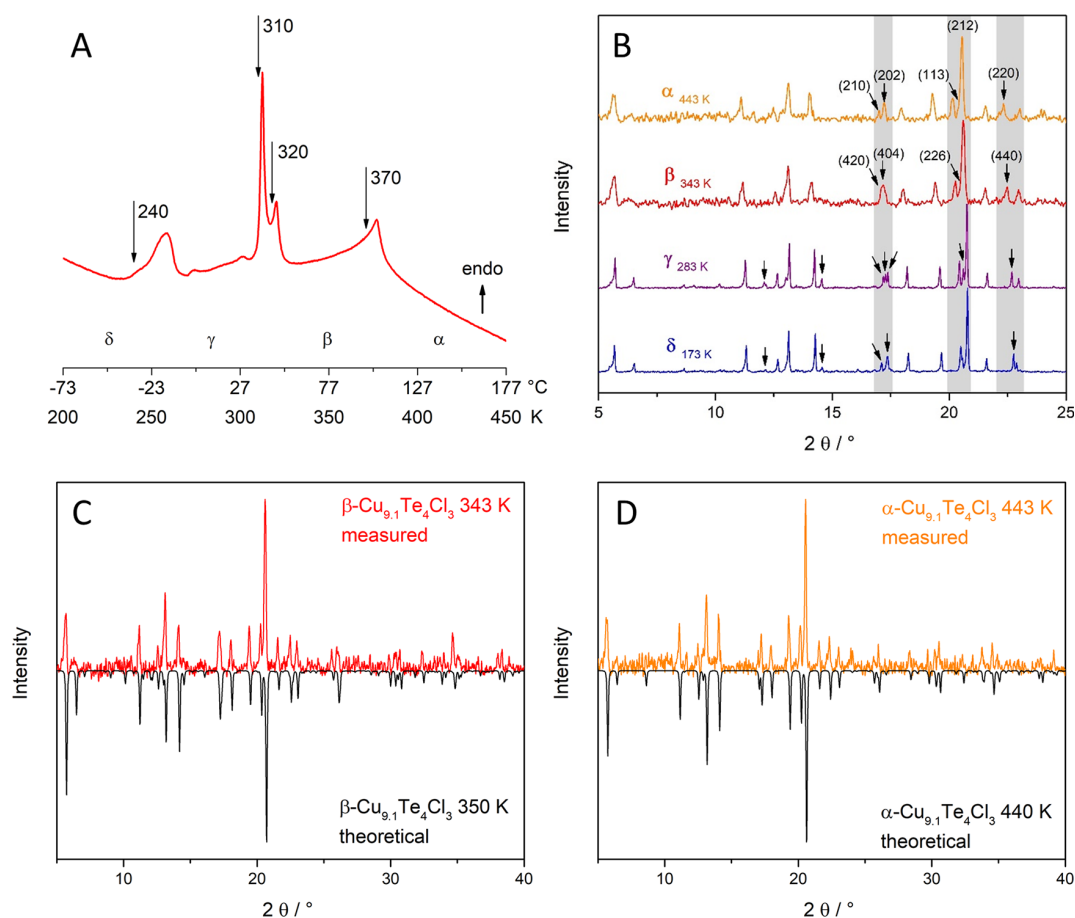
Figure 4. (A) Results from DSC analysis of $Cu_{9.1}Te_4Cl_3$. Section between 200 and 450 K. All thermal effects are reversible in consecutive cycles. Selected regions discussed in the text are emphasized in gray. (B) Powder diffraction pattern of all four polymorphs of $Cu_{9.1}Te_4Cl_3$. (C and D) Powder diffraction pattern of β- and α-$Cu_{9.1}Te_4Cl_3$ and calculated pattern drawn with negative intensities.

240 K. Single crystal structure determination using synchrotron radiation will be conducted shortly to verify these findings.

Powder Diffraction. Powder diffraction patterns measured at 443, 343, 283, and 173 K correspond to the α-, β-, γ- and δ-polymorphs (Figure 4B). Both the α- and the β-polymorphs fit well with patterns calculated from the single-crystal data (Figure 4, parts C and D). As can be seen in Figure 4, both reflection patterns show only small deviations, which corroborate that there are only slight changes in the crystal structure as a consequence of ordering of the copper atoms due to the decreasing ion mobility with decreasing temperature. Regarding the reflections designating the 210, 202, and 220 reflections around 17 and 22° 2θ in the α-polymorph and the corresponding 420, 404, and 440 reflections in the β-polymorph, some splitting can be observed. Based on structure chemical considerations and our experience with the silver compound, we assume that this observation is associated with the distortion of the Cl Kagomé nets in the β-polymorph. Whether this assumption is valid has to be verified by additional experiments. Going from the β- to the γ- and δ-polymorph, additional splitting of these reflections can be observed, indicating further distortion of the Kagomé nets with decreasing temperature. In the reflection pattern of both high-temperature polymorphs (α and β), the 113 and the 226 reflections overlap with the strong 212 reflection at 20° 2θ, but

in the γ-polymorph, the corresponding reflection is shifted to lower angles, and both reflections are resolved. We assume some distortion of the Te-6^3-networks here. Due to the expected remaining disorder in the copper substructure of the low temperature polymorphs, we did not perform model calculations, and we intend to determine the low temperature structures instead (therefore we will conduct single crystal structure determination using synchrotron radiation shortly). Furthermore, some additional weak reflections occur in the diffraction patterns of low-temperature polymorphs, substantiating further symmetry reduction upon cooling.

Raman Spectroscopy. The occurrence of elongated, predominantly covalent Te–Te-bonds in $Cu_{9.1}Te_4Cl_3$ was substantiated by Raman spectroscopy. A broad band was observed at 121 cm^{-1}, which can be assigned to the stretching mode of the elongated Te–Te unit, in good agreement with the suggested structure model. Previously published frequencies for Te–Te modes in tellurium, polytellurides, and free polytelluride complexes include 170 cm^{-1} in Te, 168 cm^{-1} in $Ag_{10}Te_4Br_3$, and 160 cm^{-1} in $[Cd_4Te_{12}]^{4-}$ relating to bond lengths around 2.8 Å.[5,20,21] In the title compound, the predominantly covalently bonded dumbbells form Te-strands with alternating short (3.20–3.27 Å) and long (3.83–3.88 Å) Te–Te distances. The elongation of the bonds leads to lower bonding energies, resulting in smaller frequencies in the Raman spectrum. $Cu_{9.1}Te_4Cl_3$ is very sensitive toward decomposition
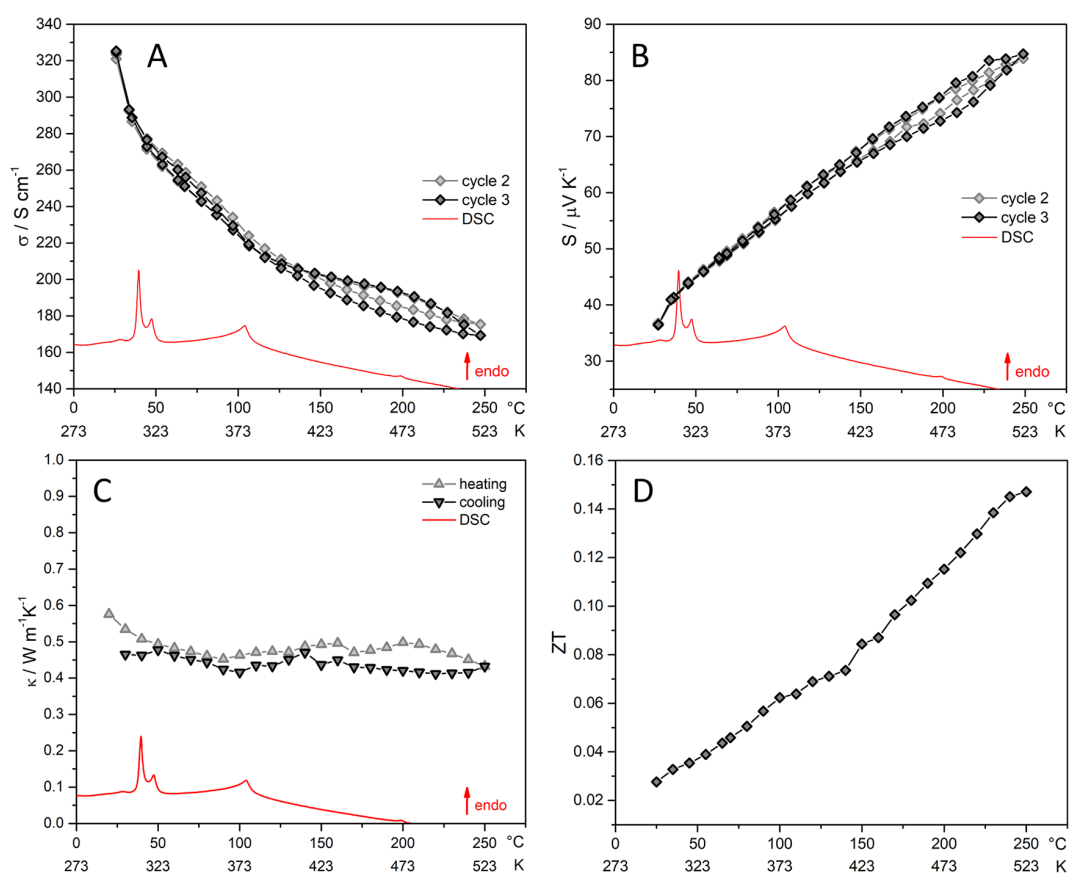
Figure 5. Thermoelectric characterization measurements of $Cu_{9.1}Te_4Cl_3$ with DSC data (red curves). (A) Electric conductivity. (B) Seebeck coefficient. (C) Thermal conductivity. (D) Calculated figure of merit ZT.

during the Raman experiment. Upon a slight increase of the laser power, the compound decomposed and showed a sharp and defined mode of elemental tellurium instead. Details are given in the Supporting Information.

Thermoelectric Properties. The Seebeck coefficient and the electrical conductivity were determined simultaneously between room temperature and 523 K (Figure 5). Besides slight deviations concerning the first heating step, all values are reproducible in three consecutive cycles. Therefore, cycles two and three were used for further evaluation. The Seebeck coefficient of $Cu_{9.1}Te_4Cl_3$ at room temperature is 36 $\mu V\ K^{-1}$, and it increases linearly with temperature to 85 $\mu V\ K^{-1}$ at 523 K, which is higher than in the thermoelectric compound Cu_2Te in this temperature range by a factor of about 2.[22] The electrical conductivity decreases from 325 S cm^{-1} at room temperature to 169 S cm^{-1} at 523 K. This matches, together with the magnitude of the Seebeck coefficient, rather the behavior of a metal than of a semiconductor. While the Seebeck coefficient increases more or less linearly with the temperature, the progression of the electrical conductivity shows two points of inflection around the temperatures of the phase transitions. The electrical conductivity of $Cu_{9.1}Te_4Cl_3$ at 298 K is much higher than in the insulator CuCl (8.05×10^{-5} S cm^{-1}) but about a magnitude lower than in Cu_2Te (around 10^3 S cm^{-1}).[22,23] In comparison with the semiconductor $Ag_{10}Te_4Br_3$, the electrical conductivity is about 3 orders of magnitude higher but the absolute value of the Seebeck coefficient is much lower. $Ag_{10}Te_4Br_3$ exhibits Seebeck

coefficients between +310 and −940 $\mu V\ K^{-1}$ while undergoing p−n−p switching during the $\alpha-\beta$ phase transition, whereas $Cu_{9.1}Te_4Cl_3$ shows the behavior of a p-type conductor over the whole measured temperature range.[2]

The thermal conductivity is quite low between 0.4 and 0.6 W $m^{-1}\ K^{-1}$, which is comparable with the thermal conductivity of the coinage metal polytelluride halide $Ag_{10}Te_4Br_3$ (0.27−0.43 W $m^{-1}\ K^{-1}$ in the temperature range 250−390 K)[2] and about 1 order of magnitude lower than the thermal conductivity in Cu_2Te (between 2 and 4 W $m^{-1}\ K^{-1}$ at room temperature according to different studies).[22,24,25] Since the compound is sensitive to laser light, which had already been noticed in the Raman measurements, the sample showed a slight decomposition tendency during the laser-flash measurement. As it was possible to reproduce the values of the first cycle with lower laser power in a smaller temperature range in consecutive cycles, the first cycle was used for further evaluation (for details, see the Supporting Information).

To estimate the lattice thermal conductivity κ_{ph}, the electronic contribution of the thermal conductivity κ_{el} was subtracted from the total thermal conductivity. As can be seen in Figure S6 in the Supporting Information k_{ph} and k_{el} contribute equally to the total thermal conductivity. To calculate κ_{el}, the Wiedemann−Franz law was used, which is defined as $\kappa_{el} = L \cdot T \cdot \sigma$, where L is the Lorenz number (2.44×10^{-8} W $\Omega\ K^{-2}$), T = absolute temperature, and σ = electrical conductivity.[26]

The low thermal conductivity in combination with the relatively high electrical conductivity of $Cu_{9.1}Te_4Cl_3$ leads to ZT values from 0.028 at room temperature to 0.15 at 523 K, which is in the same range as in the case of Cu_2Te.[22] With respect to the figure of merit, it outperforms the p−n−p compound $Ag_{10}Te_4Cl_3$ (maximum ZT value of 0.017 at 390 K) by 1 order of magnitude. On the other hand, the ZT value should not be over interpreted due to the somehow limited potential of the mixed-conducting title compound as thermoelectric material due to the high ion conductivity. Within our experimental framework, $Cu_{9.1}Te_4Cl_3$ shows reproducible results and robustness but this will not be the case in thermoelectric generators after long-term usage.

The unlike behavior of both of the coinage metal polytelluride halides $Cu_{9.1}Te_4Cl_3$ and $Ag_{10}Te_4Br_3$ regarding electronic properties can be explained by slight deviations in the crystal structure. The structures of polymorphic $Cu_{9.1}Te_4Cl_3$ are quite similar (but not isotypic) to those of $Ag_{10}Te_4Br_3$ considering the alternate stacking of anion networks interpenetrated by predominantly covalently bonded Te-units parallel to the stacking direction.[5] Both compounds are tetramorphic and show anisotropic ion conductivity.[6] Nonetheless, $Ag_{10}Te_4Br_3$ shows a significant change in the thermoelectric features undergoing the phase transitions triggered by internal redox processes during the formation of equidistant Te-chains while in $Cu_{9.1}Te_4Cl_3$ the thermoelectric properties are changed continuously.[2] Reasons are differences in the predominantly covalently bonded Te-units and in the cation distribution. In the case of $Ag_{10}Te_4Br_3$, predominantly covalently bonded Te_4-units consisting of Te_2-dumbbells and two additional linear coordinated Te atoms interpenetrate the anionic tellurium network. As can be seen in Figure 2, in the low temperature polymorphs these units are separated by an almost linear coordinating silver position. As a result of the increasing ion mobility, silver tends to leave this site in the high temperature polymorphs leading to oligomerization of the Te-units accompanied by internal redox processes. As a result, an equidistant Te chain is realized. This process is accompanied by a significant increase of the electron mobility along the chain leading to a switch of the type of conductivity from p- to n-type and vice versa.

In $Cu_{9.1}Te_4Cl_3$, even in the low temperature polymorphs, all copper positions are scattered around the central $[Te_2]$ dumbbell strand and there is no linear coordinating copper position within the Te-strands. Therefore, no structural frustration or equidistant chain formation takes place undergoing the phase transitions.

In a series of substitution experiments in $Ag_{10}Te_4X_3$, with X = Cl, Br, I, it was shown that the ability of the formation of the equidistant chain is directly correlated to the distance between two 6^3 Te nets stacked along the c-axis and thereby the c lattice parameter. It was shown that an optimal stabilization of the polymorphs containing the equidistant Te-chain takes place in $Ag_{10}Te_4Br_{2.8}I_{0.2}$ with $c = 15.356(2)$ Å (equivalent two times the distance between two 6^3 Te nets).[27]

As we already discussed earlier, the distance between two neighboring 6^3 Te nets is smaller in $Cu_{9.1}Te_4Cl_3$ than in $Ag_{10}Te_4Br_3$ due to the different sizes of the halides as well as the cations. In the case of the title compound, the c parameter is 14.19(1) Å (equivalent to twice the distance between two 6^3 Te nets) in the β-polymorph while the same distance in $Ag_{10}Te_4Br_3$ is 15.374(1) Å at room temperature. In $Cu_{9.1}Te_4Cl_3$ the c lattice parameter seems to be too short to allow such a formation of an equidistant Te-chain within the framework of the given Te- and Br-nets. A possible doubling of the c axis will not solve that problem because only the distance between the two anion nets determines the ability to form such a chain. To induce the formation of the equidistant chain, an increase of the c lattice parameter (or more precisely the distance between the 6^3 Te and the 3.6.3.6 Br nets) seems to be necessary which might be realized by a substitution of Cl by higher homologues.

In the case of $Ag_{10}Te_4Br_3$, there are partial substitutions in the anionic (Br by Cl, I, and Te by S, Se) as well as in the cationic substructure (Ag by Cu).[27−29] In the latter case, Ag was substituted up to 50% by Cu under retention of the $Ag_{10}Te_4Br_3$ crystal structure.[29] Now it seems intriguing to address the influence of silver substitution in $Cu_{9.1}Te_4Cl_3$ on the electrical and thermoelectric properties.

Although the thermoelectric performance of the new compound is not competitive to commercial thermoelectric materials like Bi_2Te_3, PbTe, and $Pb_{1−x}Ga_xTe$ reaching ZT values of 0.7−0.9 in the temperature range investigated here, it must be taken into account that the material has not yet been optimized for any thermoelectric application.[30,31] On the basis of effective-mass modeling, the charge carrier concentration may be optimized by targeted doping. This may enhance the relatively low electrical conductivity of the material and lead to a better thermoelectric performance. Subsequently, nanostructuring (either nanostructuring directly[32] or by a second phase[33]) might be a way to further reduce the still very low thermal conductivity. Another aspect needs to be mentioned here which may render a thermoelectric optimization obsolete. In general, solid ion conductors lack long-term stability if used as thermoelectric materials due to the significant mass transport under thermoelectric operation.

Due to close structural relationship to the p−n−p switching in $Ag_{10}Te_4Cl_3$, it might be possible to tune the title material toward the initiation of p−n−p switching.

■ CONCLUSION AND OUTLOOK

The new compound $Cu_{9.1}Te_4Cl_3$ contains isolated $Cl^−$ and $Te^{2−}$ anions in the form of alternately stacked Kagomé and honeycomb nets interpenetrated by one-dimensional, predominantly covalently bonded Te-strands. Mobile Cu ions coordinate this anion framework in an almost liquid-like fashion. It exhibits very low thermal conductivity in combination with reasonable electric conductivity. Even with its low Seebeck coefficient, it outperforms $Ag_{10}Te_4Br_3$, which features a Seebeck that is higher by 1 order of magnitude. By improvement of the electrical conductivity via doping, the new material might have the potential to enhance its thermoelectric performance.

Furthermore, the anion substructure of $Cu_{9.1}Te_4Cl_3$, precisely the $[Te_2]$ dumbbell chain, can be regarded as a Peierls distorted intermediate stage heading for another p−n−p switching material like $Ag_{10}Te_4Br_3$. p−n−p switching in $Ag_{10}Te_4Br_3$ is induced by the structural frustration and Peierls distortion of an equidistant Te chain toward linear Te_4 units. For $Cu_{9.1}Te_4Cl_3$, we only observe a chain of $[Te_2]$ dumbbells which are not able to undergo a transition to an equidistant stage, mainly due to structural reasons. Via substitution in the cation and anion substructure, it might be possible to induce p−n−p switching in this copper compound by an enlargement of the lattice in the direction of the Peierls distortion.

Acting as a link between the classes of p−n−p switching compounds and thermoelectric materials, optimization of the properties of $Cu_{9.1}Te_4Cl_3$ are needed to push it in either direction.

■ ASSOCIATED CONTENT

ⓢ Supporting Information

The Supporting Information is available free of charge on the ACS Publications website at DOI: 10.1021/acs.inorg-chem.9b00453.

> Phase analysis of the bulk material, additional crystallo-graphic data, DSC data, Raman spectra, and full thermoelectric data including the first measurement cycles (PDF)

Accession Codes

CCDC 1896966−1896967 contain the supplementary crystallographic data for this paper. These data can be obtained free of charge via www.ccdc.cam.ac.uk/data_request/cif, or by emailing data_request@ccdc.cam.ac.uk, or by contacting The Cambridge Crystallographic Data Centre, 12 Union Road, Cambridge CB2 1EZ, UK; fax: +44 1223 336033.

■ AUTHOR INFORMATION

Corresponding Author

*(T.N.) E-mail: tom.nilges@tum.de.

ORCID ⓞ

Constantin Hoch: 0000-0003-2687-178X
Oliver Oeckler: 0000-0003-0149-7066
Tom Nilges: 0000-0003-1415-4265

Notes

The authors declare no competing financial interest.

■ ACKNOWLEDGMENTS

■ REFERENCES

(1) Bell, L. E. Cooling, heating, generating power, and recovering waste heat with thermoelectric systems. *Science* **2008**, *321* (5895), 1457−1461.

(2) Nilges, T.; Lange, S.; Bawohl, M.; Deckwart, J. M.; Janssen, M.; Wiemhöfer, H.- D.; Decourt, R.; Chevalier, B.; Vannahme, J.; Eckert, H.; et al. Reversible switching between p-and n- type conduction in the semiconductor $Ag_{10}Te_4Br_3$. *Nat. Mater.* **2009**, *8* (2), 101−108.

(3) Xiao, C.; Qin, X.; Zhang, J.; An, R.; Xu, J.; Li, K.; Cao, B.; Yang, J.; Ye, B.; Xie, Y. High thermoelectric and reversible pnp conduction type switching integrated in dimetal chalcogenide. *J. Am. Chem. Soc.* **2012**, *134* (44), 18460−18466.

(4) Delaire, O.; Marty, K.; Stone, M. B.; Kent, P. R.; Lucas, M. S.; Abernathy, D. L.; Mandrus, D.; Sales, B. C. Phonon softening and metallization of a narrow-gap semiconductor by thermal disorder. *Proc. Natl. Acad. Sci. U. S. A.* **2011**, *108* (12), 4725−4730.

(5) Lange, S.; Nilges, T. $Ag_{10}Te_4Br_3$: A new silver(I) (poly)-chalcogenide halide solid electrolyte. *Chem. Mater.* **2006**, *18* (10), 2538−2544.

(6) Lange, S.; Bawohl, M.; Wilmer, D.; Meyer, H.-W.; Wiemhöfer, H.-D.; Nilges, T. Polymorphism, structural frustration, and electrical properties of the mixed conductor $Ag_{10}Te_4Br_3$. *Chem. Mater.* **2007**, *19* (6), 1401−1410.

(7) Guin, S. N.; Banerjee, S.; Sanyal, D.; Pati, S. K.; Biswas, K. Origin of the order-disorder transition and the associated anomalous change of thermopower in $AgBiS_2$ nanocrystals: A combined experimental and theoretical study. *Inorg. Chem.* **2016**, *55* (12), 6323−6331.

(8) Guin, S. N.; Pan, J.; Bhowmik, A.; Sanyal, D.; Waghmare, U. V.; Biswas, K. Temperature dependent reversible p−n−p type con-duction switching with colossal change in thermopower of semi-conducting AgCuS. *J. Am. Chem. Soc.* **2014**, *136* (36), 12712−12720.

(9) Shi, Y.; Assoud, A.; Sankar, C. R.; Kleinke, H. A new pnp conduction switching material with extraordinarily low thermal conductivity. *Chem. Mater.* **2017**, *29* (21), 9565−9571.

(10) Osters, O.; Blazek, G.; Nilges, T. Comments on Peierls-distorted indium chains in In_4Se_{3-x}. *Z. Anorg. Allg. Chem.* **2013**, *639* (3−4), 497−501.

(11) Rhyee, J.-S.; Lee, K. H.; Lee, S. M.; Cho, E.; Kim, S. I.; Lee, E.; Kwon, Y. S.; Shim, J. H.; Kotliar, G. Peierls distortion as a route to high thermoelectric performance in In_4Se_{3-x} crystals. *Nature* **2009**, *459* (7249), 965−968.

(12) STOE &Cie GmbH. *X-AREA: Program for the Acquisition and Analysis of Data, version 1.76.*; Stoe&Cie GmbH: Darmstadt, Germany, 2015.

(13) Palatinus, L.; Chapuis, G. SUPERFLIP−a computer program for the solution of crystal structures by charge flipping in arbitrary dimensions. *J. Appl. Crystallogr.* **2007**, *40*, 786−790.

(14) Petricek, V.; Duéek, M.; Palatinus, L. *JANA 2006, The Crystallographic Computing System.*; Institute of Physics: Praha, Czech Republic, 2006.

(15) Dusza, L. Combined solution of the simultaneous heat loss and finite pulse corrections with the laser flash method. *High Temp. - High Pressures* **1995**, *27/28*, 467−473.

(16) Pauling, L. *The Nature of the Chemical Bond.*, 3rd ed.; Cornell University Press: Ithaca, NY, 1960; Vol. *260*.

(17) Yanagisawa, S.; Tashiro, M.; Anzai, S. Crystal structure of magnesium ditelluride. *J. Inorg. Nucl. Chem.* **1969**, *31* (4), 943−946.

(18) Böttcher, P.; Getzschmann, J.; Keller, R. Zur Kenntnis der Dialkalimetalldichalkogenide-Na_2S_2, K_2S_2, $_2S_2$, Rb_2S_2, K_2Se_2, $Rb_2Se_{22}Te_2$, $_2Te_2$ und Rb_2Te_2. *Z. Anorg. Allg. Chem.* **1993**, *619* (3), 476−488.

(19) Adenis, C.; Langer, V.; Lindqvist, O. Reinvestigation of the structure of tellurium. *Acta Crystallogr., Sect. C: Cryst. Struct. Commun.* **1989**, *45* (6), 941−942.

(20) Weidlein, J.; Müller, U.; Dehnicke, K. *Schwingungsspektroskopie.*, 2nd ed. G. Thieme-Verlag: Stuttgart, Germany, and New York, 1988.

(21) Kim, K.-W.; Kanatzidis, M. G. Synthesis, structure and properties of the polychalcogenides $[M_4Te_{12}]^{4+}$ (M = Cd, Hg). *Inorg. Chim. Acta* **1994**, *224* (1−2), 163−169.

(22) He, Y.; Zhang, T.; Shi, X.; Wei, S.-H.; Chen, L. High thermoelectric performance in copper telluride. *NPG Asia Mater.* **2015**, *7* (8), No. e210.

(23) Matsui, T.; Wagner, J. B. Investigations on a high conductivity solid electrolyte system, RbCl + CuCl. *J. Electrochem. Soc.* **1977**, *124* (6), 941−944.

(24) Ballikaya, S.; Chi, H.; Salvador, J. R.; Uher, C. Thermoelectric properties of Ag-doped Cu_2Se and Cu_2Te. *J. Mater. Chem. A* **2013**, *1* (40), 12478−12484.

(25) Kurosaki, K.; Goto, K.; Kosuga, A.; Muta, H.; Yamanaka, S. Thermoelectric and thermophysical characteristics of Cu_2Te-Tl_2Te pseudo binary system. *Mater. Trans.* **2006**, *47* (6), 1432−1435.

(26) Franz, R.; Wiedemann, G. Ueber die Wärme-Leitungsfähigkeit der Metalle. *Ann. Phys.* **1853**, *165* (8), 497−531.

(27) Nilges, T.; Bawohl, M.; Lange, S. Structural and electrical property tuning of a mixed conductor by partial anion substitution. *Z. Naturforsch., B: J. Chem. Sci.* **2007**, *62* (7), 955−964.

(28) Nilges, T.; Bawohl, M. Structures and thermal properties of silver(I) (poly)chalcogenide halide solid solutions $Ag_{10}Te_{4-(q, p)}Q_{(q, p)}Br_3$ with Q= S, Se. *Z. Naturforsch., B: J. Chem. Sci.* **2008**, *63* (6), 629−636.

(29) Giller, M.; Bawohl, M.; Gerstle, A. P.; Nilges, T. Copper substitution and mixed cation effect in $Ag_{10}Te_4Br_3$. *Z. Anorg. Allg. Chem.* **2013**, *639* (14), 2379−2381.

(30) Tritt, T. M. Holey and unholey semiconductors. *Science* **1999**, *283* (5403), 804−805.

(31) Su, X.; Hao, S.; Bailey, T. P.; Wang, S.; Hadar, I.; Tan, G.; Song, Z.-B.; Zhang, Q.; Uher, C.; Wolverton, C.; Tang, X.; Kanatzidis, M. G. Weak electron phonon coupling and deep level impurity for high thermoelectric performance $Pb_{1x}Ga_xTe$. *Adv. Energy Mater.* **2018**, *8*, 1800659.

(32) Deng, R.; Su, X.; Zheng, Z.; Liu, W.; Yan, Y.; Zhang, Q.; Dravid, V. P.; Uher, C.; Kanatzidis, M. G.; Tang, X. Thermal conductivity in $Bi_{0.5}Sb_{1.5}Te_{3+x}$ and the role of dense dislocation arrays at grain boundaries. *Science Adv.* **2018**, *4*, No. eaar5606.

(33) Deng, R.; Su, X.; Hao, S.; Zheng, Z.; Zhang, M.; Xie, H.; Liu, W.; Yan, Y.; Wolverton, C.; Uher, C.; Kanatzidis, M. G.; Tang, X. High thermoelectric performance in $Bi_{0.46}Sb_{1.54}Te_3$ nanostructured with ZnTe. *Energy Environ. Sci.* **2018**, *11*, 1520−1535.

Supporting Information

$Cu_{9.1}Te_4Cl_3$: A thermoelectric compound with low thermal and high electrical conductivity

Anna Vogel[a], Thomas Miller,[b] Constantin Hoch,[b] Matthias Jakob,[c] Oliver Oeckler,[c] Tom Nilges[a]

a) Technical University Munich (TUM), Synthesis and Characterization of Innovative Materials, Department of Chemistry, Lichtenbergstraße 4, 85748 Garching b. München, Germany

b) University of Munich (LMU), Department of Chemistry, Butenandtstraße 5-13, 81377 Munich, Germany

c) Leipzig University, Faculty of Chemistry and Mineralogy; Institute for Mineralogy, Crystallography and Materials Science, Scharnhorststraße 20, 04275 Leipzig, Germany

Sample preparation and isolation of $Cu_{9.1}Te_4Cl_3$.

To date no phase pure synthesis of $Cu_{9.1}Te_4Cl_3$ is possible. The crude bulk material always contains a second phase (beside large $Cu_{9.1}Te_4Cl_3$ crystals) that was assigned to another unknown copper polytelluride chloride with very similar crystal structure and composition (see Figure S1 and S2). It hast to be taken into account that the powder X-ray diffractogram in Figure S2 has been measured at room temperature. This is close to the temperature of the α – β phase transition and lead to slight deviations in the intensities of the reflections. Characterization of the side phase is still underway. To gain phase pure $Cu_{9.1}Te_4Cl_3$ the large crystals were collected and ground in a

mortar. According to Figure 3C and D this procedure leads to phase pure $Cu_{9.1}Te_4Cl_3$ which was used for all further experiments.
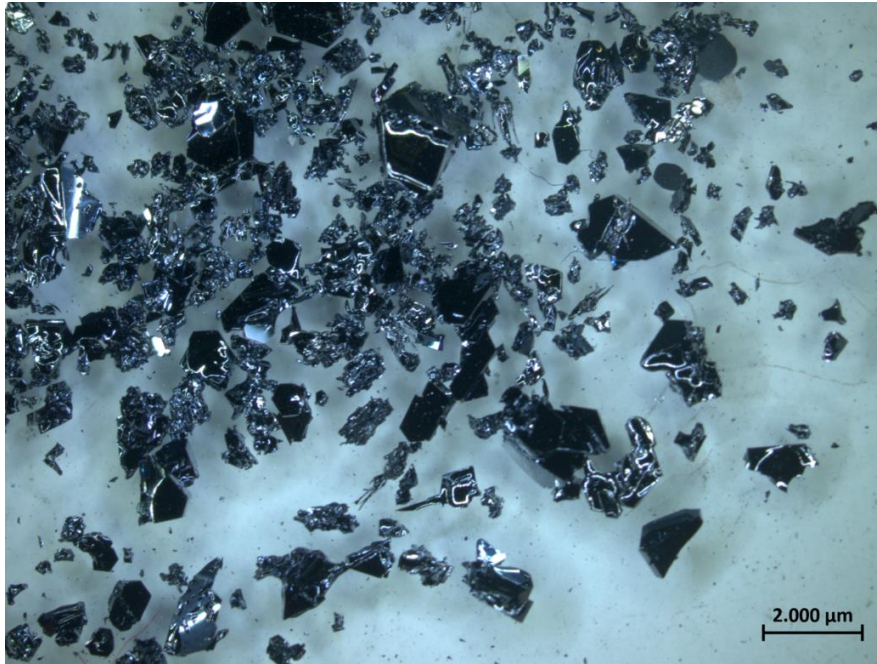
Figure S1. $Cu_{9.1}Te_4Cl_3$ bulk material. The large black crystals are phase pure $Cu_{9.1}Te_4Cl_3$, the smaller particles contain $Cu_{9.1}Te_4Cl_3$ as well as another unknown copper polytelluride chloride. (Photo: Anna Vogel)
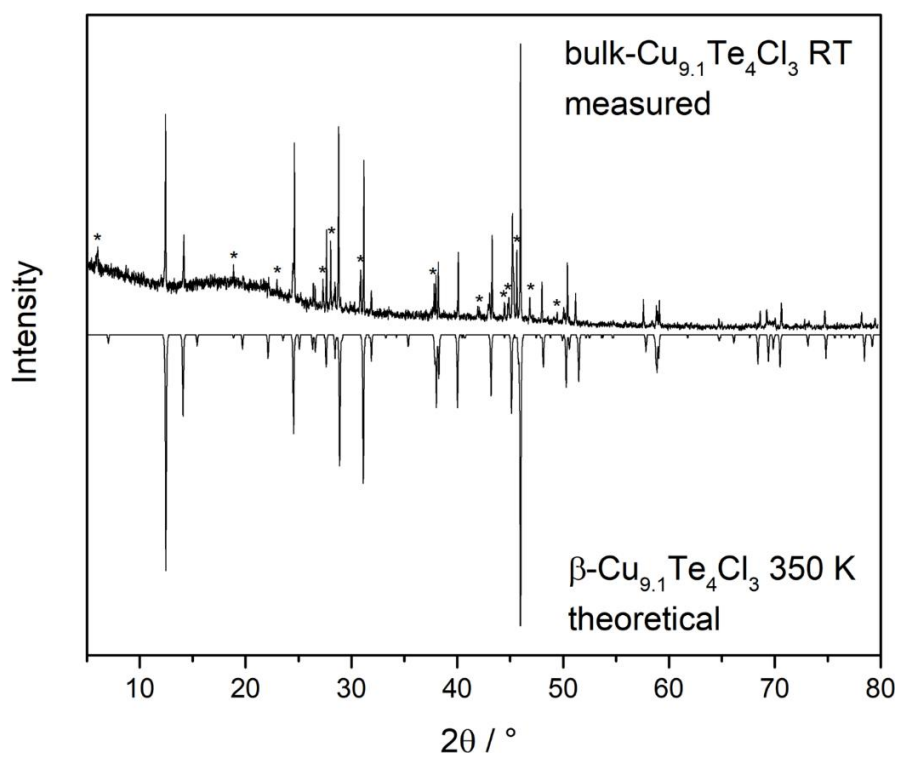
Figure S2. Powder X-ray diffractogram of $Cu_{9.1}Te_4Cl_3$ bulk material. Main phase is $Cu_{9.1}Te_4Cl_3$ (large crystals), side phase (*) is another unknown copper polytelluride chloride.

Structure refinement.

Table S1. Atomic coordinates and site occupancy factors of α-Cu$_{9.1}$Te$_4$Cl$_3$.

Atom	Wyckoff position	Site symmetry	sof	x	y	z
Te1	2c	$\bar{6}m2$	1	2/3	1/3	0
Te2	2e	6mm	1	0	0	0.26923(16)
Cl1	3g	mmm	1	1/2	0	1/2
Cu1	6j	$m2m$	0.465(10)	1	0.2760(7)	0
Cu2	12o	.m.	0.261(5)	1.2101(6)	0.4201(13)	-0.3003(5)
Cu3	12n	..m	0.264(6)	1.3499(13)	0	-0.1982(11)

Table S2. Anisotropic displacement parameters of α-Cu$_{9.1}$Te$_4$Cl$_3$.

Atom	U_{11}	U_{22}	U_{33}	U_{12}	U_{13}	U_{23}
Te1	0.0260(3)	0.0260(3)	0.0326(5)	0.01299(17)	0	0
Te2	0.0269(3)	0.0269(3)	0.0460(6)	0.01345(17)	0	0
Cl1	0.0285(7)	0.0271(9)	0.0244(9)	0.0135(4)	0	0
Cu1	0.076(3)	0.0674(16)	0.068(2)	0.0382(13)	0	0
Cu2	0.066(2)	0.054(3)	0.0315(18)	0.0269(13)	-0.0006(7)	-0.0011(14)
Cu3	0.062(2)	0.085(4)	0.077(4)	0.042(2)	0.0033(18)	0

Table S3. Anisotropic anharmonic displacement parameters of α-Cu$_{9.1}$Te$_4$Cl$_3$.

Atom	C_{111}	C_{112}	C_{113}	C_{122}	C_{123}
Cu1	0	-0.017(3)	0	-0.017(3)	0
Cu2	-0.005(4)	0.002(3)	0	0.017(13)	0
Cu3	-0.024(7)	-0.039(6)	0	-0.039(6)	0
	C_{133}	C_{222}	C_{223}	C_{233}	C_{333}
Cu1	0	0	0	0	0
Cu2	0	0	0.03(3)	0	0
Cu3	0	-0.017(4)	0	0	0

Table S4. Atomic coordinates and site occupancy factors of β-Cu$_{9.1}$Te$_4$Cl$_3$.

Atom	Wyckoff position	Site symmetry	sof	x	y	z
Te1	2c	-6$m2$	1	1/3	2/3	1/4
Te2	6h	$mm2$	1	0.32672(15)	0.16336(8)	1/4
Te3	4e	3m.	1	0	0	0.11396(18)
Te4	6h	$mm2$	1	0.16787(7)	-0.16787(7)	1/4

Te5	2d	-6m2	1	2/3	1/3	1/4
Te6	12k	.m.	1	0.50092(3)	0.00185(6)	0.11455(8)
Cl1	12k	.m.	1	0.4998(4)	0.2499(2)	-0.0029(2)
Cl2	12i	.2.	1	0.2509(4)	0	0
Cu1	12j	m..	0.94(2)	0.3620(9)	-0.0161(13)	1/4
Cu2	24l	1	0.702(11)	0.3928(5)	0.1030(5)	0.0970(6)
Cu3	12k	.m.	0.807(13)	0.2047(5)	0.1024(3)	-0.1027(5)
Cu4	12j	m..	0.912(16)	0.1395(10)	0.1414(10)	-1/4
Cu5	12j	m..	0.839(16)	0.4992(6)	0.1460(9)	1/4
Cu6	12j	m..	0.782(18)	0.3519(8)	-0.1442(8)	1/4
Cu7	12k	.m.	0.38(4)	0.3929(7)	-0.2142(15)	0.3936(10)

Table S5. Anisotropic displacement parameters of β-Cu$_{9.1}$Te$_4$Cl$_3$.

Atom	U_{11}	U_{22}	U_{33}	U_{12}	U_{13}	U_{23}
Te1	0.0223(11)	0.0223(11)	0.0198(15)	0.0111(5)	0.00000	0.00000
Te2	0.0249(11)	0.0217(7)	0.0217(9)	0.0124(5)	0.00000	0.00000
Te3	0.0189(7)	0.0189(7)	0.0275(13)	0.0095(4)	0.00000	0.00000
Te4	0.0250(8)	0.0250(8)	0.0205(9)	0.0153(8)	0.00000	0.00000
Te5	0.0319(13)	0.0319(13)	0.0254(17)	0.0159(6)	0.00000	0.00000
Te6	0.0200(4)	0.0203(7)	0.0329(6)	0.0101(4)	0.00027(17)	0.0005(3)
Cl1	0.0212(17)	0.0181(15)	0.0195(19)	0.0106(9)	0.0043(18)	0.0021(9)
Cl2	0.0221(17)	0.0222(18)	0.0199(19)	0.0111(9)	0.0009(9)	0.0018(18)
Cu1	0.074(4)	0.129(10)	0.074(4)	0.018(4)	0.00000	0.00000
Cu2	0.062(3)	0.070(3)	0.050(3)	0.0336(19)	0.0015(18)	-0.0006(18)
Cu3	0.040(2)	0.058(2)	0.0314(16)	0.0202(11)	0.0009(17)	0.0004(9)
Cu4	0.098(6)	0.091(6)	0.054(3)	0.050(5)	0.00000	0.00000
Cu5	0.062(3)	0.095(5)	0.064(3)	0.032(3)	0.00000	0.00000
Cu6	0.107(6)	0.090(5)	0.055(3)	0.068(4)	0.00000	0.00000
Cu7	0.075(6)	0.067(10)	0.053(6)	0.034(5)	0.0065(18)	0.013(4)

Table S6. Anisotropic anharmonic displacement parameters of β-Cu$_{9.1}$Te$_4$Cl$_3$.

Atom	C_{111}	C_{112}	C_{113}	C_{122}	C_{123}
Cu1	-0.0022(16)	-0.0025(13)	0	0.009(2)	0
Cu2	-0.0026(10)	-0.0028(7)	-0.0023(4)	-0.0041(7)	0
Cu3	-0.0021(8)	-0.0011(4)	0.0008(4)	-0.0024(5)	0.0004(2)
Cu4	0.012(3)	0.013(2)	0	0.015(3)	0
Cu5	0	-0.0052(7)	0	-0.0034(13)	0
Cu6	-0.029(4)	-0.029(3)	0	-0.029(3)	0
Cu7	-0.008(2)	-0.009(2)	-0.0024(12)	-0.011(8)	0
	C_{133}	C_{222}	C_{223}	C_{233}	C_{333}
Cu1	-0.0018(7)	-0.030(7)	0	-0.0045(8)	0
Cu2	-0.0010(4)	-0.0025(11)	-0.0020(4)	0	-0.0033(7)
Cu3	-0.0009(3)	-0.0031(8)	-0.0023(4)	-0.00046(16)	0.0008(5)

Cu4	0.0013(5)	0.021(3)	0	0	0
Cu5	0	0.014(3)	0	0.0050(6)	0
Cu6	-0.0018(6)	-0.025(3)	0	-0.0008(6)	0
Cu7	-0.0018(6)	-0.022(15)	0	-0.0036(12)	0.0052(18)

Comments on structure refinements and checkcif reports of the title compounds.

Our refinements are performed using third order displacement parameters (so called non-harmonic refinements). This procedure is necessary if crystalline solid ion conductors featuring a high grade of ion dynamics and disorder are examined. Unfortunately, checkcif is still not able to verify and check this type of refinements or better the description of the true or more realistic distribution of the atoms in such compounds. Therefore, in most cases and like in the present one, the anisotropic description of displacements (which is used by checkcif) is not sufficient enough to describe the structure and atom distribution properly. As a result many residual electron density peaks occur (often close to atom sites) which are fully described in the nonharmonic third order refinement. This can be seen by the residual electron density reported in our refinement and the one derived by checkcif. In the case where residual electron density is found in a suitable distance to other atom sites, we carefully checked if such a site must be taken into account (e.g. in β-Cu9.1Te4Cl3: Check Calcd Resid. Dens. 2.32A From Cu1 2.35 eA-3). We verified in such a case if fourth or higher order displacements or split positions will solve the problem. All reported high res. Electron densities were significantly reduced by third-order terms and further splitting was not necessary.

Another consequence of a higher order non-harmonic refinement is the increase of parameters necessary for the description of the different displacements. Therefore, the reflex/parameter ratio

is low but still sufficient. We are doing such refinements for many years now and we see such ratios in many other cases.

Errors dealing with displacement parameter ratios, sizes and disorder are due to the fact that ion mobility and disorder are intrinsic features of solid ion conductors. Common test routines like checkcif do not take such properties into account. It must also be taken into account that the structure determinations were performed at higher temperatures leads to enlarged displacements of atoms. Therefore, wrong symmetry or twinning is not the reason for such large values or differences. The occurrence of twinning was carefully checked by us.

Due to afore mentioned features checkcif calculates different R-values, other statistic parameters and residual electron densities and so on, than we did. None of the occurring differences means that the structure refinement is bad or wrong it simply shows that checkcif is not a suitable routine to verify the crystallographic data of polymorphic, highly disordered compounds.

Raman Spectroscopy.

The Raman spectrum in Figure S A was measured using a low laser power of 0.05 mW recording a total number of 300 scans. Here, a broad band was observed at 121 cm^{-1} which we assigned to the stretching mode of the elongated Te-Te unit (d(Te-Te) = 3.20 - 3.27 Å). By duplicating the laser power to 0.1 mW we observed decomposition of the compound. In Figure S B an additional sharp mode at 160 cm^{-1} with a small shoulder at 170 cm^{-1}. Examples for Raman modes in this range in tellurium compounds are the Te-Te modes in the polytelluride complex $[Cd_4Te_{12}]^{4-}$ at 160 cm^{-1} (corresponding to d(Te-Te) = 2.74 Å) [1] and in elemental tellurium at 170 cm^{-1} (d(Te-Te) = 2.8 Å). [2]
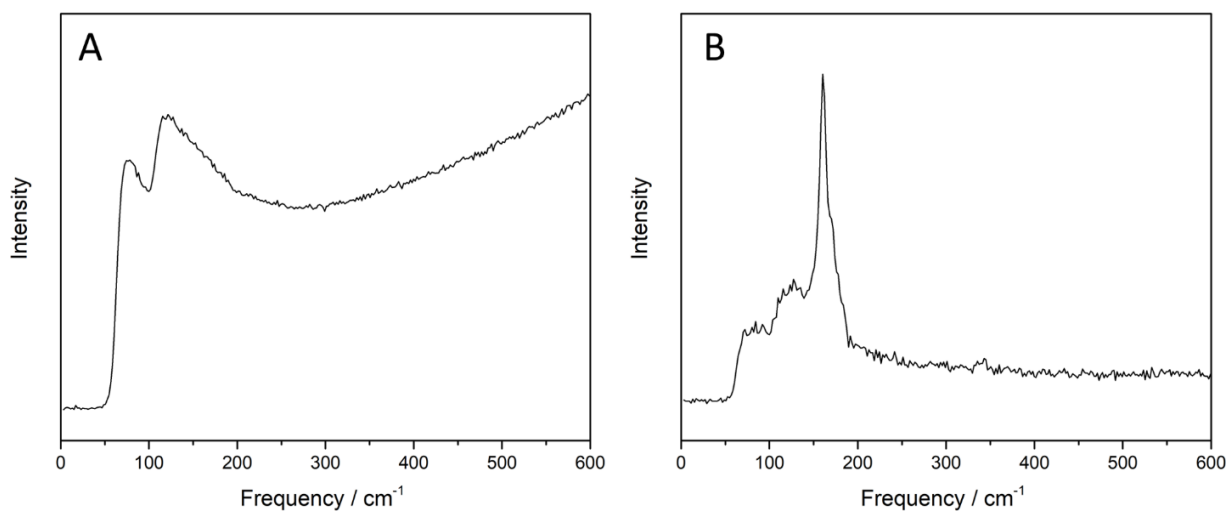
Figure S3. Raman spectra of $Cu_{9.1}Te_4Cl_3$. **A)** Spectrum recorded using a low laser power of 0.05 mW. **B)** Spectrum recorded using a higher laser power of 0.1 mW, showing decomposition of the compound.

Differential Scanning Calorimetry.

As can be seen in Figure S4 all DSC signals appear during heating and cooling experiments and are reversible in two consecutive cycles.
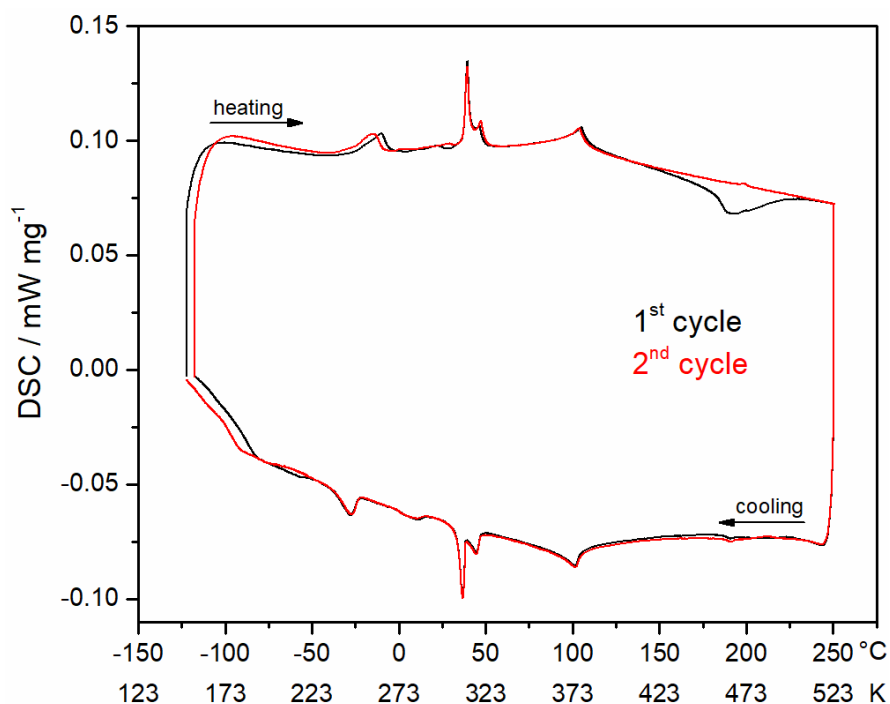
Figure S4. Full set of DSC data of $Cu_{9.1}Te_4Cl_3$ for two consecutive cycles.

Thermoelectric characterization.

As the compound shows decomposition under laser light, the execution of laser flash measurements caused some problems. As can be seen in Figure S5 C, the calculated thermal conductivity increased with every cycle when we measured between room temperature and 250 °C. This behavior might be caused by the slow decomposition of the material during the measurement. By the use of a very small laser power and a reduction of the maximal measuring temperature to 200 °C, it was possible to reproduce the values from the first cycle of the measurement in Figure S5 C in two consecutive cycles (Figure S5 D). This is why we used the first cycle represented in Figure S5 D C for the calculation of the figure of merit.

As can be seen in Figure S5 A and B, there are also slight deviations in the first cycles of the measurements of electric conductivity and Seebeck coefficient. This is why the first cycles are discarded for the calculation of the figure of merit.
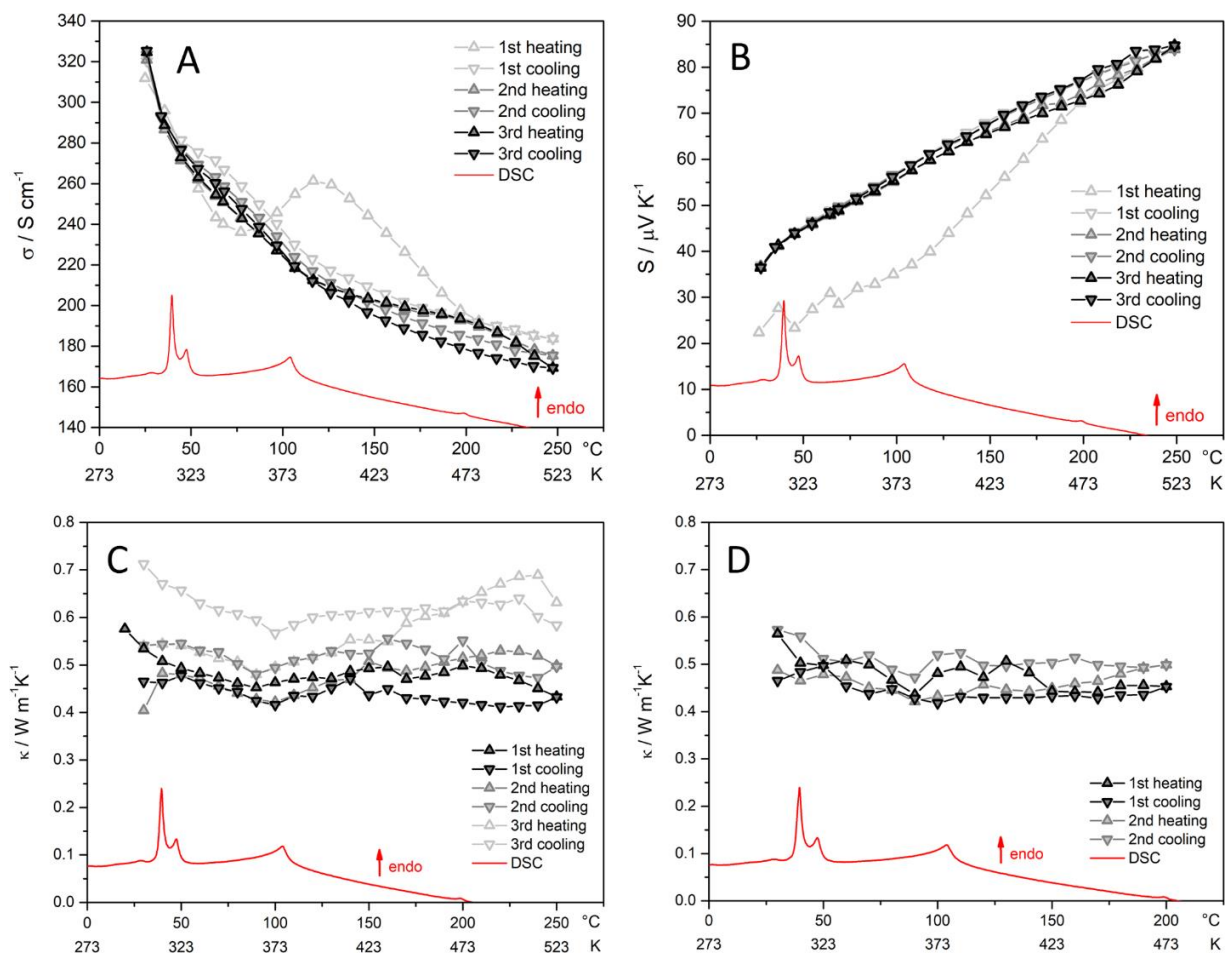
Figure S5. Thermoelectric characterization of $Cu_{9.1}Te_4Cl_3$. Measurements of **A)** electric conductivity, **B)** Seebeck coefficient, and **C** and **D)** thermal conductivity. DSC data is drawn in red.

To estimate the electronic and the lattice contributions to the thermal conductivity the Wiedemann-Franz law was used. [3]
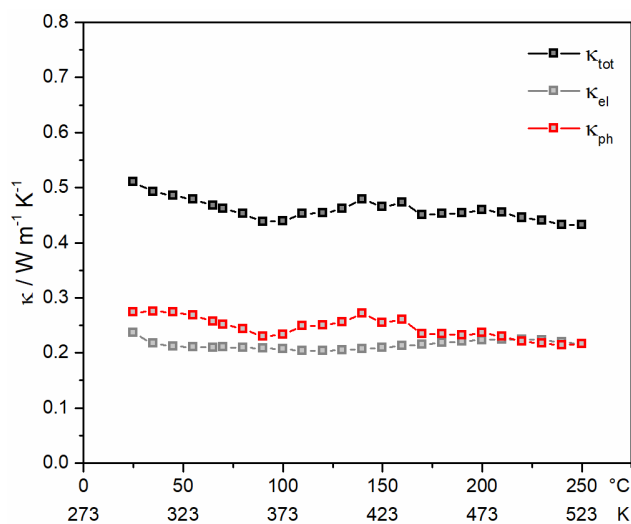
Figure S6. Lattice (κ_{ph}) and electronic (κ_{el}) contributions to the total thermal conductivity (κ_{tot}).

References.

[1] Kim, K.-W.; Kanatzidis, M.G. Synthesis, structure, and properties of the polychalcogenides $[M_4Te_{12}]^{4-}$ (M=Cd, Hg). *Inorg. Chim. Acta* **1994**, *224*(1-2), 163-169.

[2] Weidlein, J.; Müller, U.; Dehnicke, K. *Schwingungsspektroskopie*, 2nd ed. G. Thieme-Verlag: Stuttgart - New York, 1988.

[3] Franz, R.; Wiedemann, G. Ueber die Wärme-Leitungsfähigkeit der Metalle. *Ann. Phys*. **1853**, *165*(8), 497-531.

3.2   Ionendynamik und Polymorphismus in $Cu_{20}Te_{11}Cl_3$

Anna Vogel[1] und Tom Nilges[1]

[1] Technische Universität München, Fakultät für Chemie, Synthese und Charakterisierung innovativer Materialien, Lichtenbergstraße 4, 85748 Garching bei München, Deutschland

Der Artikel wurde im Juni 2021 bei der Zeitschrift *Inorganic Chemistry* eingereicht und im Oktober 2021 veröffentlicht. Ein Teil der Ergebnisse wurde von Anna Vogel im September 2019 bei der *e-conversion Conference* in Venedig, Italien und im März 2022 online bei der *30. Jahrestagung der Deutschen Gesellschaft für Kristallographie (DGK)* in München, Deutschland präsentiert.

In der vorliegenden Arbeit wird $Cu_{20}Te_{11}Cl_3$ vorgestellt, ein weiterer neuer Vertreter der Münzmetallpolychalkogenidhalogenide aus dem System Cu-Te-Cl. Die Verbindung ist trimorph mit Phasenübergängen bei 288 und 450 K. Die Kristallstrukturen der beiden Hochtemperaturphasen werden präsentiert, wobei die komplexe Strukturchemie mit mehreren Symmetrieabstiegen und systematischer Verzwillingung beim Phasenübergang beleuchtet wird. Durch die dynamische Kationen- und statische Anionenteilstruktur wird $Cu_{20}Te_{11}Cl_3$ als Cu-Ionenleiter charakterisiert. Trotz der starken strukturellen Ähnlichkeit mit der pnp-Verbindung $Ag_{10}Te_4Br_3$ (siehe Kapitel 1.2 auf Seite 4) zeigt der temperaturabhänige Seebeck-Koeffizient einen linearen Verlauf und es tritt keine pnp-Schaltung auf. Mögliche Gründe dafür werden im Folgenden diskutiert.

Die große Ionenmobilität in der vorliegenden Verbindungsklasse und deren Temperaturabhängigkeit führen, wie bereits in Kapitel 1.1 auf Seite 2 diskutiert wurde, zu Ordnung-Unordnungs-Phasenübergängen. Diese werden normalerweise von Symmetrieabstiegen begleitet, bei denen vormals statistisch verteilte mobile Ionen auf feste Plätze ausordnen. Das kann nicht nur zu Eliminierung von Symmetrieelementen und Vervielfachung der Elementarzelle führen, sondern auch zu systematischer Verzwillingung, was kristallographische Herausforderungen mit sich bringt. Der α-β-Phasenübergang in $Cu_{20}Te_{11}Cl_3$ verläuft formal über drei Symmetrieabstiege: ein translationengleicher Abstieg vom hexagonalen ins orthorhobische Kristallsystem, der von systematischer Verdrillung begleitet wird, gefolgt von zwei klassengleichen Abstiegen, bei denen eine kristallographische Achse verfünffacht und eine weitere verdoppelt wird. Die Folge ist ein kristallographischer Drilling mit extrem großer Elementarzelle. Das davon hervorge-

rufene komplexe Beugungsbild, sowie die zugrundeliegenden Symmetrieabstiege werden im Artikel in Abbildung 1 gezeigt.

$Cu_{20}Te_{11}Cl_3$ weißt größtenteils die gleichen Baueinheiten auf wie $Ag_{10}Te_4Br_3$ und $Cu_{9,1}Te_4Cl_3$, welches in Kapitel 3.1 auf Seite 28 vorgestellt wurde. Auch hier besteht die Anionenteilstruktur aus gestapelten Tellurid-6^3-Bienenwabennetzen und Halogenid-6.3.6.3-Kagoménetzen, welche von Strängen teilweise kovalent gebundener polyanionischer Tellureinheiten durchdrungen werden. Im Fall von $Cu_{20}Te_{11}Cl_3$ sind diese Einheiten die gleichen Te_4-Einheiten, bestehend aus $[Te_2]^{2-}$-Hanteln und linear koordinierenden Te^{2-}-Anionen, die in $Ag_{10}Te_4Br_3$ vorkommen und dort durch ihre strukturelle Umordnung zu äquidistanten Te-Ketten beim Phasenübergang für die pnp-Schaltung verantwortlich sind (vgl. Kapitel 1.2.2, Seite 6). In der vorliegenden Verbindung wird diese Umordnung allerdings verhindert, da die Te_4-Einheiten durch ein ungeordnetes Te-6.3.6.3-Netz voneinander getrennt sind und nicht miteinander interagieren können. Im Artikel wird die Charakteristik dieses Netzes, das aus halb besetzten Split-Positionen aufgebaut ist, diskutiert und gezeigt, dass die polyanionschen Tellureinheiten dieses aus sterischen Gründen nicht durchdringen können. Desweiteren werden mögliche sterische Gründe für das Auftreten der verschiedenen polyanionischen Tellureinheiten trotz ähnlicher chemischer Umgebung in $Cu_{20}Te_{11}Cl_3$, $Cu_{9,1}Te_4Cl_3$ und $Ag_{10}Te_4Br_3$ beleuchtet.

Der Seebeck-Koeffizient und die elektrische Leitfähigkeit von $Cu_{20}Te_{11}Cl_3$ wurden bestimmt. Unter der Annahme von ähnlich niedriger Wärmeleitfähigkeit wie in $Cu_{9,1}Te_4Cl_3$ und $Ag_{10}Te_4Br_3$ wurde ein wahrscheinlicher thermoelektrischer Gütefaktor ZT zwischen 0,15 und 0,3 berechnet, was sich in der gleichen Größenordnung wie bei $Cu_{9,1}Te_4Cl_3$ bewegt.

Beiträge der Autoren: A.V. synthetisierte die Verbindung, führte alle Experimente durch und löste die Kristallstrukturen. A.V. und T.N. diskutierten die kristallographischen Herausforderungen und schrieben das Manuskript.

Ion Dynamics and Polymorphism in $Cu_{20}Te_{11}Cl_3$

Anna Vogel and Tom Nilges*

Read Online

ACCESS | Metrics & More | Article Recommendations | Supporting Information

ABSTRACT: Coinage metal polychalcogenide halides are an intriguing class of materials, and many representatives are solid ion conductors and thermoelectric materials. The materials show high ion mobility, polymorphism, and various attractive interactions in the cation and anion substructures. Especially the latter feature leads to complex electronic structures and the occurrence of charge-density waves (CDWs) and, as a result, the first p−n−p switching materials. During our systematic investigations for new p−n−p switching materials in the Cu−Te−Cl phase diagram, we were able to isolate polymorphic $Cu_{20}Te_{11}Cl_3$, which we characterized structurally and with regard to its electronic and thermoelectric properties. $Cu_{20}Te_{11}Cl_3$ is trimorphic, with phase transitions occurring at 288 and 450 K. The crystal structures of two polymorphs, the α phase, stable above 450 K, and the β polymorph (288−450 K), are reported, and the complex structure chemistry featuring twinning upon a phase change is illustrated. We identified a dynamic cation substructure and a static anion substructure for all polymorphs, characterizing $Cu_{20}Te_{11}Cl_3$ as a solid Cu-ion conductor. Temperature-dependent measurements of the Seebeck coefficient and total conductivity were performed and substantiated a linear response of the Seebeck coefficient, a lack of CDWs, and no p−n−p switching. Reasons for a lack of CDWs in $Cu_{20}Te_{11}Cl_3$ are discussed and illustrated in the context of existing p−n−p switching materials.
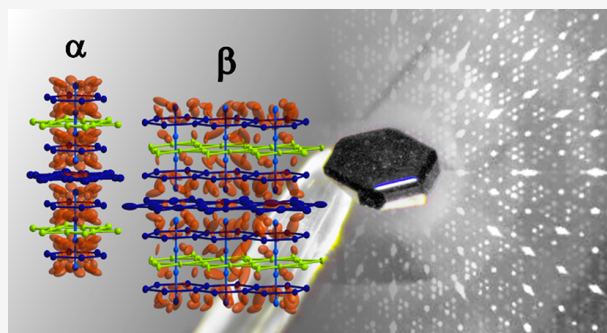
INTRODUCTION

Today, the huge demand on green energy requires the optimization of processes and the development of efficient energy conversion and storage materials. Here, mixed conductors are of potential interest for use in a large variety of energy applications.[1] Besides their application in data storage as phase-change materials and resistivity switching memories,[2−4] they play a certain role in solar cells and thermoelectrics, where improvement of the efficiency is still a challenging task.[5] Ternary coinage metal (poly)chalcogenide halides are a class of mixed conductors with high potential for application as thermoelectric energy conversion materials.[6,7] They show high cation mobility and, because of their ternary character, offer the possibility for multiple ion substitution. Fine tuning of the electronic structure, which is an important parameter for optimization of the thermoelectric and electronic properties, is possible.[7] The named class of compounds summarizes the completely ionic silver(I) chalcogenide halides on the quasi binary section Ag_2Q–AgX with Q = S, Se, and Te and X = Cl, Br, and I and the coinage metal polychalcogenide halides that contain both isolated chalcogenide anions and predominantly covalently bonded polyanionic chalcogene units. Representatives of the first group are Ag_5Te_2X with X = Cl and Br[8−13] and $Ag_{19}Q_6X_7$ with Q = S, Se, and Te and X = Br and I.[14,15] In the case of $Ag_{19}Te_6Br_7$, partial substitution of Ag by Cu was successful.[15,16] Recently, the phase stability and

thermodynamic properties of the silver(I) (poly)telluride halides $Ag_{19}Te_6Cl_7$, Ag_5Te_2Cl, and $Ag_{23}Te_{12}Cl$ have been investigated in solid-state galvanic cells and reviewed in consideration of potential application as energy materials.[19] The first representative of the coinage metal polychalcogenide halides was $Ag_{10}Te_4Br_3$, found by our group in 2006.[20] This polymorphic compound represents the first material that is capable of reversible switching between p and n types of semiconduction without a change of composition, which is displayed by the change of the sign of the Seebeck coefficient.[21,22] The origin for this p−n−p switching effect is a charge-density wave (CDW), caused by a Peierls distortion within a Te chain in the polychalcogenide substructure. This CDW is driven by the continuous interaction of the polyanionic Te unit with the surrounding mobile cations at different temperatures. Until now, other materials that have been discovered to show this p−n−p switching behavior are the chalcogenides $AgBiSe_2$, $AgCuS$, and $Tl_2Ag_{12}Se_7$.[23−26] $In_4Se_{3−x}$ shows related modulations of the Seebeck coefficient
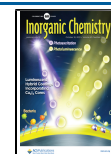
but no switch in the type of semiconduction.[27,28] For $Ag_{10}Te_4Br_3$, substitutions of the chalcogenides (Te by S and Se)[16] and the halides (Br by Cl and I)[17] as well as the coinage metal (Ag by Cu)[18] exist. $Cu_{9.1}Te_4Cl_3$, the first coinage metal polychalcogenide halide with exclusively Cu as coinage metal, has previously been published.[29] It outperforms $Ag_{10}Te_4Br_3$ in terms of the thermoelectric properties by 1 order of magnitude with a ZT of 0.15 at 250 °C. A microcrystalline side product in the synthesis of $Cu_{9.1}Te_4Cl_3$ attracted attention and was finally identified as $Cu_{20}Te_{11}Cl_3$, the second representative with Cu as coinage metal. The title compound has very similar structure features and structure units compared to $Ag_{10}Te_4Br_3$ but, because of the compositional change, also obvious differences. It turned out that those differences effectuate huge differences in the electronic behavior. $Cu_{20}Te_{11}Cl_3$ is polymorphic like $Ag_{10}Te_4Br_3$ and performs several order−disorder phase transitions but does not exhibit p−n−p switching. In contrast to the latter, it contains two different sets of polyanion Te substructures but, unfortunately, no effective CDW mechanism to initiate p−n−p switching. The occurrence of two instead of only one polyanionic structure units interacting with the mobile cations resulted in a very complex structure chemistry, which is still not fully understood. Here we present the structural, thermal, and thermoelectric properties of two polymorphs of $Cu_{20}Te_{11}Cl_3$. It serves as a model compound to deepen the understanding of the p−n−p switching effect and the mechanism behind.

EXPERIMENTAL SECTION

Synthesis. $Cu_{20}Te_{11}Cl_3$ was prepared from a 17:3:11 mixture of Cu (Chempur, 99,999%), copper(I) chloride (Alfa Aesar, 97%), and Te (Chempur, 99,999%) on a gram scale. The starting materials were sealed into evacuated silica glass ampules, heated to 1320 K, held at this temperature for 3 h, and quenched in an ice bath. The crude product was finely ground and annealed at 720 K for 5 days, followed by slow cooling to room temperature. This synthesis route leads to a phase-pure black crystalline material that is stable in air.

X-ray Diffraction (XRD) Experiments. Powder XRD data were collected with a STOE STADI P powder diffractometer equipped with a position-sensitive Mython 1K detector using Cu Kα_1 radiation (λ = 1.54060 Å). Data evaluation was performed with the STOE *WinXPOW* software.[30] Two single-crystal XRD measurements at 200 and 330 K were performed on a STOE Stadivari single-crystal diffractometer equipped with a DECTRIS hybrid pixel detector and an Oxford Cryostream plus system using Mo K$\alpha_{1/2}$ radiation (λ = 0.71075 Å). One high-temperature single-crystal XRD measurement at 540 K was executed directly at STOE & Cie GmbH, Darmstadt, Germany. The measurement was performed on a STOE Stadivari single-crystal diffractometer with a DECTRIS PILATUS3 X CdTe detector and a STOE heating system using Ag K$\alpha_{1/2}$ radiation (λ = 0.56083 Å). Data reduction was performed with the STOE *X-AREA* software,[31] and the structures were solved using the charge-flipping algorithm,[32] implemented in the *JANA2006* program suite.[33] The data sets were corrected for Lorentz and polarization effects. Numerical absorption correction was performed based on an optimized crystal shape derived from symmetry-equivalent reflections. Space groups for the polymorphs were determined by careful analysis of the Laue symmetry and extinction conditions as well as group−subgroup relations. In the case of systematically twinned β-$Cu_{20}Te_{11}Cl_3$, twin integration was performed, and the structure was subsequently solved using hklf5 data.

Thermal Analysis. Phase-pure crystalline $Cu_{20}Te_{11}Cl_3$ was transferred to an Al crucible, and differential scanning calorimetry (DSC) was performed using a Netzsch DSC 200 F3Maia apparatus. All measurements were performed under a N_2 atmosphere in a temperature range of 143−523 K with a heating/cooling rate of 10 K

h^{-1}. The thermal effects were derived from onset temperatures, and the enthalpies were determined by integration.

Measurement of the Electric Conductivity and Seebeck Coefficient. Finely ground phase-pure $Cu_{20}Te_{11}Cl_3$ was pressed under vacuum to a pellet of 13 mm diameter and 0.77 mm thickness, reaching 90% of the crystallographic density using a Maassen press tool and a Maassen MP150 lab press. The Seebeck coefficient was measured perpendicular to the pressing direction with a NETZSCH SBA 458 Nemesis under a continuous argon flow with a flow rate of 60 mL min^{-1}. A temperature difference of at least ΔT = 2 K was applied, and three full cycles were measured as shown in the supplement.

RESULTS AND DISCUSSION

Thermal Analysis. Thermal analysis was performed for $Cu_{20}Te_{11}Cl_3$ in order to verify ion dynamics and to check the occurrence of polymorphism. Like the structurally related polytelluride halides $Ag_{10}Te_4Br_3$ and $Cu_{9.1}Te_4Cl_3$, $Cu_{20}Te_{11}Cl_3$ is a polymorphic compound and shows several thermal effects in a narrow temperature range below the synthesis temperature.[21,29] As can be seen in Figure 6, the DSC analysis shows two endothermic effects at 298 and 450 K that are assigned the $\gamma \rightarrow \beta$ and $\beta \rightarrow \alpha$ phase transitions. Full DSC data are shown in Figure S2. All effects are reversible and have been measured from different independently prepared samples in two consecutive cycles for each run. The small phase transition enthalpies presented in Table 1 point toward second-order-

Table 1. Results from Thermal Analysis of $Cu_{20}Te_{11}Cl_3$[a]

phase transition	T (onset value) (K)	enthalpy (kJ mol^{-1})
$\gamma \rightarrow \beta$	288(1)	2.6
$\beta \rightarrow \alpha$	450(1)	0.52

[a]Standard deviations are in parentheses.

type order−disorder phase transitions. One thermal effect is present very close to room temperature, which renders any physicochemical characterization at room temperature problematic. This aspect must also be considered for the storage of $Cu_{20}Te_{11}Cl_3$. We recommend storing $Cu_{20}Te_{11}Cl_3$ at temperatures significantly away from room temperature to minimize thermal stress on the sample.

Crystal Chemistry. The following section deals with the complex structure chemistry of polymorphic $Cu_{20}Te_{11}Cl_3$ and includes general considerations and symmetry reduction along the different polymorphs (Figure 1A). Inspired by the results from thermal analysis, we performed temperature-dependent single-crystal XRD measurements at 540, 330, and 200 K. For crystallographic data, see Table 2. The high-temperature polymorph α-$Cu_{20}Te_{11}Cl_3$ crystallizes hexagonally, in the space group $P6/mmm$, with a = 7.3297(9) Å, c = 14.7594(12) Å, and V = 686.71(12) Å^3 at 540 K. A reciprocal cell representation is given in Figure 1B. The diffraction image of β-$Cu_{20}Te_{11}Cl_3$ shown in Figure 1E shows, besides the strong main reflections related to α-$Cu_{20}Te_{11}Cl_3$, weaker superstructure reflections that are arranged in a triangular way between the main reflections. This can be assigned the characteristic pattern generated by a 3-fold twin. Systematic twinning is not uncommon in this class of compounds because γ-$Ag_{10}Te_4Br_3$ crystallizes in a 3-fold twin as well.[20,21] In the present case, the unit cell of β-$Cu_{20}Te_{11}Cl_3$ can be derived by the symmetry reduction from the hexagonal to orthorhombic crystal system, which is accompanied by 3-fold twinning, followed by quintuplication of the a axis. Additional doubling
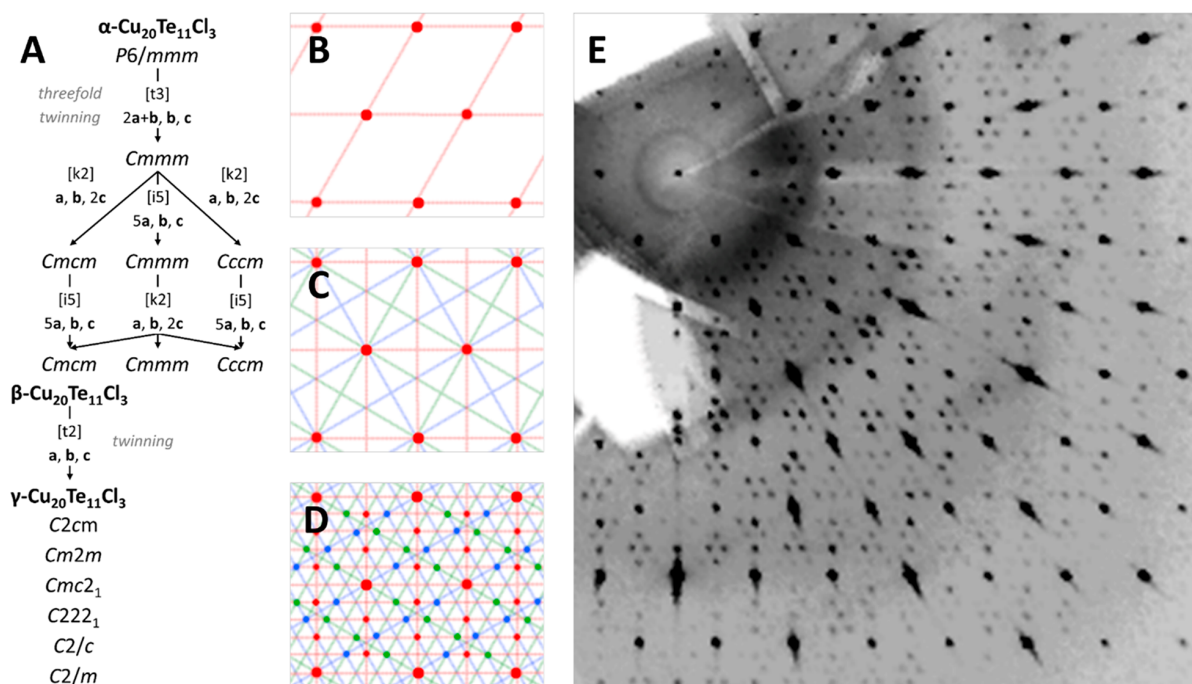
Figure 1. (A) Bärnighausen tree for symmetry reduction from α-$Cu_{20}Te_{11}Cl_3$, crystallizing in the space group $P6/mmm$, to β-$Cu_{20}Te_{11}Cl_3$, crystallizing in the space group $Cmcm$, including quintupling of the a axis and doubling of the c axis. Further *translationengleiche* symmetry reductions possibly lead to γ-$Cu_{20}Te_{11}Cl_3$. Scheme of diffraction patterns in the 001 direction generated by the symmetry reductions shown in part A. (B) Primitive hexagonal unit cell of the superstructure model. (C) 3-fold-twinned set of orthorhombic C-centered unit cells after the t3 step. Red, green, and blue lines represent the different twin domains. (D) 3-fold-twinned set of orthorhombic C-centered unit cells with a quintupled a axis and a doubled c axis (i5 and k2). (E) Projection of five planes ($hk0-4$) of the single-crystal XRD pattern data of β-$Cu_{20}Te_{11}Cl_3$ at 330 K.

of the c axis leads to an orthorhombic cell with $a = 36.4362(10)$ Å, $b = 12.628(2)$ Å, $c = 29.586(2)$ Å, and $V = 13613(2)$ Å³. Thus, as shown in Figure 1D, with systematic extinction that is elicited by C-centering, the exact pattern of the diffraction image is derived. To determine the correct space group of β-$Cu_{20}Te_{11}Cl_3$, a Bärnighausen tree featuring all possible symmetry reductions, leading from the supergroup $P6/mmm$ to the proposed 3-fold C-centered orthorhombic model (including twining), was established and is shown in Figure 1A. The phase transition occurs by a *translationengleiche* symmetry reduction of index 3 (t3) to the space group $Cmmm$, followed by two *klassengleiche* symmetry reductions (k2 and i5), at which the c axis is doubled and the a axis is quintuplicated. Because C-centering is required for the β polymorph, this approach leads to three possible space groups: $Cmmm$, $Cmcm$, and $Cccm$. The best results were achieved by refinement in $Cmcm$.

Another phase transition takes place at 288 K. Reciprocal space analysis (diffraction pattern shown in Figure S1) points strongly toward retention of the cell dimensions and C-centering. Hence, we suppose a *translationengleiche* symmetry reduction to possible orthorhombic space groups $Cmc2$, $Cm2m$, $Cmc2_1$, and $C222_1$ or monoclinic $C2/c$ and $C2/m$. Because this type of phase transition is typically attended by twinning, which might lead to 6-fold twins, correct space group identification as well as structure refinement is difficult. Thus, the structure solution of γ-$Cu_{20}Te_{11}Cl_3$ is still under examination and will be reported soon.

Crystal Structure Description. In the following, the crystal structure of α- and β-$Cu_{20}Te_{11}Cl_3$ will be discussed. For a better understanding of the complex crystal structure, the anion and cation substructures are described separately.

Anion Substructure. In Figure 2A, the anion substructure of α-$Cu_{20}Te_{11}Cl_3$ is denoted. The crystal structure of $Cu_{20}Te_{11}Cl_3$ exhibits similarities to those of the structurally related coinage metal polytelluride halides $Ag_{10}Te_4Br_3$[20] and $Cu_{9.1}Te_4Cl_3$[29] but also contains new structure features that have not been reported in this material class before. Similar to the other compounds in its class, $Cu_{20}Te_{11}Cl_3$ can be described topologically by anion networks. To define the anion nets, we connected anions of the same type neighbored to each other on certain layers in the unit cell. Those layers are stacked along one crystallographic axis and are vertically interpenetrated by partially covalently bonded Te_n units. In the case of $Cu_{20}Te_{11}Cl_3$, a chloride 6.3.6.3 kagomé net propagating parallel to the ab plane is located between two telluride 6^3 honeycomb nets. In both network types, the distances [d(Te−Te) = 4.22 Å and d(Cl−Cl) = 3.65 Å at 540 K] are larger than 2 times the van der Waals radii [d_{vdW}(Te) = 2.06 Å and d_{vdW}(Cl) = 1.80 Å].[34] The three parallel nets are interpenetrated by linear $[Te_4]^{6-}$ units, built of a $[Te_2]^{2-}$ dumbbell and two coordinated Te^{2-} anions through every hexagonal void of the kagomé net. At 540 K, the bond length of the $[Te_2]^{2-}$ dumbbell is 2.94 Å and the distance of the coordinating Te^{2-} anion to the dumbbell is 3.71 Å. The common values for $[Te_2]^{2-}$ dumbbells at room temperature are 2.70 Å in $MgTe_2$[35] and 2.86 Å in α-K_2Te_2.[36] $Ag_{10}Te_4Br_3$ contains the same Te_4 structure motif with Te−Te distances of 2.79 and 3.60 Å, respectively, at room temperature.[20] In $Cu_{20}Te_{11}Cl_3$, the $[Te_4]^{6-}$ motif is embedded in one 6.3.6.3 Cl net and two 6^3 Te nets, stacked in the c direction and separated

Table 2. Data from Single-Crystal XRD Experiments of α- and β-Cu$_{20}$Te$_{11}$Cl$_3$

	α-Cu$_{20}$Te$_{11}$Cl$_3$	β-Cu$_{20}$Te$_{11}$Cl$_3$
refined composition	Cu19.6(6)Te$_{11}$Cl$_3$	Cu18.3(6)Te$_{11}$Cl$_3$
molar mass (g mol^{-1})	2756.6	2671.1
cryst size (mm)	0.2 × 0.2 × 0.05	0.1 × 0.1 × 0.05
cryst shape/color		block/black
cryst syst	hexagonal	orthorhombic
space group	$P6/mmm$	$Cmcm$
Z	1	20
a (Å)	7.3290(8)	36.4362(10)
b (Å)		12.628(2)
c (Å)	14.7563(11)	29.586(2)
V (Å^3)	686.43(12)	13613(2)
T (K)	540	330
ρ_{calc} (g cm^{-3})	6.67	6.52
diffractometer		STOE Stadivari
radiation (Å)	0.56083	0.71075
μ (cm^{-1})	139.5	257.8
$F(000)$	1192	23058
θ range (deg)	1.09−25.73	2.68−25
hkl ranges	−10 to +5, 0 to +11, 0 to +22	−43 to +43, −15 to +15, −35 to +34
no. reflns	1438	255697
twin matrices (by rows)		$T_{1/2} = \begin{pmatrix} \frac{1}{2} & -\frac{3}{10} & 0; & \frac{5}{2} & \frac{1}{2} & 0; & 0 & 0 & 1 \end{pmatrix}$
		$T_{1/3} = \begin{pmatrix} -\frac{1}{2} & -\frac{3}{10} & 0; & \frac{5}{2} & -\frac{1}{2} & 0; & 0 & 0 & 1 \end{pmatrix}$
R_{int}	0.0574	0.1678
data/param	507/73	5233/1043
R/wR [$I > 3\sigma(I)$]	0.0387/0.0723	0.0353/0.0544
R/wR (all data)	0.0569/0.0794	0.0931/0.0874
GOF	1.65	1.26
residual electron density max/min (e Å^{-3})	−1.28/+1.40	−2.36/+2.43

Figure 2. (A) Anion substructure of α-Cu$_{20}$Te$_{11}$Cl$_3$. The unit cell is highlighted in gray. The parameter d_{nets} equals the distance between every second Te 6^3 net, and r_{void} equals the radius of the voids in the anionic networks. Both parameters are marked in red. Light-blue dots represent the Te sites of the vertically interpenetrating [Te$_4$]$^{6-}$ subunits (built of a [Te$_2$]$^{2-}$ dumbbell and two coordinated Te^{2-} ions) for better differentiation. Structure sections of (B) α- and (C) β-Cu$_{20}$Te$_{11}$Cl$_3$. The displacement parameters are represented with 90% probability.

from each other by a previously unseen disordered 6.3.6.3 Te kagomé net. In this net, every Te position is half-occupied at a close distance of 0.74 Å to the next neighbor. A brief discussion of this feature is given later on (Figure 3). If a disorder phenomenon like, for instance, two randomly oriented and therefore interpenetrating 6.3.6.3 Te nets or an arrangement of different [Te$_2$]$^{2-}$ dumbbells on this net are expected, the resulting nearest Te−Te distance within such units is 3.02 Å according to our measurements. This distance is comparable to the Te−Te distance in the [Te$_2$]$^{2-}$ dumbbell of the Te$_4$ structure motif in the remaining Cu$_{20}$Te$_{11}$Cl$_3$ anion substructure. Such a disorder phenomenon within the Te substructure is common for coinage metal polychalcogenide halides and was previously observed for the [Te$_4$]$^{6-}$ unit substructure in Ag$_{10}$Te$_4$Br$_3$ at elevated temperatures (Figure 4D). For Ag$_{10}$Te$_4$Br$_3$, this disorder phenomenon vanished upon cooling and ordering in distinct [Te$_4$]$^{6-}$ units occurred (Figure 4B). This situation can be described as a Peierls distortion of a linearly arranged Te chain. As a conclusion, we can expect that the disordered 6.3.6.3 Te network might consist of disordered or mobile [Te$_2$]$^{2-}$ dumbbells.

To explain the nature of the 6.3.6.3 Te net in a chemically sensible manner, two models will be discussed to explain the disorder present in the α polymorph: two statistically disordered and overlaid distorted 6.3.6.3 Te nets and a situation featuring disordered [Te$_2$]$^{2-}$ dumbbells.

One possibility to describe the disordered net is the statistical distribution of two distorted 6.3.6.3 Te nets like those found in synthetic Stützite Ag$_{5-x}$Te$_3$,[37] which are randomly oriented within the structure in Cu$_{20}$Te$_{11}$Cl$_3$. The anion substructure of Stützite and its 6.3.6.3 Te net are shown in Figure 3A. As shown in Figure 3B, the disordered 6.3.6.3 Te net in Cu$_{20}$Te$_{11}$Cl$_3$ can be described with two resonance structures corresponding to the Stützite-type 6.3.6.3 Te net in opposite orientations. The Stützite-type 6.3.6.3 Te net contains intercoordinated [Te$_9$]$^{12-}$ triangles composed of three [Te$_2$]$^{2-}$ dumbbells interconnected by coordinating Te^{2-} anions. The Te−Te distances at 500 K in the resonance structures are 3.02 Å within the [Te$_2$]$^{2-}$ dumbbell and 3.67 Å to the coordinating Te^{2-} anion, which correspond well to the distances in Stützite Ag$_{5-x}$Te$_3$ with 2.84 and 3.61 Å, respectively, at room temperature.[37] In this case, the resonance structures can be described by a $\sqrt{3} \times \sqrt{3}$ superstructure and would lead to a total charge of [Te$_{11}$Cl$_3$]$^{21-}$ composed of ([Te$_2$]$^{2-}$)$_2$(Te^{2-})$_7$(Cl$^-$)$_3$.

As shown in Figure 3C, the network can also be described by four different resonance structures, where each position is
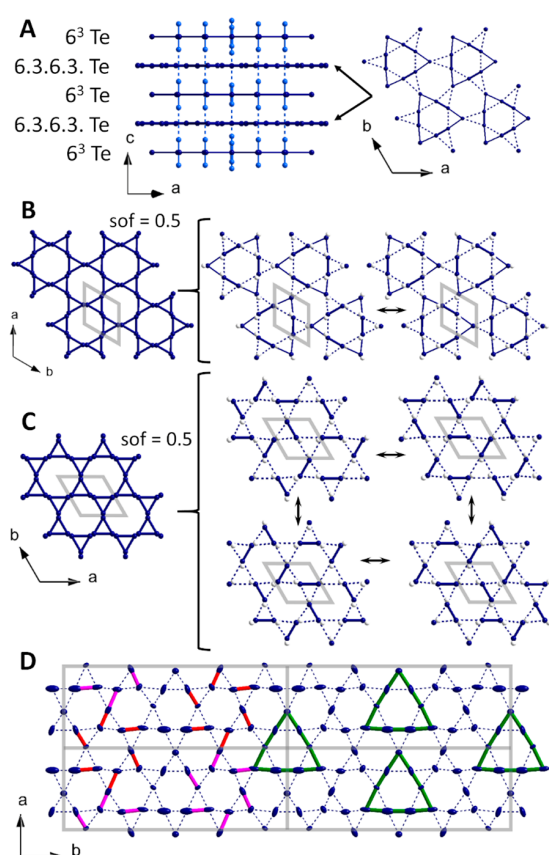
Figure 3. (A) Anion substructure of synthetic Stützite $Ag_{5-x}Te_3$ and its distorted 6.3.6.3 Te net.[37] Light-blue dots represent the Te sites of the vertically interpenetrating strands for better differentiation. (B) Scheme of the Stützite-type model describing the nature of the disordered 6.3.6.3 Te net in $Cu_{20}Te_{11}Cl_3$: two Stützite-type 6.3.6.3 Te nets in opposite orientations lead together to a split position network, where every position is occupied in one of two cases. (C) Scheme of the disordered dumbbell model: four underlying resonance structures composed of $[Te_2]^{2-}$ dumbbells arranged in a distorted 6.3.6.3 kagomé net lead together to a split position network where every position is occupied in two of four cases. (D) Partially disordered 6.3.6.3 Te net of β-$Cu_{20}Te_{11}Cl_3$. Four unit cells are drawn. Structure features related to the Stützite-type kagomé nets are drawn in green. Structure features related to the disordered dumbbell model are marked in red and purple.

occupied in two of the four cases, resulting in half-occupied split positions. Every resonance structure is composed of $[Te_2]^{2-}$ dumbbells arranged in a distorted kagomé net that can be described by a 2×2 superstructure of the split position network. The single resonance structures can be transferred into one another by a shift of $^1/_2 a$ or $^1/_2 b$ of the supercell. Also a situation with dynamically fluctuating dumbbells across the net plane is possible. In that case, we could expect charge fluctuations and a two-dimensional CDW propagating in the ab plane. Such a CDW should lead to p−n−p switching and a defined Seebeck coefficient drop during the $\alpha-\beta$ phase transition, which is obviously not the case (see the latter ion and Figure 6). This description leads to a total charge of the anion substructure of $[Te_{11}Cl_3]^{20-}$ composed of $([Te_2]^{2-})_{2.5}(Te^{2-})_6(Cl^-)_3$.

Because of static disorder even at high temperatures, a lack of CDW in the anion substructure, and the good accordance of

the refined and expected compositions of $Cu^{20+}[Te_{11}Cl_3]^{20-}$, we strongly favor the static version of the latter structure model.

In β-$Cu_{20}Te_{11}Cl_3$, a slight distortion of the 6.3.6.3 Cl and 6^3 Te planes can be observed and the $[Te_4]^{6-}$ units are divided into three sets. The Te−Te distances within the dumbbells are 2.95−2.99 Å, and the distances from the dumbbell to the coordinating Te^{2-} anion are 3.74−3.77 Å. The 6.3.6.3 Te net region shows a tendency for partial ordering, but some of the Te positions display elongated displacement parameters that point toward a split position, where the distance is too short to be properly resolved by Mo $K\alpha_{1/2}$ radiation ($\lambda = 0.71075$ Å). For disordered 6.3.6.3 Te in α-$Cu_{20}Te_{11}Cl_3$, two different models with differing resonance structures were developed (Figure 3). A statistical distribution was identified as the most probable structure model. In β-$Cu_{20}Te_{11}Cl_3$, the static nature is substantiated. The partially ordered 6.3.6.3 Te net is shown in Figure 3D. No distinct ordering toward one of the structure models illustrated in Figure 3 can be detected. Characteristic structure features related to the preferred static dumbbell model (scheme in Figure 3C) are highlighted in red and purple. Those related to the alternative structure model featuring Stützite-type kagomé nets (Figure 3B) are denoted in green.

Cation Substructure. In α-$Cu_{20}Te_{11}Cl_3$, Cu is completely disordered. Partially occupied Cu positions are arranged as 6-fold rings around the predominantly covalently bonded strands. As shown in Figure 2B, these rings are located in, above, and below the voids of the Te 6^3 net as well as in, above, and below the 6-fold rings of the split-position 6.3.6.3 Te net. Cu atoms seem to be mobile along the Te_4 units and between and within the Te networks but do not permeate the 6.3.6.3 Cl net.

In β-$Cu_{20}Te_{11}Cl_3$, Cu is still strongly disordered. Some positions are fully occupied, and the other site occupancies are higher than those in α-$Cu_{20}Te_{11}Cl_3$. The reason for that could be either static disorder or remaining partial high Cu mobility even at lower temperatures. If the disorder of the cationic substructure were only of dynamic nature, the thermal displacement parameters should be, in general, larger in the high-temperature polymorph than in the low-temperature one, and an extrapolation of the displacement parameters to 0 K must be possible. However, the thermal displacement parameters of Cu are in the same magnitude in both polymorphs, which points strongly toward a certain fraction of static disorder of Cu in β-$Cu_{20}Te_{11}Cl_3$. A comparison of the averaged thermal displacement parameters can be found in Table S7.

Structural Classification of Coinage Metal Polychalcogenide Halides. Obviously, the anion substructure of $Cu_{20}Te_{11}Cl_3$ consists of isolated $[Te_4]^{6-}$ units, which are accommodated in alternating 6.3.6.3 Cl and 6^3 Te nets and separated by disordered 6.3.6.3 Te nets. In order to investigate or substantiate this statement and to set the structure of $Cu_{20}Te_{11}Cl_3$ in a broader context, we analyzed the structures of different coinage metal polychalcogenide halides in more detail.

As stated before, the 6^3 Te net as well as the 6.3.6.3 halide net can also be found in $Ag_{10}Te_4Br_3$[20] and $Cu_{9.1}Te_4Cl_3$[29] where they are alternatingly stacked along one crystallographic axis. In Figure 4, the anion substructure of α-$Cu_{20}Te_{11}Cl_3$ is opposed to those of α-$Cu_{9.1}Te_4Cl_3$ and α- and γ-$Ag_{10}Te_4Br_3$.[20,21,29] The structure features in all three coinage
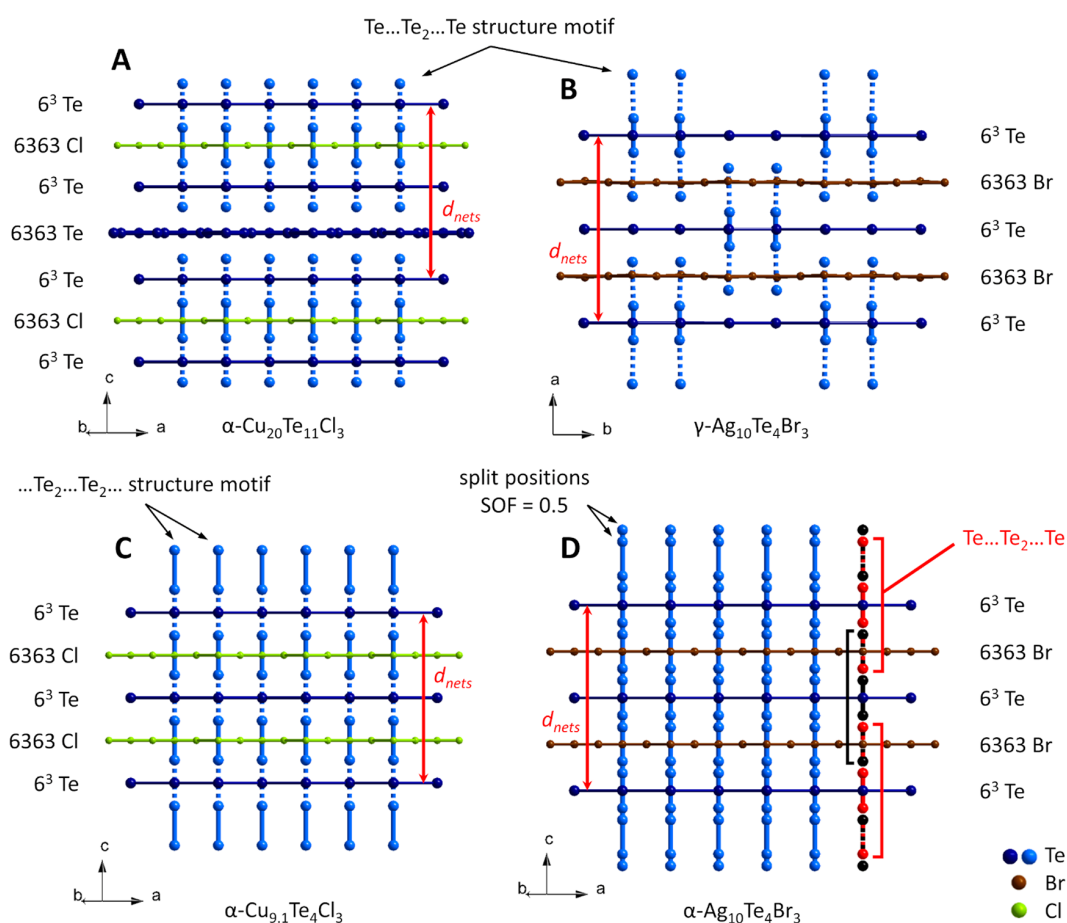
Figure 4. Projections of the anionic substructures of α-Cu$_{20}$Te$_{11}$Cl$_3$ (A), α-Cu$_{9.1}$Te$_4$Cl$_3$ (C), and α- and γ-Ag$_{10}$Te$_4$Br$_3$ (D and B).[21,29] The parameter d_{nets} equals 2 times the distance between two Te 6^3 nets and is marked in red. Light-blue dots represent the Te sites of the vertically interpenetrating strands for better differentiation.

metal polytelluride halides are very similar, but there are major differences in the stacking sequences of the topologic anion nets and the arrangement or orientation of the [Te$_4$]$^{6-}$ units perpendicular to it. We tried to find a structural reason for these differences and analyzed the accessible free space within the anion nets for additional negatively charged structure units like [Te$_2$]$^{2-}$ dumbbells or [Te$_4$]$^{6-}$ units. All cations are extremely mobile and show a high ion dynamic, which allows a strong stabilization effect for any anion substructure. Therefore, we believe that anions are the structure-directing species and all cations are flexible and dynamic enough to coordinate anions in any given mode. The optimum anion substructure is defined by attractive interactions to the cations and covalent bonding between Te atoms.

The structure feature of the interpenetrating [Te$_4$]$^{6-}$ units can also, besides in Cu$_{20}$Te$_{11}$Cl$_3$, be found in Ag$_{10}$Te$_4$Br$_3$, as shown in Figure 4B.[20] In the ladder, the [Te$_2$]$^{2-}$ dumbbells of the [Te$_4$]$^{6-}$ unit are located in the voids of the 6^3 Te net and not in the voids of the 6.3.6.3 Br net. A possible explanation is the difference in the sizes of the voids of the nets in the different compounds and how well a [Te$_2$]$^{2-}$ dumbbell fits. As a measurement, a parameter d_{gap} is defined as the free space between the atoms of the dumbbell and the surrounding ions. For the atom radii of the network ions, the ion radii after Pauling [r_{ion}(Cl$^-$) = 1.81 Å, r_{ion}(Br$^-$) = 1.96 Å, and r_{ion}(Te^{2-}) = 2.21 Å] are used, and the radius of the dumbbell atoms is

approximated by the van der Waals radius of Te [r_{vdW}(Te) = 2.06 Å].[34] On the basis of the model represented in Figure 5, d_{gap} is defined as $d_{gap} = d_{ion\ Te} - [r_{ion} + r_{vdW}(Te)]$.
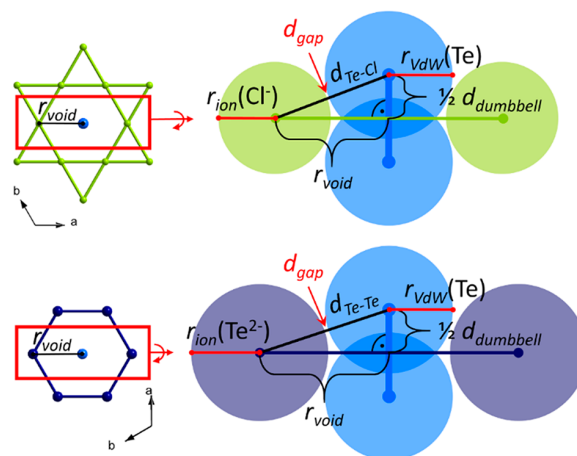
Figure 5. Schematic representation of the atom distances within a [Te$_2$]$^{2-}$ dumbbell: (light blue) interpenetrated voids of the 6.3.6.3 Cl (green) and 6^3 Te (dark blue) anion nets.

In α-$Cu_{20}Te_{11}Cl_3$, the radius of the voids in the 6.3.6.3 Cl net r_{void}(6.3.6.3 Cl) is 3.67 Å and, hence, the free space in the Cl kagomé net d_{gap}(6.3.6.3 Cl) is calculated as 0.08 Å. For a hypothetical $[Te_2]^{2-}$ dumbbell in the Te honeycomb network with r_{void}(6^3 Te) = 4.23 Å, d_{gap}(6^3 Te) would be 0.21 Å and thus only slightly larger. Because of the fact that the negative charge of the Te network is considerably higher, it seems to be more favorable for the negatively charged dumbbell to be located within the lower-charged Cl net.

In γ-$Ag_{10}Te_4Br_3$,[20] the average r_{void}(6^3 Te) = 4.56 Å results in d_{gap}(6^3 Te) = 0.50 Å, which is significantly larger than that for a hypothetical $[Te_2]^{2-}$ dumbbell located in the voids of the Br net, with r_{void}(6.3.6.3 Br) = 3.96 Å and d_{gap}(6.3.6.3 Br) = 0.17 Å. Here, the $[Te_2]^{2-}$ dumbbell can be found exclusively in the 6^3 Te net. Obviously, the large free space favors localization of the $[Te_2]^{2-}$ dumbbell in a Te instead of a Br environment. The higher polarizability of Br compared to Cl seems to not play a role for localization of the $[Te_2]^{2-}$ dumbbell.

In $Cu_{9.1}Te_4Cl_3$, shown in Figure 4C, the anion nets are interpenetrated by strands of slightly elongated $[Te_2]^{2-}$ dumbbells instead of $[Te_4]^{6-}$ units.[29] In this compound, with r_{void}(6.3.6.3 Cl) = 3.65 Å and r_{void}(6^3 Te) = 4.21 Å, the sizes of the voids in the nets are very similar to $Cu_{20}Te_{11}Cl_3$ and the dumbbells sit in the lower-charged 6.3.6.3 Cl net as well.

In summary, the origin of covalently bonded Te seems to be defined by two aspects: (a) the accessible free space for accommodating the still negatively charged $[Te_2]^{2-}$ dumbbell in an anion substructure, and (b) whether the accessible space is equal to the charge of the surrounding net. The occurrence of elongated $[Te_2]^{2-}$ dumbbells instead of a $[Te_4]^{6-}$ unit in $Cu_{9.1}Te_4Cl_3$, despite almost identical chemical and structural environments, needs further attention and discussion.

The reason for the formation of intercoordinated dumbbells instead of $[Te_4]^{6-}$ units in $Cu_{9.1}Te_4Cl_3$ might be the smaller distance between the anion nets compared to the other two compounds mentioned. We investigated the accessible space for a $[Te_4]^{6-}$ unit perpendicular to the anion nets in all compounds in order to verify whether the kind of stacking plays a certain role. For a comparison of the different structure types, d_{nets} is defined as 2 times the distance between two 6^3 Te nets. It is marked with a red arrow for all structure types represented in the schemes in Figure 4.

In γ-$Ag_{10}Te_4Br_3$ at room temperature, a fully ordered $[Te_4]^{6-}$ unit is present. Along the propagation direction of the $[Te_4]^{6-}$ units, the a axis in this case, a Peierls-distorted arrangement of Te is present. The accessible distance d_{nets} is 15.40 Å and incorporates one $[Te_4]^{6-}$ unit with a total length of 10.00 Å.[20] This results in a distance between two noninteracting $[Te_4]^{6-}$ units of 5.40 Å, which is well above 2 times the van der Waals radius of 4.12 Å [d_{vdW}(Te) = 2.06 Å].[34] In α-$Cu_{9.1}Te_4Cl_3$, featuring elongated $[Te_2]^{2-}$ dumbbells, we found a much smaller distance of d_{nets} = 14.19 Å, which entails that intercoordination and a certain attractive interaction between the slightly elongated dumbbells is possible. Obviously, this dumbbell arrangement seems more favorable than the formation of $[Te_4]^{6-}$ units.[29] When $Cu_{20}Te_{11}Cl_3$ is compared with $Cu_{9.1}Te_4Cl_3$, every second 6.3.6.3 Cl net in $Cu_{9.1}Te_4Cl_3$ is replaced by a 6.3.6.3 Te net, as described above. Because this type of network with its larger atoms (Te vs Cl) needs more space, d_{nets} is elongated to 14.70 Å. Hence, in a hypothetical chain of dumbbells, the distance between the single dumbbells would be too long for direct

dumbbell−dumbbell intercoordination, and $[Te_4]^{6-}$ units are realized instead.

When $Cu_{20}Te_{11}Cl_3$ is compared with $Ag_{10}Te_4Br_3$, the distribution of the $[Te_4]^{6-}$ units along the c and a axes, respectively, differs (Figure 4A,B). While in $Ag_{10}Te_4Br_3$ the units are arranged alternatingly in a zigzag manner, able to interpenetrate all anion nets, in $Cu_{20}Te_{11}Cl_3$, they are parallel abreast separated by disordered 6.3.6.3 Te nets.[20] With r_{void}(6.3.6.3.Te) = 3.67 Å, the radius of the voids in this network type is much smaller than that in the 6^3 Te net [r_{void}(6^3 Te) = 4.23 Å], and it acts as an impermeable separator, which avoids propagation of the interaction of neighboring $[Te_4]^{6-}$ units perpendicular to the nets. The occurrence of a CDW along the Te chain is not possible.

In α-$Ag_{10}Te_4Br_3$, the high-temperature polymorph above 390 K, the Peierls-distorted situation of $[Te_4]^{6-}$ units vanishes and a highly mobile equidistant chain of Te represented by Te split positions is realized. This feature can be seen in the scheme in Figure 4D.[21,22] In the high-temperature polymorph α-$Cu_{20}Te_{11}Cl_3$, measured at 540 K, this effect does not occur and the Peierls distortion does not vanish. All $[Te_4]^{6-}$ units are still ordered. The reason is the disordered 6.3.6.3 Te net that was shown above, which acts as an impermeable separator for the $[Te_4]^{6-}$ units.

Seebeck Coefficient. To test for p−n−p switching, as it occurs in $Ag_{10}Te_4Br_3$, we measured the electrical conductivity and Seebeck coefficient between room temperature and 523 K.

The electric conductivity varies between 264 S cm^{-1} at room temperature and 274 S cm^{-1} at 523 K, which are the same order of magnitude as those in $Cu_{9.1}Te_4Cl_3$. The increase of the electric conductivity with increasing temperature corresponds to the behavior of a semiconductor. In semimetallic $Cu_{9.1}Te_4Cl_3$, the electric conductivity is not substantially higher and ranges between 325 S cm^{-1} at 298 K and 169 S cm^{-1} at 523 K.[29] $Ag_{10}Te_4Br_3$ exhibits much lower total electric conductivity (4.1 × 10^{-3} at room temperature) than the other two representatives of its class.[22]

As can be seen in Figure 6, the Seebeck coefficient of $Cu_{20}Te_{11}Cl_3$ shows linear behavior, and we detected no discontinuities in the given range. The Seebeck coefficient of $Cu_{20}Te_{11}Cl_3$ increases with increasing temperature from 66 μV K^{-1} at room temperature to 84 μV K^{-1} at 523 K, which are slightly higher than those in the case of $Cu_{9.1}Te_4Cl_3$ (36 μV
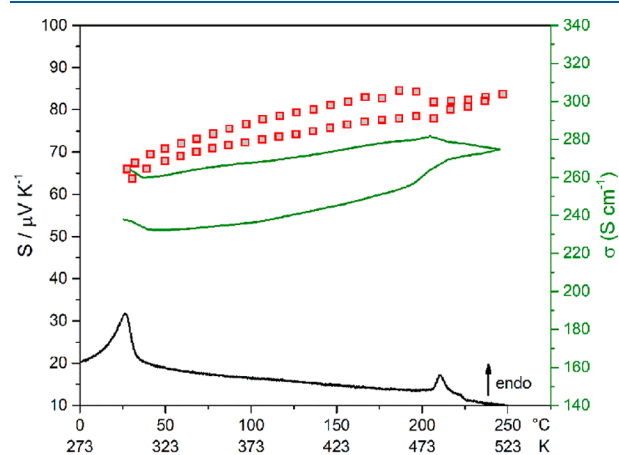
Figure 6. Seebeck coefficient (red squares) and electric conductivity (green line) of $Cu_{20}Te_{11}Cl_3$. A DSC curve is given (black line).

K^{-1} at 298 K and 85 $\mu V\ K^{-1}$ at 523 K).[29] Both copper polytelluride chlorides show p-type semiconducting behavior over the whole temperature range, whereas in $Ag_{10}Te_4Br_3$, it switches between $+310$ and $-940\ \mu V\ K^{-1}$ during the $\alpha-\beta$ phase transition.[22] As stated earlier, the p−n−p switching effect in $Ag_{10}Te_4Br_3$ is induced by the transformation of ordered $[Te_4]^{6-}$ units to the highly mobile equidistant chain of Te split positions in α-$Ag_{10}Te_4Br_3$. This transition occurs via internal redox processes at which $[Te_2]^{2-}$ bonds are broken and new $[Te_2]^{2-}$ dumbbells are built from two single Te^{2-} anions and can be regarded as a CDW. Given that $Cu_{20}Te_{11}Cl_3$ contains the impermeable disordered 6.3.6.3 Te kagomé net that separates the $[Te_4]^{6-}$ units and, thus, in α-$Cu_{20}Te_{11}Cl_3$ still all $[Te_4]^{6-}$ units are ordered, no such CDW effect can occur and no p−n−p switching can be observed. Usually, p−n−p switching causes a broad and significant response in the Seebeck experiment, which occurs significantly above and below the actual phase-transition temperature. This is the case for all materials known to perform p−n−p switching and is well-documented in the literature.[22−26] Because of our limited temperature range for Seebeck experiments in our group, starting from room temperature toward higher temperatures, we were not able to monitor the entire $\beta-\gamma$ phase transition in $Cu_{20}Te_{11}Cl_3$ around room temperature. As illustrated in Figure 6, the Seebeck coefficient does not show any pronounced drop around room temperature, and we are sure that p−n−p switching does not take place during this transition.

Taking a thermal conductivity between 0.3 and 0.6 W m^{-1} K^{-1} into account (estimated from the measured data for $Ag_{10}Te_4Br_3$ and $Cu_{9.1}Te_4Cl_3$), we predict a maximum ZT value between 0.15 and 0.3 at 500 K, which is in the same range as that for $Cu_{9.1}Te_4Cl_3$ and not competitive with state-of-the-art thermoelectric materials.

■ CONCLUSION AND OUTLOOK

$Cu_{20}Te_{11}Cl_3$ shows an intriguing structure chemistry and is characterized by two order−disorder phase transitions. The new compound structurally fits well into the class of coinage metal polychalcogenide halides because it is built of topologic anion nets stacked in one direction that are interpenetrated by partially covalently bonded chalcogene strands. A new structure feature also containing covalently bonded chalcogen is the disordered 6.3.6.3 Te net. This net can be described by two models: a disordered arrangement of $[Te_2]^{2-}$ dumbbells or two statistically distributed Stützite-type 6.3.6.3 Te nets in an opposite orientation. Ordering of that disordered 6.3.6.3 Te net might be achieved by modification of the cell parameters by the implementation of higher or lower homologues into the crystal structure. That is an approach that we will follow in the future to ascertain the nature of the new network type. The Seebeck coefficient and electric conductivity are in the same ranges as those reported for $Cu_{9.1}Te_4Cl_3$. $Ag_{10}Te_4Br_3$, a structurally closely related material, exhibits a huge drop of the Seebeck coefficient accompanied by p−n−p switching induced by a CDW based on the re-formation of a strand of $[Te_4]^{6-}$ units to a mobile equidistant Te chain. In the case of $Cu_{20}Te_{11}Cl_3$, the Seebeck coefficient shows linear behavior and no p−n−p switching, although it inhibits comparable strands of $[Te_4]^{6-}$ units. The reason for that difference is the existence of a disordered and static 6.3.6.3 Te net that acts as a separator between the $[Te_4]^{6-}$ units capable of hindering the formation of a CDW in the polychalcogenide substructure.

■ ASSOCIATED CONTENT

ⓈI Supporting Information
The Supporting Information is available free of charge at https://pubs.acs.org/doi/10.1021/acs.inorgchem.1c01764.

Additional crystallographic data, full DSC data, Laue representations of γ-$Cu_{20}Te_{11}Cl_3$, and comments on the crystallographic challenges and disorder in the cationic substructure (PDF)

Accession Codes
CCDC 2089006 and 2089011 contain the supplementary crystallographic data for this paper. These data can be obtained free of charge via www.ccdc.cam.ac.uk/data_request/cif, or by emailing data_request@ccdc.cam.ac.uk, or by contacting The Cambridge Crystallographic Data Centre, 12 Union Road, Cambridge CB2 1EZ, UK; fax: +44 1223 336033.

■ AUTHOR INFORMATION

Corresponding Author
Tom Nilges − *Synthesis and Characterization of Innovative Materials, Department of Chemistry, Technical University of Munich, Garching bei München 85748, Germany;* ⓞ orcid.org/0000-0003-1415-4265; Email: tom.nilges@tum.de

Author
Anna Vogel − *Synthesis and Characterization of Innovative Materials, Department of Chemistry, Technical University of Munich, Garching bei München 85748, Germany*

Complete contact information is available at:
https://pubs.acs.org/10.1021/acs.inorgchem.1c01764

Author Contributions
A.V. synthesized the compound, carried out the experiments and solved all structures. A.V. and T.N. discussed the crystallographic challenges and contributed to the final version of the manuscript.

Notes
The authors declare no competing financial interest.

■ REFERENCES
(1) Riess, I. Mixed ionic-electronic conductors - material properties and applications. *Solid State Ionics* **2003**, *157* (1−4), 1−17.
(2) Wuttig, M.; Yamada, N. Phase-change materials for rewriteable data storage. *Nat. Mater.* **2007**, *6* (11), 824−832.
(3) Van Ruitenbeek, J. Silver nanoswitch. *Nature* **2005**, *433* (7021), 21−22.
(4) Waser, R.; Aono, M. Nanoionics-based resistive switching memories. *Nat. Mater.* **2007**, *6* (11), 833−840.
(5) Vining, C. B. An inconvenient truth about thermoelectrics. *Nat. Mater.* **2009**, *8* (2), 83−85.

(6) Nilges, T.; Bawohl, M.; Lange, S.; Messel, J.; Osters, O. Highly dynamic chalcogen dhains in silver(I) (poly)chalcogenide halides: A new concept for thermoelectrics? *J. Electron. Mater.* **2010**, *39* (9), 2096−2104.

(7) Nilges, T.; Bawohl, M.; Osters, O.; Lange, S.; Messel, J. Silver(I)-(poly)chalcogenide halides - ion and electron high potentials. *Z. Phys. Chem.* **2010**, *224* (10−12), 1505−1531.

(8) Blachnik, R.; Dreisbach, H. A. The phase diagrams of Ag_2X-AgY (X = S, Se, Te; Y = Cl, Br, I): Mixtures and the structure of Ag_5Te_2Cl. *J. Solid State Chem.* **1985**, *60* (1), 115−122.

(9) Doert, T.; Rönsch, E.; Schnieders, F.; Böttcher, P.; Sieler, J. Die Kristallstruktur der Tieftemperaturmodifikation von Ag_5Te_2Cl. *Z. Anorg. Allg. Chem.* **2000**, *626* (1), 89−93.

(10) Messel, J.; Nilges, T. Structure chemical aspects of silver(I) chalcogenide halides and preparation of the x = 1 member of the solid solution $Ag_5Te_2Cl_{1-x}Br_x$. *Z. Naturforsch., B: J. Chem. Sci.* **2008**, *63* (9), 1077−1082.

(11) Nilges, T.; Nilges, S.; Pfitzner, A.; Doert, T.; Böttcher, P. Structure-property relations and diffusion pathways of the silver ion conductor Ag_5Te_2Cl. *Chem. Mater.* **2004**, *16* (5), 806−812.

(12) Nilges, T.; Dreher, C.; Hezinger, A. Structures, phase transitions and electrical properties of $Ag_5Te_{2-y}Se_yCl$ (y = 0 - 0.7). *Solid State Sci.* **2005**, *7* (1), 79−88.

(13) Nilges, T.; Lange, S. $Ag_5Te_2Cl_{1-x}Br_x$ (x = 0 - 0.65) and $Ag_5Te_{2-y}S_yCl$ (y = 0 - 0.3): Variation of physical properties in silver(I) chalcogenide halides. *Z. Anorg. Allg. Chem.* **2005**, *631* (15), 3002−3012.

(14) Nilges, T.; Messel, J.; Bawohl, M.; Lange, S. Silver(I) chalcogenide halides $Ag_{19}Te_6Br_7$, $Ag_{19}Te_6Br_{5.4}I_{1.6}$, and $Ag_{19}Te_5SeBr_7$. *Chem. Mater.* **2008**, *20* (12), 4080−4091.

(15) Nilges, T. The solid solutions $M_{19}Q_6X_7$ with M = Ag, Cu; Q = S, Se, Te and X = S, Se, Te. *Z. Anorg. Allg. Chem.* **2008**, *634* (12-13), 2185−2190.

(16) Nilges, T.; Bawohl, M. Structures and thermal properties of silver(I) (poly)chalcogenide halide solid solutions $Ag_{10}Te_{4-(q, p)}Q_{(q, p)}Br_3$ with Q = S, Se. *Z. Naturforsch., B: J. Chem. Sci.* **2008**, *63* (6), 629−636.

(17) Nilges, T.; Bawohl, M.; Lange, S. $Ag_{10}Te_4Br_{3-x}Cl_x$ and $Ag_{10}Te_4Br_{3-y}I_y$: Structural and electrical property tuning of a mixed conductor by partial anion substitution. *Z. Naturforsch., B: J. Chem. Sci.* **2007**, *62* (7), 955−964.

(18) Giller, M.; Bawohl, M.; Gerstle, A. P.; Nilges, T. Copper substitution and mixed cation effect in $Ag_{10}Te_4Br_3$. *Z. Anorg. Allg. Chem.* **2013**, *639* (14), 2379−2381.

(19) Moroz, M.; Tesfaye, F.; Demchenko, P.; Prokhorenko, M.; Prokhorenko, S.; Lindberg, D.; Reshetnyak, O.; Hupa, L. Synthesis and thermodynamic investigation of energy materials in the Ag-Te-Cl system by the solid-state galvanic cells. *JOM* **2021**, *73*, 1487−1494.

(20) Lange, S.; Nilges, T. $Ag_{10}Te_4Br_3$: A new silver(I) (poly)-chalcogenide halide solid electrolyte. *Chem. Mater.* **2006**, *18* (10), 2538−2544.

(21) Lange, S.; Bawohl, M.; Wilmer, D.; Meyer, H.-W.; Wiemhöfer, H.-D.; Nilges, T. Polymorphism, structural frustration and electrical properties of the mixed conductor $Ag_{10}Te_4Br_3$. *Chem. Mater.* **2007**, *19* (6), 1401−1410.

(22) Nilges, T.; Lange, S.; Bawohl, M.; Deckwart, J. M.; Janssen, M.; Wiemhöfer, H.-D.; Decourt, R.; Chevalier, B.; Vannahme, J.; Eckert, H.; Weihrich, R. Reversible switching between p-and n-type conduction in the semiconductor $Ag_{10}Te_4Br_3$. *Nat. Mater.* **2009**, *8* (2), 101.

(23) Xiao, C.; Qin, X.; Zhang, J.; An, R.; Xu, J.; Li, K.; Cao, B.; Yang, J.; Ye, B.; Xie, Y. High thermoelectric and reversible pnp conduction type switching integrated in dimetal chalcogenide. *J. Am. Chem. Soc.* **2012**, *134* (44), 18460−18466.

(24) Guin, S. N.; Pan, J.; Bhowmik, A.; Sanyal, D.; Waghmare, U. V.; Biswas, K. Temperature dependent reversible p−n−p type conduction switching with colossal change in thermopower of semiconducting AgCuS. *J. Am. Chem. Soc.* **2014**, *136* (36), 12712−12720.

(25) Guin, S. N.; Banerjee, S.; Sanyal, D.; Pati, S. K.; Biswas, K. Origin of the order−disorder transition and the associated anomalous change of thermopower in $AgBiS_2$ nanocrystals: a combined experimental and theoretical study. *Inorg. Chem.* **2016**, *55* (12), 6323−6331.

(26) Shi, Y.; Assoud, A.; Sankar, C. R.; Kleinke, H. $Tl_2Ag_{12}Se_7$: a new pnp conduction switching material with extraordinarily low thermal conductivity. *Chem. Mater.* **2017**, *29* (21), 9565−9571.

(27) Rhyee, J.-S.; Lee, K. H.; Lee, S. M.; Cho, E.; Kim, S. I.; Lee, E.; Kwon, Y. S.; Shim, J. H.; Kotliar, G. Peierls distortion as a route to high thermoelectric performance in $In_4Se_{3-\delta}$ crystals. *Nature* **2009**, *459* (7249), 965.

(28) Osters, O.; Blazek, G.; Nilges, T. Comments on Peierls-distorted indium chains in In_4Se_{3-x}. *Z. Anorg. Allg. Chem.* **2013**, *639* (3-4), 497−501.

(29) Vogel, A.; Miller, T.; Hoch, C.; Jakob, M.; Oeckler, O.; Nilges, T. $Cu_{9.1}Te_4Cl_3$: A thermoelectric compound with low thermal and high electrical conductivity. *Inorg. Chem.* **2019**, *58* (9), 6222−6230.

(30) *WinXPOW*, version 3.05; STOE & Cie GmbH: Darmstadt, Germany, 2011.

(31) *X-AREA*, version 1.76; STOE & Cie GmbH: Darmstadt, Germany, 2015.

(32) Palatinus, L.; Chapuis, G. SUPERFLIP - a computer program for the solution of crystal structures by charge flipping in arbitrary dimensions. *J. Appl. Crystallogr.* **2007**, *40*, 786−790.

(33) Petrıcek, V.; Dušek, M.; Palatinus, L. *JANA2006, The Crystallographic Computing System*; Institute of Physics: Praha, Czech Republic, 2006.

(34) Pauling, L. *The Nature of the Chemical Bond*, 3rd ed.; Cornell University Press: Ithaca, NY, 1960; Vol. *260*.

(35) Yanagisawa, S.; Tashiro, M.; Anzai, S. Crystal structure of magnesium ditelluride. *J. Inorg. Nucl. Chem.* **1969**, *31* (4), 943−946.

(36) Böttcher, P.; Getzschmann, J.; Keller, R. Zur Kenntnis der Dialkalimetalldichalkogenide β-Na_2S_2, K_2S_2, α-Rb_2S_2, β-Rb_2S_2, K_2Se_2, Rb_2Se_2, α-K_2Te_2, β-K_2Te_2 und Rb_2Te_2. *Z. Anorg. Allg. Chem.* **1993**, *619* (3), 476−488.

(37) Peters, J.; Conrad, O.; Bremer, B.; Krebs, B. Die Kristallstruktur des synthetischen Stützits, $Ag_{5-x}Te_3$. *Z. Anorg. Allg. Chem.* **1996**, *622* (11), 1823−1832.

Supporting information

Ion dynamics and polymorphism in $Cu_{20}Te_{11}Cl_3$

Anna Vogel, Tom Nilges

Technical University Munich, Synthesis and Characterization of Innovative Materials, Department of Chemistry, Lichtenbergstraße 4, 85748 Garching b. München, Germany

Structure refinement.

Refinements of α-$Cu_{20}Te_{11}Cl_3$ and β-$Cu_{20}Te_{11}Cl_3$ were performed using 3rd order displacement parameters (so called non-harmonic refinements). This procedure is necessary if crystalline solid ion conductors featuring a high grade of ion dynamics and disorder are examined. Atomic coordinates, site occupancy factors, and displacement parameters are given for both polymorphs.

Table S1. Atomic coordinates and site occupancy factors of α-$Cu_{20}Te_{11}Cl_3$.

Atom	Wyckoff position	Site symmetry	sof	x	y	z
Te1	2e	6mm	1	0	0	0.10007(7)
Te2	2e	6mm	1	0	0	0.35149(8)
Te3	4h	3m.	1	0.6667	0.3333	0.23550(5)
Te4	6m	mm2	0.5	0.46994(12)	0.9399(2)	0.5
Cl1	3f	mmm	1	0.5	0	0
Cu1	12n	..m	0.369(10)	0	-0.2782(14)	0.2365(4)
Cu2	12n	..m	0.316(8)	0	-0.3672(6)	0.3303(4)
Cu3	12o	.m.	0.286(9)	0.426(2)	0.2132(10)	0.0971(4)
Cu4	6m	mm2	0.266(10)	0.1159(9)	0.8841(9)	0.5
Cu5	12n	..m	0.276(10)	0	-0.337(2)	0.1367(12)
Cu6	12o	.m.	0.254(8)	0.2173(9)	-0.2173(9)	0.3814(7)

Table S2. Anisotropic displacement parameters of α-Cu$_{20}$Te$_{11}$Cl$_3$.

Atom	U_{11}	U_{22}	U_{33}	U_{12}	U_{13}	U_{23}
Te1	0.0304(3)	0.0304(3)	0.0304(5)	0.0152(2)	0	0
Te2	0.0338(3)	0.0338(3)	0.0401(6)	0.0169(2)	0	0
Te3	0.0326(3)	0.0326(3)	0.0400(4)	0.01629(14)	0	0
Te4	0.0647(8)	0.0576(11)	0.0393(7)	0.0288(5)	0	0
Cu1	0.069(3)	0.067(2)	0.107(4)	0.034(2)	0	-0.018(2)
Cu2	0.073(3)	0.067(2)	0.084(3)	0.037(2)	0	-0.007(2)
Cu3	0.078(5)	0.087(4)	0.043(3)	0.039(2)	-0.013(2)	-0.0063(10)
Cu4	0.083(4)	0.083(4)	0.066(4)	0.058(4)	0	0
Cu5	0.185(13)	0.096(5)	0.085(5)	0.092(6)	0	-0.008(3)
Cu6	0.104(5)	0.104(5)	0.068(4)	0.058(5)	0.006(2)	-0.006(2)

Table S3. Anisotropic and 3rd order anharmonic displacement parameters of α-Cu$_{20}$Te$_{11}$Cl$_3$.

Atom	C_{111}	C_{112}	C_{113}	C_{122}	C_{123}
Cu1	0	0.038(5)	-0.011(2)	0.038(5)	-0.0057(10)
Cu2	0	0.014(4)	0.013(2)	0.014(4)	0.0067(12)
Cu3	0.10(2)	0.048(8)	-0.012(2)	0.037(8)	-0.0058(12)
Cu4	-0.023(8)	-0.009(3)	0	0.009(3)	0
Cu5	0	0.10(2)	-0.07(2)	0.10(2)	-0.035(8)
Cu6	0	-0.027(4)	-0.016(4)	0.027(4)	-0.026(4)
	C_{133}	C_{222}	C_{223}	C_{233}	C_{333}
Cu1	0	0.031(6)	0	-0.0101(10)	0
Cu2	0	0	0	0	0
Cu3	0	0.031(12)	0	0	0
Cu4	0	0.023(8)	0	0	0
Cu5	0	0.10(2)	-0.025(6)	0	0
Cu6	0	0	-0.016(4)	0	0

Table S4. Atomic coordinates and site occupancy factors of β-Cu$_{20}$Te$_{11}$Cl$_3$.

Atom	Wyckoff position	Site symmetry	sof	x	y	z
Te1	8f	$m..$	1	1/2	0.1699(3)	0.11687(14)
Te2	16h	1	1	0.40014(3)	-0.00163(11)	0.05008(4)
Te3	16h	1	1	0.30025(4)	0.5004(2)	0.04980(8)
Te4	8f	$m..$	1	1/2	-0.4970(3)	0.1768(2)
Te5	8f	$m..$	1	1/2	0.50273(14)	0.05047(8)
Te6	16h	1	1	0.39962(4)	-0.3347(3)	0.11742(7)
Te7	16h	1	1	0.39973(9)	0.3310(2)	0.11764(5)
Te8	8f	$m..$	1	1/2	-0.1650(4)	0.11774(10)
Te9	16h	1	1	0.30011(5)	0.5008(2)	0.17737(7)
Te10	16h	1	1	0.20071(6)	0.3375(3)	0.11740(6)
Te11	16h	1	1	0.30088(5)	0.1649(3)	0.11768(7)
Te12	16h	1	1	0.40009(3)	-0.0017(2)	0.17706(8)
Te13	8g	$..m$	1	0.09961(7)	0.0347(2)	1/4

Te14	8*g*	..*m*	1	0.3525(2)	0.2649(3)	1/4
Te15	4*c*	*m2m*	1	0	0.4627(6)	1/4
Te16	8*g*	..*m*	1	0.19874(10)	0.4845(5)	1/4
Te17	8*g*	..*m*	1	0.4492(3)	0.2459(5)	1/4
Te18	8*g*	..*m*	1	0.2609(2)	0.2359(4)	1/4
Te19	8*g*	..*m*	1	0.16269(9)	0.2663(5)	1/4
Te20	8*g*	..*m*	1	0.05427(13)	0.2361(5)	1/4
Cl1	4*b*	2/*m*	1	1/2	0	0
Cl2	16*h*	1	1	0.15036(12)	0.2476(3)	-0.0009(2)
Cl3	8*e*	2..	1	0.2997(2)	0	0
Cl4	16*h*	1	1	0.04966(13)	0.2484(4)	0.9981(2)
Cl5	8*d*	-1	1	1/4	1/4	0
Cl6	8*e*	2..	1	0.1001(2)	0	0
Cu1	16*h*	1	1	0.4011(2)	-0.2092(6)	0.0502(2)
Cu2	8*f*	*m*..	1	1/2	-0.2914(5)	0.0501(4)
Cu3	16*h*	1	1	0.3379(2)	0.0908(7)	0.0532(3)
Cu4	16*h*	1	1	0.4380(2)	0.4128(5)	0.0533(3)
Cu5	16*h*	1	0.70(2)	0.2355(2)	0.4206(8)	0.0520(3)
Cu6	16*h*	1	0.562(14)	0.3084(2)	0.7010(7)	0.0522(3)
Cu7	16*h*	1	0.72(2)	0.4628(2)	0.0809(6)	0.0536(2)
Cu8	16*h*	1	0.61(2)	0.3295(4)	0.3616(8)	0.1257(5)
Cu9	16*h*	1	0.46(2)	0.3546(2)	0.3789(10)	0.0510(4)
Cu10	16*h*	1	0.60(2)	0.2317(2)	0.1319(11)	0.1197(2)
Cu11	16*h*	1	0.63(2)	0.1246(4)	-0.0040(7)	0.1636(5)
Cu12	16*h*	1	0.58(2)	0.4247(5)	0.1185(14)	0.1184(3)
Cu13	16*h*	1	0.64(2)	0.2745(4)	0.376(2)	0.1211(3)
Cu14	16*h*	1	0.45(2)	0.1599(3)	0.1750(11)	0.1682(6)
Cu15	16*h*	1	0.566(14)	0.3679(2)	-0.1318(11)	0.1209(2)
Cu16	16*h*	1	0.52(2)	0.4698(3)	-0.0001(9)	0.1599(4)
Cu17	16*h*	1	0.57(2)	0.2269(2)	0.5187(7)	0.1710(4)
Cu18	16*h*	1	0.67(2)	0.3419(3)	0.0883(8)	0.1940(3)
Cu19	16*h*	1	0.64(2)	0.4289(2)	-0.6083(9)	0.1979(3)
Cu20	16*h*	1	0.52(2)	0.4353(3)	-0.5210(9)	0.1591(4)
Cu21	16*h*	1	0.45(2)	0.3242(4)	0.0164(12)	0.1594(6)
Cu22	8*g*	..*m*	0.65(2)	0.2668(4)	0.4323(9)	1/4
Cu23	8*g*	..*m*	0.57(2)	0.3646(4)	0.055(2)	1/4
Cu24	16*h*	1	0.57(2)	0.4742(3)	-0.6222(12)	0.1190(4)
Cu25	16*h*	1	0.52(2)	0.3760(4)	0.1319(8)	0.1178(5)
Cu26	16*h*	1	0.55(2)	0.4714(5)	0.0984(10)	0.1962(4)
Cu27	8*f*	*m*..	0.65(3)	1/2	-0.276(2)	0.1933(7)
Cu28	16*h*	1	0.51(2)	0.1707(2)	0.1266(7)	0.1209(3)
Cu29	16*h*	1	0.46(2)	0.1050(2)	0.2743(13)	0.1963(6)
Cu30	16*h*	1	0.45(2)	0.4314(3)	-0.1343(7)	0.1226(5)
Cu31	16*h*	1	0.48(2)	0.4675(4)	-0.3673(8)	0.1264(5)
Cu32	16*h*	1	0.36(2)	0.4369(4)	-0.1956(9)	0.1622(8)
Cu33	8*g*	..*m*	0.44(2)	0.4734(5)	-0.5732(11)	1/4
Cu34	16*h*	1	0.32(2)	0.2382(4)	0.3676(12)	0.1939(5)
Cu35	8*g*	..*m*	0.42(2)	0.3319(5)	0.5448(13)	1/4
Cu36	16*h*	1	0.32(2)	0.2276(6)	0.186(2)	0.1662(6)
Cu37	16*h*	1	0.515(2)	0.4656(4)	-0.2942(13)	0.1558(5)
Cu38	8*g*	..*m*	0.44(2)	0.0637(5)	0.565(2)	1/4
Cu39	16*h*	1	0.26(2)	0.3579(5)	0.1799(14)	0.1709(6)
Cu40	16*h*	1	0.24(2)	0.3324(4)	0.3300(14)	0.1610(5)

Cu41	16h	1	0.38(2)	0.2617(6)	0.314(2)	0.1640(8)
Cu42	16h	1	0.68(3)	0.1322(5)	0.045(3)	0.0542(9)
Cu43	16h	1	0.40(2)	0.1354(6)	-0.116(2)	0.1935(7)
Cu44	16h	1	0.37(2)	0.3693(4)	-0.1874(12)	0.1724(5)
Cu45	16h	1	0.28(2)	0.4350(4)	0.1698(13)	0.1693(6)
Cu46	16h	1	0.22(2)	0.2414(5)	0.606(2)	0.0591(5)

Table S5. Anisotropic displacement parameters of β-Cu$_{20}$Te$_{11}$Cl$_3$.

Atom	U_{11}	U_{22}	U_{33}	U_{12}	U_{13}	U_{23}
Te1	0.0261(13)	0.0371(14)	0.0286(11)	0	0	0.0030(10)
Te2	0.0174(11)	0.0260(13)	0.0265(7)	-0.0023(4)	0.0004(5)	0.0003(5)
Te3	0.0185(11)	0.0292(12)	0.0261(6)	-0.0001(4)	0.0004(6)	0.0005(6)
Te4	0.0225(13)	0.0259(14)	0.0400(12)	0	0	0.0068(8)
Te5	0.0181(13)	0.0275(14)	0.0267(10)	0	0	0.0001(7)
Te6	0.0262(11)	0.0230(11)	0.0335(9)	-0.0007(5)	0.0006(5)	0.0033(8)
Te7	0.0258(11)	0.0272(11)	0.0315(9)	0.0024(5)	0.0010(5)	0.0000(8)
Te8	0.0257(13)	0.0342(14)	0.0364(12)	0	0	-0.0044(10)
Te9	0.0236(11)	0.0262(12)	0.0425(7)	0.0027(5)	0.0013(6)	-0.0011(7)
Te10	0.0219(10)	0.0280(11)	0.0329(9)	-0.0003(5)	0.0038(5)	-0.0010(7)
Te11	0.0217(10)	0.0307(12)	0.0346(9)	0.0002(5)	0.0032(6)	-0.0006(8)
Te12	0.0241(12)	0.0257(13)	0.0414(9)	-0.0014(5)	-0.0005(6)	-0.0028(6)
Te13	0.0397(13)	0.0247(11)	0.0313(12)	0.0092(8)	0	0
Te14	0.154(4)	0.0281(12)	0.0300(14)	-0.010(2)	0	0
Te15	0.054(2)	0.038(2)	0.033(2)	0	0	0
Te16	0.052(2)	0.088(3)	0.0319(12)	0.031(2)	0	0
Te17	0.206(5)	0.046(2)	0.0343(14)	-0.003(2)	0	0
Te18	0.094(3)	0.0326(12)	0.0343(13)	0.0031(13)	0	0
Te19	0.0441(13)	0.055(2)	0.0370(13)	-0.0155(11)	0	0
Te20	0.042(2)	0.106(3)	0.0368(12)	-0.030(2)	0	0
Cl1	0.013(5)	0.026(6)	0.045(7)	0	0	-0.009(4)
Cl2	0.026(4)	0.028(4)	0.029(3)	-0.014(3)	0.003(2)	-0.003(2)
Cl3	0.004(4)	0.028(4)	0.055(5)	0	0	0.005(4)
Cl4	0.029(4)	0.032(4)	0.028(3)	0.010(3)	0.005(3)	0.001(2)
Cl5	0.027(4)	0.035(5)	0.024(4)	0.010(3)	-0.008(3)	-0.002(3)
Cl6	0.010(5)	0.038(5)	0.043(6)	0	0	0.000(4)
Cu1	0.050(2)	0.053(2)	0.055(3)	0	0.009(2)	0.003(2)
Cu2	0.067(3)	0.059(3)	0.054(4)	0	0	-0.004(2)
Cu3	0.038(2)	0.124(5)	0.071(4)	0.027(2)	0.001(2)	-0.027(3)
Cu4	0.048(2)	0.148(5)	0.068(3)	-0.033(2)	0.004(2)	0.027(3)
Cu5	0.030(4)	0.241(9)	0.085(4)	-0.046(4)	-0.007(2)	0.074(5)
Cu6	0.095(5)	0.043(4)	0.074(5)	-0.010(3)	0.058(4)	-0.013(3)
Cu7	0.022(3)	0.237(6)	0.074(4)	-0.057(3)	0.006(2)	-0.058(3)
Cu8	0.045(4)	0.062(5)	0.130(10)	-0.007(3)	0.043(5)	-0.049(5)
Cu9	0.098(6)	0.176(9)	0.106(7)	0.111(5)	-0.060(5)	-0.057(6)
Cu10	0.023(3)	0.106(6)	0.047(4)	-0.020(3)	0.014(3)	0.009(4)
Cu11	0.056(5)	0.024(3)	0.085(7)	0.010(2)	-0.003(3)	-0.005(2)
Cu12	0.128(9)	0.126(11)	0.041(4)	0.003(7)	0.022(5)	0.015(4)
Cu13	0.077(6)	0.132(10)	0.051(5)	0.006(6)	-0.008(4)	-0.008(4)
Cu14	0.100(7)	0.099(8)	0.150(10)	0.064(5)	-0.065(6)	-0.029(6)
Cu15	0.029(3)	0.092(5)	0.040(4)	-0.011(3)	-0.010(2)	-0.035(3)

Cu16	0.060(6)	0.058(5)	0.126(7)	-0.004(3)	0.052(5)	-0.024(3)
Cu17	0.042(4)	0.140(6)	0.113(7)	0.018(4)	0.005(4)	0.070(4)
Cu18	0.076(6)	0.170(9)	0.074(5)	-0.065(5)	-0.008(3)	-0.007(4)
Cu19	0.151(6)	0.107(6)	0.057(5)	0.034(5)	-0.035(4)	0.006(4)
Cu20	0.160(10)	0.141(9)	0.259(11)	-0.052(6)	-0.046(7)	-0.081(7)
Cu21	0.063(8)	0.080(9)	0.092(11)	0.006(5)	-0.001(6)	-0.013(4)
Cu22	0.047(6)	0.055(5)	0.095(8)	-0.019(4)	0	0
Cu23	0.019(5)	0.073(8)	0.101(9)	0.006(4)	0	0
Cu24	0.099(6)	0.091(8)	0.076(6)	-0.010(4)	-0.043(4)	0.024(5)
Cu25	0.094(7)	0.061(5)	0.049(5)	0.007(3)	-0.043(5)	0.009(3)
Cu26	0.24(2)	0.089(6)	0.060(5)	0.034(6)	0.052(5)	0.002(4)
Cu27	0.045(6)	0.17(2)	0.060(7)	0	0	0.015(6)
Cu28	0.043(4)	0.047(4)	0.052(5)	0.008(3)	-0.012(3)	0.012(3)
Cu29	0.044(5)	0.119(11)	0.065(8)	-0.018(4)	-0.013(4)	-0.004(5)
Cu30	0.027(4)	0.062(5)	0.056(6)	0.024(3)	0.017(3)	0.013(3)
Cu31	0.051(6)	0.084(7)	0.096(10)	0.014(4)	-0.043(6)	-0.003(3)
Cu32	0.037(6)	0.056(7)	0.065(11)	0.005(4)	-0.033(5)	0.001(4)
Cu33	0.17(2)	0.080(7)	0.077(8)	-0.094(7)	0	0
Cu34	0.047(6)	0.181(13)	0.039(6)	0.066(7)	-0.019(4)	-0.024(6)
Cu35	0.027(7)	0.27(2)	0.051(8)	-0.015(7)	0	0
Cu36	0.202(14)	0.081(10)	0.19(2)	-0.052(9)	-0.133(11)	0.068(10)
Cu37	0.077(7)	0.099(8)	0.153(12)	0.008(5)	-0.038(7)	-0.008(5)
Cu38	0.038(7)	0.10(2)	0.058(8)	0.003(5)	0	0
Cu39	0.066(11)	0.097(12)	0.063(10)	0.044(7)	-0.045(6)	-0.010(7)
Cu40	0.102(10)	0.155(13)	0.138(11)	-0.031(9)	0.046(8)	-0.072(9)
Cu41	0.028(8)	0.099(8)	0.055(9)	-0.016(4)	-0.025(4)	-0.006(6)
Cu42	0.123(10)	0.92(5)	0.29(2)	0.17(2)	-0.084(9)	-0.43(3)
Cu43	0.066(8)	0.197(2)	0.073(9)	-0.047(9)	0.004(5)	-0.039(10)
Cu44	0.102(10)	0.080(9)	0.176(13)	0.042(6)	0.070(9)	0.019(6)
Cu45	0.026(7)	0.22(2)	0.073(11)	-0.009(7)	-0.019(6)	-0.013(6)
Cu46	0.168(14)	0.37(3)	0.094(10)	0.146(13)	0.086(8)	0.025(11)

Table S6. 3rd order anharmonic displacement parameters of β-Cu$_{20}$Te$_{11}$Cl$_3$.

Atom	C_{111}	C_{112}	C_{113}	C_{122}	C_{123}
Te1	0	-0.00011(3)	0	0	0
Te3	0	0	0	0	0.000123(13)
Te4	0	0	-0.00010(2)	0	0
Te5	0	0	0	0	0
Te6	0	0	-0.000062(10)	0.00010(5)	0.00006(2)
Te7	-0.000094(14)	0	0	-0.00021(6)	0.00010(2)
Te8	0	-0.00014(3)	-0.000078(14)	0	0
Te9	0	0	-0.000095(11)	0.00008(6)	0
Te10	-0.000074(13)	0.00013(2)	-0.000037(9)	0	0
Te11	0	0	0	0.00008(6)	0
Te12	0	0	-0.000066(12)	0	0
Te13	0	-0.00026(4)	0	-0.00029(8)	0
Te14	0.00043(9)	0.00050(8)	0	-0.0002(2)	0
Te15	0	0	0	0	0
Te16	0	0.00093(7)	0	0.0045(3)	0
Te17	0.0004(2)	0.00086(14)	0	0.0012(3)	0

Te18	-0.00117(9)	0.00014(7)	0	0	0
Te19	0	0.00009(4)	0	-0.00030(13)	0
Te20	0.00024(3)	0.00048(6)	0	-0.0058(3)	0
Cu1	0.00018(4)	-0.00029(7)	0.00025(3)	0.0007(2)	-0.00030(5)
Cu2	0	0.00014(11)	0.00024(5)	0	0
Cu3	0	-0.00034(8)	0.00017(3)	-0.0038(4)	0.00090(11)
Cu4	0.00014(4)	0.00039(10)	0.00018(3)	-0.0072(6)	-0.00150(13)
Cu5	-0.00021(6)	0.0006(2)	0	-0.0127(14)	-0.0035(3)
Cu6	0.0024(2)	-0.0012(2)	0.0017(2)	0.0004(3)	-0.0011(2)
Cu7	0.00010(4)	-0.0009(2)	0.00016(4)	0.0143(11)	-0.0034(2)
Cu8	-0.00034(7)	0.00024(14)	-0.00036(8)	0.0036(5)	-0.0023(3)
Cu9	-0.0031(3)	-0.0100(8)	0.0022(2)	-0.025(2)	0.0090(7)
Cu10	0	-0.00003(13)	0	0.0049(6)	0.00107(13)
Cu11	-0.00047(9)	0	-0.00013(5)	-0.0006(2)	-0.00005(8)
Cu12	-0.0011(2)	-0.0035(5)	-0.00022(10)	-0.0011(14)	-0.0014(3)
Cu13	0.00022(11)	0.0023(3)	0	-0.0019(10)	0.0001(2)
Cu14	-0.0026(3)	-0.0067(7)	0.0025(3)	-0.011(2)	0.0070(7)
Cu15	0	0.00082(13)	0	-0.0043(5)	0.00049(11)
Cu16	-0.00052(12)	0	-0.00082(13)	0	0
Cu17	0	-0.0004(2)	-0.00019(7)	0.0065(9)	0.0016(3)
Cu18	0.00070(14)	-0.0027(4)	0	0.014(2)	0
Cu19	-0.0046(3)	-0.0055(5)	0.0016(2)	-0.0083(10)	0.0019(3)
Cu20	0.0007(4)	-0.0007(9)	0.0007(5)	0.011(3)	-0.0133(12)
Cu21	-0.0011(2)	0.0010(2)	-0.00050(12)	0.0022(7)	-0.0004(2)
Cu22	0.00052(12)	-0.0013(2)	0	0.0012(5)	0
Cu23	-0.00011(7)	0.00075(13)	0	-0.0006(5)	0
Cu24	0.0016(2)	0.0009(2)	-0.00077(10)	-0.0053(7)	-0.0007(2)
Cu25	0.0012(2)	-0.0014(2)	-0.00084(13)	-0.0055(5)	0
Cu26	0.008(2)	0.0044(9)	0.0014(3)	0.0056(9)	0.0022(3)
Cu27	0	0.0005(2)	-0.00032(7)	0	0
Cu28	0	-0.0015(2)	-0.00013(5)	-0.0029(4)	0
Cu29	0	0	-0.00020(6)	0	0.0013(2)
Cu30	0	0.00060(13)	-0.00004(5)	0.0048(5)	0
Cu31	0.00020(9)	-0.0004(2)	0.00032(11)	-0.0054(7)	-0.0008(2)
Cu32	0	-0.0003(2)	0.00035(7)	0.0003(5)	0
Cu33	0.0082(14)	-0.011(2)	0	0.013(2)	0
Cu34	-0.00068(14)	-0.0044(6)	0.00054(11)	-0.020(3)	0.0011(4)
Cu35	-0.00044(14)	0.0024(4)	0	0.001(2)	0
Cu36	-0.0036(8)	0.0064(11)	0.0077(10)	-0.005(2)	-0.0066(11)
Cu37	0.0005(2)	0.0005(3)	-0.0013(2)	0.0013(8)	0
Cu38	0.00027(11)	0	0	0	0
Cu39	-0.0009(3)	-0.0029(7)	0.0012(2)	-0.010(2)	0.0014(4)
Cu40	-0.0021(7)	0.0075(14)	-0.0049(8)	0.000(4)	0.004(2)
Cu41	-0.00042(14)	0	0.00026(9)	-0.0005(6)	0
Cu42	0.0006(2)	0.0053(9)	-0.0018(3)	-0.007(4)	0
Cu43	0.0001(2)	-0.0021(5)	0	0.011(3)	-0.0016(4)
Cu44	0.0019(4)	0.0039(6)	0.0024(4)	0.0055(12)	0.0047(7)
Cu45	0	0	0.00067(11)	0.006(3)	0.0022(5)
Cu46	0.0066(10)	0.021(3)	0.0080(10)	0.013(9)	0.030(3)
	C_{133}	C_{222}	C_{223}	C_{233}	C_{333}
Te1	0	0	-0.00030(13)	-0.00027(6)	-0.00022(4)
Te3	0	-0.0002(4)	0.00001(7)	0	-0.00007(2)
Te4	0	0.0025(5)	0.00052(13)	0	0.00002(4)

Te5	0	0	0.00018(10)	0	0
Te6	0	0.0007(4)	0	-0.00017(5)	0
Te7	-0.000052(11)	0	0	0.00012(5)	0
Te8	0	0.0010(6)	0	0	0
Te9	0	-0.0015(4)	0.00063(9)	0	0
Te10	0	0.0005(4)	0	0.00038(4)	0
Te11	0	-0.0014(4)	-0.00018(8)	-0.00009(5)	0
Te12	0	0.0005(4)	0.00031(11)	0.00013(4)	0
Te13	0	0	0	0	0
Te14	-0.00018(3)	0	0	0.00033(6)	0
Te15	0	0.0025(9)	0	0.00029(8)	0
Te16	-0.00008(2)	0.019(2)	0	0	0
Te17	0	0.0011(9)	0	0	0
Te18	0	0.0019(6)	0	0.00024(6)	0
Te19	0	-0.0089(9)	0	-0.00087(7)	0
Te20	0	0.027(2)	0	-0.00073(8)	0
Cu1	0.00011(3)	-0.0032(11)	0	0	0.00030(9)
Cu2	0	0	-0.0007(3)	0	0.0008(2)
Cu3	-0.00023(5)	-0.031(3)	0.0060(7)	-0.0018(2)	0.0011(2)
Cu4	-0.00035(5)	0.069(4)	0.0123(9)	0.0023(2)	0.00050(12)
Cu5	-0.00085(9)	0.158(13)	0.035(3)	0.0067(7)	0.0006(2)
Cu6	0.00135(14)	0	0	-0.0015(2)	0.0005(2)
Cu7	0.00061(6)	-0.172(10)	0.038(2)	-0.0057(4)	0
Cu8	0.0009(3)	0	0.0048(10)	-0.0058(9)	0.0052(8)
Cu9	-0.0025(2)	-0.050(8)	0.023(2)	-0.0083(8)	0.0006(3)
Cu10	0.00021(6)	-0.020(3)	-0.0020(6)	-0.0008(2)	0
Cu11	0.00027(8)	-0.0024(11)	0.0009(3)	0.00027(2)	-0.0018(3)
Cu12	0	-0.033(7)	-0.0037(10)	-0.0004(3)	0
Cu13	0.00034(8)	0.020(6)	0.0017(8)	0.0008(3)	0
Cu14	-0.0024(3)	-0.021(5)	0.007(2)	-0.0071(9)	0.0022(6)
Cu15	-0.00010(5)	0.005(3)	0.0012(5)	-0.0007(2)	0
Cu16	-0.0023(2)	-0.010(2)	0.0018(6)	0.0025(3)	-0.0050(5)
Cu17	0.00078(12)	0.089(7)	0.028(2)	0.0076(7)	0.0018(3)
Cu18	0.00059(9)	-0.083(9)	0.0032(10)	-0.0024(4)	0
Cu19	0.00041(11)	-0.004(3)	0.0014(7)	-0.0007(3)	0
Cu20	0.0119(9)	-0.109(13)	0.041(4)	0	-0.019(2)
Cu21	0.0004(2)	0.022(5)	-0.0035(10)	0	-0.0019(5)
Cu22	0	0	0	-0.0015(3)	0
Cu23	0.00020(10)	-0.021(4)	0	-0.0003(4)	0
Cu24	0.00040(10)	0.023(4)	0.0062(10)	0.0016(3)	0
Cu25	0.00072(12)	0	0.0012(5)	0	-0.0006(2)
Cu26	0	0.015(3)	0	-0.0003(3)	0.0007(2)
Cu27	0	0.041(11)	0.0041(14)	0	0.0003(2)
Cu28	0.00038(7)	0	0.0008(4)	-0.0009(2)	0
Cu29	0	-0.041(7)	0.0036(12)	0	0.0009(3)
Cu30	-0.00019(7)	0	-0.0033(5)	0.0008(2)	0.0008(2)
Cu31	-0.0010(2)	0	0.0063(10)	0	0.0034(6)
Cu32	-0.00060(12)	0	-0.0033(8)	0	-0.0010(4)
Cu33	0	-0.020(4)	0	0.0015(4)	0
Cu34	0.00011(10)	-0.11(2)	0.011(2)	0.0011(4)	-0.0008(2)
Cu35	-0.00025(12)	-0.27(3)	0	0.0020(6)	0
Cu36	-0.0097(11)	-0.005(5)	-0.006(2)	0.0009(14)	0.0033(11)
Cu37	0.0023(4)	0.012(4)	0	0	-0.0062(10)

Cu38	-0.00068(12)	0.023(9)	0	0.0023(5)	0
Cu39	0	0	0	0	0
Cu40	-0.0069(11)	0.09(3)	-0.050(9)	0.018(3)	-0.008(2)
Cu41	-0.00027(11)	-0.010(4)	0	0.0019(4)	-0.0008(3)
Cu42	0	-0.58(9)	0.034(14)	0.009(4)	-0.006(2)
Cu43	0	-0.07(2)	0.015(3)	-0.0032(8)	0.0007(3)
Cu44	0.0025(7)	0.020(5)	0	0.0025(12)	0.010(2)
Cu45	-0.0006(2)	-0.19(3)	0	-0.0024(9)	0.0016(5)
Cu46	0.0045(8)	-0.31(7)	0.092(13)	0.021(3)	0.0005(7)

Comments on crystallographic challenges and *checkcif* procedure.

As $Cu_{20}Te_{11}Cl_3$ features, even at lower temperatures, a very high grade of disorder, refinement of third order non-harmonic parameters for many sites is necessary. That approach causes a relatively poor data/parameter ratio (especially in β-$Cu_{20}Te_{11}Cl_3$ with its huge unit cell and large number of atom positions) but leads to significantly better description of the crystal structure. Unfortunately, the *checkcif* program is not able to handle those non-harmonic parameters what leads to deviations in the calculation of some values (eg residual electron density, R-values calculated by checkcif compared to the ones from refinement programs) and consequently false alarms.

Residual electron density calculated from checkcif routines for α-$Cu_{20}Te_{11}Cl_3$ are based on anisotropic displacement parameters while our date are derived from 3rd order non-harmonic data (see below). Due to the huge ion mobility Cu is strongly disordered and displacements are heavily non-harmonic. This causes relatively large residual electron density peaks in the checkcif routine close to Cu atoms, which are not present in our non-harmonically refined structure model. Also the R-values are affected by this aspect and therefore differ slightly.

```
PLAT927_ALERT_1_A Reported and Calculated wR2 Differ by ......... -0.0850 Check
```

Therefore all alert level A points in our checkcif are caused by the checkcif routine and not a false or inadequate structure refinement.

Furthermore, as β-$Cu_{20}Te_{11}Cl_3$ is systematically twinned, twin integration and structure solution using hklf5 data is necessary and was applied in this case. As the subsequent twin fcf data cannot be read by *checkcif* a proper checking is not possible. Still, the appearance of large and non-harmonic displacement parameters is a common phenomenon in the class of highly mobile and strongly disordered ion conductors, even if partial ordering occurs. Often dynamic disorder turns to static disorder which also demands non-harmonic refinement strategies. We therefore used non-harmonic refinements also for many sites in β-$Cu_{20}Te_{11}Cl_3$. This is the reason why the Data/Parameter ratio is low and many parameters were used to describe the disorder phenomena. Also large and strongly anisotropic parameters for Cu and also all neighboring anions are a direct consequence of this phenomenon.

```
PLAT088_ALERT_3_A Poor Data / Parameter Ratio .................... 5.96 Note

PLAT213_ALERT_2_A Atom Cu7 has ADP max/min Ratio ..... 6.4 prolat
```

Level A points in the checkcif routine for β-$Cu_{20}Te_{11}Cl_3$ are caused by the afore mentioned aspects.

In summary the checkcif routine seems to be a good tool for less complex crystal structures but it is not the method of choice for our class of compounds, especially not for systematically twinned ion conductors.

The interested reader is asked to read the nice article by Spek, A.L. checkCIF validation ALERTS: what they mean and how to respond. *Acta Crystallogr E Crystallogr Commun.* **2020** *76*, 1-11 for further information.

Laue representations of γ-Cu$_{20}$Te$_{11}$Cl$_3$.
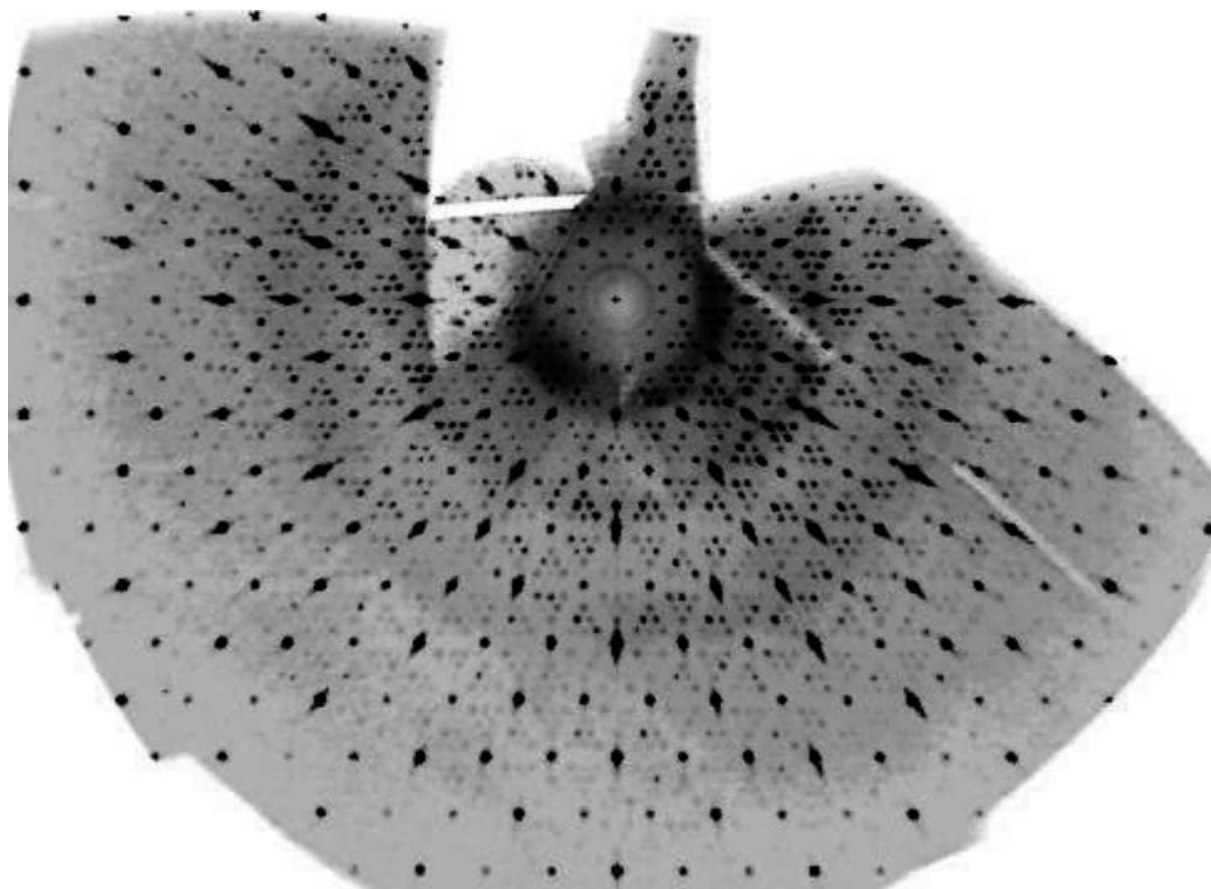
Figure S1. Projection of five plains (hk0-4) of the single crystal diffraction pattern data of γ-Cu$_{20}$Te$_{11}$Cl$_3$ at 200 K.

Comments on disorder within cationic substructure.

Both α- and β-Cu$_{20}$Te$_{11}$Cl$_3$ are strongly disordered ion conducting structures. In order to investigate the nature of the disorder within the cationic substructure we compared the average dimensions of the thermal displacement parameters in both polymorphs. If the disorder was exclusively of dynamic nature α-Cu$_{20}$Te$_{11}$Cl$_3$ (measured at 540 K) should show much larger thermal displacement parameters than β-Cu$_{20}$Te$_{11}$Cl$_3$ (measured at 330 K). As can be seen in table S7, that is not the case. The averaged thermal displacement parameters are in the same magnitude in both polymorphs and some are even larger in β-Cu$_{20}$Te$_{11}$Cl$_3$. An extrapolation of

the averaged displacements to 0K is not possible which points towards static disorder within the cationic substructure, at least in β-$Cu_{20}Te_{11}Cl_3$.

Table S7. Averaged thermal displacement parameters over all Cu sites, weighted by sof, of α- and β-$Cu_{20}Te_{11}Cl_3$.

averaged	U_{11}	U_{22}	U_{33}	U_{12}	U_{13}	U_{23}
α-$Cu_{20}Te_{11}Cl_3$	0.09752	0.08245	0.07823	0.05094	-0.00134	-0.00881
β-$Cu_{20}Te_{11}Cl_3$	0.07264	0.13882	0.08975	0.00433	-0.00647	-0.01657

Differential Scanning Calorimetry.

As can be seen in figure S2 all DSC signals appear during heating and cooling experiments and are reversible in two consecutive cycles.
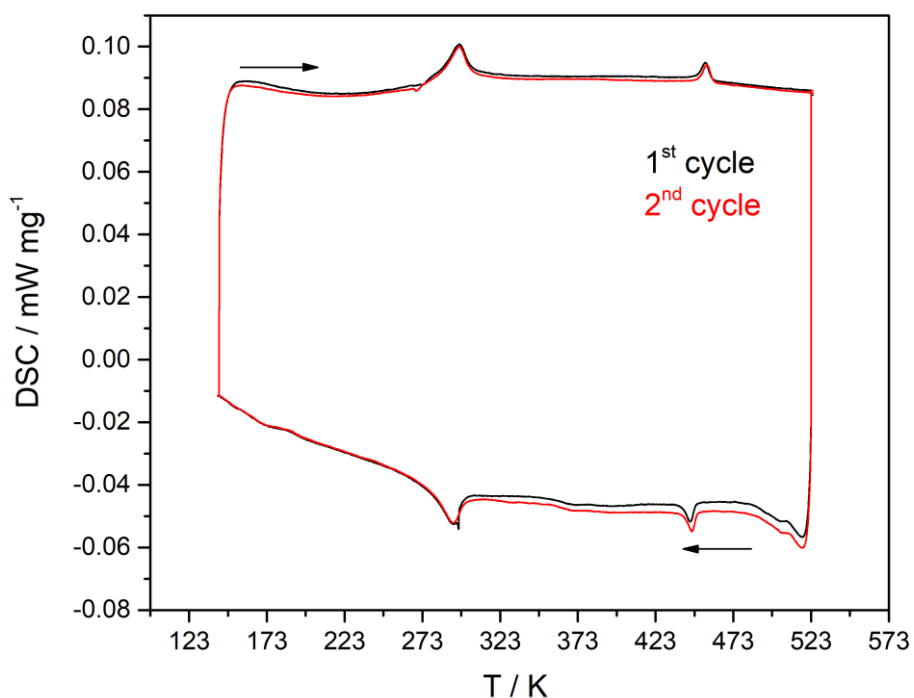
Figure S2. Full set of DSC data of $Cu_{20}Te_{11}Cl_3$ for two consecutive cycles.

3.3   Eine schaltbare Einkomponenten-Diode

Anna Vogel[1], Alfred Rabenbauer[1], Philipp Deng[1], Ruben Steib[1], Thorben Böger[2], Wolfgang Zeier[2], Renée Siegel[3], Jürgen Senker[3], Dominik Deisenberger[4], Katharina Nisi[5], Alexander Holleitner[5], Janio Venturini[1] und Tom Nilges[1]

[1] Technische Universität München, Fakultät für Chemie, Synthese und Charakterisierung innovativer Materialien, Lichtenbergstraße 4, 85748 Garching bei München, Deutschland
[2] Universität Münster, Institut für Anorganische und Analytische Chemie, Corrensstraße 30, 48149 Münster, Deutschland.
[3] Universität Bayreuth, Fakultät für Chemie, Universitätsstraße 30, Bayreuth, 95447, Deutschland.
[4] Diamond Light Source, Harwell Science and Innovation Campus, Didcot, OX11 ODE Oxfordshire, Großbritannien.
[5] Technische Universität München, Walter-Schottky-Institut und Fakultät für Physik, Am Coulombwall 4a, 85748 Garching, Deutschland.

Der Artikel wurde im September 2022 bei der Zeitschrift *Advanced Materials* eingereicht und im Oktober 2022 akzeptiert. Ein Teil der Ergebnisse wurde von Anna Vogel im September 2020 online bei der 20. *Vortragstagung für anorganische Chemie der Fachgruppen Wöhler-Vereinigung und Materialforschung* in Köln, Deutschland, im September 2021 bei den *e-conversion Poster Sessions* in München, Deutschland und von Tom Nilges im September 2021 beim *Hemdsärmelkolloquium* in Bayreuth, Deutschland präsentiert.

Das Thema dieser Arbeit ist die neue Verbindung $Ag_{18}Cu_3Te_{11}Cl_3$, die pnp-Schaltung bei Raumtemperatur zeigt. An einem Einkristall konnte durch Anlegen einer Temperaturdifferenz die erste schaltbare Einkomponenten-Diode gemessen werden. Die Kristallstrukturen der beteiligten Polymorphe werden präsentiert und mögliche Mechanismen für den pnp-Wechsel vorgeschlagen. Die physikalischen Eigenschaften der Verbindung wurden bestimmt und werden hinsichtlich möglicher Anwendungen diskutiert.

$Ag_{18}Cu_3Te_{11}Cl_3$ wird durch Substitution aus $Cu_{20}Te_{11}Cl_3$ (behandelt in Kapitel 3.2 auf Seite 50) gewonnen und kristallisiert in einer Überstruktur. Das vormals ungeordnete Te-6.3.6.3-Netz liegt geordnet als verzerrtes Kagomé-Netz vor, wie es im Mineral Stützit vorkommt. Dieses Netz besteht aus $[Te_2]^{2-}$-Hanteln und koordinierenden Te^{2-}-Anionen und kann nicht mehr durch ein Modell aus ausschließlich Hanteln beschrieben wer-

den. Daraus resultiert die Erhöhung der Gesamtladung der Anionenteilstruktur von $[Te_{11}Cl_3]^{20-}$ zu $[Te_{11}Cl_3]^{21-}$ und die damit einhergehende Erhöhung des Münzmetallgehalts. $Ag_{18}Cu_3Te_{11}Cl_3$ zeigt zwei Phasenübergänge bei 216 und 288 K, wobei oberhalb des α-β-Übergang bei 288 K ein pnp-Wechsel stattfindet. Der Effekt ist außergewöhnlich stark und mit 70 K auch ungewöhnlich breit. Im Artikel werden zwei mögliche Mechanismen diskutiert. Im Te-6.3.6.3-Netz tritt oberhalb des α-β-Phasenübergangs eine Split-Position auf, die auf die Formation einer neuen $[Te_2]^{2-}$-Hantel hindeutet. Es wird vermutet, dass hier ein ähnlicher Mechanismus über interne Redoxreaktionen abläuft wie bei $Ag_{10}Te_4Br_3$ (vgl. Kapitel 1.2.2, Seite 6), mit dem Unterschied, dass er nicht eindimensional entlang der Te-Stränge, sondern zweidimensional im Kagomé-Netz abläuft. Die Mobilität beginnt mit dem Phasenübergang und nimmt linear mit der Temperatur zu. Desweiteren wird beobachtet, dass sich die Abstände bestimmter Ag/Cu-Positionen nach dem Phasenübergang annähern, anstatt mit der thermischen Expansion auseinander zu driften. Das deutet auf d^{10}-d^{10}-Wechselwirkungen hin, wie sie schon in Ag_5Te_2Cl (vgl. Kapitel 1.3.4, Seite 10) beobachtet wurden. Hier verursachen sie einen signifikanten und sehr breiten Abfall der Thermokraft nach dem Phasenübergang, woraus gefolgert wird, dass auch in $Ag_{18}Cu_3Te_{11}Cl_3$ d^{10}-d^{10}-Wechselwirkungen zur pnp-Schaltung beitragen können.

$Ag_{18}Cu_3Te_{11}Cl_3$ weißt eine sehr niedrige Wärmeleitfähigkeit auf, was vorteilhaft ist, weil dadurch ein Temperaturgradient zur Erzeugung einer Diode oder eines Transistors lange aufrecht erhalten werden kann. Die Bandlücke wurde durch PL-Messung bestimmt und liegt mit 1,35 eV nahe des Maximums der Effizienz für single-junction-Solarzellen, welches durch das Schockley-Queisser-Limit definiert ist. Die Anwendung als Thermoelektrikum wird durch die niedrige elektrische Leitfähigkeit begrenzt.

Durch Anlegen eines Temperaturgradienten über den pn-Übergang hinweg konnte durch Strom/Spannungs-Messung an einem Einkristall die erste schaltbare Einkomponenten-Diode beobachtet werden. Da vor und nach dieser Messung ausgeführte isotherme Messungen ohmsches Verhalten zeigen, konnte die Schaltbarkeit und Reversibilität der erzeugten Diode nachgewiesen werden.

Beiträge der Autoren: A.V. synthetisierte die Verbindung, führte die DSC, die EDX, sowie die Pulver- und Einkristall-XRD durch und löste die Kristallstrukturen. A.R. und P.D. führten die Strom/Spannungs-Messungen durch. R.St. designte die PCBs. T.B. und W.Z. führten die LFA durch und bestimmten die Wärmeleitfähigkeit. R.Si. und J.S. führten die Festkörper-NMR durch. A.R. und D.D. führten druckabhängige Pulver-XRD durch und bestimmten den Bulk-Modulus. K.N. und A.H. führten die PL aus. A.V., J.V. und T.N. schrieben das Manuskript. Alle Autoren diskutierten die Ergebnisse und überarbeiteten das Manuskript.

A Switchable One-Compound Diode

Anna Vogel, Alfred Rabenbauer, Philipp Deng, Ruben Steib, Thorben Böger,
Wolfgang G. Zeier, Renée Siegel, Jürgen Senker, Dominik Daisenberger, Katharina Nisi,
Alexander W. Holleitner, Janio Venturini,* and Tom Nilges*

A diode requires the combination of p- and n-type semiconductors or at least the defined formation of such areas within a given compound. This is a prerequisite for any IT application, energy conversion technology, and electronic semiconductor devices. Since the discovery of the pnp-switchable compound $Ag_{10}Te_4Br_3$ in 2009, it is in principle possible to fabricate a diode from a single material without adjusting the semiconduction type by a defined doping level. Often a structural phase transition accompanied by a dynamic change of charge carriers or a charge density wave within certain substructures are responsible for this effect. Unfortunately, the high pnp-switching temperature between 364 and 580 K hinders the application of this phenomenon in convenient devices. This effect is far removed from a suitable operation temperature at ambient conditions. $Ag_{18}Cu_3Te_{11}Cl_3$ is a room temperature pnp-switching material and the first single-material position-independent diode. It shows the highest ever reported Seebeck coefficient drop that takes place within a few Kelvin. Combined with its low thermal conductivity, it offers great application potential within an accessible and applicable temperature window. $Ag_{18}Cu_3Te_{11}Cl_3$ and pnp-switching materials have the potential for applications and processes where diodes, transistors, or any defined charge separation with junction formation are utilized.

1. Introduction

The pn-junction is the most elementary building block of semiconducting devices, being found in diodes, transistors, sensors, and solar cells, to name a few. Currently, two different materials with opposite majority carriers are used to create a pn-junction. Nevertheless, some selected materials have previously been shown to switch between p- and n-conduction due to variations in temperature. In this context, the utilization of a single-material, thermally-controlled pn-junction would allow direct control of the character of these semiconducting devices including the position of the junction or its properties. Today, four different semiconducting materials are known to be capable of changing the mechanism of charge carrier transport between p- and n-type conduction. The first reported compound was $Ag_{10}Te_4Br_3$.[1–3] This material switches reversibly between p-type to n-type conduction at $T_{pnp} = 390$ K during an order-disorder phase transition of the cation substructure, driven by a charge density wave within the telluride substructure. Upon further heating or cooling down below the phase transition temperature the material switches back from n-type to p-type conduction. Later, AgBiSe$_2$ ($T_{pnp} = 580$ K), AgCuS ($T_{pnp} = 364$ K), and Tl$_2$Ag$_{12}$Se$_7$ ($T_{pnp} = 410$ K) were also discovered to show a comparable pnp-switch at elevated temperatures.[4–6] In all reported cases, the interplay of a highly

A. Vogel, A. Rabenbauer, P. Deng, R. Steib, J. Venturini, T. Nilges
School of Natural Sciences (NAT)
Department of Chemistry
Synthesis and Characterization of Innovative Materials group
Technical University of Munich
Lichtenbergstraße 4, 85748 Garching b. München, Germany
E-mail: janio.venturini@tum.de; tom.nilges@tum.de
T. Böger, W. G. Zeier
Institute of Inorganic and Analytical Chemistry
University of Münster
Corrensstraße 28/30, 48149 Münster, Germany

The ORCID identification number(s) for the author(s) of this article can be found under https://doi.org/10.1002/adma.202208698.

T. Böger
International Graduate School for Battery Chemistry, Characterization, Analysis, Recycling and Application (BACCARA)
University of Münster
Corrensstraße 40, 48149 Münster, Germany
R. Siegel, J. Senker
Inorganic Chemistry III
University of Bayreuth
Universitätsstraße 30, 95447 Bayreuth, Germany
D. Daisenberger
Diamond Light Source
Harwell Science and Innovation Campus
Didcot, Oxfordshire OX11 ODE, UK
K. Nisi, A. W. Holleitner
Walter Schottky Institute and Physics Department
TU Munich, Am Coulombwall 4a, 85748 Garching b. München, Germany

dynamic substructure and the rearrangement of complementary structural units causes a modulation of the entire defect configuration and a switch of the semiconducting mechanism. A common building principle of all known pnp-switching materials is that they contain mobile d^{10} ions and a chalcogenide substructure, which interact with each other in a synergistic manner. Following this concept, the utilization of pn-switching materials in applications requires energy-friendly access to the switch close to the application temperature. Here, we report on a silver chalcogenide halide where the pn switch can be operated at room temperature without a huge and complex energy demand.

2. Results and Discussion

2.1. Structure Chemistry of $Ag_{18}Cu_3Te_{11}Cl_3$

Our group has recently prepared a material that shows pnp-switching close to room temperature: $Ag_{18}Cu_3Te_{11}Cl_3$.

The crystal structures of the relevant polymorphs of this compound were determined from single crystals by temperature-dependent X-ray diffraction measurements (XRD). The structures can be described by a simple topological approach where neighboring anions are connected in such a way that different layers are realized: a Te 6^3 honeycomb net, a Cl 6.3.6.3 kagomé net, and a distorted Te 6.3.6.3 kagomé net (see **Figure 1**a). The layers are stacked along one crystallographic axis in the following sequence: Te 6^3 – Cl 6.3.6.3 – Te 6^3 – Te 6.3.6.3. While the Te 6^3 and the Cl 6.3.6.3 nets consist only of isolated Te^{2-} or Cl^- ions, the distorted Te 6.3.6.3 net is composed of $[Te_2]^{2-}$ dumbbells and additional coordinating Te^{2-} ions (see Figure 1b). More details concerning the structure are denoted in Figure S1 (Supporting Information). A similar Te 6.3.6.3 layer can also be found in the mineral stützite ($Ag_{55-x}Te_3$, Figure S2, Supporting Information).[7] Another feature of the anion substructure is the polyanionic Te_4 unit that vertically interpenetrates the Te 6^3 and Cl 6.3.6.3 nets. These units consist of a covalently-bonded $[Te_2]^{2-}$ dumbbell and two linearly
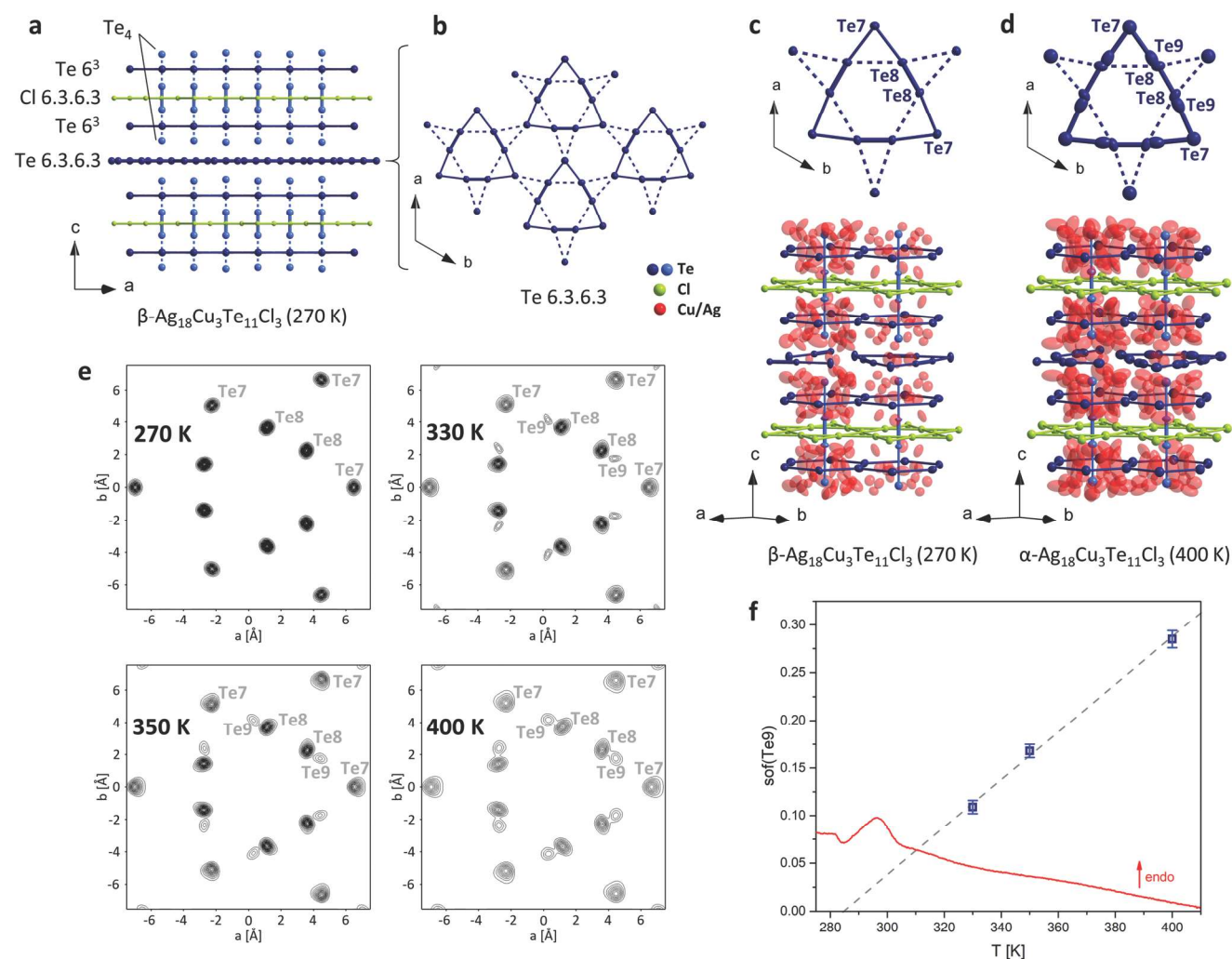
Figure 1. a) Scheme of anion substructure of β-$Ag_{18}Cu_3Te_{11}Cl_3$. b) Distorted Te 6.3.6.3 net. c,d) Structure sections of β- and α-$Ag_{18}Cu_3Te_{11}Cl_3$. Te nets are drawn in dark blue and Te_4 units in light blue for better differentiation. Displacement parameters are drawn at 70% probability. e) Joint probability density function (jpdf) images of sections of the Te 6.3.6.3 net at 270, 330, 350, and 400 K. One contour line represents 0.3 e $Å^{-3}$. f) Site occupancy factors (sof) of Te9 plotted against temperature (blue), linear fit (grey), and DSC (red).

**ADVANCED
SCIENCE NEWS**

www.advancedsciencenews.com

**ADVANCED
MATERIALS**

www.advmat.de

coordinating Te^{2-} ions. The latter are located at distances closer than twice the van der Waals radius of tellurium (d_{vdW}(Te) = 2.06 Å),[8] illustrating a certain attractive bonding interaction. All other anions are well-separated from each other without showing any kind of bonding interaction. Similar Te_4 units can be found in $Ag_{10}Te_4Br_3$, the first ever described pnp-switching material (see Figures S2 and S3, Supporting Information).[1–3] The anion substructure of $Ag_{10}Te_4Br_3$ is closely related to that of $Ag_{18}Cu_3Te_{11}Cl_3$ – stacked Te 6^3 and Br 6.3.6.3 nets with interpenetrating Te_4 units – but the mechanisms of pnp-switching that will be discussed in the following are utterly different. The mobile and highly disordered d^{10} cations in $Ag_{18}Cu_3Te_{11}Cl_3$ are distributed in a liquid-like manner within the Te substructure (see Figure 1c,d) while the Cl 6.3.6.3 net acts as a separator for the mobile d^{10} ions. No silver or copper cations are distributed or located within this layer. All cation positions (red spheres in Figure 1c,d) in $Ag_{18}Cu_3Te_{11}Cl_3$ are mixed (by variable amounts of Cu^+ and Ag^+) and partially occupied. $Ag_{18}Cu_3Te_{11}Cl_3$ exhibits a high 2D ion mobility parallel to the (001) layer. This feature is substantiated by solid-state nuclear magnetic resonance (NMR) spectroscopy (as shown in Figure 4). Structural similarities to the mineral stützite and other coinage metal chalcogenide halides, like previously published $Cu_{20}Te_{11}Cl_3$, $Cu_{9.1}Te_4Cl_3$, and $Ag_{10}Te_4Br_3$, are discussed in the Supporting Information (shown in Figures S1 and S2, Supporting Information).[1–3,7,9,10]

2.2. Polymorphism

$Ag_{18}Cu_3Te_{11}Cl_3$ is a polymorphic compound that shows two reversible order-disorder phase transitions at 216(3) and 288(3) K (onset values from differential scanning calorimetry (DSC), **Figure 2**a). The important phase transition for the pnp-switch is the latter, where β-$Ag_{18}Cu_3Te_{11}Cl_3$ – stable between 216 and 288 K – converts to α-$Ag_{18}Cu_3Te_{11}Cl_3$, the phase present above room temperature. Single crystal structure determinations revealed that the symmetry and therefore also the space group does not change and the cell volume increases continuously without a significant volume discontinuity while undergoing the transition (see **Table 1**). While some physical properties, like the total electrical conductivity, increase continuously without any abrupt change in the temperature window around room temperature, the Seebeck coefficient drops significantly right after the β-α phase transition (Figure 2a). The origin of this intriguing Seebeck modulation effect needs to be identified and discussed. In β-$Ag_{18}Cu_3Te_{11}Cl_3$, a triangular arrangement of Te_2 dumbbells (Te8 sites) and additional coordinating Te neighbors (Te7 sites) create an ordered Te 6.3.6.3 net. Right after the phase transition to α-$Ag_{18}Cu_3Te_{11}Cl_3$ at 288 K, we observe emerging disorder in the Te 6.3.6.3 net (Figure 1d). While the net is fully ordered in the β-polymorph, the occurrence of additional Te sites (Te9) in close vicinity to the Te_2 dumbbells can be identified after the transition. Temperature-dependent joint probability density function (jpdf) plots are given in Figure 1e, where the population of the Te9 site close to the dumbbell sites is represented. The distance between Te9 and Te7 (2.96(4) Å at 330 K) is very similar to the dumbbell distance between two Te8 (2.795(7) Å at 330 K), from which we can

conclude that a new dumbbell is formed at this position. Temperature-dependent single crystal XRD measurements for α-$Ag_{18}Cu_3Te_{11}Cl_3$ at 330(1), 350(1) and 400(1) K illustrate that the occupation of Te9 increases linearly with temperature, while that of Te8 decreases. The linear fit crosses the x-axis right at the onset of the phase transition. Further details concerning the temperature-dependent structure analysis are summarized in the Supporting Information section.

2.3. Physical Properties and Possible Applications

The most striking feature during this transition is the variation of the thermopower or Seebeck coefficient. $Ag_{18}Cu_3Te_{11}Cl_3$ displays a gigantic drop of the Seebeck coefficient of over 3000 µV K^{-1} (at ≈295 K) followed by an increase of the thermopower by 4500 µV K^{-1} (320 to 360 K) within a small temperature window of only 50 K (see Figure 2a). Such huge thermopower modulations within 50 K of more than 4 mV K^{-1} close to ambient temperature have never been observed before. This feature should enable the utilization of $Ag_{18}Cu_3Te_{11}Cl_3$ in sensors and power applications at room temperature. The previously mentioned materials show changes of only 1400 µV K^{-1} in $Ag_{10}Te_4Br_3$, 750 µV K^{-1} in $AgBiSe_2$, 700 µV K^{-1} in $AgCuS$, and 400 µV K^{-1} in $Tl_2Ag_{12}Se_7$ during the pnp-switch.[1,4–6] $Ag_{18}Cu_3Te_{11}Cl_3$ is able to create large voltage drops in a temperature window close to room temperature where manifold applications – e.g. solar cells, catalysts, and sensors – operate. Photoluminescence measurements of $Ag_{18}Cu_3Te_{11}Cl_3$ show two Lorentzian emission lines at 1.35 and 1.5 eV, located in the infrared (Figure 2b). Thermal activation and initiation of the pnp-effect are thus possible by light irradiation. This optical behavior may allow the utilization in solar cells since the band gaps are close to the maximal efficiency for single junction solar cells, as defined by the Shockley–Queisser limit (Figure S7, Supporting Information).[11] The material also shows an extremely low thermal diffusivity, which is beneficial for the application of $Ag_{18}Cu_3Te_{11}Cl_3$ as diodes/transistors due to the maintenance of the thermal gradient and therefore the p- and n- regions (Figure 2c). The thermal diffusivity of $Ag_{18}Cu_3Te_{11}Cl_3$ of 0.08 mm^2 s^{-1} is lower than the values of water (0.135 mm^2 s^{-1}) and polymers like polycarbonate (0.148 mm^2 s^{-1}), polyethylene (0.283 mm^2 s^{-1}), and polystyrene (0.137 mm^2 s^{-1}).[12,13] The thermal conductivity does not change significantly between 260 and 380 K and varies around ≈0.14 W m^{-1} K^{-1} (Figure 2c). This very low and rather temperature-independent thermal conductivity of $Ag_{18}Cu_3Te_{11}Cl_3$ is either caused by its excellent phonon scattering capability due to the intrinsic high cation mobility or by diffuson-mediated thermal transport. The latter mechanism has been recently identified and discussed for silver-ion conducting argyrodites.[14] The calculated thermoelectric figure of merit ZT of 10^{-2} at 320 K is rather low due to the poor electrical conductivity (see Figure 2d). Due to possible applications as thin-layer and bulk material we determined the bulk modulus of this compound via high-pressure XRD experiments. Using a 3rd-order Birch–Murnaghan equation of state fit we derived a bulk modulus of 28.2(11) GPa (Figure 2 e,f, and Figure S4 a,b, Supporting Information).[15] This value is slightly higher than the calculated bulk modulus of

**ADVANCED
SCIENCE NEWS**

www.advancedsciencenews.com

**ADVANCED
MATERIALS**

www.advmat.de
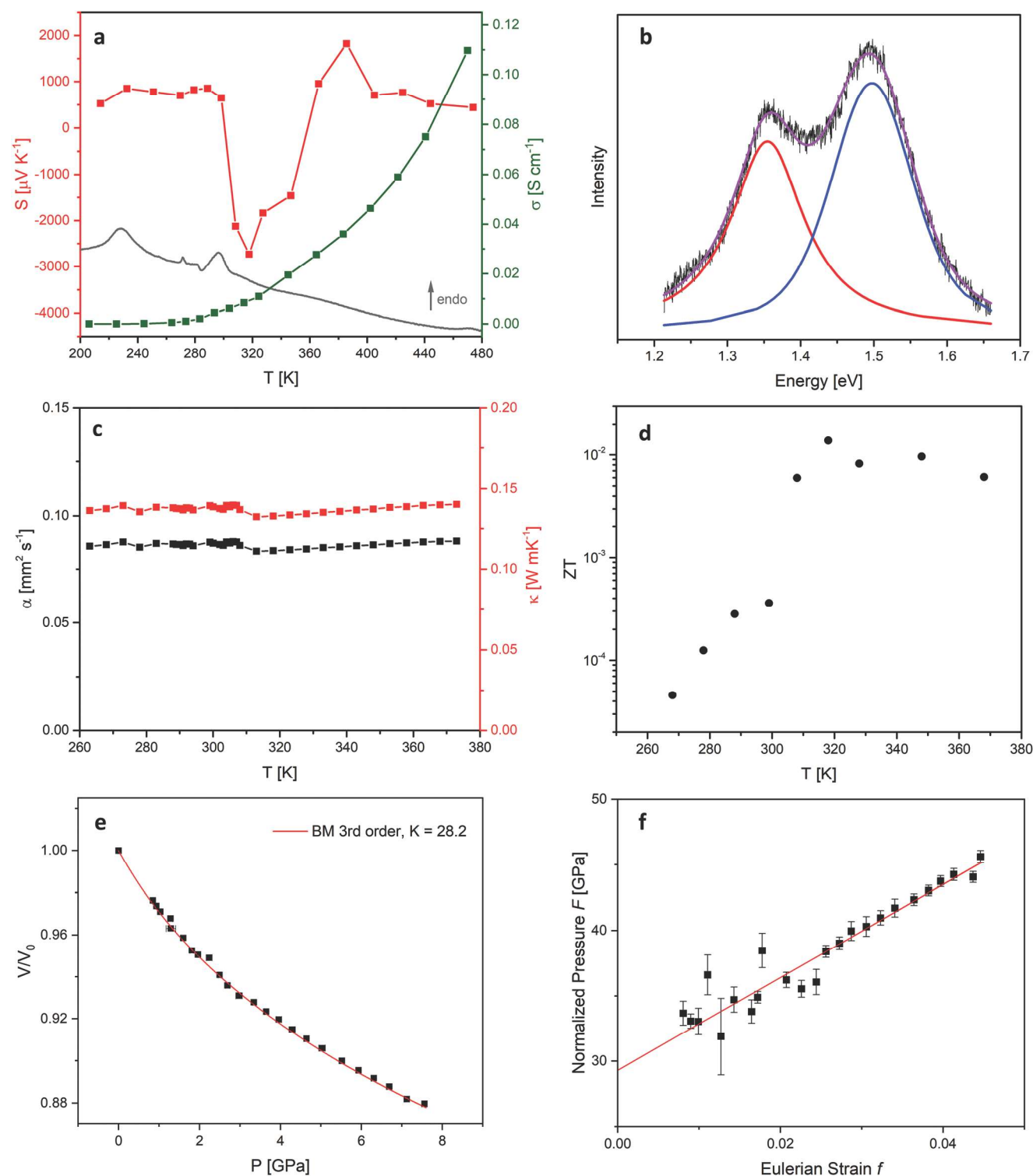
Figure 2. Physical properties of $Ag_{18}Cu_3Te_{11}Cl_3$. a) The Seebeck coefficient (red) varies between 625 µV K^{-1} (298 K) before, and −2731 µV K^{-1} (317 K) and 1824 µV K^{-1} (386 K) directly after the β-α phase transition. DSC (grey) illustrates the reversible endothermic thermal effects at 216(3) and at 288(3) K (onset values, the small effect at 273 K is due to water impurity in liquid nitrogen). The total electrical conductivity (green) varies between 6 mS cm^{-1} (300 K) and 110 mS cm^{-1} (470 K). b) Photoluminescence measurements (black) show Lorentzian emissions at 1.35 (red) and 1.50 eV (blue). c) Thermal conductivities (red) calculated from thermal diffusivity (black) measurements cumulate in very low values of ≈0.14 W m^{-1} K^{-1} around the β-α phase transition. Effective phonon scattering takes place around room temperature. d) Calculated thermoelectric figure of merit *ZT* value of $Ag_{18}Cu_3Te_{11}Cl_3$. The error was estimated to 10%. e) Bulk modulus determination of α-$Ag_{18}Cu_3Te_{11}Cl_3$ from a 3rd-order fit using the Birch–Murnaghan equation of state resulting in K_0 = 28.2(11) GPa and K' = 12.7(8). An *F-f* plot is given in (f).

Table 1. Single crystal XRD data of α- and β-$Ag_{18}Cu_3Te_{11}Cl_3$ at 270, 330, 350, and 400 K.

	β-$Ag_{18}Cu_3Te_{11}Cl_3$	α-$Ag_{18}Cu_3Te_{11}Cl_3$	α-$Ag_{18}Cu_3Te_{11}Cl_3$	α-$Ag_{18}Cu_3Te_{11}Cl_3$
Temperature [K]	270(1)	330(1)	350(1)	400(1)
Refined composition	$Ag_{17.1(3)}Cu_{2.85(6)}Te_{11}Cl_3$	$Ag_{17.2(5)}Cu_{2.87(8)}Te_{11}Cl_3$	$Ag_{17.2(4)}Cu_{2.86(6)}Te_{11}Cl_3$	$Ag_{16.4(5)}Cu_{2.74(9)}Te_{11}Cl_3$
Molar mass [g mol^{-1}]	3537.7	3548.3	3542.4	3455.8
Crystal size [mm]		0.1 × 0.05 × 0.05		0.2 × 0.1 × 0.1
Crystal shape/color		block/black		
Crystal system	hexagonal		hexagonal	
Space group	$P6_3/mcm$		$P6_3/mcm$	
Z	6		6	
a [Å]	13.4709(12)	13.5506(12)	13.5651(12)	13.5775(12)
c [Å]	30.818(2)	30.7723(19)	30.8198(12)	30.822(3)
V [Å^3]	4843.1(7)	4893.4(7)	4911.4(6)	4920.7(8)
ρ_{calc} [g cm^{-3}]	7.2777	7.2246	7.186	6.9971
Diffractometer		STOE Stadivari		
Radiation [Å]		0.71073 (Mo $K_{\alpha1/2}$)		
μ [cm^{-1}]	22.16	21.771	21.656	21.114
F[000]	9061	9089	9074	8847
θ range [°]	3.04 – 30.13	3.01 – 29.99	3 – 30	3 – 29.99
hkl range	−18/ +9, 0/ +9, 0/ +43	−19/ +9, 0/ +19, 0/ +38	−19/ +9, 0/ +19, −43/ +43	−18/ +19, −18/ +19, −43/ +41
No. of reflections	8811	8099	17785	67811
R_{int}	0.0431	0.0613	0.0938	0.1913
Data/parameters	2053 / 275	1736 / 285	2154 / 301	2330 / 308
R / wR [I > 3σ (I)]	0.0375 / 0.0637	0.0370 / 0.0598	0.0378 / 0.0625	0.0370 / 0.0726
R / wR [all]	0.0887 / 0.0794	0.1169 / 0.1169	0.1117 / 0.0839	0.1476 / 0.1238
Goodness of fit	1.23	0.98	1.13	1.12
Res. elec. dens. max / min [e Å^{-3}]	−1.84 / +1.56	−1.47 / +1.26	−1.62 / +0.88	−1.53 / +1.30

Cu_2Te K_0 = 22.9 GPa.[16] We observed no further phase transitions; at room temperature α-$Ag_{18}Cu_3Te_{11}Cl_3$ maintains the same structure up to ≈8 GPa.

2.4. Mechanism of the pnp-Switch

An important point to elucidate is the mechanism of the pnp-transition in $Ag_{18}Cu_3Te_{11}Cl_3$. The Seebeck coefficient is defined by the Mott equation:[17,18]

$$S = -\frac{\pi^2}{3}\frac{k_B^2 T}{e}\left[\frac{1}{n}\frac{dn(E)}{dE} + \frac{1}{\mu}\frac{d\mu(E)}{dE}\right]_{E=E_F} \quad (1)$$

where S, k_B, e, n, and μ are the Seebeck coefficient, Boltzmann constant, electron charge, charge carrier concentration, and carrier mobility, respectively. This equation may be understood as the partial derivative of the density of states (DOS) analyzed at the Fermi energy. As such, changes in the magnitude and signal of the Seebeck coefficient represent variation in the local state of the DOS at E_F. Two effects in $Ag_{18}Cu_3Te_{11}Cl_3$ are responsible for such modulation of the DOS and the resulting pn-switch that occurs right after the β-α phase transition.

One is localized in the heaviest atom (Te) substructure, and the other in the d^{10} cation substructure. The effect in the Te substructure can be regarded as a local 2D charge density wave (CDW) within the 6.3.6.3 Te kagomé net. The disorder phenomenon and the occupancy of additional Te sites within the kagomé net lead to significant atomic rearrangements and charge fluctuations. In **Figure 3**a, the proposed mechanism of the atomic rearrangement in the Te 6.3.6.3 net is illustrated. A partial local rearrangement of Te_2 dumbbells causes the observed variation in occupancy of Te8 and Te9 sites in the kagomé net. The Te_2 dumbbell – which is fully localized in β-$Ag_{18}Cu_3Te_{11}Cl_3$ – is shifted toward the corners of the Te triangle (see Figure 3a) within the kagomé net. This dynamic rearrangement is only possible through internal redox processes with charge fluctuation. Electron delocalization and transport are thus enabled via this dynamic process within the Te substructure in α-$Ag_{18}Cu_3Te_{11}Cl_3$. The temporary excess of free electrons leads to an upward shift of the Fermi level. As even small amounts of free electrons have a considerable impact on the electron-hole balance in semiconductors, the temporary availability of electrons leads to pn-switching during the phase transition. The observed broad Seebeck modulation and drop – in comparison to the other known pnp-compounds – might be explained by the continuous temperature-driven

**ADVANCED
SCIENCE NEWS**
www.advancedsciencenews.com

**ADVANCED
MATERIALS**
www.advmat.de
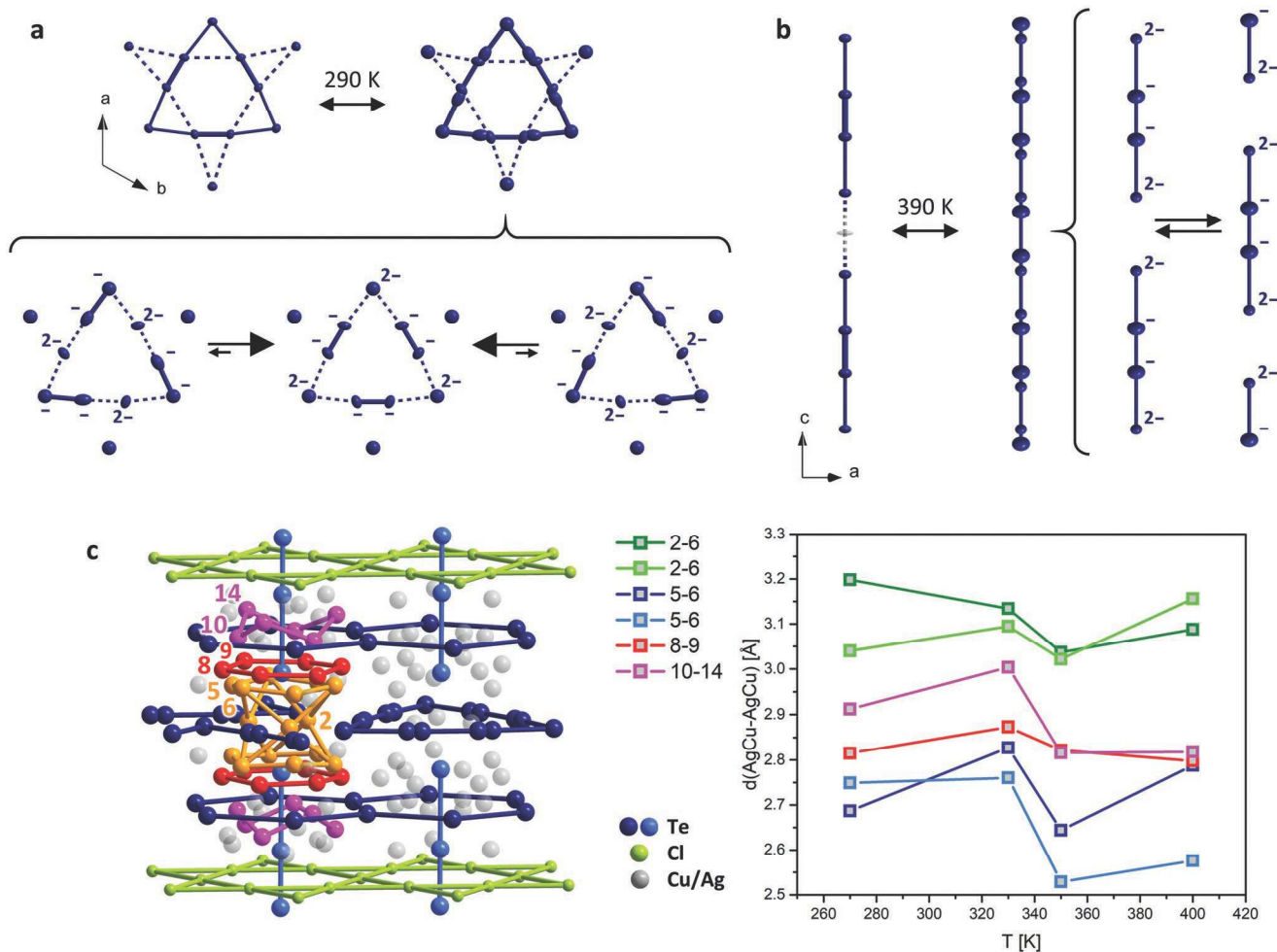
Figure 3. Mechanism of pnp-switching. a) Structure sections of Te 6.3.6.3 in β- and α-Ag$_{18}$Cu$_3$Te$_{11}$Cl$_3$. Proposed mechanism of dumbbell rearrangement in α-Ag$_{18}$Cu$_3$Te$_{11}$Cl$_3$. b) Structure sections of the isolated Te$_4$ strands and the equidistant Te chain that is formed during the β- to α-Ag$_{10}$Te$_4$Br$_3$ phase transition. c) Mixed occupied Ag/Cu sites in Ag$_{18}$Cu$_3$Te$_{11}$Cl$_3$. d^{10}-d^{10} interactions in the coinage metal substructure shorten the coinage metal distances. After the β-α phase transition, the d^{10} ions interact with each other and show reduced bond distances upon heating. Four different cation site couples are selected to illustrate this phenomenon, and their bond lengths are given as a function of temperature. Ag/Cu bond distances are defined by the maxima of electron density derived from the so-called mode positions, which were identified after the integration of the probability density functions of non-harmonically refined displacements for each ion.

occupation of the Te9 site that is necessary to induce the pn-transition.[1,4–6] A comparable mechanism of atomic rearrangements in the Te substructure can be found in pnp-switching Ag$_{10}$Te$_4$Br$_3$. In this case, the rearrangement of strands of Te$_4$ units leads to a 1D CDW. The reorganization from a strand of oligomeric Te$_4$ units to a dynamically disordered equidistant Te-chain (shown in Figure 3b) occurs in a similar manner via internal redox processes. This phenomenon in Ag$_{10}$Te$_4$Br$_3$ also allows the delocalization of electrons along the equidistant Te chain and the temporary generation of extra conduction electrons in higher band states, resulting in an upward shift of the Fermi level, and consequently causing the observed pn-switching after the phase transition temperature of 390 K. In the Ag$_{10}$Te$_4$Br$_3$ high-temperature α-polymorph, the mobility within the Te-strands becomes too high to enable constructive delocalization of electrons and therefore the system switches back to p-type conduction.[1]

In Ag$_{18}$Cu$_3$Te$_{11}$Cl$_3$ a partial 2D CDW occurs. According to our single crystal structure determination data, we see a temperature-dependent population of an additional Te site (Te9) at the onset of the β-α phase transition (Figure 1e). The population increases linearly with temperature up to 28.5% at 400 K, which is a clear indicator of a dynamic process instead of a static disorder.

To further investigate this phenomenon, ^{125}Te solid-state MAS NMR experiments were acquired at various temperatures (**Figure 4**a). As reported previously, the isolated Te^{2-} ions are located in the chemical shift range between 1600 and 1900 ppm (referenced to (CH$_3$)$_2$Te), while resonances for the polytelluride [Te$_n$]$^{m-}$ units in the kagomé net occur at chemical shifts ranging from 600 to 900 ppm.[1,19] These atoms are also characterized by a much larger chemical shift anisotropy ($\approx$800 ppm vs 300 ppm for the isolated species) due to the anisotropic environment originated by the Te—Te bond. The resonances between

**ADVANCED
SCIENCE NEWS**

www.advancedsciencenews.com

**ADVANCED
MATERIALS**

www.advmat.de
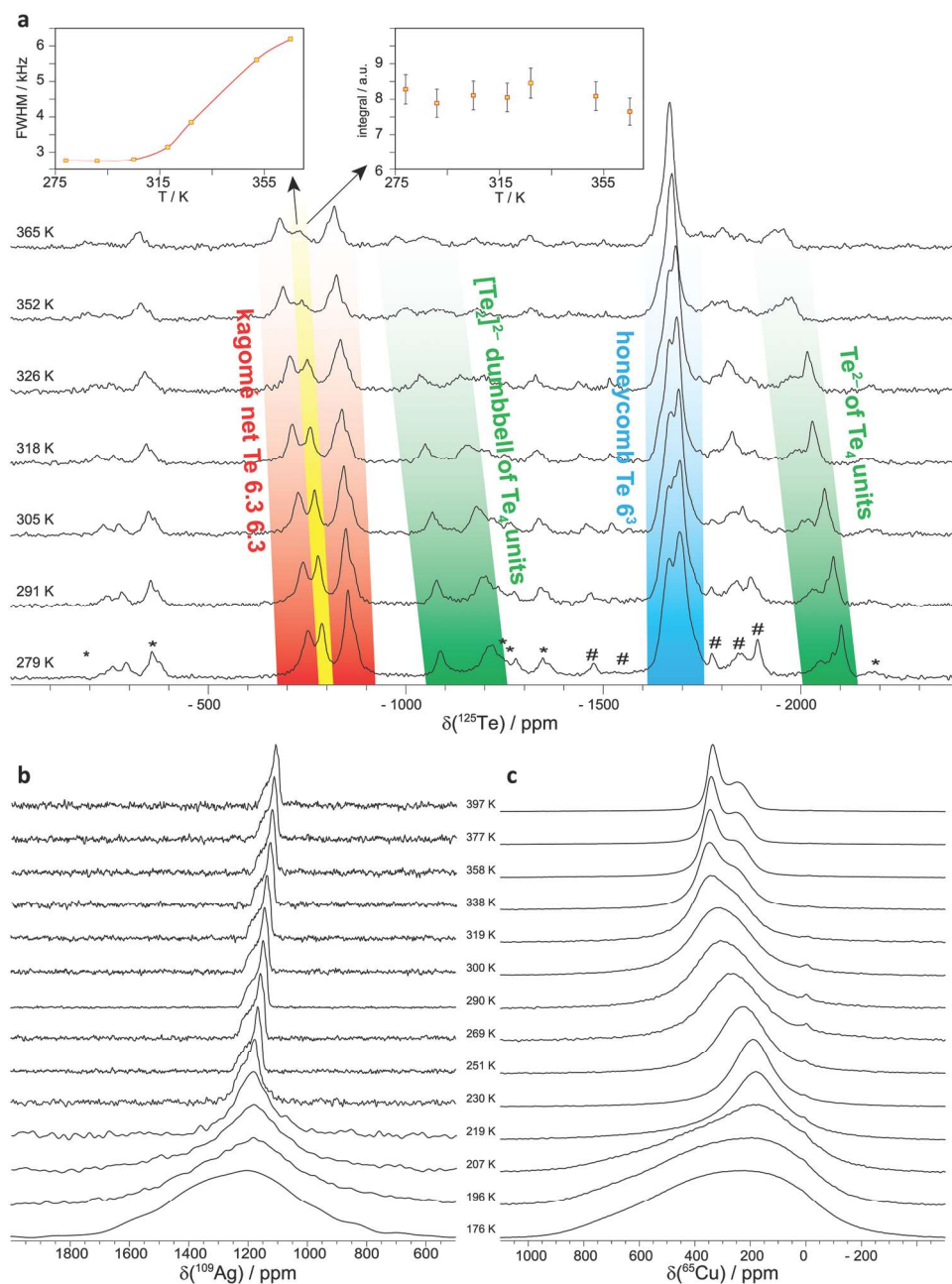
Figure 4. Solid-state NMR spectra of $Ag_{18}Cu_3Te_{11}Cl_3$ at different temperatures. a) ^{125}Te MAS spectra with color-coded assignment of the characteristic Te subunits. The resonance where coalescence occurs is marked in yellow. The corresponding typical trends for the full width at half maximum (FWHM) and integral for this resonance are given in the insets. The asterisks marks spinning sidebands and the hashtags the impurities. b) ^{109}Ag and c) ^{65}Cu static spectra.

1000 and 1200 ppm as well as the ones between 1900 and 2100 ppm could be assigned to the atoms in Te_4 units, the former corresponding to the $[Te_2]^{2-}$ dumbbells and the latter to the Te^{2-} of the Te_4 units. Except for the isolated Te^{2-} within the honeycomb layer (1600 to 1800 ppm), all the other ^{125}Te resonances shift downfield significantly with increasing temperature (Figure 4a; Figure S5a, Supporting Information). Within the group of resonances assigned to the kagomé net (700 to 900 ppm), the Te atoms drifting the most are the ones at 750 and 790 ppm. In addition, the amplitude of the change

with temperature for the resonance at 790 ppm is particularly striking. While constant below 315 K, its full width at half maximum (FWHM), almost doubles while retaining the overall integral up to 365 K. This behavior is characteristic of the onset of a coalescence phenomenon under MAS conditions.[20] For a ^{125}Te enriched sample, we observed that the magnitude of the chemical shift anisotropy (CSA) for the same resonance (see Figure S5b, Supporting Information) decreases within the same temperature range, supporting the hypothesis of coalescence. This phenomenon substantiates the onset of dynamic

ADVANCED
SCIENCE NEWS
www.advancedsciencenews.com

ADVANCED
MATERIALS
www.advmat.de

disorder of the Te atoms within the kagomé net with correlation times on the order of tens of kHz. The disorder corresponds to a chemical exchange between isolated Te^{2-} atoms and $[Te_2]^{2-}$ dumbbells as suggested by the diffraction data (Figure 1e). As the onset temperature for the dynamic exchange coincides with the initiation of the pnp-switch, both effects are likely linked.

Temperature-dependent XRD and ^{109}Ag and ^{65}Cu solid-state NMR data suggest that the pnp-switch is also connected to changes in the dynamic disorder of the d^{10} ion substructure. The first phase transition observed at 216(3) K is accompanied by a pronounced narrowing of the ^{109}Ag and ^{65}Cu resonances (Figure 4b,c). Thus, above 220 K, both cations exhibit fast motion. The remaining narrow shape for the ^{109}Ag NMR spectra, typical for an almost axially symmetric chemical shift anisotropy, is in line with a restriction of the ion mobility in two dimensions parallel to the (001) layer.[21] Diffraction data suggest that silver and copper are mixed within these layers. Nevertheless, the presence of two resonances at 1160 and 1164 ppm in the ^{109}Ag MAS NMR spectrum, at chemical shifts comparable to similar compounds, suggests two slightly different environments in the cation layers.[1]

In contrast to the lineshape of the ^{109}Ag NMR spectra, which is temperature-independent above 270 K, the lineshape of the ^{65}Cu NMR signal in the temperature range of the pnp-switch is temperature-dependent and even develops an anisotropic shape (quadrupolar and chemical shift interaction) toward higher temperatures. This effect is most likely caused by the attraction of the silver and copper ions right after the β-α phase transition, as also indicated by the drop in bond lengths between the d^{10} ions observed in temperature-dependent single crystal structure determinations at 270, 330, 350, and 400 K (Figure 3c). Usually, bond lengths tend to extend upon temperature increase; instead, we see a significant decrease upon heating. This effect may tune the Seebeck coefficient as already shown for Ag_5Te_2Cl, a system in which d^{10}-d^{10} interactions were identified as the only source for thermopower modulations.[22] The occurrence of lineshape changes only in the ^{65}Cu resonance suggests a drastic additional change in the Cu mobility around the room temperature β-α phase transition and the consequently stronger d^{10}-d^{10} interactions in the copper sub-ensemble. As discussed earlier on, this feature should also contribute to the modulation of the DOS close to the Fermi level. The sum of both discussed aspects causes the enormous Seebeck coefficient drop, with an unprecedented intensity of 4,500 mV K^{-1}.

2.5. The Position-Independent, Switchable One-Component Diode

The most intriguing property of $Ag_{18}Cu_3Te_{11}Cl_3$ is the pnp-switch at room temperature. It may allow the generation of diodes and transistors by a simple change of temperature. In order to verify the diode behavior of $Ag_{18}Cu_3Te_{11}Cl_3$, we investigated the system at two different temperature conditions and setups. A crystal was mounted onto gold pads with metallic indium so that both ends of the sample are contacted (see **Figure 5**a,b). The first setup was chosen so that the system operates in the β-$Ag_{18}Cu_3Te_{11}Cl_3$ phase, slightly below

room temperature. The second setup includes a temperature gradient to bring the system into the pn-transition regime, already in the α-$Ag_{18}Cu_3Te_{11}Cl_3$ phase. Here we used a 295 to 308 K gradient where the hot side is supposedly n- and the cold side p-conducting.

At 283 K we find a linear U/I curve upon polarization between ±1.5 V (Figure 5c). The absence of a Schottky diode behavior indicates that the indium contact is ohmic. After unilaterally increasing the temperature, we were able to apply a temperature gradient of 308 to 295 K to the crystal. Now, the U/I curve is significantly different. The hot side should transition to the electron-conducting n-phase while, at the opposite end, holes remain as majority carriers, effectively creating a pn-junction across the semiconductor. Indeed, a rectifying behavior can be seen in the U/I curves measured under a temperature gradient, with a forward current over 10 times larger than the reverse current at ±1.0 V, as can be seen in Figure 5c. A junction potential of 0.3 V is determined for the transitory diode. Upon cooling back to 283 K, the system transitions to its starting configuration (the β-phase), and measurements yield the same linear U/I curve as before the application of the gradient. This reversibility clearly rules out the formation of additional semiconducting phases between the indium solder and $Ag_{18}Cu_3Te_{11}Cl_3$ during our measurements upon polarization or temperature treatment. To further substantiate this assumption, we used a different solder material to contact $Ag_{18}Cu_3Te_{11}Cl_3$. Using lead/tin solder we find the same behavior and diode formation as in the case of the indium solder (Figure S6a, Supporting Information).

If U/I measurements are performed isothermally (without an applied, defined temperature gradient) the material behaves ohmically even in the pn-transition range. This observation rules out the formation of a Schottky diode at higher temperatures (299 to 331 K, see Figure 5e). Furthermore, the curves also indicate the absence of effects caused by polarization and mass transport due to the mobile Ag and Cu ions.

These findings substantiate the creation of a thermally-induced single-material pn-junction. Before we step into the discussion, the type of junction that is formed here needs to be addressed and defined. A heterojunction is generated by contacting two dissimilar materials where one is a p- and the other an n-type semiconductor, as is the case of GaAs/GaAlAs lasers. On the other hand, a homojunction is generated by different doping characters in a given material without affecting its structure, such as an n-Si/p-Si junction. As shown earlier, the defect structure of the studied compound varies during the pn-switch but the symmetry and general structural units remain virtually unchanged. Therefore, according to symmetry considerations, the interface between the two phases could be defined as a homojunction. However, regarding the defined property change, the thermal signature in DSC, and the significant changes in defect and electronic structure, the term heterojunction may also partially explain the electronic situation. Neither of the current terms correctly encompasses the real structure of this novel system. Thus, we define a new type of junction, an ambijunction, to illustrate the ambivalent character in this new material.

The switching time of this single crystal diode (forward–reverse direction) has been assessed via the application of

**ADVANCED
SCIENCE NEWS**

www.advancedsciencenews.com

**ADVANCED
MATERIALS**

www.advmat.de
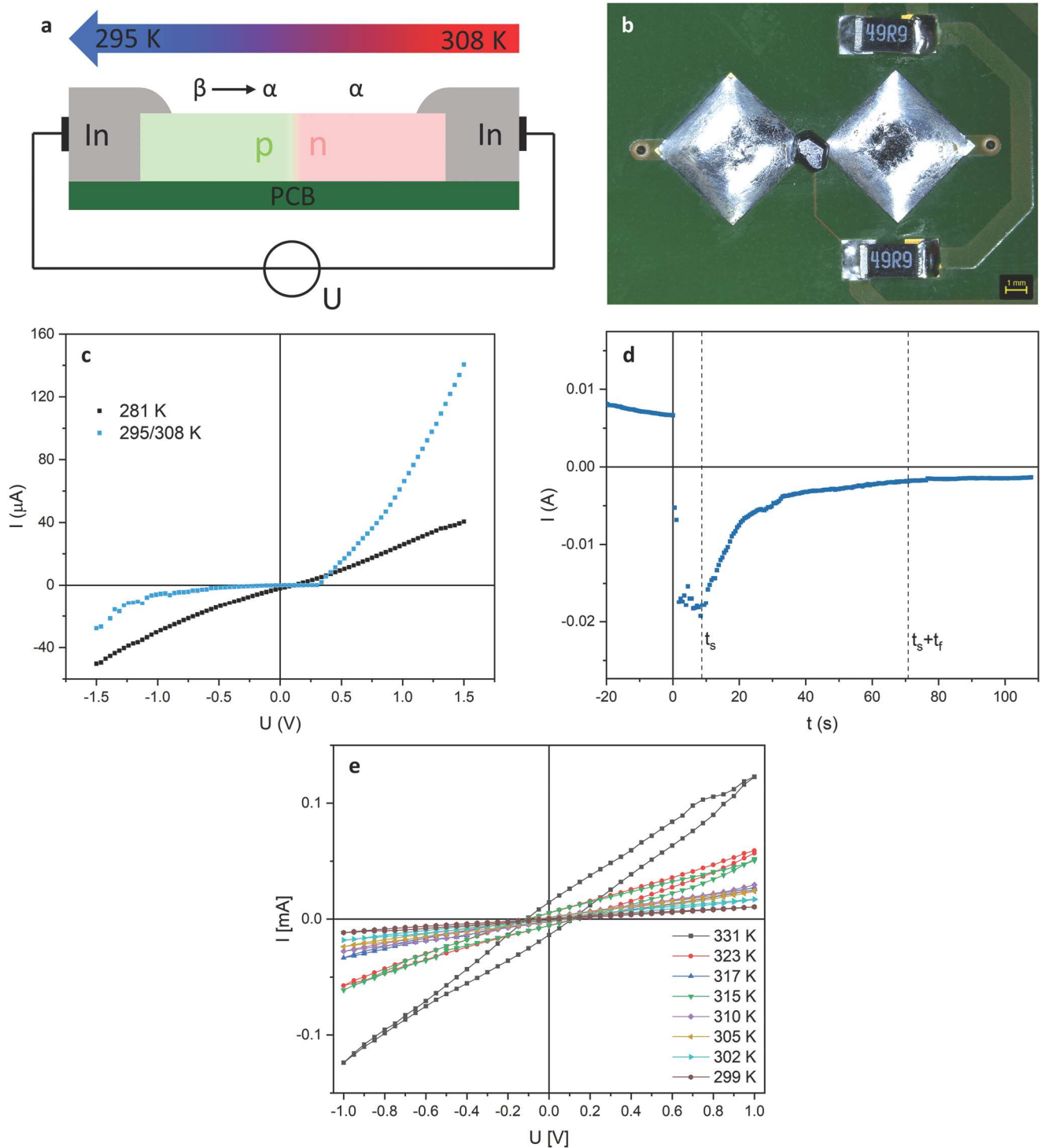
Figure 5. Diode fabrication and *U/I* characterization. a) Scheme of the measurement set-up. b) Single crystal of $Ag_{18}Cu_3Te_{11}Cl_3$ mounted on top of Au electrodes and contacted with metallic In. The 49 Ω resistances used to apply a temperature gradient via resistivity heating can be found next to the right contact. c) *U/I* plot measured at 281 K within β-$Ag_{18}Cu_3Te_{11}Cl_3$ (black line) and after applying temperature to the system to create a gradient of 13 K between 295(1) and 308(1) K (blue line). d) Switching time of the diode under the same thermal gradient. A 5 V forward was applied, followed by a −5 V reverse current at $t = 0$. The errors of the measured values are located within the points. e) To ensure that no Schottky diode is being formed in the applied temperature ranges, we also measured isothermal *U/I* curves for $Ag_{18}Cu_3Te_{11}Cl_3$ up to 331 K. When the entire crystal was held at the same temperature, no rectifying character was found. A conductivity increase was seen at higher temperatures as is expected for a semiconductor. The errors of the measured values are located within the points.

**ADVANCED
SCIENCE NEWS**

www.advancedsciencenews.com

**ADVANCED
MATERIALS**

www.advmat.de

a 5 V forward potential for 60 s to induce the build-up of the minority carrier at the quasi-neutral regions surrounding the junction (Figure 5d). Subsequently, the device was turned off via the application of a reverse −5 V potential. The linear removal of the excess minority carrier leads to a steady current that is much larger than the saturation current of the device. The switching time t_s for the removal of the excess carriers in this system was ≈8.7 s. After this time, the current decays exponentially toward the saturation limit of the device. The fall time t_f – needed to reach 10% of the initial reverse current – was estimated at 62.4 s.

The initiation of this diode effect is determined in our experimental setup as a sum of the time constants of the several different thermal transport phenomena taking place. Heat must be transferred from the resistance via the metallic contact to the sample. This non-optimized process takes a while, generally a few minutes. This aspect of the measurement setup will be optimized in the future. The full inversion of the p- and n-regions in the given experiment can be realized in minutes in this experimental setup for a mm-sized crystal. This secondary switching process (change of direction besides on–off states) may also be optimized by downscaling of the crystals.

The observed switching is a further indication that the thermal gradient successfully induces the creation of a pn-junction, as this is the only likely source for the shape of the current decay displayed by the device. Furthermore, the long times associated with t_s and t_f again rule out the creation of a Schottky diode instead of a true pn-junction, as the operation in the first is associated with majority carriers, which display higher mobilities, leading to very fast switching. These measurements unambiguously illustrate the creation of the first-ever single-material functional pn-junction, without the need for nanostructuring or advanced architectures, as the diode behavior is an intrinsic property of the bulk material itself. In the future, we intend to downscale the device and material size from the mm to the μ meter regime. This will speed up temperature dissipation and operating speed drastically.

The question arises if the pn-junction formation is unique for $Ag_{18}Cu_3Te_{11}Cl_3$. We selected another pnp-switching material, AgCuS, with a higher switching temperature of 364 K to verify if a diode can also be formed for this material. This is indeed the case: in a temperature gradient of 333(1) to 365(1) K, this material also forms a diode at room temperature while its behavior is ohmic. The measurement can be found in Figure S6b (Supporting Information).

2.6. Impact on Electronics and Energy-Related Science

With the simple and defined creation of a working pn-junction and the consequent diode formation, the process in general, and the compound, in particular, have huge application potential in energy-related science. A single-junction solar cell might be realizable, wherein the pn-junction is generated in a certain temperature gradient directly on the device. Such pn-ambijunction formation and the intrinsic charge separation might be a source for effective water splitting purposes, either stand-alone or as a tandem photoelectrochemical (PEC)-thermoelectrical (TE) device.[23] One step further from the position-independent

or position-variable diode is the generation of a position-independent bipolar junction transistor (BJT) with a larger gradient also encompassing the other p-conducting temperature region of $Ag_{18}Cu_3Te_{11}Cl_3$. Similarly, a field effect transistor (FET) may be constructed with the application of heat at the source and drain regions, with the channel below the transition temperature. With the appropriate design, a single device could work as a resistance, a diode, or a transistor, depending on the temperature gradient and the position of the connections. A variation of the FET could also be realized where the role of the regular gate is substituted by a thermal gate. The inversion layer at the interface between the channel and gate would be created and controlled by temperature instead of local polarization. Such thermal effect transistor (TET) could also be exploited in the recycling of thermal waste generated in the normal operation of FETs, leading to the creation of even more processing units. Due to the possibility of generating a diode or transistor at the place where it is occasionally needed, a new IT architecture might be possible, not demanding the preparation of different p- and n-doped regions to form rectifying devices, or a preadjustment of the architecture to manipulate the charge carrier density by gate biasing.[24–26] Recently AgI was used to program WSe_2 devices that can be reversibly transformed into transistors with switchable carrier types. Homojunctions with switchable polarities were generated using superionic silver iodide as a medium to polarize WSe_2 by van der Waals or dispersive interactions via an ion gradient in AgI. Unfortunately, such a device requires the deposition and alignment of several materials and a high-temperature treatment of 147 °C to reverse the polarization by initiating silver ion conductivity in AgI.[27] Instead, in the case of $Ag_{18}Cu_3Te_{11}Cl_3$, only one material needs to be deposited, and external stimuli that are able to increase the temperature by a few Kelvin may be used to address the necessary junction formation. This junction may either be kept present in a stable temperature gradient or canceled by its removal. The observed effect is also intrinsic to the bulk material, without the need for nanostructuring or complex architectures. The temperature range in which the effect occurs is also very convenient. For comparison, Wu, Wang, and collaborators recently reported superconducting heterostructures, so-called field-free Josephson diodes, with rectifying character.[28] Although impressive, the diode behavior is only observed close to 0 K, hindering the viability of these devices in most practical applications. In our system, the application temperature at ambient conditions is more beneficial and useful.

Another huge field for semiconductors and the utilization of opposite charge carriers is electrocatalysis. Using the described diode formation effect in electrocatalytic reactions can open a wide field of applications. Recently, it has been shown that ultra-thin semiconductors can be used as effective electrocatalysts, although they suffer from low intrinsic carrier concentrations.[29]

3. Conclusion

In this work, the polymorphic compound $Ag_{18}Cu_3Te_{11}Cl_3$, a newly discovered addition to the class of coinage metal chalcogenide halides, was successfully synthesized. The β-α phase

transition takes place close to room temperature, and at the same time enables reversible switching from an n- to p-type semiconductor and back. For the first time, this allows the fabrication of a commercially viable, easily accessible single-material diode. In our case, we are able to generate opposite charge carriers and n- or p-type semiconductor regions in bulk materials by a simple temperature gradient and at positions where opposite charge carriers are needed. With an appropriate setup, electrocatalysis can be initiated where a suitable temperature gradient is provided on one side and the reaction takes place on the opposite side of a thin-layer device. Future optimization in temperature control should enable the realization of a single-material transistor, potentially leading to novel applications and devices. The newly described phenomenon of the temperature gradient-induced, position-independent, and switchable pn-junction should lead to the observation of emergent anomalous effects. Thus, the nascent field of single-material electronic devices begins.

4. Experimental Section

Synthesis: $Ag_{18}Cu_3Te_{11}Cl_3$ was prepared from a stoichiometric mixture of silver (Chempur, 99.999%), copper(I) chloride (Alfa Aesar, 97%), and tellurium (Chempur, 99.999%) on a gram scale. The starting materials were sealed into evacuated silica glass ampules, heated to 1320(1) K, held at this temperature for 3 h, and quenched in an ice bath. The crude product was finely ground and annealed for 7 days at 660(1) K followed by slow cooling to room temperature. This synthesis route led to phase pure black crystalline products.

XRD Experiments: Powder XRD data were collected with a Stoe STADI P powder diffractometer equipped with a position-sensitive Mythen 1K detector using Cu $K_{\alpha1}$ radiation (λ = 1.54060 Å, curved Ge(111) monochromator). Data analysis was performed using the STOE WinXpow software package.[30] Single crystal XRD measurements were performed at 200(1), 270(1), 330(1), 350(1), and 400(1) K on a Stoe STADIVARI diffractometer fitted with Mo $K_{\alpha1/2}$ radiation (λ = 0.71073 Å), a Dectris hybrid pixel detector and an Oxford Cryostream plus system. Data reduction was performed using the Stoe X-AREA package.[31] Structures were solved using the charge-flipping algorithm implemented in the Jana 2006 program suite.[32,33] Numerical absorption correction was performed based on an optimized crystal shape derived from symmetry-equivalent reflections. Space groups were determined by careful analysis of Laue symmetry and extinction conditions. While the structure of γ-$Ag_{18}Cu_3Te_{11}Cl_3$ (200 K) was still not solved due to severe twinning, the data for β-$Ag_{18}Cu_3Te_{11}Cl_3$ (270 K) and α-$Ag_{18}Cu_3Te_{11}Cl_3$ (at 330 K, 350 K, and 400 K) were deposited with the Cambridge Structure Database (https://www.ccdc.cam.ac.uk/structures/): CSD 2201919 (270 K); CSD 2201916 (330 K); CSD 2201917 (350 K); CSD 2201918 (400 K)

Thermal Analysis: Phase pure crystalline material was transferred to an aluminum crucible and differential scanning calorimetry (DSC) was performed with a Netzsch DSC 200 F3 Maia device. The measurement was conducted under N_2 atmosphere in the temperature range of 143 to 523 K with a heating–cooling rate of 10 K min^{-1}. The thermal effects were derived from the onset temperatures. Data analysis was performed using the Netzsch Proteus Thermal Analysis software package.[34]

Measurements of Electrical Conductivity and Seebeck Coefficient: Finely ground phase pure $Ag_{18}Cu_3Te_{11}Cl_3$ was pressed under vacuum to a pellet of 13 mm diameter and 1.23 mm thickness reaching 90% of the crystallographic density. The Seebeck coefficient and the electric conductivity were measured simultaneously directly at Netzsch with a Netzsch SBA 458 Nemesis under a continuous helium flow. The electrical conductivity was determined using the four-point probe.

The technical measurement error was ±7% for the Seebeck coefficient and ±5% for the electrical conductivity. Data analysis was performed with the Netzsch SBA-measurement software package.[35]

Thermal Diffusivity Measurements: Thermal diffusivity was measured by laser flash analysis (LFA) on an LFA 467 HyperFlash setup (Selb, Germany) in an atmosphere of pure nitrogen. The ignition voltage of the flash lamp was set to 250 V and the pulse width was 600 μs. The hot-pressed pellet with a diameter of 10 mm and a thickness of 2.0 mm was spray-coated with a graphite layer to enhance emissivity. An improved version of the model proposed by Cape and Lehman was employed to calculate the thermal diffusivity.[36,37] Data analysis was performed using the Netzsch Proteus Thermal Analysis software package.[38] Thermal conductivity was obtained from thermal diffusivity measurements using the following equation:

$$\kappa = \alpha \times \rho \times c_p \tag{2}$$

with α = thermal diffusivity of the material, ρ = density of the material, c_p = specific heat capacity, and κ = thermal conductivity. The Dulong–Petit rule was applied to approximate the specific molar heat capacity of the material in the given temperature range of 260 to 380 K.

Photoluminescence Spectroscopy: Photoluminescence spectra were recorded at room temperature using a WITec alpha300R equipped with an Olympus LMPlanFL N 50 × / 0.5 objective. The pressed pellet was irradiated with a 532 nm laser with 0.15 mW and a 300 g mm^{-1} grating. Each measurement was integrated for 30 s with 3 accumulations.

Solid-State NMR: In order to reduce measuring time for solid-state ^{125}Te NMR spectroscopy, $Ag_{18}Cu_3Te_{11}Cl_3$ using enriched ^{125}Te (STB Isotope Germany, ^{125}Te content 94%) was prepared. The crude ^{125}Te powder was purified in a hydrogen stream at 673 K to remove traces of tellurium oxide. The same synthesis protocol reported earlier on was followed, taking the different molecular weights of the enriched ^{125}Te into account.

^{125}Te MAS NMR experiments were carried out on a Bruker 400 Avance III HD spectrometer (B_0 = 9.4 T) working at a ^{125}Te frequency of 126.1 MHz. The samples were confined in the middle third of the rotor to minimize temperature gradients and were spun at 62.5 kHz using a Bruker double resonance 1.3 mm MAS probe. The single-pulse MAS spectra were obtained after a 90° pulse of 0.95 μs with recycling delays of 0.5 – 4.0 s. ^{125}Te was referenced to $(CH_3)_2$Te, using $Te(OH)_6$ as a secondary reference. The chemical shift anisotropies were extracted from the profiles of the MAS spectra using TopSpin 3.6.3. ^{109}Ag and ^{65}Cu were acquired on a Bruker 600 Avance III HD spectrometer (B_0 = 14.1 T) working at 28.0 and 170.5 MHz for ^{109}Ag and ^{65}Cu, respectively. For ^{109}Ag and ^{65}Cu MAS experiments, the samples were spun at 40.0 and 62.5 kHz, using a Bruker 1.3 mm double resonance probe. ^{109}Ag single-pulse experiment was acquired after a 90° pulse of 5.5 μs and a recycle delay of 2.0 s. ^{65}Cu MAS spectra were obtained using a rotor-synchronized spin-echo experiment with a 90° pulse of 1.2 μs and a recycle delay of 10 ms. ^{109}Ag and ^{65}Cu static experiments were acquired with a triple-resonance wideline probe using a spin echo experiment with 90° pulses of 7.5 and 2.1 μs, respectively, and echo delays of 40 and 10 μs, respectively. Recycle delays ranged from 5 to 300 s for ^{109}Ag and from 5 to 20 ms for ^{65}Cu. ^{109}Ag was referenced to $AgNO_3$ solution and ^{65}Cu to powdered CuCl. All temperatures were calibrated using $Pb(NO_3)_2$.

Diode Measurements: A single crystal was mounted onto a printed circuit board (PCB) with the aid of indium (Alfa Aesar, 99.999%) or tin/lead (Stannol, composition Sn:Pb:Cu = 60:39:1 wt.%) contacts (Figure 5a,b). To apply a temperature gradient to the crystal, two 49 Ω resistances were placed next to one of the In contacts to create localized heating on one side of the mounted crystal and thus induce a temperature gradient across the device.

β-$Ag_{18}Cu_3Te_{11}Cl_3$: Measurements were conducted inside a refrigerator set to 281(1) K, to start the experiment safely within the β-$Ag_{18}Cu_3Te_{11}Cl_3$ phase. This temperature was chosen to be also in a certain thermal distance to the β-α phase transition. A temperature gradient of 295 to 308 K was applied to the sample by using an external current passing through the 49 Ω resistances. The external current was supplied by a QJE PS6005 switching power supply.

AgCuS: For AgCuS the isothermic temperature point was room temperature (298(1) K) and the temperature gradient of 333(1) to 365(1) K was generated using the aforementioned procedure.

Temperature was controlled by an external thermocouple (RSpro Thermometer device, Ni/Cr/Ni type thermocouple, accuracy ±1K) at the contacts during the measurements. Conductivity measurements were performed using a Keithley 2450 SourceMeter. Voltage errors are ±0.015% and current errors are ±0.03%. This digital multimeter was operated with the aid of KickStart *I–V* Characterizer App. Measurements were performed at a scanning speed of 0.06 V s^{-1}. Data analysis was performed with the Keithley Kickstart *I–V* Characterizer App software package.[39]

Semi-Quantitative Phase Analyses: Energy dispersive X-ray spectroscopy (EDX) was performed using a JOEL JCM-6000 NeoScop with an integrated JOEL JED-2200 EDX unit. The acceleration voltage was set to 15 kV. The EDX results were averaged from at least three different points, selected randomly on the crystal surface. The samples were fixed on a graphite holder with a conductive adhesive polymer tape from PLANO GmbH. More details in the Supporting Information section.

Bulk Modulus Determination: Pressure-dependent determinations of the $Ag_{18}Cu_3Te_{11}Cl_3$ cell parameters were conducted at the I15 beamline at Diamond light source, Ditcot, Great Britain. The applied X-ray wavelength was set to $\lambda = 0.4246$ Å. A LeToullec-style membrane diamond anvil cell was used to apply pressure in the range from ambient to 8 GPa. The diamond anvils had 300-micron culets and the gasket material was rhenium. Ruby was used as the internal pressure calibration standard and daphne oil was used as a pressure transmitting medium.[40] Ruby fluorescence was measured with a laser system, and the diffractometer raw data were transferred into a processable format with DAWN.[41] The pressure of each data point was measured by collecting ruby spectra before and after the XRD measurement. A pressure equilibration time of 10 min was applied prior to the pressure and XRD data acquisition. A peak fitting routine with Pseudo-Voigt profiles embedded in the FITYK software suite was used to achieve exact pressure data.[42] XRD data were refined using the JANA 2006 program suite.[33] The determined cell parameters at ambient pressure were used as starting model. A LeBail fitting routine, a Legendre polynomial function with 18 background parameters, and a Pseudo-Voigt profile were used to refine the XRD data profile. Cell parameters were determined for each data point with an unrestricted refinement of the cell parameters. The space group $P6_3/mcm$ determined at ambient pressure was applied in the entire pressure range. No change in symmetry in this pressure regime was detected. For each new cell refinement, the previous cell parameters were used as a starting model. Data after the cell parameter refinements are summarized in Table S18 (Supporting Information).

The acquired pressure data was fitted with a Birch–Murnaghan equation of state (EoS):[15]

$$P=\frac{3}{2}K_0\left[\left(\frac{V}{V_0}\right)^{-\frac{7}{3}}-\left(\frac{V}{V_0}\right)^{-\frac{5}{3}}\right]\left\{1+\frac{3}{4}(K'-4)\left[\left(\frac{V}{V_0}\right)^{-\frac{2}{3}}-1\right]\right\} \tag{3}$$

with P = applied pressure in GPa, K_0 = bulk modulus in GPa, K' = pressure derivate of bulk modulus, V_0 = cell volume at ambient pressure in Å^3, and V = cell volume at a given pressure P in Å^3 to determine the bulk modulus K_0. The software EoSFit7c was used for the fitting.[43]

Using the cell volume at ambient pressure of $V_0 = 4898(4)$ Å^3, which was determined by single crystal structure determination experiments, values of $K_0 = 28.2(11)$ GPa and $K' = 12.7(8)$ from a 3rd-order EOS fit was calculated. In order to verify the significance of the fit the Eulerian strain f:

$$f=\frac{1}{2}\left[\left(\frac{V}{V_0}\right)^{-\frac{2}{3}}-1\right] \tag{4}$$

was plotted against the normalized pressure F:

$$F=\frac{P}{3f\times(1+2f)^{\frac{5}{2}}} \tag{5}$$

which is shown in Figure 2f. According to the *F-f* plot values of $K_0 = 29.3$ GPa and $K' = 12.1$ were found. The *F-f* plot substantiates the significance of K' in the EOS which significantly deviates from a 2nd-order representation of $K' = 4$. More details are in the Supporting Information section in chapter 3.

[CCDC 2201916/2201917/2201918 /2201919 contains the supplementary crystallographic data for this paper. These data can be obtained free of charge from The Cambridge Crystallographic Data Centre via www.ccdc.cam.ac.uk/data_request/cif.]

Supporting Information

Supporting Information is available from the Wiley Online Library or from the author.

Acknowledgements

Conflict of Interest

The authors declare no conflict of interest.

Data Availability Statement

The data that support the findings of this study are available from the corresponding author upon reasonable request.

Keywords

[1] T. Nilges, S. Lange, M. Bawohl, J. M. Deckwart, M. Janssen, H.-D. Wiemhöfer, R. Decourt, B. Chevalier, J. Vannahme, H. Eckert, R. Weihrich, *Nat. Mater.* **2009**, *8*, 101.

[2] S. Lange, T. Nilges, *Chem. Mater.* **2006**, *18*, 2538.

**ADVANCED
SCIENCE NEWS**

www.advancedsciencenews.com

**ADVANCED
MATERIALS**

www.advmat.de

[3] S. Lange, M. Bawohl, D. Wilmer, H.-W. Meyer, H.-D. Wiemhöfer, T. Nilges, *Chem. Mater.* **2007**, *19*, 1401.

[4] C. Xiao, X. Qin, J. Zhang, R. An, J. Xu, K. Li, B. Cao, J. Yang, B. Ye, Y. Xie, *J. Am. Chem. Soc.* **2012**, *134*, 18460.

[5] S. N. Guin, J. Pan, A. Bhowmik, D. Sanyal, U. V. Waghmare, K. Biswas, *J. Am. Chem. Soc.* **2014**, *136*, 12712.

[6] Y. Shi, A. Assoud, C. R. Sankar, H. Kleinke, *Chem. Mater.* **2017**, *29*, 9565.

[7] J. Peters, O. Conrad, B. Bremer, B. Krebs, *Z. Anorg. Allg. Chem.* **1996**, *622*, 1823.

[8] L. Pauling, *The Nature of the Chemical Bond*, 3rd ed., Cornell University Press, Ithaca, NY **1960**.

[9] A. Vogel, T. Nilges, *Inorg. Chem.* **2021**, *60*, 15233.

[10] A. Vogel, T. Miller, C. Hoch, M. Jakob, O. Oeckler, T. Nilges, *Inorg. Chem.* **2019**, *58*, 6222.

[11] W. Shockley, H. J. Queisser, *J. Appl. Phys.* **1961**, *32*, 510.

[12] D. W. James, *J. Mater. Sci.* **1968**, *3*, 540.

[13] X. Zhang, M. Fujii, *Polym. Eng. Sci.* **2003**, *43*, 1755.

[14] T. Bernges, R. Hanus, B. Wankmiller, K. Imasato, S. Lin, M. Ghidiu, M. Gerlitz, M. Peterlechner, S. Graham, G. Hautier, Y. Pei, M. R. Hansen, G. Wilde, G. J. Snyder, J. George, M. T. Agne, W. G. Zeier, *Adv. Energy Mater.* **2022**, *12*, 2200717.

[15] F. Birch, *Phys. Rev.* **1947**, *71*, 809.

[16] S. Hasan, P. Adhikari, K. Baral, W.-Y. Ching, *AIP Adv.* **2020**, *10*, 75216.

[17] Q. Yang, J. Lee, B. Feng, Y. Ikuhara, G. Kim, H. J. Cho, H. Jeen, H. Ohta, *ACS Appl. Electron. Mater.* **2020**, *2*, 2250.

[18] M. Cutler, N. F. Mott, *Phys. Rev.* **1969**, *181*, 1336.

[19] K. J. D. MacKenzie, M. E. Smith, *Multinuclear Solid-State Nuclear Magnetic Resonance of Inorganic Materials*, Pergamon, Oxford, UK **2002**.

[20] A. D. Bain, *Prog. Nucl. Magn. Reson. Spectrosc.* **2003**, *43*, 63.

[21] C. D. Keenan, M. M. Herling, R. Siegel, N. Petzold, C. R. Bowers, E. A. Rössler, J. Breu, J. Senker, *Langmuir* **2013**, *29*, 643.

[22] T. Nilges, O. Osters, M. Bawohl, J.-L. Bobet, B. Chevalier, R. Decourt, R. Weihrich, *Chem. Mater.* **2010**, *22*, 2946.

[23] J.-Y. Jung, D. Woong Kim, D.-H. Kim, T. Joo Park, R. B. Wehrspohn, J.-H. Lee, *Sci. Rep.* **2019**, *9*, 9132.

[24] D. Li, M. Chen, Z. Sun, P. Yu, Z. Liu, P. M. Ajayan, Z. Zhang, *Nat. Nanotechnol.* **2017**, *12*, 901.

[25] R. Cheng, F. Wang, L. Yin, Z. Wang, Y. Wen, T. A. Shifa, J. He, *Nat. Electron.* **2018**, *1*, 356.

[26] J.-W. Chen, S.-T. Lo, S.-C. Ho, S.-S. Wong, T.-H.-Y. Vu, X.-Q. Zhang, Y.-D. Liu, Y.-Y. Chiou, Y.-X. Chen, J.-C. Yang, Y.-C. Chen, Y.-H. Chu, Y.-H. Lee, C.-J. Chung, T.-M. Chen, C.-H. Chen, C.-L. Wu, *Nat. Commun.* **2018**, *9*, 3143.

[27] S.-J. Lee, Z. Lin, J. Huang, C. S. Choi, P. Chen, Y. Liu, J. Guo, C. Jia, Y. Wang, L. Wang, Q. Liao, I. Shakir, X. Duan, B. Dunn, Y. Zhang, Y. Huang, X. Duan, *Nat. Electron.* **2020**, *3*, 630.

[28] H. Wu, Y. Wang, Y. Xu, P. K. Sivakumar, C. Pasco, U. Filippozzi, S. S. P. Parkin, Y.-J. Zeng, T. McQueen, M. N. Ali, *Nature* **2022**, *604*, 653.

[29] Y. He, Q. He, L. Wang, C. Zhu, P. Golani, A. D. Handoko, X. Yu, C. Gao, M. Ding, X. Wang, F. Liu, Q. Zeng, P. Yu, S. Guo, B. I. Yakobson, L. Wang, Z. W. Seh, Z. Zhang, M. Wu, Q. J. Wang, H. Zhang, Z. Liu, *Nat. Mater.* **2019**, *18*, 1098.

[30] Stoe, *WinXPOW*, Stoe & Cie GmbH, Darmstadt, Germany, **2011**.

[31] Stoe, *X-AREA*, Stoe & Cie GmbH, Darmstadt, Germany, **2015**.

[32] L. Palatinus, G. Chapuis, *J. Appl. Crystallogr.* **2007**, *40*, 786.

[33] V. Petrıcek, M. Dušek, L. Palatinus, *The Crystallographic Computing System*, Institute of Physics, Praha, Czech Republic **2006**.

[34] Netzsch GmbH, *Proteus Thermal Analysis*, Netzsch Gerätebau GmbH, Selb, Germany **2010**.

[35] Netzsch GmbH, *NetzschSBA-Measurement*, Netzsch Gerätebau GmbH, Selb, Germany **2016**.

[36] J. A. Cape, G. W. Lehman, *J. Appl. Phys.* **1963**, *34*, 1909.

[37] J. Blumm, J. Opfermann, *High Temp.-High Pressures* **2002**, *34*, 515.

[38] Netzsch GmbH, *Proteus LFA Analysis*, Netzsch Gerätebau GmbH, Selb, Germany **2021**.

[39] Keithley Instruments LLC, *Kickstart I-V Characterizer App*, Tektronix Inc., Beaverton, United States, **2021**.

[40] K. Syassen, *High Pressure Res.* **2008**, *28*, 75.

[41] J. Filik, A. W. Ashton, P. C. Y. Chang, P. A. Chater, S. J. Day, M. Drakopoulos, M. W. Gerring, M. L. Hart, O. V. Magdysyuk, S. Michalik, A. Smith, C. C. Tang, N. J. Terrill, M. T. Wharmby, H. Wilhelm, *J. Appl. Crystallogr.* **2017**, *50*, 959.

[42] M. Wojdyr, *J. Appl. Crystallogr.* **2010**, *43*, 1126.

[43] R. J. Ross, M. Alvaro, J. Gonzalez-Platas, *Z. Kristallogr. Cryst. Mater.* **2014**, *229*, 405.

Supporting Information

A switchable one-compound diode

Anna Vogel, Alfred Rabenbauer, Philipp Deng, Ruben Steib, Thorben Böger, Wolfgang G. Zeier, Renée Siegel, Jürgen Senker, Dominik Daisenberger, Katharina Nisi, Alexander W. Holleitner, Janio Venturini[*], Tom Nilges[*]

Structure chemistry of coinage metal (poly)chalcogenide

The structures of coinage metal (poly)chalgocenides are complex and hard to describe with standard procedures like a) close packing arrangement of atoms with void filling procedures, or b) the definition of cluster or other complex subunits and their connection or distribution, or other recent and frequently used procedures. The cations in coinage metal (poly)chalcogenides show a dynamic disorder in general due to the intrinsic high cation mobility of d^{10} ions. Polymorphism is a general property caused by order-disorder phenomena of the cations. Anions are often ordered except for covalently-bonded substructures which also tend to show ion dynamics under certain circumstances. We describe the complexity of the structure by using a topologic description of the anion substructure by the definition of anion layers of isolated anions without any homoatomic bonding interactions (isolated ions), and the illustration of partially and fully covalently bonded polyanion subunits in the structure. In the following we will discuss the 'evolution' of the title compound $Ag_{18}Cu_3Te_{11}Cl_3$ by successive substitution of Cu by Ag in $Cu_{20}Te_{11}Cl_3$.

Cu$_{20}$Te$_{11}$Cl$_3$, the Ag$_x$Cu$_{21-x}$Te$_{11}$Cl$_3$ substitution series, and the end member Ag$_{18}$Cu$_3$Te$_{11}$Cl$_3$

The title compound has been discovered finally after a long-lasting evolution and optimization process from more simple systems. To understand the idea behind our title compound one has to start with an also rather complex compound, Cu$_{20}$Te$_{11}$Cl$_3$. Similar to the other coinage metal (poly)chalcogenide halides, the anionic substructure of recently published Cu$_{20}$Te$_{11}$Cl$_3$ can be topologically described by stacked anion nets that are interpenetrated by polyanionic Te$_4$ units (Te$\cdots$Te$-$Te$\cdots$Te).[1] These nets were defined by connecting neighboring anions of the same type on certain layers in the unit cell. The distances of the anions within the nets are generally above two times the van-der-Waals radii according to Pauling and the connecting lines do not represent chemical bonds but are only drawn based on topological grounds. In the case of Cu$_{20}$Te$_{11}$Cl$_3$ every second anion net is a Te 6^3 honeycomb net and every second net between the Te 6^3 nets is a Cl 6.3.6.3 kagomé net. Both net types have already been observed in Ag$_{10}$Te$_4$Br$_3$ and Cu$_{9.1}$Te$_4$Cl$_3$ where they are stacked alternatingly.[2–4] However, in α-Cu$_{20}$Te$_{11}$Cl$_3$ every second position between two Te 6^3 nets is occupied by a disordered Te 6.3.6.3 net. The polyanionic Te$_4$ units are built by a [Te$_2$]$^{2-}$ dumbbell and two linearly coordinating Te^{2-} anions and interpenetrate the Te 6^3 and Cl 6.3.6.3 nets but are separated by the disordered Te 6.3.6.3 net.[1] A scheme of the anion sublattice of the crystal structure is shown in **Figure S1c**. A full section of the crystal structure is given in in **Figure S3**.

In our previously published study we discussed two models that describe the chemical nature of the disordered Te 6.3.6.3 net: disordered dumbbells and two statistically distributed stützite-type distorted kagomé nets in opposing orientations. For Cu$_{20}$Te$_{11}$Cl$_3$ we strongly favor the statistic distribution of [Te$_2$]$^{2-}$ dumbbells because the resulting total charge of the anionic substructure [Te$_{11}$Cl$_3$]$^{20-}$ composed of ([Te$_2$]$^{2-}$)$_{2.5}$(Te^{2-})$_6$(Cl$^-$)$_3$ is in good accordance with the refined composition of Cu^{20+}[Te$_{11}$Cl$_3$]$^{20-}$ and a dynamic fluctuation within the network would

provoke a charge density wave (CDW) that would lead to a defined drop of the Seebeck coefficient, which was not observed.[1]

In order to release ordering of the disordered Te 6.3.6.3 net by enlargement of the unit cell, Cu was substituted stepwise by Ag in $Cu_{20}Te_{11}Cl_3$. The synthesis led to phase pure products up to an Ag:Cu ratio of 6:1. Higher Ag:Cu ratios led to the formation of Ag_5Te_2Cl as side product.[5,6] **Figure S1a** denotes powder diffraction pattern of the stepwise substitution of Cu by Ag. Indexing of the main reflections shows a linear increase of the unit cell volume but splitting of some weaker reflections (highlighted in grey in **Figure S1a**) points toward the formation of a super structure.

Single crystal XRD of $Ag_{18}Cu_3Te_{11}Cl_3$ confirms that assumption. The formation of a ($\sqrt{3}$ x $\sqrt{3}$ x 2) super structure (in relation to α-$Cu_{20}Te_{11}Cl_3$) is released by the ordering of the disordered Te 6.3.6.3 net (see **Figure S1d**). While in $Cu_{20}Te_{11}Cl_3$ it can be described by statistically distributed $[Te_2]^{2-}$ dumbbells, in $Ag_{18}Cu_3Te_{11}Cl_3$ the Te-Te distances are too long for the formation of dumbbells only. The formerly disordered net orders to a distorted Te 6.3.6.3 kagomé net similar to the one found in synthetic stützite.[7] The transition from $[Te_2]^{2-}$ dumbbells to dumbbells and non-bonded Te^{2-} ions in the net causes the increase of the total negative charge of the anion substructure from $[Te_{11}Cl_3]^{20-}$ in $Cu_{20}Te_{11}Cl_3$ to $[Te_{11}Cl_3]^{21-}$ in $Ag_{18}Cu_3Te_{11}Cl_3$. Hence, the real coinage metal content of the products of the substitution series ranges between $M_{20}Te_{11}Cl_3$ and $M_{21}Te_{11}Cl_3$ with M = Ag, Cu and can be written as $(Ag_xCu_{1-x})_{20+\delta}Te_{11}Cl_3$ with δ = 0-1 and x = 0 to $\frac{6}{7}$ (**Figure S1b**). Nevertheless, the starting composition for all samples was chosen as $Ag_xCu_{21-x}Te_{11}Cl_3$, as the exact coinage metal content is defined by the bonding situation in the anion substructure. The very small amount of spare MCl which results from this small deviation between the starting composition and the realized composition would deposit separated from the main product on the cooler side of the ampoule during

synthesis. The composition $Ag_{18}Cu_3Te_{11}Cl_3$ of the end member of the series was substantiated by EDX measurements that can be withdrawn from **Table S17**.
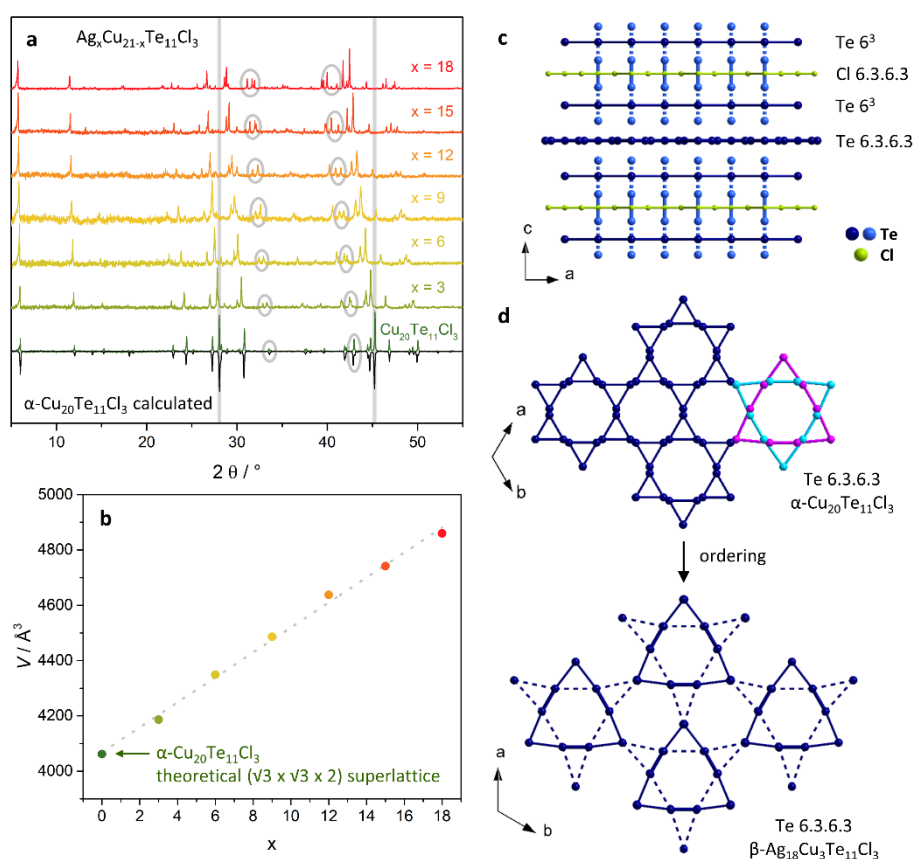
Figure S1. $Ag_{18}Cu_3Te_{11}Cl_3$ was first synthesized by substituting Cu by Ag in recently published $Cu_{20}Te_{11}Cl_3$.[9] The elongation of Te-Te-distances causes the formation of a ($\sqrt{3}$ x $\sqrt{3}$ x 2) super structure and an increase in anion charge from $[Te_{11}Cl_3]^{20-}$ to $[Te_{11}Cl_3]^{21-}$. a) Powder XRD pattern of $Cu_{20}Te_{11}Cl_3$ and $Ag_xCu_{21-x}Te_{11}Cl_3$ with x = 3 - 18. Calculated diffractograms are drawn downwards for clarity. b) Evolution of unit cell volume of $Ag_xCu_{21-x}Te_{11}Cl_3$ with increasing x from x = 3 to 18 compared to the volume of a theoretical ($\sqrt{3}$ x $\sqrt{3}$ x 2) super cell of α-$Cu_{20}Te_{11}Cl_3$. c) Scheme of anionic substructure of $Cu_{20}Te_{11}Cl_3$ and $Ag_{18}Cu_3Te_{11}Cl_3$. d) Disordered Te 6.3.6.3 net of α-$Cu_{20}Te_{11}Cl_3$ and ordered Te 6.3.6.3 net of β-$Ag_{18}Cu_3Te_{11}Cl_3$.

Structure similarities

To set the very complex crystal chemistry of $Ag_{18}Cu_3Te_{11}Cl_3$ and $Cu_{20}Te_{11}Cl_3$ into some context, we compare the structure to related compounds. Besides the mineral stützite the

compounds are related to the other coinage metal polytelluride halides $Cu_{9.1}Te_4Br_3$ and $Ag_{10}Te_4Br_3$, the first reported pnp material.[2–4,7] All structures can be described by a simple topological approach where the anion substructure is defined by different layers stacked along a crystallographic axis, interpenetrated by polyanionic Te units (see **Figure S2**). In stützite ($Ag_{5–x}Te_3$), only Te 6^3 and Te 6.3.6.3 nets exist that are stacked alternatingly, interpenetrated by elongated Te_2 dumbbells. The Te 6.3.6.3 net is built of $[Te_2]^{2–}$ dumbbells and additional coordinating $Te^{2–}$ ions. The replacement of the Te 6.3.6.3 nets by Cl 6.3.6.3 kagomé nets results in the anion substructure of $Cu_{9.1}Te_4Cl_3$. The smaller Cl atoms in comparison to Te induce the bond length decrease of the elongated dumbbells. While they are still slightly elongated in $Cu_{9.1}Te_4Cl_3$ (the reason of the slight excess of coinage metal), they are able to coordinate to strands of dumbbells. The replacement of the Cl by larger Br leads to the anion substructure of $Ag_{10}Te_4Br_3$. Here, another important structural feature emerges: oligomeric Te_4 units (built up of $Te^{2–}$-$[Te_2]^{2–}$-Te^{2-}) that switch to dynamically disordered equidistant Te-chains during the pnp switch. Those units interpenetrate the two other anion nets. In $Ag_{18}Cu_3Te_{11}Cl_3$, every second halide 6.3.6.3 net is again replaced by a Te 6.3.6.3 net as in stützite. Here, the Te 6.3.6.3 net separates the Te_4 units and they are arranged in a parallel manner on the same height (regarding the c-axis) unlike the zigzag arrangement in $Ag_{10}Te_4Br_3$ where they interpenetrate all layers. All mentioned anion substructures and anion layers are shown in **Figure S2**.
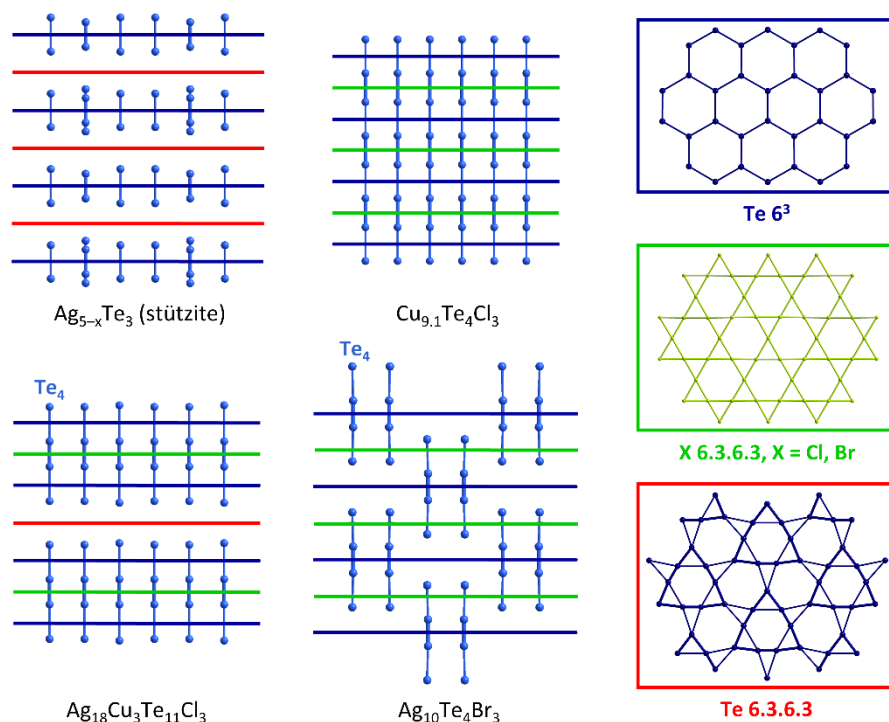
Figure S2. Building units and related structures: schemes of the anion substructures of synthetic stützite $Ag_{5-x}Te_3$, $Cu_{9.1}Te_4Cl_3$, $Ag_{18}Cu_3Te_{11}Cl_3$ and $Ag_{10}Te_4Br_3$.[2,3,7,10] The anion building units of all four compounds are staked Te 6^3 honeycomb nets, halide 6.3.6.3 kagomé nets and distorted Te 6.3.6.3 kagomé nets that consist of $[Te_2]^{2-}$ dumbbells and coordinating Te^{2-} anions with interpenetrating strands of $[Te_2]^{2-}$ dumbbells or Te_4 units (built up of Te^{2-}-$[Te_2]^{2-}$-Te^{2-}). Distances are represented proportional.

Related pnp-switch in Ag₁₀Te₄Br₃

In $Ag_{10}Te_4Br_3$ a rearrangement of the Te_4 units is responsible for the pnp-switch.[8] In γ-$Ag_{10}Te_4Br_3$ stable between 290 and 317 K all Te_4 units are fully ordered. In β-$Ag_{10}Te_4Br_3$ (317 to approx. 390 K) one third of the strands is rearranged to equidistant mobile Te-chains, and in α-$Ag_{10}Te_4Br_3$ (realized above 390 K) only equidistant mobile Te-chains exist. The rearrangement of the strands is triggered by increasing Ag mobility. The Ag1 position that separates two Te_4 units in γ-$Ag_{10}Te_4Br_3$ becomes partially occupied and the coordinating Te^{2-} ions of the Te_4 units are able to approach each other to form a new dumbbell. Structure sections of the α- and β-polymorph as well as the Seebeck-drop are shown in **Figure S3**.
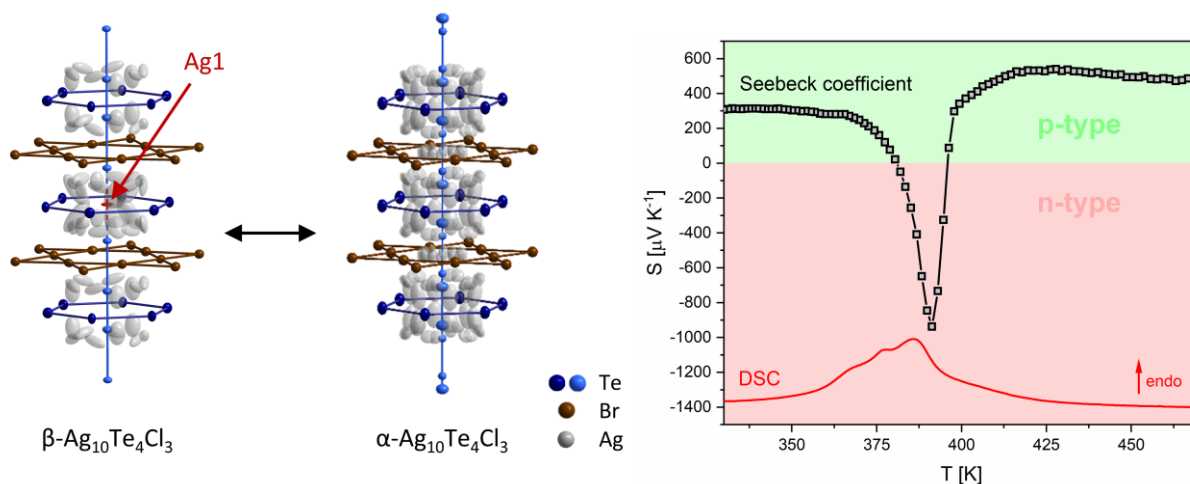
Figure S3. Structure sections of β- and α-$Ag_{10}Te_4Br_3$ and Seebeck-drop.

Structure refinement and extended crystal chemistry discussion

All refinements were performed using 3rd order displacement parameters (so called non-harmonic refinement). This procedure is necessary to reduce residual electron density if crystalline solid ion conductors feature a high grade of ion dynamics and disorder. This procedure typically leads to a high number of parameters and therefore to a poor data/parameter ratio. To decrease the number of parameters, insignificant 3rd order parameters were set to 0 and fixed in the last refinement step. Atomic coordinates, site occupancy factors, and displacement parameters are given for all refinements in **Table S1-S12**. In the case of mixed Ag/Cu sites, Ag and Cu were constrained to have the same positional and displacement parameters. As it is not possible to differentiate between Ag and Cu on partially occupied sites with large displacement parameters, the Ag:Cu ratio was constrained at 6:1, reflecting the initial composition as substantiated by EDX measurements (represented in **Table S17**).

According to DSC measurements, $Ag_{18}Cu_3Te_{11}Cl_3$ exhibits two broad phase transitions at 216(3) K and at 288(3) K, with the latter extending over a temperature interval around room temperature. The polymorphs are assigned γ-, β- and α-$Ag_{18}Cu_3Te_{11}Cl_3$ with increasing temperature. Similar to the other pnp-switching compounds, the drop of thermopower in

$Ag_{18}Cu_3Te_{11}Cl_3$ is initiated by an order-disorder phase transition, in that case the β-α transition around room temperature.

Single crystal XRD measurements have been performed at 200(1), 270(1), 330(1), 350(1), and 400(1) K in order to evaluate the structural changes upon and after the β-α transition in more detail.

In the structure refinement, third order anharmonic replacement parameters are used for Ag/Cu due to high ion mobility. As in α-$Ag_{18}Cu_3Te_{11}Cl_3$, mobility in the Te 6.3.6.3 net is released, third order anharmonic replacement parameters are also used for the Te atoms in the net, namely Te7, Te8, and Te9. In order to discuss atomic distances in the right manner, mode positions have been determined by calculating probability density functions (pdf). The mode position represents the true maximum of electron density of a given position that can differ from the refined position due to the anharmonicity of the displacement. A brief explanation for this procedure is given elsewhere.[9,10] Mode positions are shown in **Table S14-S17** and are used in the following discussion.

β-$Ag_{18}Cu_3Te_{11}Cl_3$ crystallizes in hexagonal symmetry in space group $P6_3/mcm$, with $a =$ 13.4709(12) Å and $c =$ 30.818(2) Å at 270 K. Details of the single crystal XRD measurements can be withdrawn from **Table 1**. The structural features of the anion substructure, excluded the Te 6.3.6.3 net, are similar to those of $Cu_{20}Te_{11}Cl_3$: three parallel anion nets (a Cl 6.3.6.3 net between two Te 6^3 nets) vertically interpenetrated by linear Te_4 units that are built by a $[Te_2]^{2-}$ dumbbell and two coordinating Te^{2-} ions.[1] Unlike in $Cu_{20}Te_{11}Cl_3$, those structure units are not separated by a fully disordered Te 6.3.6.3 net but by a distorted ordered one (see **Figure S1c**). Similar to the Te 6.3.6.3 net in synthetic stützite, it consists of $[Te_2]^{2-}$ dumbbells and additional coordinating Te^{2-} anions (see **Figure S1d**).[7] The dumbbell Te-Te distance is 2.81 Å and the distance to the coordinating Te^{2-} anion is 3.67 Å. These correspond well to values for $[Te_2]^{2-}$ at room temperature that can be found in literature: 2.84 Å in the Te 6.3.6.3 net in stützite,

2.70 Å in $MgTe_2$, 2.86 Å in α-K_2Te_2, or the dumbbell distance in the Te_4 units in β-$Ag_{18}Cu_3Te_{11}Cl_3$ with 2.81 - 2.83 Å.[7,11,12] The distance of the coordinating Te^{2-} anion to the $[Te_2]^{2-}$ dumbbell in the 6.3.6.3 net is comparable to the appropriate distance in stützite (3.61 Å) and the distance of the coordinating Te^{2-} anion in the Te_4 units in β-$Ag_{18}Cu_3Te_{11}Cl_3$ (3.85 – 4.05 Å).[7]

The cations are very mobile and flow around the anion substructure as a quasi-liquid. The electron density is distributed over multiple partially occupied positions with large displacement parameters. As it is not possible to differentiate between Ag and Cu under these circumstances, the ratio Ag:Cu = 6:1 is constrained in every position. That ratio was gathered from the initial weight and substantiated by EDX measurements. Under that requirement, the site occupancy factors were refined without restrictions. This approach resulted in the refined sum formula $Ag_{17.1(3)}Cu_{2.85(6)}Te_{11}Cl_3$ that meets the expectations. The mixed Ag/Cu positions are located around the Te_4 strands between the anion nets and in the voids of the Te nets. The displacement parameters indicate mobility in two dimensions. As no Ag/Cu probability can be found within the Cl 6.3.6.3 net, this net seems to hinder a three-dimensional distribution of the d^{10} ions and the third direction (along the c-axis) is blocked.

Similar to β-$Ag_{18}Cu_3Te_{11}Cl_3$, α-$Ag_{18}Cu_3Te_{11}Cl_3$ crystallizes in $P6_3/mcm$ with $a = 13.5775$ Å and $c = 30.822$ Å at 400 K. The main difference to β-$Ag_{18}Cu_3Te_{11}Cl_3$ can be found in the Te 6.3.6.3 net, where disorder emerges. Even after careful examination of the diffraction pattern we found no hints for a symmetry change which would lead to another space group. The dumbbell position Te8 splits into two positions. At 400 K the original dumbbell distance Te8-Te8 is 2.83 Å, the distance between the split positions Te8-Te9 is 0.98 Å, and the distance between the newly emerging position Te9 and the originally coordinating Te7 is 2.82 Å, which corresponds to a proper $[Te_2]^{2-}$ dumbbell bond length as well.

The cation substructure is very similar to the β-polymorph. As expected, the displacement parameters increase with increasing temperature and ion mobility.

The crystal structure of γ-$Ag_{18}Cu_3Te_{11}Cl_3$ is more complex than those of α- and β-$Ag_{18}Cu_3Te_{11}Cl_3$ as we assume twinning. It is still under examination and, as it is not involved in pnp-switching. This structure will be published in an upcoming study.

Table S1. Positional parameters of β-$Ag_{18}Cu_3Te_{11}Cl_3$ at 270 K.

Atom	Wyckhoff position	site	sof	x	y	z
Te1	4e	3.m	1	1	1	0.04584(4)
Te2	8h	3..	1	0.6667	0.3333	0.04563(3)
Te3	4e	3.m	1	1	1	0.17736(6)
Te4	8h	3..	1	0.6667	0.3333	0.17046(4)
Te5	12k	..m	1	0.66206(6)	0.66206(6)	0.11342(3)
Te6	12k	..m	1	1	0.66866(8)	0.11287(3)
Te7	6g	m2m	1	0.56757(8)	0	0.25
Te8	12j	m..	1	0.31161(6)	0.12031(6)	0.25
Cl1	6f	..2/m	1	0.5	0	0
Cl2	12i	..2	1	0.83559(10)	0.6712(2)	0
Ag1	6g	m2m	0.241(9)	1	0.9043(13)	0.25
Cu1	6g	m2m	0.0401(14)	1	0.9043(13)	0.25
Ag2	12j	m..	0.662(5)	0.6501(2)	0.4484(2)	0.25
Cu2	12j	m..	0.1103(9)	0.6501(2)	0.4484(2)	0.25
Ag3	12k	..m	0.25(2)	0.574(2)	0.574(2)	0.1883(8)
Cu3	12k	..m	0.042(3)	0.574(2)	0.574(2)	0.1883(8)
Ag4	12k	..m	0.467(5)	1	0.7922(4)	0.19141(9)
Cu4	12k	..m	0.0779(8)	1	0.7922(4)	0.19141(9)
Ag5	24l	1	0.155(5)	0.6282(8)	0.5096(9)	0.1989(4)
Cu5	24l	1	0.0259(9)	0.6282(8)	0.5096(9)	0.1989(4)
Ag6	24l	1	0.254(6)	0.5506(6)	0.8516(14)	0.1777(4)
Cu6	24l	1	0.0424(11)	0.5506(6)	0.8516(14)	0.1777(4)
Ag7	24l	1	0.301(4)	1.1141(5)	0.8549(5)	0.1610(2)
Cu7	24l	1	0.0501(7)	1.1141(5)	0.8549(5)	0.1610(2)
Ag8	24l	1	0.263(8)	0.4761(10)	0.5438(6)	0.1701(4)
Cu8	24l	1	0.0439(13)	0.4761(10)	0.5438(6)	0.1701(4)
Ag9	24l	1	0.393(5)	0.5843(3)	0.7844(4)	0.16429(10)
Cu9	24l	1	0.0654(9)	0.5843(3)	0.7844(4)	0.16429(10)
Ag10	24l	1	0.252(6)	0.5623(7)	0.4331(9)	0.1132(5)
Cu10	24l	1	0.0419(10)	0.5623(7)	0.4331(9)	0.1132(5)
Ag11	24l	1	0.425(5)	0.8857(4)	0.8240(4)	0.11922(11)
Cu11	24l	1	0.0709(8)	0.8857(4)	0.8240(4)	0.11922(11)
Ag12	24l	1	0.210(6)	0.7639(10)	0.5222(11)	0.1222(7)
Cu12	24l	1	0.0350(11)	0.7639(10)	0.5222(11)	0.1222(7)
Ag13	24l	1	0.252(6)	0.5326(11)	0.4191(12)	0.0674(3)
Cu13	24l	1	0.0419(11)	0.5326(11)	0.4191(12)	0.0674(3)
Ag14	24l	1	0.292(7)	0.767(2)	0.5558(6)	0.0696(3)

Cu14	24*l*	1	0.0487(11)	0.767(2)	0.5558(6)	0.0696(3)
Ag15	12*k*	..*m*	0.724(5)	1	0.8055(3)	0.0542(2)
Cu15	12*k*	..*m*	0.1207(9)	1	0.8055(3)	0.0542(2)
Ag16	24*l*	1	0.369(7)	0.6707(3)	0.5325(4)	0.0524(3)
Cu16	24*l*	1	0.0615(12)	0.6707(3)	0.5325(4)	0.0524(3)

Table S2. Anisotropic displacement parameters of β-Ag$_{18}$Cu$_3$Te$_{11}$Cl$_3$ at 270 K.

Atom	U_{11}	U_{22}	U_{33}	U_{12}	U_{13}	U_{23}
Te1	0.0378(3)	0.0378(3)	0.0211(5)	0.0189(2)	0	0
Te2	0.0553(3)	0.0553(3)	0.0227(4)	0.0277(2)	0	0
Te3	0.0507(5)	0.0507(5)	0.0545(9)	0.0254(2)	0	0
Te4	0.0478(3)	0.0478(3)	0.0450(5)	0.0239(2)	0	0
Te5	0.0458(3)	0.0458(3)	0.0511(5)	0.0121(3)	-0.0073(3)	-0.0073(3)
Te6	0.0525(5)	0.0660(4)	0.0453(5)	0.0263(2)	0	0.0055(4)
Te7	0.0351(4)	0.0434(6)	0.0829(9)	0.0217(3)	0	0
Te8	0.0353(3)	0.0299(3)	0.0349(3)	0.0129(3)	0	0
Ag1	0.078(6)	0.127(8)	0.154(11)	0.039(3)	0	0
Cu1	0.078(6)	0.127(8)	0.154(11)	0.039(3)	0	0
Ag2	0.0501(8)	0.0483(9)	0.097(2)	0.0266(7)	0	0
Cu2	0.0501(8)	0.0483(9)	0.097(2)	0.0266(7)	0	0
Ag3	0.179(14)	0.179(14)	0.140(11)	0.095(11)	0.081(9)	0.081(9)
Cu3	0.179(14)	0.179(14)	0.140(11)	0.095(11)	0.081(9)	0.081(9)
Ag4	0.072(2)	0.0727(14)	0.062(2)	0.0361(8)	0	0.0041(9)
Cu4	0.072(2)	0.0727(14)	0.062(2)	0.0361(8)	0	0.0041(9)
Ag5	0.057(4)	0.093(5)	0.132(7)	0.012(3)	0.017(3)	-0.061(5)
Cu5	0.057(4)	0.093(5)	0.132(7)	0.012(3)	0.017(3)	-0.061(5)
Ag6	0.144(7)	0.131(7)	0.157(10)	-0.032(5)	-0.012(3)	0.056(7)
Cu6	0.144(7)	0.131(7)	0.157(10)	-0.032(5)	-0.012(3)	0.056(7)
Ag7	0.062(2)	0.075(2)	0.088(3)	0.027(2)	-0.011(2)	-0.015(2)
Cu7	0.062(2)	0.075(2)	0.088(3)	0.027(2)	-0.011(2)	-0.015(2)
Ag8	0.148(7)	0.056(3)	0.137(5)	0.033(3)	0.093(4)	0.028(3)
Cu8	0.148(7)	0.056(3)	0.137(5)	0.033(3)	0.093(4)	0.028(3)
Ag9	0.0553(13)	0.061(2)	0.070(2)	0.0219(10)	0.0065(10)	0.0091(11)
Cu9	0.0553(13)	0.061(2)	0.070(2)	0.0219(10)	0.0065(10)	0.0091(11)
Ag10	0.053(3)	0.148(7)	0.29(2)	0.048(3)	0.054(5)	0.069(7)
Cu10	0.053(3)	0.148(7)	0.29(2)	0.048(3)	0.054(5)	0.069(7)
Ag11	0.0673(14)	0.082(2)	0.081(2)	-0.0082(12)	0.0083(10)	0.0004(10)
Cu11	0.0673(14)	0.082(2)	0.081(2)	-0.0082(12)	0.0083(10)	0.0004(10)
Ag12	0.109(6)	0.068(5)	0.39(2)	-0.001(3)	-0.106(9)	0.066(8)
Cu12	0.109(6)	0.068(5)	0.39(2)	-0.001(3)	-0.106(9)	0.066(8)
Ag13	0.215(10)	0.254(10)	0.111(5)	0.198(9)	0.062(4)	0.055(4)
Cu13	0.215(10)	0.254(10)	0.111(5)	0.198(9)	0.062(4)	0.055(4)
Ag14	0.244(12)	0.074(3)	0.087(4)	0.023(5)	0.066(7)	0.004(2)
Cu14	0.244(12)	0.074(3)	0.087(4)	0.023(5)	0.066(7)	0.004(2)
Ag15	0.102(2)	0.0695(8)	0.130(3)	0.0510(8)	0	0.0343(11)
Cu15	0.102(2)	0.0695(8)	0.130(3)	0.0510(8)	0	0.0343(11)
Ag16	0.093(3)	0.084(2)	0.123(4)	0.046(2)	0.008(2)	-0.048(2)
Cu16	0.093(3)	0.084(2)	0.123(4)	0.046(2)	0.008(2)	-0.048(2)

Table S3. Anharmonic displacement parameters of β-Ag$_{18}$Cu$_3$Te$_{11}$Cl$_3$ at 270 K.

Atom	C_{111}	C_{112}	C_{113}	C_{122}	C_{123}
Ag1	0	0.021(3)	0	0.021(3)	0
Cu1	0	0.021(3)	0	0.021(3)	0
Ag2	-0.0016(4)	-0.0029(3)	0	-0.0033(3)	0
Cu2	-0.0016(4)	-0.0029(3)	0	-0.0033(3)	0
Ag3	-0.021(9)	-0.027(7)	-0.009(2)	-0.027(7)	0
Cu3	-0.021(9)	-0.027(7)	-0.009(2)	-0.027(7)	0
Ag4	0	0	-0.0025(2)	0	-0.00123(10)
Cu4	0	0	-0.0025(2)	0	-0.00123(10)
Ag5	0	0.0042(13)	-0.0018(4)	-0.0058(13)	0
Cu5	0	0.0042(13)	-0.0018(4)	-0.0058(13)	0
Ag6	0	0.016(2)	-0.0067(13)	0	0.0043(7)
Cu6	0	0.016(2)	-0.0067(13)	0	0.0043(7)
Ag7	-0.0084(11)	-0.0065(7)	0.0016(3)	-0.0043(7)	0.0013(2)
Cu7	-0.0084(11)	-0.0065(7)	0.0016(3)	-0.0043(7)	0.0013(2)
Ag8	0.026(4)	-0.0038(9)	0	0	0
Cu8	0.026(4)	-0.0038(9)	0	0	0
Ag9	0	-0.0023(3)	0	-0.0036(4)	0
Cu9	0	-0.0023(3)	0	-0.0036(4)	0
Ag10	0.0060(11)	0.0055(8)	-0.0034(6)	0	-0.0011(7)
Cu10	0.0060(11)	0.0055(8)	-0.0034(6)	0	-0.0011(7)
Ag11	0.0052(7)	0.0033(6)	0.0014(2)	-0.0082(6)	-0.00206(13)
Cu11	0.0052(7)	0.0033(6)	0.0014(2)	-0.0082(6)	-0.00206(13)
Ag12	-0.036(5)	-0.0051(11)	0.019(3)	0	0
Cu12	-0.036(5)	-0.0051(11)	0.019(3)	0	0
Ag13	0.035(5)	0.021(3)	-0.0138(13)	0	-0.0162(13)
Cu13	0.035(5)	0.021(3)	-0.0138(13)	0	-0.0162(13)
Ag14	-0.040(12)	-0.029(4)	-0.012(2)	0.009(2)	-0.0034(5)
Cu14	-0.040(12)	-0.029(4)	-0.012(2)	0.009(2)	-0.0034(5)
Ag15	0	0.0031(4)	0.0047(2)	0.0031(4)	0.00237(12)
Cu15	0	0.0031(4)	0.0047(2)	0.0031(4)	0.00237(12)
Ag16	0	-0.0043(6)	0.0043(4)	-0.0052(5)	0.0024(3)
Cu16	0	-0.0043(6)	0.0043(4)	-0.0052(5)	0.0024(3)
	C_{133}	C_{222}	C_{223}	C_{233}	C_{333}
Ag1	0	0.043(7)	0	0	0
Cu1	0	0.043(7)	0	0	0
Ag2	0	-0.0032(4)	0	0	0
Cu2	0	-0.0032(4)	0	0	0
Ag3	-0.0013(4)	-0.021(9)	-0.009(2)	-0.0013(4)	0
Cu3	-0.0013(4)	-0.021(9)	-0.009(2)	-0.0013(4)	0
Ag4	0	-0.0057(7)	0	0	0
Cu4	0	-0.0057(7)	0	0	0
Ag5	0	-0.026(3)	0.016(2)	-0.0075(7)	0.0025(3)
Cu5	0	-0.026(3)	0.016(2)	-0.0075(7)	0.0025(3)
Ag6	0	-0.014(5)	-0.007(2)	-0.0034(8)	-0.0035(6)
Cu6	0	-0.014(5)	-0.007(2)	-0.0034(8)	-0.0035(6)
Ag7	-0.00114(10)	-0.0038(10)	0.0009(2)	0	0
Cu7	-0.00114(10)	-0.0038(10)	0.0009(2)	0	0
Ag8	-0.0026(3)	-0.0028(9)	0.0019(3)	0	-0.0013(2)

Cu8	-0.0026(3)	-0.0028(9)	0.0019(3)	0	-0.0013(2)
Ag9	0	-0.0080(7)	0	0	0
Cu9	0	-0.0080(7)	0	0	0
Ag10	-0.0021(7)	0.027(5)	0.000(2)	0.0060(8)	-0.0034(8)
Cu10	-0.0021(7)	0.027(5)	0.000(2)	0.0060(8)	-0.0034(8)
Ag11	0	0.0050(10)	0.0016(2)	0	0
Cu11	0	0.0050(10)	0.0016(2)	0	0
Ag12	-0.010(2)	0.008(3)	0.007(2)	0.0076(14)	0.010(2)
Cu12	-0.010(2)	0.008(3)	0.007(2)	0.0076(14)	0.010(2)
Ag13	-0.0032(3)	-0.028(4)	-0.020(2)	-0.0038(4)	0
Cu13	-0.0032(3)	-0.028(4)	-0.020(2)	-0.0038(4)	0
Ag14	-0.0012(3)	0	0	0	0
Cu14	-0.0012(3)	0	0	0	0
Ag15	0	0.0020(4)	0.0020(2)	0.00123(9)	0.00133(10)
Cu15	0	0.0020(4)	0.0020(2)	0.00123(9)	0.00133(10)
Ag16	0	0	0.0026(3)	-0.0020(2)	0.0013(2)
Cu16	0	0	0.0026(3)	-0.0020(2)	0.0013(2)

Table S4. Positional parameters of α-Ag$_{18}$Cu$_3$Te$_{11}$Cl$_3$ at 330 K.

Atom	Wyckoff position	site	sof	x	y	z
Te1	4e	3.m	1	1	1	0.04590(6)
Te2	8h	3..	1	0.6667	0.3333	0.04569(4)
Te3	4e	3.m	1	1	1	0.17394(8)
Te4	8h	3..	1	0.6667	0.3333	0.17098(6)
Te5	12k	..m	1	0.66136(8)	0.66136(8)	0.11399(5)
Te6	12k	..m	1	1	0.66844(8)	0.11352(5)
Te7	6g	m2m	1	0.5632(3)	0	0.25
Te8	12j	m..	0.891(9)	0.3147(2)	0.1191(4)	0.25
Te9	12j	m..	0.109(9)	0.331(2)	0.186(3)	0.25
Cl1	6f	..2/m	1	0.5	0	0
Cl2	12i	..2	1	0.83474(14)	0.6695(3)	0
Ag1	6g	m2m	0.424(11)	1	0.8976(9)	0.25
Cu1	6g	m2m	0.071(2)	1	0.8976(9)	0.25
Ag2	12j	m..	0.657(10)	0.6504(2)	0.4464(4)	0.25
Cu2	12j	m..	0.110(2)	0.6504(2)	0.4464(4)	0.25
Ag3	12k	..m	0.39(2)	0.576(3)	0.576(3)	0.1867(11)
Cu3	12k	..m	0.065(3)	0.576(3)	0.576(3)	0.1867(11)
Ag4	12k	..m	0.460(10)	1	0.7894(8)	0.1925(2)
Cu4	12k	..m	0.077(2)	1	0.7894(8)	0.1925(2)
Ag5	24l	1	0.245(10)	0.6370(13)	0.512(2)	0.1979(7)
Cu5	24l	1	0.041(2)	0.6370(13)	0.512(2)	0.1979(7)
Ag6	24l	1	0.277(9)	0.572(2)	0.8607(14)	0.1845(3)
Cu6	24l	1	0.0461(14)	0.572(2)	0.8607(14)	0.1845(3)
Ag7	24l	1	0.327(6)	1.1134(6)	0.8619(5)	0.1612(2)
Cu7	24l	1	0.0545(10)	1.1134(6)	0.8619(5)	0.1612(2)
Ag8	24l	1	0.200(11)	0.4625(11)	0.5365(13)	0.1683(4)
Cu8	24l	1	0.033(2)	0.4625(11)	0.5365(13)	0.1683(4)
Ag9	24l	1	0.316(6)	0.5821(5)	0.7857(6)	0.1649(2)
Cu9	24l	1	0.0527(11)	0.5821(5)	0.7857(6)	0.1649(2)

Ag10	24l	1	0.242(10)	0.5435(8)	0.4049(13)	0.1082(9)
Cu10	24l	1	0.040(2)	0.5435(8)	0.4049(13)	0.1082(9)
Ag11	24l	1	0.369(7)	0.8882(5)	0.8093(4)	0.1088(3)
Cu11	24l	1	0.0616(12)	0.8882(5)	0.8093(4)	0.1088(3)
Ag12	24l	1	0.264(9)	0.7560(10)	0.5358(10)	0.1116(5)
Cu12	24l	1	0.044(2)	0.7560(10)	0.5358(10)	0.1116(5)
Ag13	24l	1	0.219(9)	0.5477(10)	0.4256(12)	0.0723(7)
Cu13	24l	1	0.037(2)	0.5477(10)	0.4256(12)	0.0723(7)
Ag14	24l	1	0.174(7)	0.7839(10)	0.5523(9)	0.0701(5)
Cu14	24l	1	0.0289(11)	0.7839(10)	0.5523(9)	0.0701(5)
Ag15	12k	..m	0.709(10)	1	0.8060(4)	0.05309(13)
Cu15	12k	..m	0.118(2)	1	0.8060(4)	0.05309(13)
Ag16	24l	1	0.455(8)	0.6712(4)	0.5310(6)	0.0529(3)
Cu16	24l	1	0.0758(13)	0.6712(4)	0.5310(6)	0.0529(3)

Table S5. Anisotropic displacement parameters of α-Ag$_{18}$Cu$_3$Te$_{11}$Cl$_3$ at 330 K.

Atom	U_{11}	U_{22}	U_{33}	U_{12}	U_{13}	U_{23}
Te1	0.0501(5)	0.0501(5)	0.0346(10)	0.0251(2)	0	0
Te2	0.0603(4)	0.0603(4)	0.0339(7)	0.0302(2)	0	0
Te3	0.0596(6)	0.0596(6)	0.071(2)	0.0298(3)	0	0
Te4	0.0612(4)	0.0612(4)	0.0627(10)	0.0306(2)	0	0
Te5	0.0576(4)	0.0576(4)	0.0663(10)	0.0222(5)	-0.0048(4)	-0.0048(4)
Te6	0.0600(6)	0.0638(5)	0.0658(10)	0.0300(3)	0	0.0032(5)
Te7	0.0555(7)	0.0592(9)	0.0872(13)	0.0296(4)	0	0
Te8	0.0462(7)	0.038(2)	0.0493(8)	0.0154(10)	0	0
Te9	0.111(11)	0.09(2)	0.054(8)	0.088(12)	0	0
Ag1	0.072(4)	0.133(6)	0.157(8)	0.036(2)	0	0
Cu1	0.072(4)	0.133(6)	0.157(8)	0.036(2)	0	0
Ag2	0.077(2)	0.074(2)	0.127(3)	0.0409(11)	0	0
Cu2	0.077(2)	0.074(2)	0.127(3)	0.0409(11)	0	0
Ag3	0.29(2)	0.29(2)	0.24(2)	0.09(2)	0.15(2)	0.15(2)
Cu3	0.29(2)	0.29(2)	0.24(2)	0.09(2)	0.15(2)	0.15(2)
Ag4	0.129(4)	0.138(4)	0.100(4)	0.065(2)	0	-0.001(3)
Cu4	0.129(4)	0.138(4)	0.100(4)	0.065(2)	0	-0.001(3)
Ag5	0.147(8)	0.154(8)	0.186(13)	0.077(5)	-0.009(6)	-0.069(8)
Cu5	0.147(8)	0.154(8)	0.186(13)	0.077(5)	-0.009(6)	-0.069(8)
Ag6	0.27(2)	0.167(8)	0.100(6)	0.057(9)	-0.002(5)	0.035(6)
Cu6	0.27(2)	0.167(8)	0.100(6)	0.057(9)	-0.002(5)	0.035(6)
Ag7	0.088(3)	0.090(2)	0.111(4)	0.043(2)	-0.019(2)	-0.023(2)
Cu7	0.088(3)	0.090(2)	0.111(4)	0.043(2)	-0.019(2)	-0.023(2)
Ag8	0.146(7)	0.047(3)	0.117(8)	0.043(3)	0.061(6)	0.019(4)
Cu8	0.146(7)	0.047(3)	0.117(8)	0.043(3)	0.061(6)	0.019(4)
Ag9	0.075(2)	0.077(3)	0.081(3)	0.030(2)	0.003(2)	-0.003(2)
Cu9	0.075(2)	0.077(3)	0.081(3)	0.030(2)	0.003(2)	-0.003(2)
Ag10	0.126(6)	0.159(8)	0.58(3)	0.103(6)	0.191(9)	0.199(12)
Cu10	0.126(6)	0.159(8)	0.58(3)	0.103(6)	0.191(9)	0.199(12)
Ag11	0.073(2)	0.101(2)	0.280(7)	0.017(2)	0.002(2)	0.050(3)
Cu11	0.073(2)	0.101(2)	0.280(7)	0.017(2)	0.002(2)	0.050(3)
Ag12	0.130(8)	0.106(6)	0.64(3)	-0.007(4)	0.002(9)	0.028(6)
Cu12	0.130(8)	0.106(6)	0.64(3)	-0.007(4)	0.002(9)	0.028(6)

Ag13	0.119(6)	0.171(9)	0.158(12)	0.101(6)	0.058(7)	0.051(6)
Cu13	0.119(6)	0.171(9)	0.158(12)	0.101(6)	0.058(7)	0.051(6)
Ag14	0.191(10)	0.075(5)	0.086(7)	0.019(4)	0.003(4)	0.021(4)
Cu14	0.191(10)	0.075(5)	0.086(7)	0.019(4)	0.003(4)	0.021(4)
Ag15	0.151(3)	0.103(2)	0.136(3)	0.0754(14)	0	0.0348(14)
Cu15	0.151(3)	0.103(2)	0.136(3)	0.0754(14)	0	0.0348(14)
Ag16	0.152(4)	0.117(3)	0.149(4)	0.078(3)	0.006(3)	-0.043(3)
Cu16	0.152(4)	0.117(3)	0.149(4)	0.078(3)	0.006(3)	-0.043(3)

Table S6. Anharmonic displacement parameters of α-Ag$_{18}$Cu$_3$Te$_{11}$Cl$_3$ at 330 K.

Atom	C_{111}	C_{112}	C_{113}	C_{122}	C_{123}
Te7	-0.0027(4)	-0.0016(2)	0	-0.0016(2)	0
Te8	0.0007(4)	-0.0007(3)	0	-0.0003(3)	0
Te9	-0.06(2)	-0.044(14)	0	-0.038(14)	0
Ag1	0	0.0032(12)	0	0.0032(12)	0
Cu1	0	0.0032(12)	0	0.0032(12)	0
Ag2	0	-0.0026(4)	0	-0.0038(5)	0
Cu2	0	-0.0026(4)	0	-0.0038(5)	0
Ag3	-0.11(2)	0.071(12)	-0.017(3)	0.071(12)	0.020(4)
Cu3	-0.11(2)	0.071(12)	-0.017(3)	0.071(12)	0.020(4)
Ag4	0	0	0	0	0
Cu4	0	0	0	0	0
Ag5	0	-0.015(2)	0	-0.022(3)	0.0026(7)
Cu5	0	-0.015(2)	0	-0.022(3)	0.0026(7)
Ag6	0.10(2)	0.063(9)	0	0.053(6)	0.0077(13)
Cu6	0.10(2)	0.063(9)	0	0.053(6)	0.0077(13)
Ag7	-0.013(2)	-0.0042(7)	0.0020(4)	0	0.0015(2)
Cu7	-0.013(2)	-0.0042(7)	0.0020(4)	0	0.0015(2)
Ag8	0	-0.015(2)	0.0050(9)	-0.0069(13)	0
Cu8	0	-0.015(2)	0.0050(9)	-0.0069(13)	0
Ag9	0	0	0	-0.0027(5)	0
Cu9	0	0	0	-0.0027(5)	0
Ag10	-0.043(6)	-0.036(5)	-0.047(5)	-0.027(5)	-0.027(4)
Cu10	-0.043(6)	-0.036(5)	-0.047(5)	-0.027(5)	-0.027(4)
Ag11	0.0087(11)	0.0071(7)	0	-0.0048(7)	-0.0018(3)
Cu11	0.0087(11)	0.0071(7)	0	-0.0048(7)	-0.0018(3)
Ag12	-0.051(7)	0	0	-0.009(3)	0.013(2)
Cu12	-0.051(7)	0	0	-0.009(3)	0.013(2)
Ag13	0	-0.018(3)	-0.0075(11)	-0.040(6)	-0.0140(13)
Cu13	0	-0.018(3)	-0.0075(11)	-0.040(6)	-0.0140(13)
Ag14	0	-0.051(5)	-0.024(2)	0	0
Cu14	0	-0.051(5)	-0.024(2)	0	0
Ag15	0	0.0067(7)	0.0053(4)	0.0067(7)	0.0026(2)
Cu15	0	0.0067(7)	0.0053(4)	0.0067(7)	0.0026(2)
Ag16	0	-0.0083(12)	0.0057(6)	-0.0099(14)	0.0035(3)
Cu16	0	-0.0083(12)	0.0057(6)	-0.0099(14)	0.0035(3)
	C_{133}	C_{222}	C_{223}	C_{233}	C_{333}
Te7	0.00011(5)	0	0	0	0
Te8	0.00008(3)	-0.0009(6)	0	-0.00009(4)	0
Te9	-0.0016(6)	-0.04(2)	0	-0.0014(6)	0

Ag1	0	0.038(5)	0	0	0
Cu1	0	0.038(5)	0	0	0
Ag2	0	-0.0048(7)	0	0	0
Cu2	0	-0.0048(7)	0	0	0
Ag3	0	-0.11(2)	-0.017(3)	0	0
Cu3	0	-0.11(2)	-0.017(3)	0	0
Ag4	0	-0.019(2)	0.0012(4)	0.0009(2)	0
Cu4	0	-0.019(2)	0.0012(4)	0.0009(2)	0
Ag5	0	-0.027(5)	0.015(2)	-0.0079(13)	0.0033(8)
Cu5	0	-0.027(5)	0.015(2)	-0.0079(13)	0.0033(8)
Ag6	0.0017(5)	0.015(5)	0	0	0
Cu6	0.0017(5)	0.015(5)	0	0	0
Ag7	-0.0010(2)	-0.0049(10)	0	0	0
Cu7	-0.0010(2)	-0.0049(10)	0	0	0
Ag8	0.0012(3)	-0.002(2)	0	0	0
Cu8	0.0012(3)	-0.002(2)	0	0	0
Ag9	0	-0.0056(12)	0.0013(2)	0	0
Cu9	0	-0.0056(12)	0.0013(2)	0	0
Ag10	-0.039(4)	-0.017(6)	-0.005(4)	-0.014(3)	-0.027(3)
Cu10	-0.039(4)	-0.017(6)	-0.005(4)	-0.014(3)	-0.027(3)
Ag11	0	0	-0.0097(7)	-0.0152(6)	-0.0110(5)
Cu11	0	0	-0.0097(7)	-0.0152(6)	-0.0110(5)
Ag12	0	0.005(4)	0	0.037(3)	0
Cu12	0	0.005(4)	0	0.037(3)	0
Ag13	0	-0.077(10)	-0.022(2)	-0.0023(5)	0.0016(4)
Cu13	0	-0.077(10)	-0.022(2)	-0.0023(5)	0.0016(4)
Ag14	0.0018(4)	0	-0.0038(6)	0	0.0015(2)
Cu14	0.0018(4)	0	-0.0038(6)	0	0.0015(2)
Ag15	0	0.0029(8)	0	0	0
Cu15	0	0.0029(8)	0	0	0
Ag16	0	-0.003(2)	0	0	0
Cu16	0	-0.003(2)	0	0	0

Table S7. Positional parameters of α-$Ag_{18}Cu_3Te_{11}Cl_3$ at 350 K.

Atom	Wyckhoff position	site	sof	x	y	z
Te1	4e	3.m	1	1	1	0.04590(3)
Te2	8h	3..	1	0.6667	0.3333	0.04561(2)
Te3	4e	3.m	1	1	1	0.17336(5)
Te4	8h	3..	1	0.6667	0.3333	0.17085(3)
Te5	12k	..m	1	0.66143(5)	0.66143(5)	0.11392(3)
Te6	12k	..m	1	1	0.66857(6)	0.11352(3)
Te7	6g	m2m	1	0.5602(2)	0	0.25
Te8	12j	m..	0.832(7)	0.3155(2)	0.1181(4)	0.25
Te9	12j	m..	0.168(7)	0.3377(14)	0.178(2)	0.25
Cl1	6f	..2/m	1	0.5	0	0
Cl2	12i	..2	1	0.83379(9)	0.6676(2)	0
Ag1	6g	m2m	0.390(9)	1	0.8964(6)	0.25
Cu1	6g	m2m	0.065(2)	1	0.8964(6)	0.25
Ag2	12j	m..	0.541(8)	0.6509(2)	0.4463(3)	0.25

Cu2	12*j*	*m*..	0.0901(13)	0.6509(2)	0.4463(3)	0.25
Ag3	12*k*	..*m*	0.252(11)	0.594(2)	0.594(2)	0.1948(3)
Cu3	12*k*	..*m*	0.042(2)	0.594(2)	0.594(2)	0.1948(3)
Ag4	12*k*	..*m*	0.383(7)	1	0.7856(6)	0.1932(2)
Cu4	12*k*	..*m*	0.0638(12)	1	0.7856(6)	0.1932(2)
Ag5	24*l*	1	0.242(7)	0.6399(8)	0.5076(8)	0.1979(4)
Cu5	24*l*	1	0.0403(11)	0.6399(8)	0.5076(8)	0.1979(4)
Ag6	24*l*	1	0.249(5)	0.5498(12)	0.845(2)	0.1839(3)
Cu6	24*l*	1	0.0415(9)	0.5498(12)	0.845(2)	0.1839(3)
Ag7	24*l*	1	0.436(6)	1.1184(3)	0.8700(4)	0.16349(11)
Cu7	24*l*	1	0.0726(10)	1.1184(3)	0.8700(4)	0.16349(11)
Ag8	24*l*	1	0.364(8)	0.4627(6)	0.5486(7)	0.1676(2)
Cu8	24*l*	1	0.0606(13)	0.4627(6)	0.5486(7)	0.1676(2)
Ag9	24*l*	1	0.429(7)	0.5793(6)	0.7838(6)	0.16452(12)
Cu9	24*l*	1	0.0715(12)	0.5793(6)	0.7838(6)	0.16452(12)
Ag10	24*l*	1	0.246(7)	0.5451(6)	0.4007(10)	0.1044(3)
Cu10	24*l*	1	0.0409(11)	0.5451(6)	0.4007(10)	0.1044(3)
Ag11	24*l*	1	0.356(5)	0.8884(4)	0.8059(3)	0.1083(2)
Cu11	24*l*	1	0.0594(9)	0.8884(4)	0.8059(3)	0.1083(2)
Ag12	24*l*	1	0.213(7)	0.7584(9)	0.5346(7)	0.1053(4)
Cu12	24*l*	1	0.0354(11)	0.7584(9)	0.5346(7)	0.1053(4)
Ag13	24*l*	1	0.211(6)	0.5327(12)	0.4197(12)	0.0693(4)
Cu13	24*l*	1	0.0352(10)	0.5327(12)	0.4197(12)	0.0693(4)
Ag14	24*l*	1	0.207(7)	0.7757(8)	0.5556(8)	0.0729(5)
Cu14	24*l*	1	0.0346(11)	0.7757(8)	0.5556(8)	0.0729(5)
Ag15	12*k*	..*m*	0.570(7)	1	0.8063(3)	0.0543(2)
Cu15	12*k*	..*m*	0.0951(12)	1	0.8063(3)	0.0543(2)
Ag16	24*l*	1	0.367(7)	0.6664(9)	0.5288(7)	0.0533(2)
Cu16	24*l*	1	0.0611(12)	0.6664(9)	0.5288(7)	0.0533(2)

Table S8. Anisotropic displacement parameters of α-Ag$_{18}$Cu$_3$Te$_{11}$Cl$_3$ at 350 K.

Atom	U_{11}	U_{22}	U_{33}	U_{12}	U_{13}	U_{23}
Te1	0.0516(3)	0.0516(3)	0.0249(4)	0.0258(2)	0	0
Te2	0.0595(3)	0.0595(3)	0.0262(3)	0.0297(2)	0	0
Te3	0.0590(4)	0.0590(4)	0.0623(7)	0.0295(2)	0	0
Te4	0.0611(3)	0.0611(3)	0.0562(5)	0.0306(2)	0	0
Te5	0.0583(3)	0.0583(3)	0.0588(5)	0.0225(3)	-0.0042(3)	-0.0042(3)
Te6	0.0617(4)	0.0645(4)	0.0568(5)	0.0308(2)	0	0.0009(3)
Te7	0.0619(6)	0.0645(7)	0.0703(6)	0.0323(3)	0	0
Te8	0.0462(6)	0.0382(11)	0.0413(8)	0.0119(5)	0	0
Te9	0.096(8)	0.18(2)	0.043(4)	0.106(10)	0	0
Ag1	0.069(3)	0.123(4)	0.153(5)	0.0346(13)	0	0
Cu1	0.069(3)	0.123(4)	0.153(5)	0.0346(13)	0	0
Ag2	0.0736(12)	0.0682(12)	0.112(2)	0.0412(8)	0	0
Cu2	0.0736(12)	0.0682(12)	0.112(2)	0.0412(8)	0	0
Ag3	0.178(10)	0.178(10)	0.135(7)	0.074(10)	0.079(6)	0.079(6)
Cu3	0.178(10)	0.178(10)	0.135(7)	0.074(10)	0.079(6)	0.079(6)
Ag4	0.121(3)	0.167(5)	0.092(3)	0.060(2)	0	-0.008(2)
Cu4	0.121(3)	0.167(5)	0.092(3)	0.060(2)	0	-0.008(2)
Ag5	0.138(5)	0.160(5)	0.186(7)	0.079(4)	-0.022(4)	-0.082(5)
Cu5	0.138(5)	0.160(5)	0.186(7)	0.079(4)	-0.022(4)	-0.082(5)
Ag6	0.173(7)	0.154(9)	0.102(4)	0.006(4)	-0.007(3)	0.021(5)
Cu6	0.173(7)	0.154(9)	0.102(4)	0.006(4)	-0.007(3)	0.021(5)
Ag7	0.098(2)	0.110(2)	0.105(2)	0.0431(13)	-0.0120(11)	-0.0194(12)
Cu7	0.098(2)	0.110(2)	0.105(2)	0.0431(13)	-0.0120(11)	-0.0194(12)
Ag8	0.165(4)	0.115(3)	0.117(3)	0.068(3)	0.066(3)	0.020(2)
Cu8	0.165(4)	0.115(3)	0.117(3)	0.068(3)	0.066(3)	0.020(2)
Ag9	0.109(2)	0.111(2)	0.093(2)	0.055(2)	0.013(2)	0.009(2)
Cu9	0.109(2)	0.111(2)	0.093(2)	0.055(2)	0.013(2)	0.009(2)
Ag10	0.139(4)	0.183(6)	0.406(11)	0.125(4)	0.156(5)	0.157(7)
Cu10	0.139(4)	0.183(6)	0.406(11)	0.125(4)	0.156(5)	0.157(7)
Ag11	0.074(2)	0.091(2)	0.297(5)	0.0124(11)	0.024(2)	0.050(2)
Cu11	0.074(2)	0.091(2)	0.297(5)	0.0124(11)	0.024(2)	0.050(2)
Ag12	0.144(5)	0.090(3)	0.368(12)	0.000(3)	0.011(3)	-0.060(5)
Cu12	0.144(5)	0.090(3)	0.368(12)	0.000(3)	0.011(3)	-0.060(5)
Ag13	0.157(7)	0.182(7)	0.172(7)	0.141(6)	0.071(5)	0.065(5)
Cu13	0.157(7)	0.182(7)	0.172(7)	0.141(6)	0.071(5)	0.065(5)
Ag14	0.119(7)	0.075(3)	0.169(10)	0.020(3)	-0.010(4)	0.000(4)
Cu14	0.119(7)	0.075(3)	0.169(10)	0.020(3)	-0.010(4)	0.000(4)
Ag15	0.166(3)	0.0973(13)	0.134(2)	0.083(2)	0	0.0400(10)
Cu15	0.166(3)	0.0973(13)	0.134(2)	0.083(2)	0	0.0400(10)
Ag16	0.163(6)	0.110(3)	0.137(3)	0.084(4)	0.019(3)	-0.042(2)
Cu16	0.163(6)	0.110(3)	0.137(3)	0.084(4)	0.019(3)	-0.042(2)

Table S9. Anharmonic displacement parameters of α-Ag$_{18}$Cu$_3$Te$_{11}$Cl$_3$ at 350 K.

Atom	C_{111}	C_{112}	C_{113}	C_{122}	C_{123}
Te7	-0.0055(3)	-0.0034(2)	0	-0.0034(2)	0
Te8	0.0005(3)	-0.0005(2)	0	0.0003(2)	0
Te9	-0.031(9)	-0.047(12)	0	-0.07(2)	0

Ag1	0	0.0063(8)	0	0.0063(8)	0
Cu1	0	0.0063(8)	0	0.0063(8)	0
Ag2	0	-0.0039(3)	0	-0.0055(4)	0
Cu2	0	-0.0039(3)	0	-0.0055(4)	0
Ag3	-0.007(4)	-0.009(3)	0	-0.009(3)	0
Cu3	-0.007(4)	-0.009(3)	0	-0.009(3)	0
Ag4	0	-0.0020(10)	-0.0026(4)	-0.0020(10)	-0.0013(2)
Cu4	0	-0.0020(10)	-0.0026(4)	-0.0020(10)	-0.0013(2)
Ag5	0	-0.009(2)	-0.0029(7)	-0.025(3)	0.0040(9)
Cu5	0	-0.009(2)	-0.0029(7)	-0.025(3)	0.0040(9)
Ag6	0.018(4)	0.015(2)	0	0.017(3)	0.0056(7)
Cu6	0.018(4)	0.015(2)	0	0.017(3)	0.0056(7)
Ag7	-0.0075(9)	-0.0034(4)	0.0032(2)	0	0.0025(2)
Cu7	-0.0075(9)	-0.0034(4)	0.0032(2)	0	0.0025(2)
Ag8	0.009(2)	0	0.0077(6)	0.0052(9)	0.0041(4)
Cu8	0.009(2)	0	0.0077(6)	0.0052(9)	0.0041(4)
Ag9	0.0028(10)	-0.0030(7)	0	-0.0083(8)	0
Cu9	0.0028(10)	-0.0030(7)	0	-0.0083(8)	0
Ag10	-0.058(5)	-0.062(6)	-0.052(3)	-0.063(7)	-0.051(4)
Cu10	-0.058(5)	-0.062(6)	-0.052(3)	-0.063(7)	-0.051(4)
Ag11	0.0087(7)	0.0067(5)	0	-0.0062(5)	-0.0023(3)
Cu11	0.0087(7)	0.0067(5)	0	-0.0062(5)	-0.0023(3)
Ag12	-0.029(6)	0.019(3)	-0.022(3)	-0.023(2)	0.0120(12)
Cu12	-0.029(6)	0.019(3)	-0.022(3)	-0.023(2)	0.0120(12)
Ag13	-0.029(5)	-0.040(5)	-0.016(2)	-0.053(6)	-0.021(2)
Cu13	-0.029(5)	-0.040(5)	-0.016(2)	-0.053(6)	-0.021(2)
Ag14	0.009(3)	-0.012(2)	-0.0120(13)	0	0.0023(5)
Cu14	0.009(3)	-0.012(2)	-0.0120(13)	0	0.0023(5)
Ag15	0	0.0129(7)	0.0118(5)	0.0129(7)	0.0059(3)
Cu15	0	0.0129(7)	0.0118(5)	0.0129(7)	0.0059(3)
Ag16	-0.013(4)	-0.019(3)	0.0091(8)	-0.017(2)	0.0047(4)
Cu16	-0.013(4)	-0.019(3)	0.0091(8)	-0.017(2)	0.0047(4)
	C_{133}	C_{222}	C_{223}	C_{233}	C_{333}
Te7	0.00010(2)	0	0	0	0
Te8	0.00009(2)	-0.0011(3)	0	-0.00015(2)	0
Te9	-0.0008(3)	-0.12(3)	0	-0.0013(5)	0
Ag1	0	0.041(3)	0	0	0
Cu1	0	0.041(3)	0	0	0
Ag2	0	-0.0060(6)	0	0	0
Cu2	0	-0.0060(6)	0	0	0
Ag3	0	-0.007(4)	0	0	0
Cu3	0	-0.007(4)	0	0	0
Ag4	0	-0.051(4)	0.0041(5)	0	0
Cu4	0	-0.051(4)	0.0041(5)	0	0
Ag5	-0.0014(4)	-0.051(4)	0.021(2)	-0.0101(8)	0.0041(4)
Cu5	-0.0014(4)	-0.051(4)	0.021(2)	-0.0101(8)	0.0041(4)
Ag6	0	-0.026(7)	-0.011(2)	-0.0016(4)	0
Cu6	0	-0.026(7)	-0.011(2)	-0.0016(4)	0
Ag7	0	0.0035(7)	0.0027(2)	0	0
Cu7	0	0.0035(7)	0.0027(2)	0	0
Ag8	0.0016(2)	0.009(2)	0.0039(5)	0.0014(2)	0
Cu8	0.0016(2)	0.009(2)	0.0039(5)	0.0014(2)	0
Ag9	-0.00052(8)	-0.0091(10)	0.0024(2)	0	0

Cu9	-0.00052(8)	-0.0091(10)	0.0024(2)	0	0
Ag10	-0.040(2)	-0.063(8)	-0.044(4)	-0.035(3)	-0.028(2)
Cu10	-0.040(2)	-0.063(8)	-0.044(4)	-0.035(3)	-0.028(2)
Ag11	-0.0031(3)	0	-0.0074(5)	-0.0148(5)	-0.0130(6)
Cu11	-0.0031(3)	0	-0.0074(5)	-0.0148(5)	-0.0130(6)
Ag12	0	0.003(2)	-0.007(2)	0.023(2)	-0.024(2)
Cu12	0	0.003(2)	-0.007(2)	0.023(2)	-0.024(2)
Ag13	-0.0036(4)	-0.066(7)	-0.026(2)	-0.0054(6)	0
Cu13	-0.0036(4)	-0.066(7)	-0.026(2)	-0.0054(6)	0
Ag14	0	0	0	0	0
Cu14	0	0	0	0	0
Ag15	0	0.0080(7)	0.0028(2)	0	0
Cu15	0	0.0080(7)	0.0028(2)	0	0
Ag16	0	-0.007(2)	0.0012(3)	0	0
Cu16	0	-0.007(2)	0.0012(3)	0	0

Table S10. Positional parameters of α-Ag$_{18}$Cu$_3$Te$_{11}$Cl$_3$ at 400 K.

Atom	Wyckhoff position	site	sof	x	y	z
Te1	4e	3.m	1	1	1	0.04577(5)
Te2	8h	3..	1	0.6667	0.3333	0.04573(4)
Te3	4e	3.m	1	1	1	0.17211(6)
Te4	8h	3..	1	0.6667	0.3333	0.17103(4)
Te5	12k	..m	1	0.66184(7)	0.66184(7)	0.11400(5)
Te6	12k	..m	1	1	0.66894(8)	0.11389(5)
Te7	6g	$m2m$	1	0.5513(4)	0	0.25
Te8	12j	m..	0.715(9)	0.3174(5)	0.1162(7)	0.25
Te9	12j	m..	0.285(9)	0.339(2)	0.184(3)	0.25
Cl1	6f	..2/m	1	0.5	0	0
Cl2	12i	..2	1	0.83382(14)	0.6676(3)	0
Ag1	6g	$m2m$	0.506(10)	1	0.8876(9)	0.25
Cu1	6g	$m2m$	0.084(2)	1	0.8876(9)	0.25
Ag2	12j	m..	0.455(8)	0.6701(6)	0.4423(5)	0.25
Cu2	12j	m..	0.0758(14)	0.6701(6)	0.4423(5)	0.25
Ag3	12k	..m	0.23(2)	0.613(2)	0.613(2)	0.1951(9)
Cu3	12k	..m	0.039(3)	0.613(2)	0.613(2)	0.1951(9)
Ag4	12k	..m	0.336(11)	1	0.7770(12)	0.1880(4)
Cu4	12k	..m	0.056(2)	1	0.7770(12)	0.1880(4)
Ag5	24l	1	0.197(9)	0.6505(11)	0.5064(12)	0.1952(7)
Cu5	24l	1	0.033(2)	0.6505(11)	0.5064(12)	0.1952(7)
Ag6	24l	1	0.235(10)	0.569(2)	0.8723(12)	0.1871(5)
Cu6	24l	1	0.039(2)	0.569(2)	0.8723(12)	0.1871(5)
Ag7	24l	1	0.408(9)	1.1232(6)	0.8768(6)	0.1693(4)
Cu7	24l	1	0.0680(14)	1.1232(6)	0.8768(6)	0.1693(4)
Ag8	24l	1	0.398(9)	0.469(2)	0.5511(13)	0.1715(5)
Cu8	24l	1	0.066(2)	0.469(2)	0.5511(13)	0.1715(5)
Ag9	24l	1	0.325(9)	0.5827(11)	0.7873(10)	0.1669(2)
Cu9	24l	1	0.054(2)	0.5827(11)	0.7873(10)	0.1669(2)
Ag10	24l	1	0.237(10)	0.5407(12)	0.393(2)	0.1055(8)
Cu10	24l	1	0.040(2)	0.5407(12)	0.393(2)	0.1055(8)

Ag11	24l	1	0.389(7)	0.8773(6)	0.7977(6)	0.1141(3)
Cu11	24l	1	0.0649(12)	0.8773(6)	0.7977(6)	0.1141(3)
Ag12	24l	1	0.292(11)	0.7686(14)	0.549(2)	0.1199(11)
Cu12	24l	1	0.049(2)	0.7686(14)	0.549(2)	0.1199(11)
Ag13	24l	1	0.232(9)	0.5310(14)	0.419(2)	0.0729(7)
Cu13	24l	1	0.039(2)	0.5310(14)	0.419(2)	0.0729(7)
Ag14	24l	1	0.201(9)	0.7801(13)	0.5435(8)	0.0813(4)
Cu14	24l	1	0.034(2)	0.7801(13)	0.5435(8)	0.0813(4)
Ag15	12k	..m	0.538(9)	1	0.8151(5)	0.0600(2)
Cu15	12k	..m	0.090(2)	1	0.8151(5)	0.0600(2)
Ag16	24l	1	0.285(9)	0.6630(13)	0.5229(11)	0.0556(5)
Cu16	24l	1	0.048(2)	0.6630(13)	0.5229(11)	0.0556(5)

Table S11. Anisotropic displacement parameters of α-Ag$_{18}$Cu$_3$Te$_{11}$Cl$_3$ at 400 K.

Atom	U_{11}	U_{22}	U_{33}	U_{12}	U_{13}	U_{23}
Te1	0.0629(6)	0.0629(6)	0.0366(7)	0.0315(3)	0	0
Te2	0.0661(4)	0.0661(4)	0.0408(5)	0.0330(2)	0	0
Te3	0.0676(6)	0.0676(6)	0.0688(11)	0.0338(3)	0	0
Te4	0.0729(5)	0.0729(5)	0.0670(8)	0.0365(3)	0	0
Te5	0.0662(5)	0.0662(5)	0.0770(9)	0.0291(5)	-0.0011(4)	-0.0011(4)
Te6	0.0717(7)	0.0705(6)	0.0740(9)	0.0359(4)	0	-0.0012(4)
Te7	0.0971(13)	0.0959(13)	0.0711(10)	0.0480(6)	0	0
Te8	0.064(2)	0.051(2)	0.060(2)	0.012(2)	0	0
Te9	0.089(9)	0.15(2)	0.062(5)	0.078(11)	0	0
Ag1	0.107(4)	0.125(4)	0.149(5)	0.053(2)	0	0
Cu1	0.107(4)	0.125(4)	0.149(5)	0.053(2)	0	0
Ag2	0.240(5)	0.096(3)	0.098(3)	0.067(3)	0	0
Cu2	0.240(5)	0.096(3)	0.098(3)	0.067(3)	0	0
Ag3	0.23(2)	0.23(2)	0.114(11)	0.04(2)	0.021(7)	0.021(7)
Cu3	0.23(2)	0.23(2)	0.114(11)	0.04(2)	0.021(7)	0.021(7)
Ag4	0.216(14)	0.250(11)	0.110(6)	0.108(7)	0	-0.054(4)
Cu4	0.216(14)	0.250(11)	0.110(6)	0.108(7)	0	-0.054(4)
Ag5	0.139(9)	0.134(8)	0.33(2)	0.053(6)	0.004(10)	-0.091(11)
Cu5	0.139(9)	0.134(8)	0.33(2)	0.053(6)	0.004(10)	-0.091(11)
Ag6	0.37(2)	0.211(10)	0.154(8)	0.180(9)	0.085(8)	0.039(6)
Cu6	0.37(2)	0.211(10)	0.154(8)	0.180(9)	0.085(8)	0.039(6)
Ag7	0.125(4)	0.187(5)	0.136(6)	0.054(4)	0.001(2)	-0.003(3)
Cu7	0.125(4)	0.187(5)	0.136(6)	0.054(4)	0.001(2)	-0.003(3)
Ag8	0.231(12)	0.165(8)	0.181(9)	0.119(8)	0.106(9)	0.070(7)
Cu8	0.231(12)	0.165(8)	0.181(9)	0.119(8)	0.106(9)	0.070(7)
Ag9	0.135(6)	0.176(7)	0.092(4)	0.087(5)	-0.006(3)	0.007(3)
Cu9	0.135(6)	0.176(7)	0.092(4)	0.087(5)	-0.006(3)	0.007(3)
Ag10	0.155(9)	0.25(2)	0.63(3)	0.159(10)	0.160(11)	0.26(2)
Cu10	0.155(9)	0.25(2)	0.63(3)	0.159(10)	0.160(11)	0.26(2)
Ag11	0.116(4)	0.132(3)	0.54(2)	0.026(2)	0.061(4)	-0.048(5)
Cu11	0.116(4)	0.132(3)	0.54(2)	0.026(2)	0.061(4)	-0.048(5)
Ag12	0.156(9)	0.203(14)	0.91(5)	0.087(9)	0.13(2)	0.21(2)
Cu12	0.156(9)	0.203(14)	0.91(5)	0.087(9)	0.13(2)	0.21(2)
Ag13	0.198(9)	0.234(12)	0.194(12)	0.183(9)	0.119(7)	0.110(8)
Cu13	0.198(9)	0.234(12)	0.194(12)	0.183(9)	0.119(7)	0.110(8)

Atom					
Ag14	0.171(9)	0.077(4)	0.272(10)	0.003(4)	-0.028(6)	-0.089(5)
Cu14	0.171(9)	0.077(4)	0.272(10)	0.003(4)	-0.028(6)	-0.089(5)
Ag15	0.449(10)	0.178(4)	0.175(4)	0.225(5)	0	0.048(2)
Cu15	0.449(10)	0.178(4)	0.175(4)	0.225(5)	0	0.048(2)
Ag16	0.197(12)	0.131(6)	0.145(6)	0.107(7)	-0.013(4)	-0.067(4)
Cu16	0.197(12)	0.131(6)	0.145(6)	0.107(7)	-0.013(4)	-0.067(4)

Table S12. Anharmonic displacement parameters of α-Ag$_{18}$Cu$_3$Te$_{11}$Cl$_3$ at 400 K.

Atom	C_{111}	C_{112}	C_{113}	C_{122}	C_{123}
Te7	-0.0110(8)	-0.0065(4)	0	-0.0065(4)	0
Te8	0.0018(6)	-0.0005(4)	0	0.0000(4)	0
Te9	-0.019(7)	-0.024(10)	0	-0.040(14)	0
Ag1	0	0.0101(13)	0	0.0101(13)	0
Cu1	0	0.0101(13)	0	0.0101(13)	0
Ag2	0.163(8)	0	0	-0.0171(13)	0
Cu2	0.163(8)	0	0	-0.0171(13)	0
Ag3	0	0.014(8)	-0.009(2)	0.014(8)	0
Cu3	0	0.014(8)	-0.009(2)	0.014(8)	0
Ag4	0	0	-0.018(2)	0	-0.0092(11)
Cu4	0	0	-0.018(2)	0	-0.0092(11)
Ag5	0	-0.015(3)	-0.014(2)	0	-0.013(2)
Cu5	0	-0.015(3)	-0.014(2)	0	-0.013(2)
Ag6	0.25(2)	0.21(2)	0.025(3)	0.144(14)	0.025(2)
Cu6	0.25(2)	0.21(2)	0.025(3)	0.144(14)	0.025(2)
Ag7	-0.005(2)	0	0.0035(5)	0.018(2)	0.0040(5)
Cu7	-0.005(2)	0	0.0035(5)	0.018(2)	0.0040(5)
Ag8	0.045(11)	0.025(7)	0.016(3)	0.033(7)	0.015(2)
Cu8	0.045(11)	0.025(7)	0.016(3)	0.033(7)	0.015(2)
Ag9	0.017(3)	0.010(2)	0	0	0.0013(3)
Cu9	0.017(3)	0.010(2)	0	0	0.0013(3)
Ag10	-0.014(7)	-0.035(9)	-0.025(5)	-0.068(13)	-0.039(6)
Cu10	-0.014(7)	-0.035(9)	-0.025(5)	-0.068(13)	-0.039(6)
Ag11	-0.012(2)	0	-0.0061(11)	-0.0052(11)	0
Cu11	-0.012(2)	0	-0.0061(11)	-0.0052(11)	0
Ag12	-0.064(10)	-0.016(6)	-0.016(5)	0.028(7)	0.021(4)
Cu12	-0.064(10)	-0.016(6)	-0.016(5)	0.028(7)	0.021(4)
Ag13	-0.048(8)	-0.059(8)	-0.018(2)	-0.075(10)	-0.025(3)
Cu13	-0.048(8)	-0.059(8)	-0.018(2)	-0.075(10)	-0.025(3)
Ag14	0.048(11)	-0.012(4)	-0.030(3)	0	0.0084(13)
Cu14	0.048(11)	-0.012(4)	-0.030(3)	0	0.0084(13)
Ag15	0	0.089(5)	0.084(4)	0.089(5)	0.042(2)
Cu15	0	0.089(5)	0.084(4)	0.089(5)	0.042(2)
Ag16	-0.031(8)	-0.039(7)	0.014(2)	-0.031(5)	0.0072(12)
Cu16	-0.031(8)	-0.039(7)	0.014(2)	-0.031(5)	0.0072(12)
	C_{133}	C_{222}	C_{223}	C_{233}	C_{333}
Te7	0.00013(5)	0	0	0	0
Te8	0.00013(4)	-0.0006(7)	0	-0.00036(5)	0
Te9	-0.0012(3)	-0.07(3)	0	-0.0017(5)	0
Ag1	0	0.015(3)	0	0	0
Cu1	0	0.015(3)	0	0	0

Ag2	-0.0016(2)	-0.021(2)	0	0	0
Cu2	-0.0016(2)	-0.021(2)	0	0	0
Ag3	0	0	-0.009(2)	0	0
Cu3	0	0	-0.009(2)	0	0
Ag4	0	-0.100(13)	0.010(2)	0	0
Cu4	0	-0.100(13)	0.010(2)	0	0
Ag5	0	-0.027(6)	0.015(3)	-0.017(2)	0.0089(14)
Cu5	0	-0.027(6)	0.015(3)	-0.017(2)	0.0089(14)
Ag6	0	0.073(10)	0.012(2)	0	0
Cu6	0	0.073(10)	0.012(2)	0	0
Ag7	0	0.034(4)	0.0112(9)	0	0.0014(2)
Cu7	0	0.034(4)	0.0112(9)	0	0.0014(2)
Ag8	0.0043(10)	0.035(7)	0.017(2)	0.0053(9)	0.0016(4)
Cu8	0.0043(10)	0.035(7)	0.017(2)	0.0053(9)	0.0016(4)
Ag9	-0.0009(2)	-0.009(3)	0.0057(6)	0	0
Cu9	-0.0009(2)	-0.009(3)	0.0057(6)	0	0
Ag10	-0.038(5)	-0.10(2)	-0.044(9)	-0.044(6)	-0.046(5)
Cu10	-0.038(5)	-0.10(2)	-0.044(9)	-0.044(6)	-0.046(5)
Ag11	-0.0180(13)	0	0.018(2)	-0.026(2)	-0.0143(12)
Cu11	-0.0180(13)	0	0.018(2)	-0.026(2)	-0.0143(12)
Ag12	0.021(5)	0.09(2)	0.051(7)	0.042(4)	0
Cu12	0.021(5)	0.09(2)	0.051(7)	0.042(4)	0
Ag13	-0.0033(7)	-0.092(12)	-0.032(3)	-0.0060(9)	0.0012(5)
Cu13	-0.0033(7)	-0.092(12)	-0.032(3)	-0.0060(9)	0.0012(5)
Ag14	-0.0033(10)	-0.013(3)	0.017(2)	-0.017(2)	0.0150(12)
Cu14	-0.0033(10)	-0.013(3)	0.017(2)	-0.017(2)	0.0150(12)
Ag15	0	0.063(4)	0.0204(10)	0.0015(2)	0
Cu15	0	0.063(4)	0.0204(10)	0.0015(2)	0
Ag16	0	-0.016(4)	0.0032(7)	0	0
Cu16	0	-0.016(4)	0.0032(7)	0	0

For a more realistic evaluation of atom positions and bond lengths in the case of anharmonic refinement, so called "mode positions" that represent the maximum of electron density were determined by calculating pdf (probability density functions). Mode positions of all refinements are given in **Table S13-S16**.

Table S13. Mode positions of anharmonic refined atoms in β-$Ag_{18}Cu_3Te_{11}Cl_3$ at 270 K.

Atom	x	y	z
AgCu1	0	0.8875	0.25
AgCu2	0.6527	0.4526	0.25
AgCu3	0.578	0.578	0.1924
AgCu4	0	0.799	0.193
AgCu5	0.634	0.5134	0.1944
AgCu6	0.5519	0.8487	0.185
AgCu7	0.123	0.8577	0.1606
AgCu8	0.4693	0.5512	0.1687

AgCu9	0.5843	0.7921	0.1641
AgCu10	0.5614	0.4156	0.1205
AgCu11	0.8866	0.8183	0.1172
AgCu12	0.7727	0.5178	0.114
AgCu13	0.5274	0.4213	0.0706
AgCu14	0.769	0.5622	0.0715
AgCu15	0	0.8024	0.0489
AgCu16	0.6718	0.5322	0.0483

Table S14. Mode positions of anharmonic refined atoms in α-Ag$_{18}$Cu$_3$Te$_{11}$Cl$_3$ at 330 K.

Atom	x	y	z
Te7	0.5666	0	0.25
Te8	0.3129	0.1225	0.25
Te9	0.3515	0.2026	0.25
AgCu1	0	0.8837	0.25
AgCu2	0.6511	0.4504	0.25
AgCu3	0.5829	0.5829	0.1926
AgCu4	0	0.7958	0.192
AgCu5	0.634	0.5228	0.1932
AgCu6	0.5492	0.8539	0.1857
AgCu7	0.1218	0.8671	0.162
AgCu8	0.4595	0.5435	0.1666
AgCu9	0.584	0.7882	0.1636
AgCu10	0.5526	0.4046	0.1138
AgCu11	0.884	0.8156	0.1172
AgCu12	0.7716	0.5206	0.1149
AgCu13	0.5412	0.4367	0.073
AgCu14	0.7789	0.5567	0.0715
AgCu15	0	0.8022	0.0517
AgCu16	0.6712	0.5324	0.0529

Table S15. Mode positions of anharmonic refined atoms in α-Ag$_{18}$Cu$_3$Te$_{11}$Cl$_3$ at 350 K.

Atom	x	y	z
Te7	0.566	0	0.25
Te8	0.3125	0.1218	0.25
Te9	0.3498	0.2011	0.25
AgCu1	0	0.8811	0.25
AgCu2	0.653	0.4512	0.25
AgCu3	0.5972	0.5972	0.1939
AgCu4	0	0.8002	0.1932
AgCu5	0.6399	0.5016	0.1941
AgCu6	0.5401	0.8506	0.1874
AgCu7	0.1202	0.8673	0.1607
AgCu8	0.4602	0.546	0.1652
AgCu9	0.5831	0.7861	0.1625
AgCu10	0.5542	0.408	0.1125
AgCu11	0.8873	0.8149	0.1171

AgCu12	0.7676	0.5208	0.1158
AgCu13	0.5359	0.4284	0.0726
AgCu14	0.7712	0.5612	0.0791
AgCu15	0	0.8033	0.0501
AgCu16	0.6736	0.5291	0.0514

Table S16. Mode positions of anharmonic refined atoms in α-$Ag_{18}Cu_3Te_{11}Cl_3$ at 400 K.

Atom	x	y	z
Te7	0.5594	0	0.25
Te8	0.3131	0.1204	0.25
Te9	0.3531	0.2034	0.25
AgCu1	0	0.8786	0.25
AgCu2	0.6549	0.4491	0.25
AgCu3	0.6079	0.6079	0.2001
AgCu4	0	0.7927	0.1892
AgCu5	0.6446	0.5038	0.1953
AgCu6	0.5482	0.8677	0.1877
AgCu7	0.17	0.8714	0.1631
AgCu8	0.4597	0.5488	0.1664
AgCu9	0.5825	0.7867	0.1652
AgCu10	0.5505	0.4045	0.1128
AgCu11	0.8873	0.8149	0.1171
AgCu12	0.7676	0.5208	0.1158
AgCu13	0.5359	0.4284	0.0726
AgCu14	0.7712	0.5612	0.0791
AgCu15	0	0.8033	0.0501
AgCu16	0.6736	0.5291	0.0514

EDX measurements.

Area measurements have been performed on one crystal facet of two different single crystals. The average Ag:Cu ratio is 52.71:8.66, or 6.09:1, matching the initial composition of $Ag_{18}Cu_3Te_{11}Cl_3$.

Table S17. EDX data of two crystal faces of different $Ag_{18}Cu_3Te_{11}Cl_3$ single crystals. The estimated overall error of each data point is larger than +/- 1%.

	Ag [at%]	Cu [at%]	Te [at%]	Cl [at%]
$Ag_{18}Cu_3Te_{11}Cl_3$ theoretical	51.43	8.57	31.43	8.57
crystal 1	51(1)	9(1)	30(1)	10(1)
crystal 2	54(1)	8(1)	29(1)	9(1)
Average	52.5	8.5	29.5	9.5

Bulk modulus determiation

The bulk modulus was determined to $K_0 = 28.2(11)$ GPa by a 3rd order Birch-Murnaghan Equation of State fit. 2nd and 3rd order fits are given in **Figure S4**. Unit cell parameters determined from pressure dependent XRD are shown in **Table S18**.
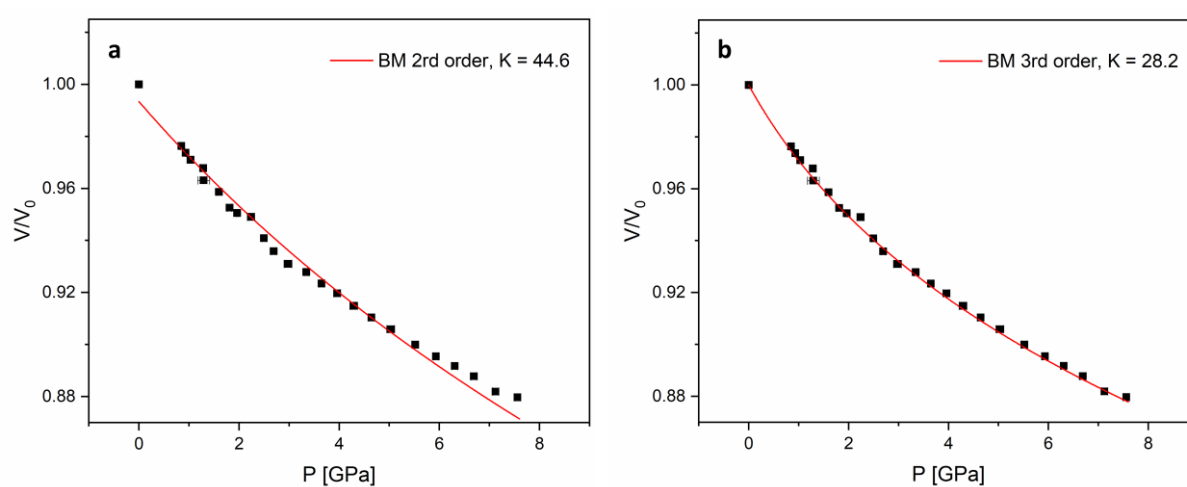

Figure S4. Data of bulk modulus measurements. 2nd (a) and 3rd (b) order Birch-Murnaghan Equation of State fit for $Ag_{18}Cu_3Te_{11}Cl_3$. Data according to **Table S18** are used. The error bars are located within the measurement points.

Table S18. Unit cell parameters determined from pressure-dependent XRD experiments. Pressure was applied via a Diamond-Anvil cell, and XRD data were collected at the Diamond Light Source, Ditcot, UK, using Synchrotron radiation.

Pressure [Gpa]	a [Å]	c [Å]	V [Å^3]	Profile R_p	Profile wR_p
0	13.5506(12)	30.772(2)	4893.4(7)	-	-
0.85	13.434(2)	30.5692(14)	4777(2)	0.0212	0.0621
0.93	13.4211(8)	30.543(2)	4764.4(9)	0.0106	0.0221
1.03	13.4103(14)	30.508(4)	4751(2)	0.0119	0.0308
1.28	13.3953(14)	30.475(4)	4735(2)	0.0125	0.0318
1.29	13.3753(12)	30.419 (3)	4712.7(13)	0.0111	0.0236
1.60	13.3542(14)	30.374(4)	4691(2)	0.0134	0.035
1.81	13.3281(13)	30.300(4)	4661(2)	0.0131	0.0301
1.96	13.319(2)	30.275(4)	4651(2)	0.0125	0.0282
2.24	13.3157(10)	30.242(4)	4643.6(14)	0.0151	0.0341
2.50	13.2841(12)	30.126(6)	4604(2)	0.0222	0.0415
2.69	13.2668(10)	30.044(4)	4579.3(14)	0.0226	0.0416
2.98	13.2418(11)	30.001(5)	4556(2)	0.0223	0.0418
3.34	13.2186(8)	30.004(4)	4540.1(12)	0.0205	0.0393
3.65	13.1974(2)	29.958(3)	4518.7(6)	0.0204	0.0391
3.96	13.1793(8)	29.917(3)	4500.1(11)	0.0207	0.0387
4.29	13.1560(9)	29.866(4)	4476.6(11)	0.021	0.0393
4.64	13.1347(9)	29.816(3)	4454.6(12)	0.0209	0.0384
5.03	13.1123(9)	29.770(3)	4432.5(11)	0.0208	0.0376
5.52	13.0836(9)	29.704(4)	4403.4(11)	0.0201	0.0365
5.93	13.0624(9)	29.653(4)	4381.6(11)	0.0201	0.0366
6.31	13.0448(9)	29.610(4)	4363.4(11)	0.0196	0.0348
6.69	13.0263(10)	29.562(4)	4344.0(13)	0.0197	0.035
7.12	12.9919(10)	29.523(4)	4315.4(12)	0.0191	0.0347
7.56	12.9848(2)	29.481(5)	4305(2)	0.0196	0.0354

Solid-state NMR
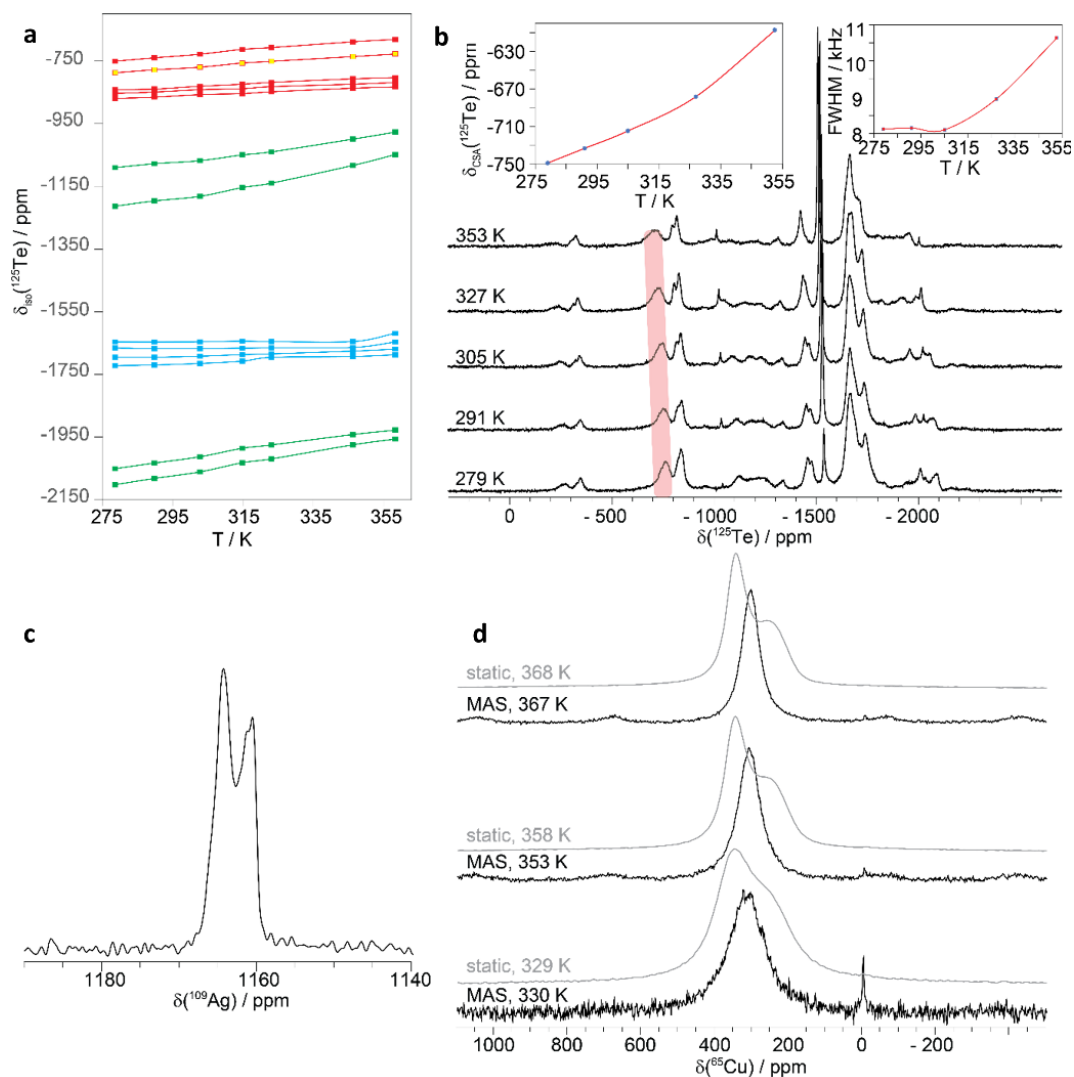
Figure S5. Solid-state NMR Data. a) Drift of the ^{125}Te isotropic chemical shifts with temperature, from the spectra shown in Figure 4. b) ^{125}Te MAS spectra (ν_{rot} = 62.5 kHz) for the ^{125}Te-enriched $Ag_{18}Cu_3Te_{11}Cl_3$ sample at different temperature. The chemical shift anisotropy and full width at half maximum as a function of temperature are shown as insets. c) ^{109}Ag MAS spectrum (ν_{rot} = 40.0 kHz) of $Ag_{18}Cu_3Te_{11}Cl_3$ acquired at room temperature. d) ^{65}Cu MAS spectrum (black, ν_{rot} = 62.5 kHz) compared to the static spectra (grey) of $Ag_{18}Cu_3Te_{11}Cl_3$ at different temperatures.

U/I-measurements

In order to rule out the formation of Schottky diodes during the measurements, $Ag_{18}Cu_3Te_{11}Cl_3$ and AgCuS crystals were tested with tin-lead instead of indium contacts.[14] **Figure S6a** shows $Ag_{18}Cu_3Te_{11}Cl_3$ contacted with tin/lead solder. It was measured isothermally at 281 K (blue curve) and within a 295-308 K temperature gradient (red curve). At 281 K we observed an almost symmetric, ohmic behavior while a diode curve was found for the 295-308 K temperature gradient. The result indicates the successful preparation of a pn-junction independent from the solder material. The same set of experiments was performed with the pnp-switching material AgCuS (**Figure S6b**).[14] This material shows a pn-transition at 361 K. An isothermal measurement was performed at 298(1) K. The temperature gradient, also leading to a diode curve was set to 333 to 365 K. The successful generation pn-junctions in the case of In (see main text) and tin/lead contacts substantiates that pnp-switching materials can be used for diodes in general.
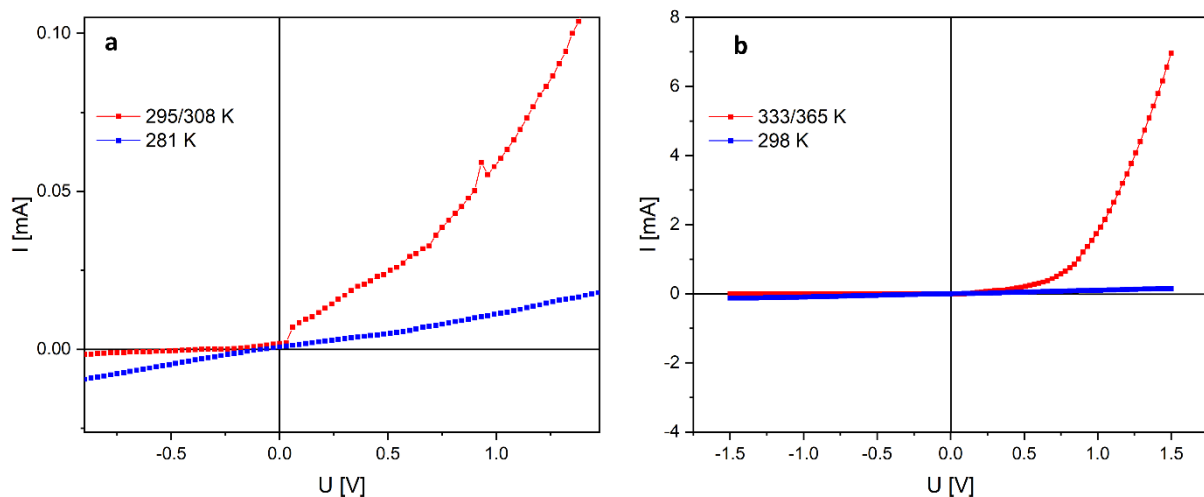
Figure S6. a) U/I measurements on $Ag_{18}Cu_3Te_{11}Cl_3$ contacted with tin/lead. Blue: isothermal at 281 K. Red: with a 295/308 K temperature gradient. b) U/I measurements on AgCuS.[13] Blue: isothermal at 298 K. Red: with a 333/365 K temperature gradient.

Schockley-Queisser limit

In 2016, Rühle published a collection of data summarizing the solar cell performance at that time (**Figure S7**).[14] $Ag_{18}Cu_3Te_{11}Cl_3$ shows an almost perfect bandgap for the realization of single junction solar cells as it is perfectly located in the efficiency maximum according to the Schockley-Queisser limit.[15]
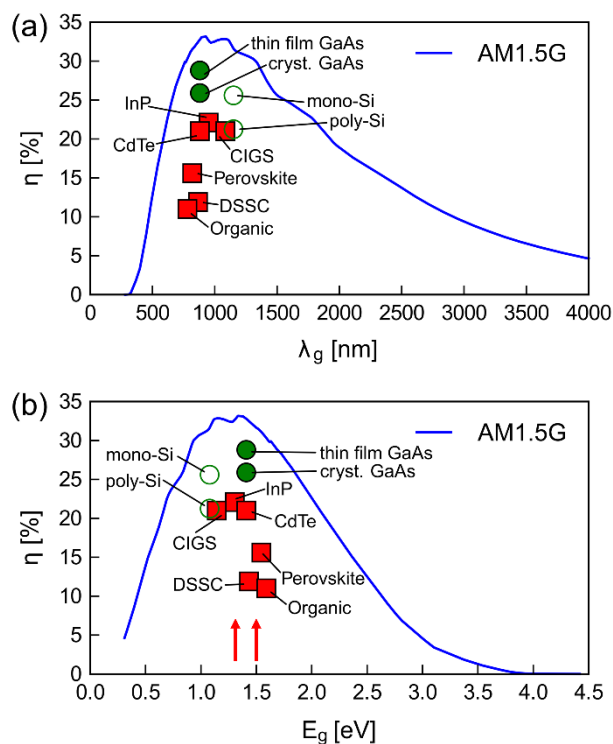
Figure S7. Schockley-Queisser limit or the maximum light to electric power conversion efficiency at 298.15K (AM1.5G source) with a) band gap wavelengths and b) energies. Red arrows denote the band gaps of 1.35 and 1.50 eV measured for $Ag_{18}Cu_3Te_{11}Cl_3$. Reprinted from *Solar Energy*, *130*, Rühle, S., Tabulated values of the Schockley-Queisser limit for single junction solar cells, 139-147, Copyright (2016), with permission from Elsevier.[14]

References (Supplement section)

[1]   A. Vogel, T. Nilges, *Inorg. Chem.* **2021**, *60*(20), 15233.

[2]   S. Lange, T. Nilges, *Chem. Mater.* **2006**, *18*(10), 2538.

[3]   S. Lange, M. Bawohl, D. Wilmer, H.-W. Meyer, H.-D. Wiemhöfer, T. Nilges, *Chem. Mater.* **2007**, *19*(6), 1401.

[4]   A. Vogel, T. Miller, C. Hoch, M. Jakob, O. Oeckler, T. Nilges, *Inorg. Chem.* **2019**, *58*(9), 6222.

[5]   R. Blachnik, H. A. Dreisbach, *J. Solid State Chem.* **1985**, *60*(1), 115.

[6]   T. Nilges, S. Nilges, A. Pfitzner, T. Doert, P. Böttcher, *Chem. Mater.* **2004**, *16*(5), 806.

[7]   J. Peters, O. Conrad, B. Bremer, B. Krebs, *Z. Anorg. Allg. Chem.* **1996**, *622*(11), 1823.

[8]   T. Nilges, S. Lange, M. Bawohl, J. M. Deckwart, M. Janssen, H.-D. Wiemhöfer, R. Decourt, B. Chevalier, J. Vannahme, H. Eckert, R. Weihrich, *Nat. Mater.* **2009**, *8*(2), 101.

[9]   W. F. Kuhs, *Acta Cryst A* **1992**, *48*(2), 80.

[10]   T. Nilges, S. Reiser, J. H. Hong, E. Gaudin, A. Pfitzner, *PCCP* **2002**, *4*(23), 5888.

[11]   S. Yanagisawa, M. Tashiro, S. Anzai, *J. Inorg. Nucl. Chem.* **1969**, *31*(4), 943.

[12]   P. Böttcher, J. Getzschmann, R. Keller, *Z. Anorg. Allg. Chem.* **1993**, *619*(3), 476.

[13]   S. N. Guin, J. Pan, A. Bhowmik, D. Sanyal, U. V. Waghmare, K. Biswas, *J. Am. Chem. Soc.* **2014**, *136*(36), 12712.

[14]   S. Rühle, *Sol. Energy* **2016**, *130*139.

[15]   W. Shockley, H. J. Queisser, *J. Appl. Phys.* **1961**, *32*(3), 510.

4 Zusammenfassung und Ausblick

Im Rahmen dieser Arbeit wurde die Substanzklasse der Münzmetall(poly)chalkogenid-halogenide untersucht, deren Vertreter sich durch komplexe Anionenteilstrukturen und hohe Ionenmobilität auszeichnen, welche üblicherweise zu zahlreichen Ordnungs-Unordnungs-Phasenübergängen führt. Diese Eigenschaften bringen das Potential zu hoher thermoelektrischer Leistungsfähigkeit sowie außergewöhnlichen elektronischen Eigenschaften, wie reversible Schaltung zwischen p- und n-Halbleitung, mit sich.

Der Materialklasse wurden drei neue Verbindungen hinzugefügt: $Cu_{9,1}Te_4Cl_3$, $Cu_{20}Te_{11}Cl_3$ und $Ag_{18}Cu_3Te_{11}Cl_3$.

$Cu_{9,1}Te_4Cl_3$ ist der erste Vertreter der Münzmetallpolychalkogenidhalogenide, der ausschließlich Cu als Münzmetall enthält. Die Verbindung wurde thermoelektrisch charakterisiert und zeigt neben hoher elektrischer Leitfähigkeit äußerst niedrige Wärmeleitfähigkeit. Diese Eigenschaften führen ohne weitere Optimierung zu einem thermoelektrischen Gütefaktor ZT des Bulk-Materials von 0,15 bei 523 K. Zwei Polymorphe der tetramorphen Verbindung wurden kristallchemisch charakterisiert.

$Cu_{20}Te_{11}Cl_3$ ist trimorph und bewegt sich hinsichtlich der thermoelektrischen Leistungsfähigkeit in der gleichen Größenordnung wie $Cu_{9,1}Te_4Cl_3$. Zwei der drei Polymorphe wurden strukturchemisch charakterisiert. Die Verbindung zeigt äußerst komplexe Kristallchemie, da der Symmetrieabstieg vom hexagonalen ins orthorhombische Kristallsystem zu systematischer Verdrilligung führt.

Beide neuen Cu-Verbindungen zeigen große strukturelle Ähnlichkeit zur bekannten pnp-schaltenden Verbindung $Ag_{10}Te_4Br_3$, weisen aber selbst keinen pnp-Übergang auf. Dieses Verhalten eröffnete die Möglichkeit durch Vergleich der Systeme den Mechanismus der pnp-Schaltung in $Ag_{10}Te_4Br_3$ zu untersuchen und die erhaltenen Erkenntnisse zur Modifikation und Optimierung der Cu-Verbindungen zu benutzen. Im Rahmen dessen gelang es durch Kationensubstitution in $Cu_{20}Te_{11}Cl_3$ die neue pnp-schaltende Verbindung $Ag_{18}Cu_3Te_{11}Cl_3$ zu synthetisieren. Diese weist nicht nur den höchsten bisher gemessenen Sprung des Seebeck-Koeffizienten auf, sondern zeigt ihr schaltendes Verhalten auch als erstes Material bei Raumtemperatur. Die beiden an der Schaltung beteiligten Polymorphe der trimorphen Verbindung wurden kristallchemisch charakterisiert und es wurde ein Mechanismus für die pnp-Schaltung vorgeschlagen und diskutiert. Durch Anlegen eines Temperaturgradienten über den pn-Übergang hinweg wurde durch Aufnahme der Strom/Spannungs-Kennlinie die erste schaltbare Einkomponenten-Diode nachgewiesen.

Da die thermoelektrischen Eigenschaften der Cu-Verbindungen am Bulk-Material gemessen und noch keine Optimierungsversuche unternommen wurden, bieten sich noch zahlreiche Möglichkeiten die thermoelektrische Leistungsfähigkeit zu verbessern.

Neben Substitutionen des Chalkogens und des Halogens sowie Doping, welche die elektrische Leitfähigkeit und den Seebeck-Koeffizienten beeinflussen, können Versuche zur Nanostrukturierung unternommen werden um die Wärmeleitfähigkeit weiter zu senken.

Der schaltbare pn-Übergang bei Raumtemperatur eröffnet zahlreiche Anwendungs-möglichkeiten im Bereich der Elektronik und der Energiekonvertierung. Eine sich durch die Erwärmung der Sonneneinstrahlung selbst einschaltende Solarzelle wäre vorstellbar, genauso wie die Anwendung der durch den pn-Übergang generierten Ladungstrennung zur Wasserspaltung oder Elektrokatalyse. Der nächste Schritt nach der Realisierung einer schaltbaren Einkomponenten-Diode wäre die Erzeugung eines temperaturgesteu-erten Bipolar- oder Feldeffekttansistors. Die pn-Schaltung kann dabei entweder durch einen Heizdraht oder ortsunabhängig durch Laserheizung ausgelöst werden. Da der lasergeheizte Punkt dabei fast beliebig verkleinert werden kann, ist eine Anwendung als Nano-Transistor denkbar.

5 Veröffentlichungen

Artikel

- **Anna Vogel**, Alfred Rabenbauer, Philipp Deng, Ruben Steib, Thorben Böger, Wolfgang Zeier, Renée Siegel, Jürgen Senker, Dominik Deisenberger, Katharina Nisi, Alexander Holleitner, Janio Venturini und Tom Nilges ‚A switchable one-component diode', *Adv. Mater.* **2022**, 2208698.

- **Anna Vogel** und Tom Nilges ‚Ion dynamics and polymorphism in $Cu_{20}Te_{11}Cl_3$', *Inorg. Chem.* **2021**, *60*(20), 15233–15241.

- **Anna Vogel**, Thomas Miller, Constantin Hoch, Matthias Jakob, Oliver Oeckler und Tom Nilges ‚$Cu_{9,1}Te_4Cl_3$: A thermoelectric compound with low thermal and high electrical conductivity', *Inorg. Chem.* **2019**, *58*(9), 6222–6230.

- Felix Reiter, Markus Pielmeier, **Anna Vogel**, Christian Jandl, Milivoj Plodinec, Christian Rohner, Thomas Lunkenbein, Katharina Nisi, Alexander Holleitner und Tom Nilges ‚SnBrP - A SnIP-type representative in the Sn-Br-P system', *Z. Anorg. Allg. Chem.* **2022**, e202100347.

- David N. Purschke, Markus R. P. Pielmeier, Ebru Üzer, Claudia Ott, Charles Jensen, Annabelle Degg, **Anna Vogel**, Naaman Amer, Tom Nilges und Frank A. Hegmann ‚Ultrafast Photoconductivity and Terahertz Vibrational Dynamics in Double-Helix SnIP Nanowires', *Adv. Mater.* **2021**, *33*(34), 2100978.

- Claudia Ott,Felix Reiter, Maximilian Baumgartner, Markus Pielmeier, **Anna Vogel**, Patrick Walke, Stefan Burger, Michael Ehrenreich, Gregor Kieslich, Dominik Daisenberger, Jeff Armstrong, Thakur Ujwal Kumare, Pawan Kumar, Shunda Chen, Davide Donadio, Lisa S. Walter, R. Thomas Weitz, Karthik Shankar und Tom Nilges ‚Flexible and ultra-soft inorganic 1D semiconductor and heterostructure systems based on SnIP', *Adv. Funct. Mater.* **2019**, *29*(18), 1900233.

- Maximilian Baumgartner, Thomas Wylezich, Franziska Baumer, Markus Pielmeier, **Anna Vogel**, Richard Weihrich und Tom Nilges ‚$NaP_{7-x}As_x$, tuning of electronic properties in a polypnictide and heading towards helical one-dimensional semiconductors', *Z. Anorg. Allg. Chem.* **2017**, *634*(23), 1881–1887.

Posterpräsentationen

- ‚$Cu_9Te_4Cl_3$ and $Ag_{10}Te_4Br_3$ - Mechanism of p-n-p-Switching in Thermoelectric Compounds‘, *19th International Symposium on the Reactivity of Solids*, Bayreuth, Deutschland, Juli **2018**.

- ‚$Cu_9Te_4Cl_3$ and $Ag_{10}Te_4Br_3$ - Investigation of p-n-p-Switching in Thermoelectric Compounds‘, *e-conversion Conference*, Venedig, Italien, September **2019**.

- ‚$Ag_{18}Cu_3Te_{11}Cl_3$ - Reversible switching between p- and n-type conduction‘, *Online-Vortragstagung für Anorganische Chemie der Fachgruppen Wöhler-Vereinigung und Festkörperchemie und Materialforschung*, Köln, Deutschland, September **2020**, online.

- ‚$Ag_{18}Cu_3Te_{11}Cl_3$ - Reversible switching between p- and n-type conduction‘, *e-conversion Poster Sessions*, München, Deutschland, September **2021**.

- ‚Polimorphism in $Cu_{20}Te_{11}Cl_3$‘, *30. Jahrestagung der Deutschen Gesellschaft für Kristallographie (DGK)*, München, Deutschland, März **2022**.

Literatur

[1] Bell, L. E. Cooling, Heating, Generating Power, and Recovering Waste Heat with Thermoelectric Systems. *Sience* **2008**, *321*(5895), 1457–1461.

[2] Harman T. C.; Taylor P. J.; Walshand M. P.; LaForge B. E. Quantum Dot Superlattice Thermoelectric Materials and Devices. *Science* **2002**, *297*(5590), 2229–2232.

[3] Mao, J.; Liu, Z.; Ren, Z. Size effect in thermoelectric materials. *npj Quant. Mater.* **2016**, *1*, 16028.

[4] Liu, M.; Yazdani, N.; Yarema, M.; Jansen, M.; Wood, V.; Sargent, E. H. Colloidal quantum dot electronics. *Nat. Electron.* **2021**, *4*, 548–558.

[5] Vining, C. B. An inconvenient truth about thermoelectrics. *Nat. Mater.* **2009**, *8*(2), 83–85.

[6] Sales, B. C. Critical Overview of Recent Approaches to Improved Thermoelectric Materials. *Int. J. Appl. Ceram. Technol.* **2007**, *4*(4), 291–296.

[7] Nilges, T.; Bawohl, M.; Lange, S.; Messel, J.; Osters, O. Highly Dynamic Chalcogen Chains in Silver(I) (Poly)Chalcogenide Halides: a New Concept for Thermoelectrics? *J. Electron. Mater.* **2010**, *39*(9), 2096–2104.

[8] Nilges, T.; Bawohl, M.; Osters, O.; Lange, S.; Messel, J. Silver (I)-(poly) chalcogenide Halides–Ion and Electron High Potentials. *Z. Phys. Chem.* **2010**, *224*, 1505–1531.

[9] Nilges, T.; Lange, S.; Bawohl, M.; Deckwart, J. M.; Janssen, M.; Wiemhöfer, H.-D.; Decourt, R.; Chevalier, B.; Vannahme, J.; Eckert, H.; Weihrich, R. Reversible switching between p- and n-type conduction in the semiconductor $Ag_{10}Te_4Br_3$. *Nat. Mater.* **2009**, *8*(2), 101–108.

[10] Milius, W. Strukturverfeinerung des Kupferionenleiters CuTeCl. *Z. anorg. allg. Chem.* **1990**, *586*(1), 175–184.

[11] Hirota, M.; Arai, M.; Sakuma, T.; Ishii, Y. Neutron Diffraction Study of CuClTe. *Electrochemistry* **2000**, *68*(6), 522–525.

[12] Beeken, R. B.; Haase, A. T.; Hoerman, B. H.; Sulzer, S. E. Ionic conduction in anion substituted CuBrTe. *Solid State Ion.* **1996**, *86*(6), 83–87.

[13] Carkner, P. M.; Haendler, H. M. The crystal structure of copper bromide telluride. *J. Solid State Chem.* **1976**, *18*(2), 183–189.

[14] von Alpen, U.; Fenner, J.; Bredel, B.; Rabenau, A.; Schluckbier, G. Über Tellurhalogenide des Kupfers mit hoher Ionen-Teilleitfähigkeit. III. Zur Phasenumwandlung von CuTeBr und zur Struktur der Hochtemperaturphase. *Z. anorg. allg. Chem.* **1978**, *438*, 5–14.

[15] Bachmann, R.; Kreuer, K.D.; Rabenau, A.; Schulz, H. Relationship between crystal structure and ionic conductivity in CuTeBr. *Acta Cryst. B* **1982**, *38*, 2361–2364.

[16] Arai, M.; Sakuma, T. Crystal Structure of β-CuBrTe. *J. Phys. Soc. Jnp.* **2001**, *70*(1), 144–147.

[17] Sakuma, T.; Kaneko, T.; Takahashi, H.; Honma, K.; Beeken, R. B. X-Ray Diffraction Study of the Low Temperature Phase Transitions of CuBrTe and CuITe. *J. Phys. Soc. Jnp.* **1992**, *61*(12), 4659–4660.

[18] Fenner, J.; Rabenau, A. Über Tellurhalogenide des Kupfers mit hoher Ionen-Teilleitfähigkeit. Die Kristallstruktur von CuTeI. *Z. Anorg. Allg. Chem* **1976**, *426*(1), 7–14.

[19] Fenner, J.; Schulz, H. Die Überstruktur des Kupfertelluridiodids CuTeI. *Acta Cryst. B* **1979**, *35*(2), 307–311.

[20] Schnieders, F.; Böttcher, P. Darstellung und Kristallstruktur von AgTeI. *Z. Kristallogr. - Cryst. Mater.* **1995**, *210*(5), 323–327.

[21] Milius, W.; Rabenau, A. The Crystal Structure of $CuSe_2Cl$. *Z. Naturforsch. B* **1988**, *43*(2), 243–244.

[22] Pfitzner, A.; Nilges, T.; Deiseroth, H.-J. $CuBrSe_2$: a Metastable Compound in the System CuBr/Se. *Z. anorg. allg. Chem.* **1999**, *625*(2), 201–206.

[23] Pfitzner, A.; Zimmerer, S. CuSeTeCl, CuSeTeBr und CuSeTeI: Verbindungen mit geordneten [SeTe]-Schrauben. *Z. anorg. allg. Chem.* **1995**, *621*(6), 969–974.

[24] Fenner, J. The crystal structure of $CuTe_2Cl$. *Acta Cryst. B* **1976**, *32*(11), 3084–3086.

[25] Pfitzner, A.; Zimmerer, S. $CuClS_{0.94}Te_{1.06}$ und $CuBrS_{0.92}Te_{1.08}$, zwei neue Kupfer(I)-chalkogenhalogenide mit neutralen [STe]-Schrauben. *Z. anorg. allg. Chem.* **1996**, *622*(2), 853–857.

[26] Milius, W. Refinement of the Crystal Structures of $CuTe_2Br$ and $CuTe_2I$. *Z. Naturforsch. B* **1989**, *44*(8), 990–992.

[27] Fenner, J.; Mootz, D. The crystal structure of gold telluride iodide AuTeI. *J. Solid State Chem.* **1978**, *24*(3–4), 367–369.

[28] Mootz, D.; Rabenau, A.; Wunderlich, H.; Rosenstein, G. The crystal structure of AuSeBr. *J. Solid State Chem.* **1973**, *6*(4), 583–586.

[29] Haendler, H.M.; Mootz, D.; Rabenau, A.; Rosenstein, G. The crystal structures of $AuTe_2Cl$ and $AuTe_2I$. *J. Solid State Chem.* **1974**, *10*(2), 175–181.

[30] Haendler, H. M.; Carkner, P. M. The crystal structure of copper bromide triselenide, $CuBrSe_3$. *J. Solid State Chem.* **1979**, *29*(1), 35–39.

[31] Sakuma, T.; Kaneko, T.; Kurita, T.; Takahashi, H. Crystal Structure of $CuBrSe_3$. *J. Phys. Soc. Japan* **1991**, *60*(5), 1608–1611.

[32] Pfitzner, A.; Zimmerer, S. Mixed chalcogen rings in copper(I) halides: crystal structures of $CuBrSe_{2.36}S_{0.64}$, $CuISe_{2.6}S_{0.4}$, and $CuISe_{1.93}Te_{1.07}$. *Z. Kristallogr. - Cryst. Mater.* **1997**, *212*(3), 203–207.

[33] Milius, W.; Rabenau, A. The crystal structure of copper iodide triselenide CuISe3, a reactant in an n-CuInSe2 based solar cell. *Mater. Res. Bull.* **1987**, *22*(11), 1493–1497.

[34] Wagener, M.; Deiseroth, H.-J.; Engelen, B.; Reiner, C.; Kong, S.T. AgX_3I (X = Se, Te) - Verbindungen mit formal neutralen cyclohexananalogen X_6-Ringen. *Z. anorg. allg. Chem.* **2004**, *630*(11), 1765.

[35] Deiseroth, H.-J.; Wagener, M.; Neumann, E. $(AgI)_2Te_6$ and $(AgI)_2Se_6$: New Composite Materials with Cyclic Te_6 and Se_6 Molecules Stabilized in the "Solid Solvent" AgI. *Eur. J. Inorg. Chem.* **2004**, *2004*(24), 4755–4758.

[36] Reuter, B.; Hardel, K. Über die Hochtemperaturmodifikation von Silbersulfidjodid. *Sci. Nat.* **1961**, *48*(6), 161.

[37] Reuter, B.; Hardel, K. Silbersulfidbromid und Silbersulfidjodid. *Angew. Chem.* **1960**, *72*(4), 138–139.

[38] Reuter, B.; Hardel, K. Silbersulfidbromid Ag_3SBr und Silbersulfidjodid Ag_3SI. II. Die Kristallstrukturen von Ag_3SBr, β- und α-Ag_3SI. *Z. anorg. allg. Chem.* **1965**, *340*(3–4), 168–180.

[39] Hull, S.; Keen, D. A., Gardner, N. J. G.; Hayes, W. The crystal structures of superionic Ag_3SI. *J. Phys.: Condens. Matter* **2001**, *13*(10), 2295.

[40] Beeken, R. B.; Wright, T.J.; Sakuma, T. Effect of chloride substitution in the fast ion conductor Ag₃SBr. *J. Appl. Phys.* **1999**, *85*(11), 7635–7638.

[41] Xianglian; Honda, H.; Basar, K.; Siagian, S.; Sakuma, T.; Takahashi, H.; Tubuqinbaer; Kawaji, H.; Atake, T. Low-Temperature Phase in Superionic Conductor Ag₃SBrₓI₁₋ₓ. *J. Phys. Soc. Japan* **2007**, *76*(11), 114603–114603.

[42] Perenthaler, E.; Schulz, H.; Beyeler, H. U. Structures and phase transition of β- and γ-Ag₃IS. *Acta Cryst. B* **1981**, *37*(5), 1017–1023.

[43] Perenthaler, E.; Schulz, H. Anharmonic temperature factors up to sixth order and atomic potentials in the fast ionic conductor α-Ag₃SI. *Solid State Ion.* **1981**, *2*(1), 43–46.

[44] Blachnik, R.; Dreisbach, H. A. The Phase Diagrams of Ag₂X-AgY (X = S, Se, Te; Y = Cl, Br, I): Mixtures and the Structure of Ag₅Te₂Cl. *J. Solid State Chem.* **1985**, *60*(1), 115–122.

[45] Doert, T.; Rönsch, E.; Schnieders, F.; Böttcher, P.; Sieler, J. Die Kristallstruktur der Tieftemperaturmodifikation von Ag₅Te₂Cl. *Z. anorg. allg. Chem.* **2000**, *626*(1), 89–93.

[46] Messel, J.; Nilges, T. Structure Chemical Aspects of Silver(I) Chalcogenide Halides and Preparation of the x = 1 Member of the Solid Solution Ag₅Te₂Cl₁₋ₓBrₓ. *Z. Naturforsch. B* **2008**, *63*(9), 1077–1082.

[47] Nilges, T.; Nilges, S.; Pfitzner, A.; Doert, T.; Böttcher, P. Structure-Property Relations and Diffusion Pathways of the Silver Ion Conductor Ag₅Te₂Cl. *Chem. Mater.* **2004**, *16*(5), 806–812.

[48] Nilges, T.; Dreher, C.; Hezinger, A. Structures, phase transitions and electrical properties of Ag₅Te₂₋ySeyCl (y = 0 - 0.7) *Solid State Sci.* **2005**, *7*(1), 79–88.

[49] Nilges, T.; Lange, S. Ag₅Te₂Cl₁₋ₓBrₓ (x = 0 - 0.65) and Ag₅Te₂₋ySyCl (y = 0 - 0.3): Variation of Physical Properties in Silver(I) Chalcogenide Halides. *Z. anorg. allg. Chem.* **2005**, *631*(15), 3002–3012.

[50] Nilges, T.; Lange, S. Ag₅Te₂₋ySeyCl und Ag₅Te₂Cl₁₋ₓBrₓ: Struktur-Eigenschaftsvariationen durch Anionenaustausch. *Z. anorg. allg. Chem.* **2004**, *630*(11), 1749–1749.

[51] Nilges, T.; Messel, J.; Bawohl, M.; Lange, S. Silver(I) Chalcogenide Halides Ag₁₉Te₆Br₇, Ag₁₉Te₆Br₅.₄I₁.₆, and Ag₁₉Te₅SeBr₇. *Chem. Mater.* **2008**, *20*(12), 4080–4091.

[52] Nilges, T. The Solid Solutions $M_{19}Q_6X_7$ with M = Ag, Cu; Q = S, Se, Te and X = S, Se, Te. *Z. anorg. allg. Chem.* **2008**, *634*(12-13), 2185–2190.

[53] Beeken, R. B.; Beeken, E. M. Ionic conductivity in Cu-substituted Ag_3SBr. *Solid State Ion.* **2000**, *136*, 463–467.

[54] Lange, S.; Nilges, T. $Ag_{10}Te_4Br_3$: A New Silver(I) (poly)Chalcogenide Halide Solid Electrolyte. *Chem. Mater.* **2006**, *18*(10), 2538–2544.

[55] Lange, S.; Bawohl, M.; Wilmer, D.; Meyer, H.-W.; Wiemhöfer, H.-D.; Nilges, T. Polymorphism, Structural Frustration, and Electrical Properties of the Mixed Conductor $Ag_{10}Te_4Br_3$. *Chem. Mater.* **2007**, *19*(6), 1401–1410.

[56] Nilges, T.; Bawohl, M. Structures and Thermal Properties of Silver(I) (Poly)chalcogenide Halide Solid Solutions $Ag_{10}Te_{4-(q,p)}Q_{(q,p)}Br_3$ with Q = S, Se. *Z. Naturforsch. B* **2008**, *63*(6), 629–636.

[57] Nilges, T.; Bawohl, M.; Lange, S. $Ag_{10}Te_4Br_{3-x}Cl_x$ and $Ag_{10}Te_4Br_{3-y}I_y$: Structural and Electrical Property Tuning of a Mixed Conductor by Partial Anion Substitution. *Z. Naturforsch. B* **2007**, *62*(7), 955–964.

[58] Giller, M.; Bawohl, M.; Gerstle, A.P.; Nilges, T. Copper Substitution and Mixed Cation Effect in $Ag_{10}Te_4Br_3$. *Z. anorg. allg. Chem.* **2013**, *639*(14), 2379–2381.

[59] Lange, S.; Bawohl, M.; Nilges, T. Crystal Structures and Thermal and Electrical Properties of the New Silver (poly)Chalcogenide Halides $Ag_{23}Te_{12}Cl$ and $Ag_{23}Te_{12}Br$. *Inorg. Chem.* **2008**, *47*(7), 2625–2633.

[60] Pfitzner, A.; Zimmerer, S. $(CuI)_3Cu_2TeS_3$: Layers of Cu_2TeS_3 in Copper(I) Iodide. *Angew. Chem. Int. Ed.* **1997**, *36*(9), 982–984.

[61] Pfitzner, A. $CuClCu_2TeS_3$: Synthesis, Structure Determination, and Raman Spectroscopic Characterization of a New Zincblende Derivative. *Inorg. Chem.* **1998**, *37*(20), 5164–5167.

[62] Pfitzner, A.; Baumann, F.; Kaim, W. $TeS_2^{\bullet-}$ Radical Anions in $CuBrCu_{1.2}TeS_2$. *Angew. Chem. Int. Ed.* **1998**, *37*(13-14), 1955–1957.

[63] Pfitzner, A. The use of copper(I) halides as a preparative tool. *Chem. Eur. J.* **2000**, *6*, 1891–1898.

[64] Pfitzner, A.; Reiser, S.; Nilges, T.; Kockelmann, W. Composite Copper Chalcogenide Halides: Neutron Powder Diffraction of $CuClCu_2TeS_3$ and Electrical Properties of $CuClCu_2TeS_3$, $(CuI)_2Cu_3SbS_3$, and $(CuI)_3Cu_2TeS_3$. *J. Solid State Chem.* **1999**, *147*(1), 170–176.

[65] Freire-Erdbrügger, C.; Jentsch, D.; Jones, P.G.; Schwarzmann, E. Preparation and Crystal Structure of [TeBr$_3$][AuBr$_4$] · $\frac{1}{2}$ Br$_2$, a Compound with "Bromine of Crystallization". *Z. Naturforsch. B* **1987**, *42*(12), 1553–1555.

[66] Fokina, Z. A.; Timoshchenko, N. I.; Lapko, V. F.; Volkov, S. V. Electron and vibration-spectra of chalcogen-chloride complexes of gold. *Ukr. Khim. Zhur.* **1982**, *48*(10), 1014–1016.

[67] Fokina, Z. A.; Lapko, V. F. X-ray study of chalcogene-chloride gold compounds. *Ukr. Khim. Zhur.* **1988**, *54*(10), 1015–1016.

[68] Jones, P. G.; Jentsch, D.; Schwarzmann, E. Trichlorosulfonium(IV) tetrachloroaurate(III). *Acta Cryst. C* **1988**, *44*(2), 210–212.

[69] Jones, P. G.; Schelbach, R.; Schwarzmann, E. Trichloroselenonium(IV) tetrachloroaurate(III). *Acta Cryst. C* **1987**, *43*(4), 607–609.

[70] Jones, P. G.; Jentsch, D.; Schwarzmann, E. The Crystal Structure of TeCl$_3^+$AuCl$_4^-$. *Z. Naturforsch. B* **1986**, *41*(11), 1483–1484.

[71] Pauling, L. *The Nature of the Chemical Bond*; Vol. 260; Cornell university press: Ithaca, NY, **1960**.

[72] Bensch, W.; Dürichen, P. Caesium Gadolinium Tetratelluride. *Acta Cryst. C* **1997**, *53*(3), 267–269.

[73] Assoud, A.; Derakhshan, S.; Soheilnia, N.; Kleinke, H. Electronic Structure and Physical Properties of the Semiconducting Polytelluride Ba2SnTe5 with a Unique Te$_5^{4-}$ Unit. *Chem. Mater.* **2004**, *16*(21), 4193–4198.

[74] Chen, X.; Huang, X.; Li, J. Rb$_4$Hg$_5$(Te$_2$)$_2$(Te$_3$)$_2$Te$_3$, [Zn(en)$_3$]$_4$In$_{16}$(Te$_2$)$_4$(Te$_3$)Te$_{22}$, and K$_2$Cu$_2$(Te$_2$)(Te$_3$): Novel Metal Polytellurides with Unusual Metal-Tellurium Coordination. *Inorg. Chem.* **2001**, *40*(6), 1341–1346.

[75] Huang, S.D. and Lai, C.P. and Barnes, C.L. Organometallic Chemistry under Hydro(solvo)thermal conditions: Synthesis and X-ray structure of (Ph$_4$P)$_2$[Mn$_3$(CO)$_9$(S$_2$)$_2$(SH)], (Ph$_4$P)[Mn$_2$(CO)$_6$(SH)$_3$], and (Ph$_4$P)$_2$[Mn$_4$(CO)$_{13}$(Te$_2$)$_3$]. *Angew. Chem. Int. Ed.* **1997**, *36*(17), 1854–1856.

[76] Shi, Y.; Assoud, A.; Sankar, C. R.; Kleinke, H. Tl$_2$Ag$_{12}$Se$_7$: a new pnp conduction switching material with extraordinarily low thermal conductivity. *Chem. Mater* **2017**, *29*(21), 9565–9571.

[77] Xiao, C.; Qin, X.; Zhang, J.; An, R.; Xu, J.; Li, K.; Cao, B.; Yang, J.; Ye, B.; Xie, Y. High thermoelectric and reversible pnp conduction type switching integrated in dimetal chalcogenide. *J. Am. Chem. Soc.* **2012**, *134*(44), 18460–18466.

[78] Guin, S. N.; Pan, J.; Bhowmik, A.; Sanyal, D.; Waghmare, U. V. and Biswas, K. Temperature dependent reversible p–n–p type conduction switching with colossal change in thermopower of semiconducting AgCuS. *J. Am. Chem. Soc.* **2014**, *136*(36), 12712–12720.

[79] Nilges, T.; Osters, O.; Bawohl, M.; Bobet, J.-L.; Chevalier, B.; Decourt, R.; Weihrich, R. Reversible property switching, thermoelectric performance, and d^{10}-d^{10} interactions in Ag_5Te_2Cl. *Chem. Mater* **2010**, *22*(9), 2946–2954.

[80] Jansen, M. Homoatomic d^{10}-d^{10} interactions: their effects on structure and chemical and physical properties. *Angew. Chem. Int. Ed.* **1987**, *26*(11), 1098–1110.

[81] Stiny, L. *Aktive elektronische Bauelemente*; Springer Vieweg: Wiesbaden, Deutschland; **2016**.

[82] Stoe & Cie GmbH, *WinXPOW* **2011**, Version 3.0.2.1.

[83] P. Villars and K. Cenzual. *Pearson's Crystal Data: Crystal Structure Database for Inorganic Compounds (on CD-ROM)*. Release 2013/2014.

[84] Yvon, K.; Jeitschko, W.; Parthe, E. LAZY PULVERIX, a computer program, for calculating X-ray and neutron diffraction powder patterns. *J. Appl. Crystallogr.* **1977**, /textit10(1), 73-74.

[85] Stoe & Cie GmbH, *X-Area* **2015**, Version 1.76.

[86] Stoe & Cie GmbH, *X-Red* **2015**, Version 1.62.2.

[87] Stoe & Cie GmbH, *X-Shape* **2015**, Version 2.18.

[88] Hahn, T. *International Tables for Crystallography, Volume A: Space group symmetry*; Kluwer Academic: Dordrecht, Niederlande; **2002**.

[89] Wondratschek, H.; Müller, U. *International Tables for Crystallography, Volume A1: Symmetry relations between space groups*; Kluwer Academic: Dordrecht, Niederlande; **2004**.

[90] Petříček, V.; Dušek, M.; Palatinus, L., *JANA2006, The Crystallographic Computing System*; Institute of Physics: Prag, Tschechien; **2006**.

[91] Petříček, V.; Dušek, M.; Palatinus, L. Crystallographic Computing System JA-NA2006: General features. *Z. Kristallogr. - Cryst. Mater.* **2014**, *229*(5), 345–352.

[92] Palatinus, L.; Chapuis, G. SUPERFLIP–a computer program for the solution of crystal structures by charge flipping in arbitrary dimensions. *J. Appl. Crystallogr.* **2007**, *40*(4), 786–790.

[93] Willis, B. T. M. Lattice vibrations and the accurate determination of structure factors for the elastic scattering of X-rays and neutrons. *Acta Crystallogr. A* **1969**, *25*(2), 277–300.

[94] Zucker, U. H.; Schulz, H. Statistical approaches for the treatment of anharmonic motion in crystals. I. A comparison of the most frequently used formalisms of anharmonic thermal vibrations. *Acta Crystallogr. A* **1982**, *38*(5), 563–568.

[95] Zucker, U. H.; Schulz, H. Statistical approaches for the treatment of anharmonic motion in crystals. II. Anharmonic thermal vibrations and effective atomic potentials in the fast ionic conductor lithium nitride (Li_3N). *Acta Crystallogr. A* **1982**, *38*(5), 568–576.

[96] Bachmann, R.; Schulz, H. Anharmonic potentials and pseudo potentials in ordered and disordered crystals. *Acta Crystallogr. A* **1984**, *40*(6), 668–675.

[97] Kuhs, W. F. Generalized atomic displacements in crystallographic structure analysis. *Acta Crystallogr. A* **1992**, *48*(2), 80–98.

[98] Petříček, V.; Dušek, M.; Plášil, J. Crystallographic computing system Jana2006: solution and refinement of twinned structures. *Z. Kristallogr. - Cryst. Mater.* **2016**, *231*(10), 583–599.

[99] Smits, F. M. Measurement of sheet resistivities with the four-point probe. *Bell Syst. Tech. J.* **1958**, *37*(3), 711–718.

[100] Valdes, L. B. Resistivity measurements on germanium for transistors. *Proc. IRE* **1954**, *42*(2), 420–427.

[101] Dusza, L. Combined solution of the simultaneous heat loss and finite pulse corrections with the laser flash method. *High Temp. High Press.* **1995**, *27*(5), 467–473.

[102] Cape, J. A.; Lehman, G. W. Temperature and finite pulse-time effects in the flash method for measuring thermal diffusivity. *J. Appl. Phys.* **1963**, *34*(7), 1909–1913.

[103] Blumm, J.; Opfermann, J. Improvement of the mathematical modeling of flash measurements. *High Temp. - High Press.* **2002**, *34*(5), 515–521.

[104] Dulong, P. L.; Petit, A. T. *Recherches sur la mesure des températures et sur les lois de la communication de la chaleur*; De l'Imprimerie royale: Paris, Frankreich; **1818**.

[105] Jephcoat, A. P.; Hemley, R.J.; Mao, H. K. X-ray diffraction of ruby (Al_2O_3:Cr^{3+}) to 175 GPa. *Phys. B C* **1988**, *150*(1–2), 115–121.

[106] Richet, P.; Xu, J.-A.; Mao, H.-K. Quasi-hydrostatic compression of ruby to 500 Kbar. *Phys. Chem. Miner.* **1988**, *16*(3), 207–211.

[107] Wojdyr, M. Fityk: A general-purpose peak fitting program. *J. Appl. Cryst.* **2010**, *43*(5), 1126–1128.

[108] Birch, F. Finite elastic strains of cubic crystals. *Phys. Rev.* **1947**, *71*, 809.

Abbildungsverzeichnis

Tabellenverzeichnis